High-order Unfitted Discretizations for Partial Differential Equations Coupled with Geometric Flow

Dissertation
for the award of the degree
Doctor rerum naturalium
of the
Georg-August-Universität Göttingen

within the doctoral program
Mathematical Sciences
of the **G**eorg-**A**ugust **U**niversity **S**chool of **S**cience

submitted by

Yimin Lou
from Hangzhou, Zhejiang, China

Göttingen, 2021

Thesis Committee

Prof. Dr. Christoph Lehrenfeld
Institute for Numerical and Applied Mathematics
Georg-August-Universität Göttingen

Prof. Dr. Gert Lube
Institute for Numerical and Applied Mathematics
Georg-August-Universität Göttingen

Members of the Examination Board

Reviewer: Prof. Dr. Christoph Lehrenfeld

Co-reviewer: Prof. Dr. Gert Lube

Further members of the Examination Board:

Prof. Dr. Ingo Witt
Mathematical Institute
Georg-August-Universität Göttingen

Prof. Dr. Viktor Pidstrygach
Mathematical Institute
Georg-August-Universität Göttingen

Prof. Dr. Dominic Schuhmacher
Institute for Mathematical Stochastics
Georg-August-Universität Göttingen

Prof. Dr. Marcus Baum
Institute of Computer Science
Georg-August-Universität Göttingen

Date of the oral examiniation: 2022-02-18

Acknowledgements

My odyssey from engineering to mathematics is challenging. Fortunately, I have encountered many wonderful people along the adventure who have made great contributions to my personal and professional development.

I owe the beginning of the endeavor to one of my best friends Dr. Yilun Wu, who was a doctoral student in the Department of Mathematics at the University of Michigan when I was a master's student in the Department of Aerospace Engineering. He drew my very initial interest from computational fluid dynamics to the underlying math, and taught me much mathematics of the major at undergraduate level. I am also grateful for the amazing lectures in both departments offered by Prof. Joel Smoller, Prof. Mark Rudelson, Prof. Krzysztof Fidkowski, Prof. Bram van Leer, and especially, Prof. Philip L. Roe who not only directed my master's project but also let me participate in his research group to work with his doctoral student Tyler B. Lung. I have learned a lot from each of them during the lovely days in Ann Arbor, MI in the United States.

Encouraged by Peter D. Lax who said in a dialogue that he urges his students to spend at least a summer as a visitor at Los Alamos National Laboratory for active programs, I began to seek an opportunity there after graduation. I am indebted to Dr. William Dai for his reference on my behalf, through which I became a visiting student at Los Alamos National Laboratory and followed Dr. Shengtai Li in the T-5 Group of Applied Mathematics and Plasma Physics, where I met some notable mathematicians like Dr. Burton Wendroff and enjoyed celebrating his 85^{th} birthday in the research group. I highly appreciate the discussions with these mathematicians, from which I felt my math background was too weak. Hence I was eager to transfer my study from engineering to mathematics, and desired to pursue a doctoral degree in applied math.

A bronze statue of J. Robert Oppenheimer stands at the center of Los Alamos town near my apartment, so that I saw it everyday at that time. Enlightened by his expedition to the leadership of the Los Alamos Laboratory for the Manhattan Project after receiving his doctoral degree under Max Born from Göttingen in 1927, I was attracted by the Mecca of Mathematics from the era of Carl Friedrich Gauss and Bernhard Riemann to that of Felix Klein and David Hilbert. During the Hilbert's years,

in 1922 the faculty of mathematics and natural sciences separated from the faculty of philosophy, when this leading center for mathematical sciences over the world was surrounded by a number of the most influential mathematicians of the 20^{th} century, e.g., Emmy Noether, Hermann Weyl, Richard Courant, and John von Neumann.

I am therefore deeply honored and grateful to my co-advisor Prof. Gert Lube for introducing me to admission to the GAUSS doctoral program in the Institute for Numerical and Applied Mathematics at the University of Göttingen in Germany once I contacted and applied. It would not have been possible for me to start my mathematical study without his kind assistance. He has also given excellent lectures on theory and numerics of partial differential equations and of fluid mechanics, which serve as a foundation of my research. Moreover, I would like to express my foremost gratitude to my supervisor Prof. Christoph Lehrenfeld, who is a superb teacher, a patient mentor, a brilliant collaborator, and a nice friend over the past years in my life. His talent and expertise in the area of numerical mathematics are impressive, and his diligence is far beyond mine as well. He is always on standby even for my naive questions. He has offered me several exciting opportunities to travel to beautiful places for delivering my presentations in mathematical conferences. I have learned a lot of knowledge from his courses and seminars on numerical partial differential equations, as well as the Oberseminars held by him and Prof. Gert Lube. I am really appreciative of all the intelligent support they have given me.

In addition to my doctoral advisors and reviewers of this dissertation, I would also like to thank Prof. Ingo F. Witt and Prof. Viktor Pidstrygach in the Mathematical Institute, from whose lectures on analysis of partial differential equations, functional analysis, and differential geometry I have greatly benefited. I am indebted to them together with Prof. Stephan Huckemann, Prof. Dominic Schuhmacher, and Prof. Marcus Baum who are willing to constitute my doctoral examination committee.

My fellow students here in the research group of Computational Partial Differential Equations have made graduate school more entertaining than it would have otherwise been. In particular, I would like to thank Janosch Preuss and Fabian Heimann for our enjoyable journeys, scientific meetings and interesting discussions, as well as Anna Clara Wendler for her proofreading of the first two chapters of this dissertation.

I am thankful beyond words to my parents for their love and encouragement. Nothing that I have endeavored to this point in my life would have been possible without the unwavering support I have received from my family.

To conclude, I gratefully acknowledge funding by the German Science Foundation (DFG) within the project "LE 3726/1-1" that financially supported my study and work.

Abstract

We consider a moving free boundary problem where a diffusion equation posed on an evolving domain bounded by a smooth surface is coupled with a mean curvature flow of the bounding surface. The evolution velocity of the geometry is not a priori known but has to be determined, as a part of the problem, by the solution to the diffusion equation and the mean curvature vector of the surface. We develop and analyze new geometrically unfitted discretization methods for solving the diffusion equation and a geometric equation of the mean curvature vector at provable high orders of accuracy. We test the methods with numerical experiments which show convergence rates predicted by our a priori error estimates. With a level set function implicitly representing the geometry, we solve an advection equation of the level set domain transported by a velocity field extended from the surface. To this end, we propose two velocity extension methods and take advantage of a high-order numerical method for hyperbolic conservation laws. By unfolding the geometrically coupled bulk-surface model into three sub-models solved using the methods, we conduct proof-of-concept numerical simulations of this solution-curvature-driven moving free boundary problem.

Table of contents

List of figures

List of tables

Chapter 1

Introduction

1.1 Genesis of the Problem

Partial differential equations (PDEs) posed on complex and evolving geometries are involved in the mathematical modeling of many phenomena in science and technology. A *free boundary problem* (FBP) arises if there is a system of PDEs to be solved for both unknown functions and unknown geometry. Furthermore, if the a priori unknown geometry is time-dependent, it is called a *moving* FBP. Free surface or multi-phase flow, fluid-structure interaction, plasma confinement, shock wave and flame propagation are notable examples of FBP where prossibly large deformations and even topological changes of the geometries give rise to the difficulty of numerical simulation.

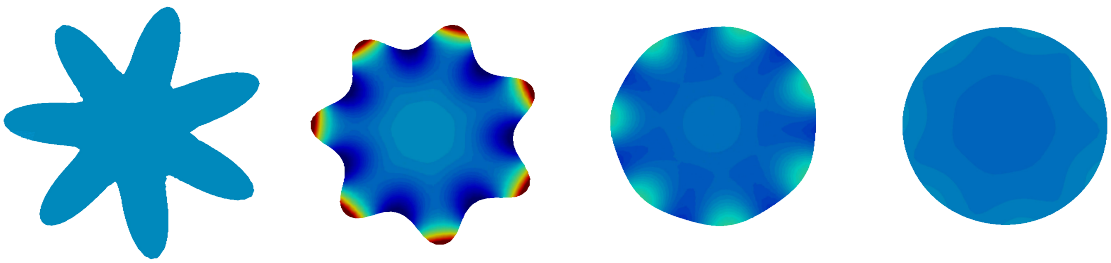

(a) $t = t_0$ (b) $t = t_1$ (c) $t = t_2$ (d) $t = t_3$

Fig. 1.1 Osmotic cell swelling problem at four time instances t_0, t_1, t_2, and t_3.

Another significant field of such applications is cell biology, especially in the process of cell division, where the geometrical shape of a cell may vary in time depending on the shape itself and the quantities subject to PDEs on the evolving cell. Figure 1.1 is a sketch of the so-called *osmotic cell swelling problem* for a cell evolving through four time instances t_0, t_1, t_2, and t_3. A biological cell is immersed in a stationary environment.

A time-dependent diffusion equation of some chemical concentration describes the diffusion phenomenon inside the cell, which gives a distribution of the solute on the selectively permeable membrane of the cell. This semi-permeable membrane is permeable to the solvent but impermeable to the solute. Hence the distribution of the solute, on the one hand, leads to a spontaneous movement of the membrane through osmotic pressure. The curved membrane, on the other hand, causes a surface tension that enforces the membrane moving towards a minimal surface, which can be measured by the mean curvature of the surface. These two forces compete against each other and together determine the acceleration of the membrane. Apart from the membrane, physical velocity is neither present in the interior nor the exterior of the cell. The short-time existence and uniqueness of classical solutions to this single-phase osmosis model have been proved in [111]. This toy model can be employed to represent the whole class of moving FBPs, which is not only at the cutting edge of theoretical and numerical PDEs, but also a rapidly expanding subject area by the emerging of an abundance of important topics and real-world applications since the famous *Stefan problem* proposed in [152], see [30] for an overview. Unlike the classical Stefan problem that describes the melting from ice to water, the osmosis model has a more sophisticated free boundary evolving subject to the geometric object – the mean curvature.

In the context of this thesis, we call such a moving FBP *geometrically coupled* if the PDEs of physics (i.e., conservation laws) are associated with some PDE of geometry (i.e., geometric flow). In the osmosis model, more specifically, we consider the membrane of the cell as a smooth bounding hypersurface embedded in a Riemannian manifold. The normal component of the velocity with which any point on the hypersurface moves depends partially on the mean curvature. The hypersurface arises as the boundary of the enclosed domain (i.e., the cell) where some PDEs of physical phenomena (i.e., diffusion) are posed, and the trace of the solution to the PDEs (i.e., the distribution of the solute on the membrane) also acts on the evolution of the bounding hypersurface. If the solution to the PDEs is trivial, the normal velocity of the hypersurface is solely given by the mean curvature, and the problem is reduced to a *mean curvature flow*. If, on the other hand, the geometric evolution is a priori known, the problem results in solving the PDEs on a *given moving domain*.

In this thesis, we only study connected closed hypersurfaces smoothly embedded and evolving in a two- or three-dimensional Euclidean space, i.e., plane curves or surfaces. Although this has greatly simplified the problem, it is still too complicated to write out an exact solution in closed form or analytic expression. Therefore, the development and analysis of the numerical methods of *high-order accuracy* and *computational efficiency*

for approximate solutions to such geometrically coupled problems is the challenging task we are dedicated to. In comparison to other related research in this subject area, we will develop geometrically *unfitted* finite element methods (FEM) with *provable* high-order error estimates, where the mesh discretization is not fitted to the evolving hypersurface but fixed as a stationary background. Based on this unfitted discretization, large deformations and topological changes of a complex geometry can be handled easily in such a way that the zero level set of a real-valued auxiliary function, i.e., *level set function*, is exploited to describe the bounding hypersurface. This approach enjoys much lower computational cost and simpler operational procedures by saving the re-meshing time in contrast to the so-called geometrically fitted methods.

1.2 Mathematical Models

We aim at solving the geometrically coupled *solution-curvature-driven* moving free boundary problem (FBP) where the evolution velocity of the bounding hypersurface is an unknown depending on the mean curvature vector and the quantities subject to PDEs posted on the enclosed domain.

Some theoretical research has been conducted towards the above-mentioned FBP and the related osmosis model where osmotic pressure from diffusion and surface tension from curvature compete with each other. In [65] the so-called closed osmometer problem, first introduced in [136], is solved analytically and numerically in one spatial dimension. For wellposedness and regularity results for the single-phase model with radially symmetric initial conditions, short-time existence and uniqueness of solutions in a proper Sobolev space are shown in [166]. Based on maximal regularity results (for parabolic systems with inhomogeneous boundary conditions), the existence and uniqueness of classical solutions on small time intervals, and on arbitrary long time intervals if the initial geometry is close to an equilibrium, are proven in [111]. A reasonable extension of the model by involving viscosity, i.e., the Stokes equations, is investigated in [110], and the existence of classical solutions for a short time to this problem is shown by the authors.

To the best of our knowledge, however, analytic solution in a closed-form expression to the geometrically coupled moving FBP is only possible under very certain conditions, e.g., linearity, regularity, symmetry, spatial dimensionality or temporal duration. In general, such an analytic solution is not known to exist even for the one-phase osmosis model – a sophisticated coupled bulk-surface model but a toy model among the class

of geometrically coupled moving FBP. Towards solving this PDE problem, we propose the following three sub-models to unfold it:

1. Provided that the evolution of a time-dependent geometry is given, we seek the solution to PDEs posed on the geometry. Let u be the solution to the parabolic diffusion equation $\partial_t u - \nu\Delta u = 0$ in a Lipschitz domain $\Omega(t) \subset \mathbb{R}^d$, $d = 2, 3$, $t \in \mathbb{R}_+$, with the boundary condition $wu + \nu\nabla u \cdot \mathbf{n} = 0$ on $\Gamma(t) := \partial\Omega(t)$ where $w(\mathbf{x}, t) \in \mathbb{R}$ is the normal velocity of $\Gamma(t)$ and $\mathbf{n}(\mathbf{x}, t) \in \mathbb{R}^d$ the outward unit normal, and $\nu \in \mathbb{R}_+$ a constant diffusion coefficient. We solve this diffusion equation on the evolving domain $\Omega(t)$ equipped with the Lipschitz boundary $\Gamma(t)$, which is time-varying under smooth motion, deformation, and even topological changes. See Figure 1.2 for a sketch of this problem and Chapter 3 for details.

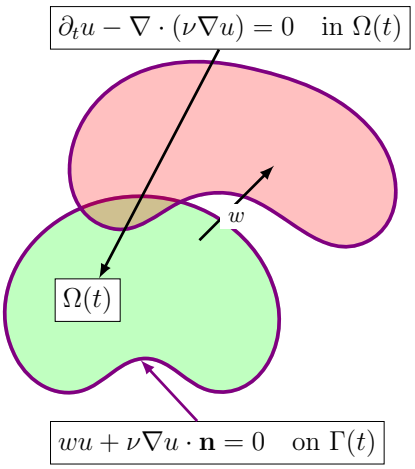

Fig. 1.2 The diffusion equation on an evolving domain with no-flux boundary condition.

2. Provided that the solution to the PDEs and the geometry at a fixed time are given, we compute the evolution velocity of the bounding hypersurface [1]. Let $\Gamma := \partial\Omega$ be the bounding surface (or plane curve) arising as the boundary of the enclosed domain such that it is sufficiently smooth to have the mean curvature κ well-defined at every point on the surface. We model the normal component of the surface velocity [2] by $w := -\alpha\kappa + \beta u|_\Gamma$, $\alpha, \beta \in \mathbb{R}_+$ that linearly depends on κ and the solution u restricted to the surface. As u is given, we seek the mean

[1] Note that a *plane curve* is a one-dimensional hypersurface embedded in $\mathbb{R}^2$ and a *surface* is a two-dimensional hypersurface embedded in $\mathbb{R}^3$, but we may occasionally mix the usage of the terms and use two-dimensional concepts for their one-dimensional counterparts, e.g., edge, facet, and volume.

[2] From here on, we identify *surface velocity* as the abbreviation for *the normal component of the velocity of the hypersurface*. Note that the surface velocity solely determines – i.e., the tangential component of the velocity of the hypersurface does not affect – the motion of the hypersurface.

curvature vector $\mathbf{H}$ by solving the geometric equation $\mathbf{H} := \kappa\mathbf{n} = -\Delta_\Gamma \mathbf{x}$ on Γ with Laplace-Beltrami operator Δ_Γ. See Figure 1.3 for a sketch of this problem and Chapter 4 for details.

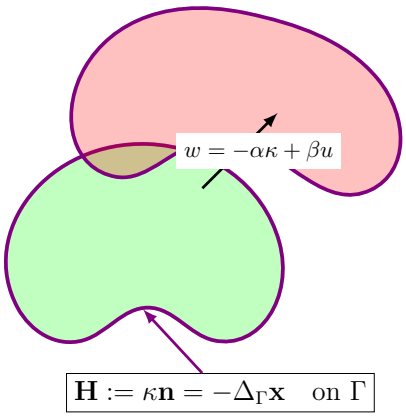

Fig. 1.3 The geometric equation of mean curvature and the velocity on the surface.

3. Provided that the surface velocity is given, we extend it onto a time-independent background domain and transport the enclosed domain of interest. Rather than a Lagrangian approach that tracks the motion of each particle of the bounding surface, we look into the geometric evolution from an Eulerian viewpoint. Let $\bar{\Omega} \supsetneq \Omega(t),\ t \in \mathbb{R}_+$ be a background domain that properly contains the moving domain with its neighborhood for all time of investigation. Let $\phi : \bar{\Omega} \times \mathbb{R}_+ \to \mathbb{R}$ be a real-valued function called level set function such that the bounding surface and the enclosed domain are represented by $\Gamma(t) = \{\mathbf{x} \in \bar{\Omega} \mid \phi(\mathbf{x}, t) = 0\}$ and $\Omega(t) = \{\mathbf{x} \in \bar{\Omega} \mid \phi(\mathbf{x}, t) < 0\}$, respectively. The surface velocity $w(\mathbf{x}, t)$ on $\Gamma(t)$ can be extended to $\mathbf{w}(\mathbf{x}, t)$ on $\bar{\Omega}$ by using an extension operator $\mathcal{E} : \mathcal{C}(\Gamma) \to \mathcal{C}(\mathbb{R}^d)$ with the restriction $\mathbf{w} = w\mathbf{n}$ on $\Gamma(t)$. With the velocity field $\mathbf{w}(\mathbf{x}, t)$, the evolution of $\Omega(t)$ described by $\phi(\mathbf{x}, t)$ can be obtained by solving the hyperbolic advection equation $\partial_t \phi + \mathbf{w} \cdot \nabla\phi = 0$ over $\bar{\Omega}$. See Figure 1.4 for a sketch of this problem and Chapter 5 for details.

Next, we will discuss the numerical methods to solve each of the three sub-models approximately.

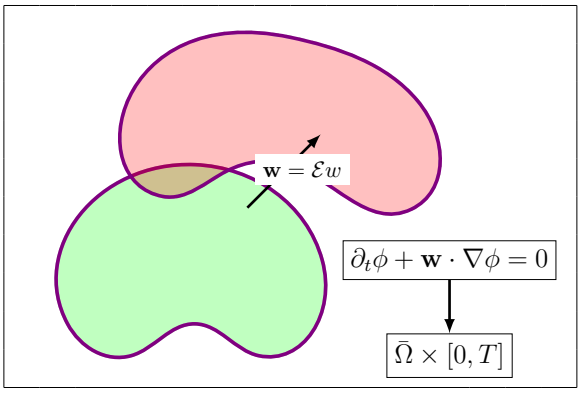

Fig. 1.4 A transport equation of the level set domain with extended velocity field.

1.3 Numerical Methods

It is either impossible or impracticable to seek analytical solutions to many advanced PDE problems, the applied math community has therefore developed a number of computational methods for numerical approximations to the exact solutions. In this section, we briefly present an overview of the numerical methods, based on which we will develop new discretizations to solve the geometrically coupled system of PDEs.

Finite element method (FEM) is one of the most popular and powerful class of techniques with solid mathematical foundation for finding approximate solutions to PDEs. It was first proposed in a seminal work of Richard Courant in 1943, cf. [48], and the first important result in the sense of mathematical analysis was due to Milos Zlámal in 1968, cf. [171]. In the context of modern FEM, there are essentially two categories with respect to the approximation of the underlying geometry: *fitted* and *unfitted* discretizations.

For geometrically stationary problems, a fitted characterization is widely used. To this end, a parametric description is exploited for domains with curved boundaries. In general, the parametrization for approximating the geometry is utilized to express the numerical solution to PDEs as well. For instance, an approach called *isogeometric analysis* integrates *finite element analysis* (FEA) into *computer-aided design* (CAD) with using a common data set, in which the basis functions for FEA are also employed to describe the geometry in CAD , cf. [47, 85]. Thanks to the explicit mapping to a reference geometry consisting of uncurved elements, higher-order approximation of the geometry can easily ally with higher-order finite element discretizations. We refer the reader to an established literature for more details, cf. [2, 52, 91, 155].

In the past decades, *discontinuous Galerkin* (DG) methods [5, 107, 134, 135], and *hybrid discontinuous Galerkin* (HDG) methods [34, 119], have been developed for more

flexibility, efficiency, and stability, by relaxing the conformity of the standard high-order FEM. Combined with the classical *Runge–Kutta* (RK) methods [94, 137] for multi-stage time steppting, *Runge–Kutta discontinuous Galerkin* (RKDG) methods have been proposed for solving time-dependent PDEs robustly at high order of accuracy in space and time, and been developed by Cockburn et al. in a series of literature, cf. [36–38, 40, 42]. The methods have found their way into the mainstream of *computational fluid dynamics* (CFD) by a wide range of real-world applications, especially to advection-dominated problems, cf. [41]. Some theoretical analysis of the RKDG methods for hyperbolic conservation laws has been presented recently, e.g., in [35, 164, 168–170].

The geometrically fitted methods above are basically developed for problems with time-independent domains. Towards geometrically non-stationary problems where the domains are time-varying, on the other hand, both fitted and unfitted discretizations have been studied. In the fitted class of approaches, i.e., *Lagrangian* framework, a computational mesh is generated for the initial geometry, and adapted to the motion of the geometry by mesh deformation in time, aiming to track the evolving geometry. A very popular approach is called *Arbitrary Lagrangian Eulerian* (ALE) formulation for problems with moving domains, cf. [43, 56]. This kind of methods, if applicable, allows standard finite element discretizations and usually obtains accurate results as a consequence. However, a major issue of this approach arises from large deformations or topological changes of the underlying geometry. Consequently, these methods are often involved in complicated and time-consuming procedures for re-meshing, and even fail in mesh manipulation.

The idea of separating the geometry description from the computational mesh gives rise to the geometrically unfitted discretization, i.e., *Eulerian* framework, which allows for a very flexible handling of the underlying geometry. To this end, a basis discretization is defined on a time-independent background mesh, and typically a simple polygonal domain. This discretization is adapted to the geometrical information according to the independently defined geometry during the evolution. One major advantage of this approach is the capability to handle complex and time-varying geometrical configurations without the computationally expensive mesh generation and re-meshing procedures, which makes it especially appealing in the applications that have dramatic evolution of the underlying geometries. For instance, in multi-phase flow or in cell dynamics, the interface of fluids or cell membrane is often moving dramatically, and the impact from the geometric evolution on the fluid dynamics or the dissolved concentrations is of particular interest.

In order to formulate a geometrically unfitted discretization, a specific description of the geometry is required, of which the choice results in a particular PDE prescribing the geometric evolution, and the discretization method in turn depends essentially on the way one selects to represent the geometry. In this thesis, we exploit the so-called *level set method*, which has been introduced since the pioneering work of Dervieux in [54], and subsequently developed by Osher and Sethian in a series of literature, cf. [29, 126, 142–146]. It has become very popular in many applications of subjects, such as computer graphics, image processing, computational geometry, optimization, computational biology, and CFD. A number of level-set data structures have been built to facilitate the utilization of the level set method in computer science, cf. [161]. The main idea of the level set method is to define a real-valued auxiliary function – level set function – whose negative level sets typically specifies an open bounded domain (i.e., the level set domain), and the zero level set consequently describes the boundary of the domain (i.e., the bounding hypersurface).

A variety of unfitted finite element discretizations exist. For non-aligned boundary value problems, *penalty methods* [8, 133], *fictitious domain method* [24, 71], *immersed boundary method* [129] have been developed. For unfitted interface problems, *extended finite element methods* (XFEM) have been proposed in [13, 14, 64, 79, 81, 115]. For PDEs posed on moving domains, several *unfitted space-time methods* [83, 97, 98, 167], and *Eulerian finite element method* (Eulerian FEM) [22, 102, 114, 157], have been developed recently. For PDEs on static or evolving surfaces, *cut finite element method* (CutFEM) and *trace finite element method* (TraceFEM) [26, 32, 73, 75, 120–124] have been studied extensively, as well as *finite cell method* (FCM) [127] and *unfitted discontinuous Galerkin* (UDG) method [11] in a similar manner.

The challenge regarding the higher order of accuracy, however, arises in the unfitted setting with implicitly represented geometry. As the mesh is not fitted to the geometry, one has to evaluate the integrals in variational formulation on *cut elements*, namely the elements cut by the interface, which is described only implicitly by a zero level set. It offers second order of accuracy for these numerical integrations based on the explicit piecewise linear interpolation of the level set function, which is sufficient for linear finite elements but not for higher-order ones. New approach is therefore required. The technique called *isoparametric mappings* proposed in [99] yields a high-order approximation of the geometry from the image of its piecewise linear representation through a parametric mapping of the underlying mesh. Armed with this approach, the resulting *isoparametric unfitted finite element method* has been analyzed for provable error bounds of optimal order. This isoparametric technique has been introduced to

merge with the unfitted space-time FEM to achieve high order of accuracy for moving domain problems in [130], and has also been analyzed with TraceFEM for surface PDE problems in [74].

Towards the coupled bulk-surface model, there are a few other computational works, e.g., the phase field approach [132], the unfitted linear space-time FEM [160], and the ALE-based model order reduction [104]. In [51] the authors present an overview of computational mean curvature flow, governed by geometric PDEs, as an essential sub-model to the problem. While in this thesis, we will focus on the geometrically unfitted discretization based on the level set method, armed with the isoparametric mappings of underlying mesh for provable high order of accuracy. Alternatively to the unfitted isoparametric space-time FEM in [130], we will develop an isoparametric Eulerian FEM for moving domain problems based on [102], but rather make use of the classical *backward differentiation formula* (BDF) [49] for higher-order implicit time stepping, which is expected to be computationally more efficient and simpler than its competitor. We will also propose a stabilized isoparametric TraceFEM for computing the discrete mean curvature vector on hypersurface, by using the stabilization methods introduced in [74], to achieve arbitrarily high-order accuracy in comparison to its low-order counterpart in [82]. In addition to these novel unfitted discretizations, the RKDG methods are employed to solve the advection problem of the level set domain at high order of accuracy in space and time. Altogether, we will exploit weak and strong coupling algorithms to integrate the aforementioned numerical methods for solving the geometrically coupled solution-curvature-driven moving free boundary problem.

Next, we will summarize the contributions and the structure of this thesis.

1.4 Outline of the Thesis

The main contributions of the work include:

- The development and the analysis of a provable higher order in space and time Eulerian FEM, based on the isoparametric mappings and the BDF time stencil applied to a discrete extended domain at each time step, for solving PDEs on a priori known evolving geometry, which enjoys low computational cost and maintains robust under large deformations or topological changes of the geometry;
- The development and the analysis of a provable arbitrarily high order and stabilized TraceFEM for computing discrete mean curvature vectors on smooth

manifolds, which is not only an interest of the mathematical community, but also itself an important topic in computer graphics and computational geometry;

- The formulation and the verification of two methods for a smooth extension of the velocity from the hypersurface to the embedding bulk, either by solving a normal diffusion equation or by applying a penalizing term over the bulk;

- The proof-of-concept numerical simulation of the geometrically coupled solution-curvature-driven moving FBP, by assembling the three sub-models through two coupling algorithms, in such a way that a hyperbolic transport equation of the level set domain is solved by the RKDG methods combined with the velocity extension methods, which is novel and challenging in the sense of nonlinear coupling and high order of accuracy.

This thesis is organized as follows:

- In Chapter 2 the theory and the mathematical models are introduced as preliminaries for solving PDEs coupled with geometric flow on embedded submanifolds. The mean curvature flow is particularly studied with definitions, theorems, and geometric properties imported from the field of differential geometry, following the similar lines in [51]. The level set method then arises from the motivation for handling the mean curvature flow that develops singularities and topological changes. To this end, a level set function represents the geometry implicitly. For exploring the geometric evolution, two different approaches are proposed and compared. After defining a velocity extension operator, the way of solving a linear hyperbolic transport equation of the level set function is chosen. Next, for the PDEs of physical phenomena posed on a prescribed time-dependent geometry, an advection-diffusion equation on single moving domain and in non-stationary two-phase interface problem is discussed, ending up with a homogeneous diffusion equation on one-phase domain that is employed in the osmosis model. A summary of all the equations integrated into a nonlinearly coupled system concludes this chapter.

- In Chapter 3 a geometrically unfitted FEM called Eulerian FEM for solving PDEs on evolving domains is introduced with the related variational formulation, cf. [102]. The basic idea is to ally CutFEM with backward Euler time stepping on a discrete extension of the domain at each time step in the spirit of the method of lines. This however gives low-order accurate discretizations in both space and time. The isoparametric mapping technique is therefore utilized for a higher-oder

approximation of the geometry. This in turn requires a transfer of functions between slightly different mapped meshes, which is comprehensively discussed and analyzed with error estimates. Combined with the BDF time stepping, a higher-order version of Eulerian FEM is developed and a priori error analysis is performed, cf. [114]. Two numerical tests for convergence study and one example to show the robustness of the method follow. A summary compares this method with its two competitors, namely the unfitted isoparametric space-time FEM and the characteristic-Galerkin FEM, which concludes this chapter.

- In Chapter 4 the stabilized finite element approximation of the mean curvature vector on connected closed hypersurfaces is introduced from [82] and improved towards a provable arbitrarily high order of accuracy. Due to the issue that the discrete mean curvature vector based on the Laplace-Beltrami operator looses two orders of convergence rate in the proper Sobolev norm, some stabilization methods have been proposed. To achieve arbitrarily high order of accuracy, the high-order facet-based derivative jump and the volume-based normal derivative stabilizations introduced in [74] are combined into the variational formulation of a stabilized isoparametric TraceFEM. A comprehensive a priori error analysis follows after investigating the related projection and mapping, coordinate embedding, trace and inverse estimates. An alternative approach of the error analysis is further performed and compared subsequently. A fundamental example of the discrete mean curvature vector of a unit circle, and an advanced example of the three-dimensional discrete mean curvature vector of a two-dimensional embedded torus, are numerically tested for extensive convergence study, which complete this chapter.

- In Chapter 5 by the extension of surface velocity and the RKDG FEM, the novel approach to transport a level set geometry is proposed. Two methods for extending velocity from surface to bulk are discussed and compared. The extension method by solving a normal diffusion equation is formulated, which describes a smoothing operator only in directions normal to the surface. And another extension method by applying a ghost penalty based on canonical extensions is also formulated. A numerical example of velocity extension by normal diffusion follows. Next, the classical RKDG FEM is introduced for solving the hyperbolic transport equation of the evolving level set domain. In particular, the 4^{th}-order explicit RK time stepping is associated with the DG finite element discretization in space to ensure uniformly high order of accuracy. The a priori error estimates are introduced

from an established literature, followed by a numerical test which conclude this chapter.

- In Chapter 6 the weak and the strong coupling algorithms are discussed and implemented in a benchmark of the shrinking circle mean curvature flow and a proof-of-concept numerical simulation of the geometrically coupled bulk-surface osmosis model. The numerical results show the nonlinearly coupled three sub-models working well.

- The last Chapter 7 concludes the achievements of this thesis, points out some open problems, and looks forward to possible future work on several interesting extensions and promising applications.

1.5 Reproducibility

A complete set of software and code for replicating all the numerical results in this thesis is provided on the `GitLab` repository https://gitlab.gwdg.de/yimin.lou/ho_unf_pdes_geom_flow.

We make use of `Netgen/NGSolve` [141] – a high performance multi-physics finite element software – for implementation of the numerical methods developed in this thesis. We also utilize `ngsxfem` [101] – an add-on library to `Netgen/NGSolve` – which enables the exploitation of geometrically unfitted discretizations, e.g., TraceFEM. Both packages are developed in `C++` with a rich `Python` interface through which we write the scripts for solving the PDE problems in our numerical experiments. Visit https://ngsolve.org for more information.

Chapter 2

PDEs Coupled with Geometric Flow

The study of *partial differential equations* (PDEs) on Riemannian manifolds is an active topic in the mathematical fields of differential geometry and geometric PDEs, cf. [31, 77, 78]. If the PDEs on a manifold (or its enclosed bulk) are associated with the geometric evolution equation that describes a geometric flow of the manifold, the complexity of the problem makes it either impossible or impracticable to be solved analytically in a closed form. It therefore motivates us to develop numerical methods for approximate solutions to such a coupled bulk-surface model problem, provided that a connected closed hypersurface is smoothly embedded and evolving in a two- or three-dimensional Euclidean space. This is the so-called geometrically coupled moving *free boundary problem* (FBP) where a coupled system of PDEs has to be solved for both unknown functions and evolving geometry. As preliminaries in this chapter, we will begin with an introduction to the basic theory of geometric flow, with an emphasis on mean curvature flow. From that we will realize the issue of singularity and topological change developed in a mean curvature flow, and thus the motivation for using the level set method arises. We will then study the mathematical models: the geometric equation of mean curvature vector, the geometric evolution equation of level set domain, and the PDEs on evolving domain, cf. Section 1.2. We will take advantage of the three sub-models to unfold the geometrically coupled moving FBP, in which the moving free boundary (i.e., the hypersurface) is driven by the mean curvature vector – as a mean curvature flow – together with the quantities subject to PDEs on the domain enclosed by the hypersurface. Finally, we will conclude with a nonlinearly coupled geometry-physics system of PDEs, by gluing the three sub-models as a whole. Starting from these theorems and models, one may explore geometrically coupled PDEs posed on the solution-curvature-driven hypersurfaces instead of their enclosed bulks, though it goes beyond the scope of this thesis.

2.1 Geometric Flow

In the field of modern differential geometry, a geometric flow is modeled from physical flow but a certian type of PDEs for a geometric object, e.g., a Riemannian metric (with intrinsic curvature in a moduli space) or an embedding (with extrinsic curvature in a parameter space). Analogously to the fundamental PDEs, indeed, the geometric flows can be classified as *elliptic*, *parabolic*, and *hyperbolic* types as well, but only the parabolic ones have been studied intensely due to the general motivation to show that a space satisfying certain geometric properties also has a unique canonical structure to which the solution converges, like a heat equation. Such a parabolic geometric flow arises as the gradient flow associated to a functional on a manifold with a geometric interpretation. In this thesis, we focus on the mean curvature flow as an extrinsic parabolic geometric flow, but the scope of this topic may be extended far beyond. For example, on a Lorentzian manifold, some geometric wave equations, e.g., the Einstein field equations and the Yang-Mills equations, can be regarded as special cases of intrinsic hyperbolic geometric flow (while the Einstein manifold as elliptic), which are of great interest in mathematical physics community, cf. [6, 9, 50, 58, 62, 92, 147, 158, 165]. Next, we draw our attention back to the well-known *parabolic* type and follow [162] to have a vista of the two classes of geometric flow.

- *Extrinsic* geometric flows are PDEs for embedded submanifolds, or more generally, immersed submanifolds. Some of the following examples are closely related to this research:
  - Mean curvature flow, the evolution of manifolds of which the normal velocity is given by the mean curvature vector, such as soap films whose critical points are minimal surfaces;
  - Curve-shortening flow, the one-dimensional case of the mean curvature flow;
  - Inverse mean curvature flow, used by Huisken and Ilmanen in [87] the proof of the time-symmetric Riemannian Penrose inequality in General Relativity;
  - Willmore flow, the $\mathcal{L}^2$-gradient flow of Willmore functional, where higher-order derivatives of mean curvature and Gauss curvature are involved in the geometric evolution, such as in minimax eversions of spheres.
- *Intrinsic* geometric flows are PDEs for the Riemannian metric, independent of any embedding or immersion. Remarkable examples of this class but irrelevant in this thesis include:

- Ricci flow, which is analogous to the mean curvature flow but intrinsic, introduced by Hamilton to prove a three-dimensional sphere theorem in [80], by Hamilton and Perelman in the proof of the Poincaré conjecture in [128], and by Brendle and Schoen in the differentiable sphere theorem in [20];
- Yamabe flow, which deforms the Riemannian metric of a noncompact manifold, and is the negative $\mathcal{L}^2$-gradient flow of the normalized total scalar curvature, restricted to a given conformal class;
- Calabi flow, which deforms a Kähler metric on a complex manifold.

We have a quick browse through various types of parabolic geometric flow above as we intend to leave the possible interesting extensions of this work to the reader (see Section 7.2 for more details), while in this thesis we will not dive into the intrinsic theory of modern differential geometry, but rather focus on the computation of discrete *mean curvature flow* and its one-dimensional case *curve-shortening flow* as the simplest example among extrinsic geometric flows.

2.1.1 Introduction to mean curvature flow

Mean curvature flow is the most natural kind of extrinsic geometric flow of submanifolds embedded in a Riemannian manifold, of which the theory has been extensively studied by the community of differential geometry ever since the pioneering work of Brakke in [18]. In the simplest case of a convex closed curve on the Eucliean plane, the properties of the so-called curve-shortening flow are described by Gage-Hamilton theorem, cf. [68, 80]. It claims that a curve will collapse to a point under the (prototype) mean curvature flow. If it is rescaled in such a way that the enclosed area is of conservation, the curve evolves towarads a circle. The Gage-Hamilton theorem combines with Grayson theorem to prove that any closed embedded curve shrinks to a single round point under the curve-shortening flow. Gage and Hamilton proved convergence to a point for convex embedded curves, and Grayson generalized this by proving that non-convex closed embedded curves must eventually become convex, allowing the Gage-Hamilton theorem to then be applied, cf. [76]. Huisken generalized the Gage-Hamilton theorem to higher dimension, cf. [86]. For the details about the aforementioned theorems we refer the reader to Subsection 2.1.5.

In the following subsections we will introduce the mean curvature flow and the related geometric properties along the similar lines in [51, Section 2]. The canonical problem of mean curvature flow is to find a family of closed compact orientable hypersurfaces $\{\Gamma(t)\}_{t\in\mathbb{R}_+}$ in $\mathbb{R}^d$ whose evolution is defined by specifying the velocity

$w(\mathbf{x},t)$ in the normal direction $\mathbf{n}$ at every point $\mathbf{x}$ on $\Gamma(t)$, cf. [51, Section 1]. A general geometric evolution equation for mean curvature $\kappa(\mathbf{x},t)$ reads

$$w(\mathbf{x},t) = f(\mathbf{x},\mathbf{n},\kappa) \qquad \text{for } \mathbf{x} \in \Gamma(t) \hookrightarrow \mathbb{R}^d,\ t \in \mathbb{R}_+ \tag{2.1}$$

where the function f depends on the application, and the dependence $\mathbf{x}$ might arise from evaluating field variables on the hypersurface which satisfy their own system of PDEs in $\mathbb{R}^d$ away from the hypersurface. For the osmotic cell swelling problem, cf. [111], we will make use of the following linear function for some parameters $\alpha, \beta \in \mathbb{R}_+$ such that

$$w = -\alpha\kappa + \beta u \qquad \text{on } \Gamma(t) \hookrightarrow \mathbb{R}^d,\ d = 2,3,\ t \in [0,T],\ T \in \mathbb{R}_+ \tag{2.2}$$

where $u(\mathbf{x},t)$ arises from the solution to the diffusion equation posed on the evolving domain $\Omega(t)$ such that $\partial\Omega(t) = \Gamma(t)$. The equation is identical to the following *prototype* mean curvature flow, i.e., *motion by mean curvature*, for a trivial selection of $u(\mathbf{x},t) \equiv 0$

$$w = -\kappa \qquad \text{on } \Gamma(t) \tag{2.3}$$

with a choice of $\alpha = 1$. This geometric evolution may be viewed as an analogue for moving hypersurfaces of the parabolic heat equation

$$\partial_t u + \Delta u = 0. \tag{2.4}$$

In the next subsection, we will import some definitions and useful results from differential geometry, cf. [51, Section 2].

2.1.2 Oriented and compact hypersurface

To begin with, we look into a certain type of hypersurfaces of interest and the related geometric properties.

Definition 1 ($\mathcal{C}^2$-hypersurface)**.** *Let $\Gamma \subset \mathbb{R}^d$, $d = 2,3$ be a subset in the d-dimensional Euclidean space. Γ is called a $\mathcal{C}^2$-smooth hypersurface embedded in $\mathbb{R}^d$, if for each point $\mathbf{x} \in \Gamma$ there exists an open neighborhood $U(\mathbf{x})$ and a function $\varphi \in \mathcal{C}^2(U)$ such that*

$$U \cap \Gamma = \{\mathbf{x} \in U \mid \varphi(\mathbf{x}) = 0\}, \qquad \text{and } \nabla\varphi \neq 0 \text{ for all } \mathbf{x} \in U \cap \Gamma. \tag{2.5}$$

The tangent space $\mathsf{T}_{\mathbf{x}}\Gamma$ is a $(d-1)$-dimensional linear subspace of $\mathbb{R}^d$ orthogonal to $\nabla\varphi(\mathbf{x})$, which is independent of the particular choice of function φ used to describe Γ, cf. [51, Subsection 2.1]. Please note that by definition a hypersurface is always a codimension-1 embedding of $\mathbb{R}^d$ ($d=2$ for plane curve, $d=3$ for surface) and *orientable*, thus excluding the manifolds like Möbius strip or Klein bottle.

Definition 2 (Orientability)**.** *A $\mathcal{C}^2$-hypersurface $\Gamma \subset \mathbb{R}^d$ is called orientable if there exists a vector field $\mathbf{n} \in \mathcal{C}^1(\Gamma, \mathbb{R}^d)$ such that $\mathbf{n}(\mathbf{x}) \perp \mathsf{T}_{\mathbf{x}}\Gamma$ and $|\mathbf{n}(\mathbf{x})| = 1$ for all $\mathbf{x} \in \Gamma$, cf. [51, Subsection 2.1].*

With the unit normal $\mathbf{n}$ on Γ one can define the *tangential gradient* of a $\mathcal{C}^1$-function f by removing the normal component from the standard $\mathbb{R}^d$ gradient if exists (or by projecting it onto the tangent space) for the coordinate embedding $\Gamma \ni \mathbf{x} \mapsto \mathbf{x} \in \mathbb{R}^d$.

Definition 3 (Tangential gradient)**.** *Let $f \in \mathcal{C}^1(\Gamma)$ be differentiable in the open neighborhood $\Gamma_\delta := U_\delta$ of Γ. We define the tangential gradient of f by*

$$\nabla_\Gamma f(\mathbf{x}) := (D_1 f(\mathbf{x}), ..., D_d f(\mathbf{x})) = \nabla f(\mathbf{x}) - (\nabla f(\mathbf{x}) \cdot \mathbf{n}(\mathbf{x}))\ \mathbf{n}(\mathbf{x}) =: P_\Gamma \nabla f(\mathbf{x})$$

where D_i, $i \in \{1, ..., d\}$ is defined as the component of the tangential gradient in each dimension, ∇ denotes the standard gradient in the Euclidean space $\mathbb{R}^d$, and P_Γ is called tangential projection.

By the definition above it is straightforward to show the following orthogonality

$$\nabla_\Gamma f(\mathbf{x}) \cdot \mathbf{n}(\mathbf{x}) = 0 \qquad \forall \mathbf{x} \in \Gamma. \tag{2.6}$$

Next we introduce the so-called *Laplace-Beltrami operator* that is an essential concept in differential geometry.

Definition 4 (Laplace-Beltrami operator)**.** *If f is furthermore a $\mathcal{C}^2$-function that is twice differentiable in the open neighborhood $\Gamma_\delta := U_\delta$ of Γ, we define the Laplace-Beltrami operator of f by*

$$\Delta_\Gamma f(\mathbf{x}) := \nabla_\Gamma \cdot \nabla_\Gamma f(\mathbf{x}) = \sum_{i=1}^{d} D_i D_i f(\mathbf{x}), \qquad \mathbf{x} \in \Gamma.$$

And we call $\nabla_\Gamma \cdot f(\mathbf{x}) := \sum_{i=1}^{d} D_i f(\mathbf{x})$ the tangential divergence of $f(\mathbf{x})$.

In addition to orientability the hypersurfaces are also required to be closed.

Definition 5 (Closedness). *A hypersurface embedded as a subset of Euclidean space is compact, by the Heine-Borel theorem, if and only if its point set is closed and bounded. A hypersurface is called closed if it is compact and without boundary. Note the difference between the closedness of hypersurfaces and the closedness of point sets.*

Remark 1 (Orientability and closedness). *Any $\mathcal{C}^\infty$-smooth closed hypersurface embedded in $\mathbb{R}^d$ is orientable, proved in [138]. In other words, a non-orientable differentiable manifold (without boundary) of dimension $d-1$ cannot be $\mathcal{C}^\infty$-embedded as closed subset of $\mathbb{R}^d$. That is also proved for compact manifolds without any differentiability hypothesis in [3].*

To conclude this subsection we introduce the following theorem that is important for defining signed distance function and applying level set method.

Theorem 1 (Jordan-Brouwer separation theorem). *Any connected compact hypersurface $\Gamma \subset \mathbb{R}^d$ divides $\mathbb{R}^d$ into two connected components, say, the disjoint inside domain Ω and outside domain $\mathbb{R}^d \setminus \overline{\Omega}$, each of which has Γ as its point set boundary, namely there exists an open bounded set $\Omega \subset \mathbb{R}^d$ such that $\Gamma = \partial\Omega$, and $\overline{\Omega}$ is itself a compact manifold.*

Proof. See [109] and [140]. □

2.1.3 Signed distance function

Provided that the $\mathcal{C}^2$-hypersurface $\Gamma \subset \mathbb{R}^d$ is connected and compact, by Theorem 1 it separates $\mathbb{R}^d$ into two connected components, and thus we can assign a *signed distance function* (or *oriented distance function*) ρ such that

$$\rho(\mathbf{x}) := \begin{cases} \operatorname{dist}(\mathbf{x}, \Gamma), & \mathbf{x} \in \mathbb{R}^d \setminus \overline{\Omega}, \\ 0, & \mathbf{x} \in \Gamma = \partial\Omega, \\ -\operatorname{dist}(\mathbf{x}, \Gamma), & \mathbf{x} \in \Omega. \end{cases} \tag{2.7}$$

See Figure 2.1 for a sketch of a signed distance field where Γ contains two circles.

Formally, the signed distance function is constructed locally based on the following tubular neighborhood theorem.

Theorem 2 (Tubular neighborhood theorem). *Let $\Gamma \subset \mathcal{M}$ be a smooth submanifold, then there exists a diffeomorphism χ from an open neighborhood of Γ in the normal*

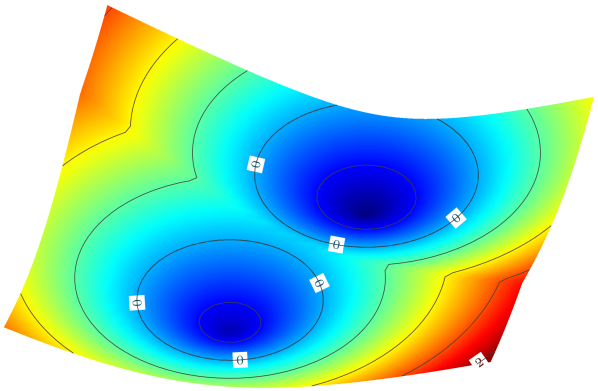

Fig. 2.1 A sketch of the signed distance function that demonstrates the distance values of 0 (where two circles represent the position of Γ) and 2.

bundle [1] $\mathsf{N}\Gamma$ *onto an open neighborhood of* Γ *in the smooth manifold* $\mathcal{M}$*. More specifically, let* Γ *be compact and embedded in* $\mathbb{R}^d$ *with the inclusion map* $\iota : \Gamma \hookrightarrow \mathbb{R}^d$*, there exists a* $\delta \in \mathbb{R}_+$ *such that* $\chi : \mathsf{N}(\Gamma, \delta) \to \mathbb{R}^d$ *is a diffeomorphism from the open neighborhood* $\mathsf{N}(\Gamma, \delta) := \{(\mathbf{x}, \mathbf{v}) \in \Gamma \times \mathbb{R}^d \mid \mathbf{v} \perp \mathsf{T}_{\mathbf{x}}\Gamma,\ \|\mathbf{v}\| < \delta\}$ *of* Γ *in the normal bundle onto the open neighborhood* $\Gamma_\delta := \{\mathbf{x} \in \mathbb{R}^d \mid |\rho(\mathbf{x})| < \delta\}$ *of* Γ *in* $\mathbb{R}^d$*. Then, for each* $\mathbf{x} \in \Gamma_\delta$ *there exists a unique closest point* $p(\mathbf{x}) \in \Gamma$*, and the map* $p : \Gamma_\delta \to \Gamma$ *called closest point projector is a submersion. It is reduced to the so-called* δ*-neighborhood theorem (or* ε*-neighborhood theorem) in the Euclidean space.*

Proof. See [19, Theorem 11.4 in Section 11 of Chapter II] and [159, Theorem 2.1 and 2.2 in Lecture 10]. □

Corollary 1 (Closest point and signed distance properties)**.** *For a* $\mathcal{C}^2$*-hypersurface* $\Gamma \hookrightarrow \mathbb{R}^d$*, the diffeomorphism may be written as*

$$\chi : \Gamma \times (-\delta, \delta) \to \mathbb{R}^d,\ (p(\mathbf{x}), \rho(\mathbf{x})) \mapsto p(\mathbf{x}) + \rho(\mathbf{x})\mathbf{n}(p(\mathbf{x})) \tag{2.8}$$

[1] For an inmmersion $\iota : \Gamma \hookrightarrow \mathcal{M}$, one may obtain the normal bundle $\mathsf{N}\Gamma$ of the submanifold Γ by taking the quotient $\mathsf{T}\mathcal{M}|_{\iota(\Gamma)}/\mathsf{T}\Gamma$ fiberwisely. If $(\mathcal{M}, \mathfrak{g})$ is a Riemannian manifold, one can identify this quotient bundle with the orthogonal complement.

for all $\mathbf{x} \in \Gamma_\delta$ *and the inverse function has the form* $\chi^{-1}(\mathbf{x}) = (p(\mathbf{x}), \rho(\mathbf{x}))$. *As a result, every point* $\mathbf{x}$ *in the open tubular neighborhood* Γ_δ *can be uniquely written as*

$$\mathbf{x} = p(\mathbf{x}) + \rho(\mathbf{x})\mathbf{n}(p(\mathbf{x})) \qquad \forall \mathbf{x} \in \Gamma_\delta, \tag{2.9}$$

where the closest point projector $p : \Gamma_\delta \to \Gamma$ *assigns precisely one* $p(\mathbf{x}) \in \Gamma$ *to each* $\mathbf{x} \in \Gamma_\delta$. *The signed distance function* $\rho : \mathbb{R}^d \to \mathbb{R}$ *is globally Lipschitz-continuous and possesses the signed distance properties such as*

$$\nabla\rho(\mathbf{x}) = \mathbf{n}(p(\mathbf{x})) \qquad \forall \mathbf{x} \in \Gamma_\delta \tag{2.10}$$

and $|\nabla\rho(\mathbf{x})| = 1$ *as a consequence.*

Proof. See [63, Appendix A], [131, Chapter 2.3], and [51, Subsection 2.2]. □

To conclude this subsection we reveal the fact that such a hypersurface can always be represented by a level set in the following lemma.

Lemma 1 (Level set hypersurface)**.** *Any connected compact hypersurface* $\Gamma \hookrightarrow \mathbb{R}^d$ *is a global level set* $\{\mathbf{x} \in \mathbb{R}^d \mid \phi(\mathbf{x}) = c,\ c \in \mathbb{R}\}$ *for some real-valued function* $\phi \in \mathcal{C}(\mathbb{R}^d)$.

Proof. By Theorem 1, Γ is the interface of two subdomains of $\mathbb{R}^d$, hence we can define a level set function $\phi \in \mathcal{C}(\mathbb{R}^d), \mathbf{x} \mapsto \rho(\mathbf{x}) \in \mathbb{R}$ to match the signed distance function (2.7) with using the tubular neighborhood theorem, which gives rise to a zero level set $\{\mathbf{x} \in \mathbb{R}^d \mid \phi(\mathbf{x}) = 0\}$ to represent Γ. □

Assumption 1 (The hypersurfaces of the geometric properties)**.** *From here on, we assume the hypersurface* Γ *is of all the desired geometric properties, namely smoothly embedded, connected, closed, orientable, and* $\mathcal{C}^\infty$*-smooth unless otherwise stated.*

2.1.4 Geometric equation of mean curvature

In this subsection we derive the geometric equation of mean curvature, and its variational formulation.

Let us first introduce a symmetric matrix (i.e., shape operator or Weingarten map)

$$\mathbb{H}_{ij}(\mathbf{x}) := D_i \mathbf{n}_j(\mathbf{x}), \qquad i, j = 1, ..., d, \qquad \mathbf{x} \in \Gamma, \tag{2.11}$$

which has $d-1$ non-zero eigenvalues $\kappa_1, ..., \kappa_{d-1}$ (in addition to a zero eigenvalue) called the *principal curvatures* of Γ, with corresponding eigenvectors $\mathbf{v}_1, ..., \mathbf{v}_{d-1}$ called *principal curvatures vectors*.

We then define the *mean curvature* as the trace of the matrix.

Definition 6 (Mean curvature)**.** *The mean curvature of* Γ *at* $\mathbf{x}$ *is defined by*

$$\kappa(\mathbf{x}) := \sum_{i=1}^{d} \mathbb{H}_{ii}(\mathbf{x}) = \sum_{i=1}^{d-1} \kappa_i(\mathbf{x}), \qquad \mathbf{x} \in \Gamma.$$

Note that another definition of the mean curvature $\kappa = \frac{1}{d-1}\sum_{i=1}^{d} \mathbb{H}_{ii}(\mathbf{x}) = \frac{1}{d-1}\sum_{i=1}^{d-1} \kappa_i(\mathbf{x})$ *exists and is commonly used elsewhere.*

By substituting the definition of $\mathbb{H}$ in (2.11), Definition 6 implies the equivalence between the mean curvature and the tangential divergence of the unit normal

$$\kappa(\mathbf{x}) = \nabla_\Gamma \cdot \mathbf{n}(\mathbf{x}), \qquad \mathbf{x} \in \Gamma. \tag{2.12}$$

In addition, by Equation 2.10 the symmetric matrix $\mathbb{H}$ is equivalent to the Hessian of the signed distance function, cf. [82, Subsection 4.1]

$$\mathbb{H} = \nabla \otimes \nabla \rho, \tag{2.13}$$

for which in the open neighborhood of Γ we have

$$\mathbb{H}(\mathbf{x}) = \sum_{i=1}^{d-1} \frac{\kappa_i^e}{1 + \rho\kappa_i^e} \mathbf{v}_i^e \otimes \mathbf{v}_i^e, \qquad \mathbf{x} \in \Gamma_\delta,\ \delta \in \mathbb{R}_+, \tag{2.14}$$

where $\mathbf{v}_1, ..., \mathbf{v}_{d-1}$ are the corresponding principal curvatures vectors and $\mathbf{v}_i^e := \mathbf{v}_i \circ p$ is an extension from Γ to Γ_δ, cf. [70, Lemma 14.7].

As an oriented hypersurface Γ has two sides, and the sign of the mean curvature κ depends on the specific choice of the unit normal $\mathbf{n}$. In order to make the sign independent of the direction choices, we define the following *mean curvature vector* that points the outward direction along with the outward unit normal $\mathbf{n}$.

Definition 7 (Mean curvature vector)**.** *For mean curvature* κ *in Definition 6 and the outward unit normal* $\mathbf{n}$*, we define the mean curvature vector by*

$$\mathbf{H} := \kappa \mathbf{n}$$

which determines the direction of velocity of the hypersurface in a mean curvature flow.

By taking the Laplace-Beltrami operator on $f(\mathbf{x}) = \mathbf{x}_j,\ j \in \{1, ..., d\}$, cf. Definition 4, and observing the identity $D_i \mathbf{x}_j = \delta_{ij} - \mathbf{n}_j \mathbf{n}_i$ (where $\delta_{ij} := [i = j]$ is the Kronecker delta)

one has

$$\Delta_\Gamma \mathbf{x}_j = -\sum_{i=1}^{d} D_i(\mathbf{n}_j \mathbf{n}_i) = -(\nabla_\Gamma \cdot \mathbf{n})\mathbf{n}_j - \nabla_\Gamma \mathbf{n}_j \cdot \mathbf{n} = -\kappa \mathbf{n}_j \tag{2.15}$$

so that the *geometric equation* of mean curvature vector we aim to solve is

$$\mathbf{H} := \kappa \mathbf{n} = -\Delta_\Gamma \mathbf{x} \qquad \text{on } \Gamma. \tag{2.16}$$

By multiplying the both sides of Equation 2.16 with a vector-valued test function $\mathbf{v} \in [\mathcal{H}^1(\Gamma)]^d$ we have the following variational formulation:
To find $\mathbf{H} \in [\mathcal{H}^1(\Gamma)]^d$ such that for all $\mathbf{v} \in [\mathcal{H}^1(\Gamma)]^d$

$$B(\mathbf{H}, \mathbf{v}) = L(\mathbf{v}) \tag{2.17}$$

where

$$B(\mathbf{H}, \mathbf{v}) = \int_\Gamma \mathbf{H} \cdot \mathbf{v} \, ds \qquad \text{and} \qquad L(\mathbf{v}) = \int_\Gamma \nabla_\Gamma \mathbf{x} : \nabla_\Gamma \mathbf{v} \, ds. \tag{2.18}$$

Remark 2 (Wellposedness)**.** *By the Lax-Milgram theorem, cf. [96, Theorem 6 in Section 6.3] and [61, Subsection 6.2.1], Equation 2.17 is wellposed if ellipticity and boundedness of the bilinear form $B(\cdot,\cdot)$ hold in addition to the bounded linear functional $L(\cdot)$ in a Hilbert space. However, the issue of wellposedness arises from the absence of the coercivity of $B(\cdot,\cdot)$ in $\mathcal{H}^1$ space, while in $\mathcal{L}^2$ space it is indeed elliptic but $L(\cdot)$ is no longer continuous. We will therefore develop stabilized numerical methods with additional stabilization terms for a discrete mean curvature vector in Chapter 4.*

2.1.5 Theory of mean curvature flow

To conclude this section we recall Subsection 2.1.1 and introduce some basic theorems based on [51, Section 3] to depict how a hypersurface evolves by the prototype mean curvature flow Equation 2.3. These results will demonstrate that the mean curvature flow may produce singularities and eventually lead to topological changes of the hypersurface. The motivation of using an Eulerian description to handle the geometry, e.g., level set method, therefore arises.

The main feature of the prototype mean curvature flow governed by Equation 2.3 is the so-called area-decreasing property. In order to reveal this property, we consider the well-known example of a shrinking sphere. Let $\Gamma(t) = \partial\mathcal{B}_R(\mathbf{x}_0) \subset \mathbb{R}^d$ be the sphere of a ball with radius $R(t)$ that is shrinking by the geometric evolution equation (2.3).

As a result, the normal velocity and the mean curvature of $\Gamma(t)$ that are given by

$$w = \partial_t R, \qquad \kappa = \frac{d-1}{R} \tag{2.19}$$

satisfy Equation 2.3 and thus yield

$$\partial_t R = -\frac{d-1}{R}. \tag{2.20}$$

The solution to this ordinary differential equation (ODE) is

$$R(t) = \left(R_0^2 - 2(d-1)t\right)^{\frac{1}{2}} \qquad \text{for } t \in [0,T),\ T = \frac{R_0^2}{2(d-1)}, \tag{2.21}$$

where the initial condition $\Gamma(0) = \partial\mathcal{B}_{R_0}(\mathbf{x}_0)$ is given. From this ODE one can deduce that $\Gamma(t)$ collapses to a point at $\mathbf{x}_0 \in \mathbb{R}^d$ as t goes to T.

Formally, this area-decreasing phenomenon can be recognized as a consequence of the following theorem.

Theorem 3 (Area-decreasing property)**.** *A family of hypersurfaces $\{\Gamma(t)\}_{t\in[0,T)}$ on Assumption 1 evolving by Equation 2.3 satisfies*

$$\frac{d}{dt}|\Gamma| + \oint_\Gamma w^2 \, ds = 0$$

where $|\Gamma|$ denotes the measure of the domain enclosed by Γ and w the normal velocity.

Proof. See [51, Lemma 3.1]. □

Remark 3. *For a smooth initial hypersurface $\Gamma(0)$, the existence of a smooth solution locally in time can be expected, based on the fact that it is the solution to a second-order parabolic problem derived from Equation 2.3. Moreover, from maximum and comparison principles one can show that two smooth compact hypersurfaces initially disjoint will remain disjoint, cf. [57]. It follows that $\Gamma(t) \subset \mathcal{B}_{R(t)}(\mathbf{x}_0)$ for $0 \le t < \min\{T, R_0^2/(2d-2)\}$ if $\Gamma(t),\ t \in [0,T)$ is a smooth solution with $\Gamma(0) \subset \mathcal{B}_{R_0}(\mathbf{x}_0)$, by using the shrinking sphere as a comparison solution. See [51, Section 3].*

The prototype mean curvature flow Equation 2.3 may produce singularities in finite time before the solution disappears, while the following theorem claims that certain initial configurations exist for which the smoothness of the solution can be preserved until it collapses to a point.

Theorem 4 (Huisken theorem)**.** *For $d \geq 3$ a uniformly convex hypersurface $\Gamma(0) \subset \mathbb{R}^d$ on Assumption 1 evolving by Equation 2.3 gives rise to a smooth solution $\Gamma(t)$ in a finite time interval $[0,T)$ that converges to a point as t goes to T. If the hypersurface is rescaled such that the enclosed volume remains conservative, it in turn converges towards a sphere as t goes to T.*

Proof. See [86] and [51, Theorem 3.2]. □

In addition, one has the following theorem for the one-dimensional case, known as the curve-shortening flow (see Figure 2.2 for a sketch).

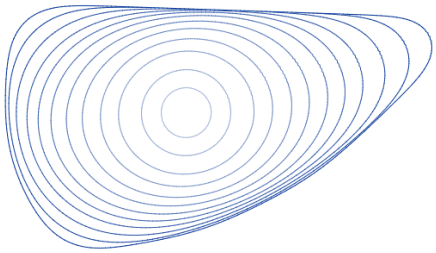

Fig. 2.2 A plane curve converges towards a circle under the curve-shortening flow. Inner curves (in lighter color) shrink from the outer curves at earlier time. Time steps between curves may not be uniform. Source: [45]

Theorem 5 (Gage-Hamilton-Grayson theorem)**.** *Provided that an embedded plane curve $\Gamma(0) \hookrightarrow \mathbb{R}^2$ on Assumption 1 starts evolving by Equation 2.3, it gives rise to a smooth embedded solution $\Gamma(t)$ in a finite time interval $[0,T)$, which converges to a round point as t goes to T.*

Proof. The result for a convex $\Gamma(0)$ is proved in [68], and later generalized for a non-convex $\Gamma(0)$ by proving that it will evolve towards convex (remaining smooth and embedded) in finite time in [76], cf. [51, Theorem 3.3]. □

Remark 4. *For $d > 2$ the analogue of Theorem 5 does* not *hold, which can be shown by picking up a suitable initial surface in a dumbbell shape that separates and develops a pinch-off singularity in the middle before the surface collapses to a point (see [51, Figure 4.5] and [76]). This geometric evolution results in a change of topology, so that a Lagrangian geometry description, e.g., the parametric approach where the topological type is fixed, will develop a singularity that is challenging to handle, cf. [51, Section 3].*

Due to the difficulty mentioned above, the question arises whether it is possible to propose a notion of solution that is capable of tracking the mean curvature flow through

a singularity. Such conceptions have been introduced and analyzed since the pioneering work of Brakke in [18] on varifold solutions based on geometric measure theory. Phase field and level set methods constitute two completely different approaches based on an Eulerian perspective, cf. [51, Section 3]. In the next section we will discuss the level set method in detail.

Remark 5 (The force balance of the osmosis model)**.** *In comparison to the prototype mean curvature flow, the situation in the osmosis model may be optimistic. Normally the osmotic pressure tends to expand the membrane, which may offset the shrinking surface tension arising from the mean curvature flow.*

2.2 Level Set Method

As we have briefly discussed in Section 1.3, the fitted and unfitted discretization methods result in the different geometry descriptions of Lagrangian and Eulerian coordinate systems. Each selection of description gives rise to a particular PDE that determines the geometric evolution. The numerical method depends substantially on the way one chooses to represent the geometry. In [51] Deckelnick and Elliott introduce four approaches of which the first two are Lagrangian and the last two are Eulerian:

- Parametric approach, an explicit description of the meshed hypersurface;
- Graphs, which regards the hypersurface as a graph with the support of a height function;
- Phase field approach, based on an approximation of the hypersurface by a diffuse interface of a width across which a phase field function has a transition;
- Level set method, which implicitly represents the hypersurface by the zero level set of an auxiliary function.

In Remark 4 we have mentioned that the Lagrangian geometry descriptions, e.g., parameterized surfaces and graphs, are challenging to handle the singularities developed through a change of topology, hence the motivation to introduce approaches from an Eulerian point of view arises. In this thesis, we focus on the level set method to describe the geometry based on Theorem 1 and Lemma 1.

The level set method has been proposed starting with the pioneering work of Dervieux in [54], and thereafter popularized by Osher and Sethian in a series of literature, cf. [29, 126, 142–146]. It has been applied in a lot of disciplines and subjects,

such as computer graphics, image processing, computational geometry, optimization, computational biology and computational fluid dynamics (CFD). Several level-set data structures have been established to facilitate the exploitation of the level set method in computer science, cf. [161].

The major advantage of the level set method is the flexibility of geometry handling that allows large deformations and even topological changes in time, without the needs of parameterizing or remeshing the interfaces, for instance, when a soap bubble splits into two, develops holes, or the reverse of these processes (see Figure 2.3 for a sketch). We therefore build the unfitted discretizations based on level set domains and interfaces.

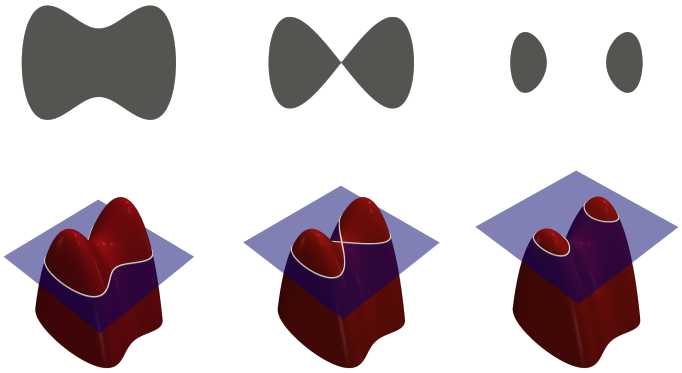

Fig. 2.3 An illustration of the level set method. First row: An evolving domain separates into two subdomains with developing a singularity and a topological change. Second row: The globally defined level set function intersects with the zero plane that represents the domain(s). Source: [44]

2.2.1 Level set function

The core idea of the level set method is to define a real-valued auxiliary function, i.e., level set function, of which the zero level set is exploited to specifies the bounding hypersurface, and the negative level set usually represent the open domain bounded by the hypersurface.

A typical choice of a level set function is the signed distance function defined by (2.7) that enjoys the signed distance properties in Corollary 1.

Definition 8 (Level set function)**.** *Let $\Gamma(t)$ be a time-dependent hypersurface in $\mathbb{R}^d$. Based on Lemma 1 we define a real-valued auxiliary function $\phi : \mathbb{R}^d \times \mathbb{R}_+ \to \mathbb{R}$ such*

that for any fixed time $t \in \mathbb{R}_+$

$$\phi(\mathbf{x},t) = \rho(\mathbf{x}) \qquad \textit{for all } \mathbf{x} \in \Gamma_\delta(t)$$

where $\rho(\mathbf{x})$ *is the signed distance function defined by* (2.7)*. Furthermore, one has*

$$\Gamma(t) = \{\mathbf{x} \in \mathbb{R}^d \mid \phi(\mathbf{x},t) = 0\}, \qquad \Omega(t) = \{\mathbf{x} \in \mathbb{R}^d \mid \phi(\mathbf{x},t) < 0\},$$
$$\mathbb{R}^d \setminus \overline{\Omega}(t) = \{\mathbf{x} \in \mathbb{R}^d \mid \phi(\mathbf{x},t) > 0\}.$$

The level set function therefore inherits all the desired properties of the signed distance function in the open tubular neighborhood $\Gamma_\delta(t)$ *of* $\Gamma(t)$*, cf. Corollary 1.*

The signed distance properties of ϕ hold in the open tubular neighborhood $\Gamma_\delta(t)$ only, which may not be preserved when $\Gamma(t)$ moves, so that ϕ will be degenerated. For a more general neighborhood of $\bigcup_{t\in\mathbb{R}_+} \Gamma(t) \times \{t\}$, one needs a normalization.

Recalling Definition 1 and taking $\varphi = \phi$, it is straightforward to show that

$$\mathbf{n} = \pm \frac{\nabla\phi}{\|\nabla\phi\|} \qquad \text{in } U \cap \Gamma \tag{2.22}$$

for $\|\cdot\|$ the standard Euclidean norm. By choosing the plus sign above with using Equation 2.12 the mean curvature κ has the following expression:

$$\kappa = \nabla_\Gamma \cdot \frac{\nabla\phi}{\|\nabla\phi\|} = \frac{1}{\|\nabla\phi\|} \sum_{i,j=1}^{d} \left(\delta_{ij} - \frac{\partial_{\mathbf{x}_i}\phi\, \partial_{\mathbf{x}_j}\phi}{\|\nabla\phi\|^2}\right) \partial^2_{\mathbf{x}_i\mathbf{x}_j}\phi. \tag{2.23}$$

This formula, however, is expected to lose two orders of accuracy in practice, due to the second order derivative of the level set function. Next, we will discuss the evolution of level set function in two different ways.

2.2.2 Level set transport equation

Recalling the prototype geometric evolution equation of mean curvature flow (2.3), by substituting (2.23) and the fact that $\partial_t\phi = -w\|\nabla\phi\|$, cf. [51, Subsection 2.5], one has equivalently to (2.3) the following parabolic PDE

$$\partial_t\phi - \sum_{i,j=1}^{d} \left(\delta_{ij} - \frac{\partial_{\mathbf{x}_i}\phi\, \partial_{\mathbf{x}_j}\phi}{\|\nabla\phi\|^2}\right) \partial^2_{\mathbf{x}_i\mathbf{x}_j}\phi = 0 \tag{2.24}$$

in a neighborhood of $\bigcup_{t\in\mathbb{R}_+}\Gamma(t)\times\{t\}$. The geometric evolution follows if we can solve this equation of level set function. However, it is highly nonlinear, degenerate parabolic and not well-defined where $\nabla\phi$ vanishes. Therefore, standard methods for parabolic PDEs fail, though it is possible to develop an existence and uniqueness theory within the framework of viscosity solutions, cf. [51, Section 6].

Alternatively, we will solve the mean curvature κ by Equation 2.16 of Laplace-Beltrami characteristics and its weak form (2.17) directly from a geometric viewpoint, to avoid all the difficulties of solving Equation 2.24. This approach gives rise to a linear hyperbolic PDE for the level set transport, which greatly simplifies the problem once the surface velocity w depending on κ is linearized with respect to the geometric evolution, and properly extended in order to provide a velocity field $\mathbf{w}$ for advection.

Let $\mathcal{X}(t)$ be the Lagrangian path of a particle moving in $\mathbb{R}^d$ for all time $t\in\mathbb{R}_+$. To represent the motion of the particle implicitly by the level set function, we set the value of $\phi(\mathcal{X}(t),t)$ to be constant along the path, which, applied to all the particles, results in

$$\begin{aligned} 0=\frac{d}{dt}\phi(\mathcal{X}(t),t)&=\frac{\partial}{\partial t}\phi(\mathcal{X}(t),t)+\frac{d}{dt}\mathcal{X}(t)\cdot\nabla\phi(\mathcal{X}(t),t)\\ &=\partial_t\phi(\mathbf{x},t)+\mathbf{w}(\mathbf{x},t)\cdot\nabla\phi(\mathbf{x},t). \end{aligned} \tag{2.25}$$

This is a linear advection equation with the global velocity field $\mathbf{w}(\mathbf{x},t)$ introduced by the material derivative. It can be written in the form of a hyperbolic conservation law

$$\partial_t\phi+\nabla\cdot\mathbf{F}(\phi)=0,\qquad \text{for the flux function}\quad \mathbf{F}(\phi):=\mathbf{w}\phi, \tag{2.26}$$

if the velocity field is assumed to be divergence-free, i.e., $\nabla\cdot\mathbf{w}\equiv 0$, but this assumption is not mandatory in our model. Physically, however, only the surface velocity $w(\mathbf{x},t)$ exists locally on the zero level set, we therefore define the following velocity extension operator to obtain the global velocity field $\mathbf{w}(\mathbf{x},t)$.

Definition 9 (Velocity extension operator)**.** *Let $w(\mathbf{x},t)$ be the normal component of the velocity of each point $\mathbf{x}$ on the hypersurface $\Gamma(t)\hookrightarrow\mathbb{R}^d$ in the direction of outward unit normal $\mathbf{n}(\mathbf{x},t)$. The specific form of $w(\mathbf{x},t)$ is given by a geometric evolution equation, e.g., Equation 2.2 or Equation 2.3. We define a generic extension operator $\mathcal{E}:\mathcal{C}(\Gamma)\to[\mathcal{C}(\mathbb{R}^d)]^d$ at each fixed time t such that*

$$\mathbf{w}:=\mathcal{E}w\qquad \textit{with the consistency restriction}\quad \mathbf{w}|_\Gamma=w\mathbf{n}.$$

Hence $\mathbf{w}(\mathbf{x},t)$ is a vector-valued velocity field over $\mathbb{R}^d$.

Remark 6 (Background domain)**.** *We have proposed a general extension operator over* $\mathbb{R}^d$ *in Definition 9. In practice, however, we only need a velocity extension onto a simple bounded background domain, denoted by* $\bar{\Omega}$*, typically a convex polygon, fixed in the Euclidean space that properly contains the hypersurface with its* δ*-neighborhood for all the time of evolution. Please distinguish the symbol* $\bar{\Omega}$ *with the short bar from the closure of the domain denoted by* $\overline{\Omega}$*. This practical extension operator may be considered as the generic extension operator restricted to the background domain, i.e.,* $\mathcal{E}|_{\bar{\Omega}}$*, but from here on we identify it with* $\mathcal{E}$ *unless otherwise stated.*

Apart from the consistency restriction, i.e., an extended velocity compatible to the surface velocity, it remains many degrees of freedom to construct the velocity extension operator. We introduce the following candidate for illustration in this chapter, but please keep in mind this is neither a unique nor an optimal choice. We will discuss and implement alternative extension operators in Chapter 5 and Chapter 6.

In order to preserve the signed distance property as much as possible for the level set function when the hypersurface moves, we would prefer the velocity extension acting as a smooth mapping only in directions normal to the hypersurface. This desired extension can be achieved by solving the following elliptic diffusion equation with the Dirichlet restriction of compatible velocity imposed on the hypersurface

$$\nabla \cdot ((\mathbf{n} \otimes \mathbf{n}) \nabla \mathbf{w}) = 0 \qquad \text{in } \bar{\Omega} \times [0,T], \tag{2.27a}$$

$$\mathbf{w} = w\mathbf{n} \qquad \text{on } \Gamma(t),\ t \in [0,T], \tag{2.27b}$$

where $\bar{\Omega} \subset \mathbb{R}^d$ is a fixed time-independent *background domain* properly containing [2] $\Gamma_\delta(t)$ for all the time of evolution, i.e., $\Gamma_\delta \subset \bar{\Omega},\ \forall t \in [0,T],\ T \in \mathbb{R}_+$. We stress that the outward unit normal $\mathbf{n}$ here is well-defined in $\bar{\Omega} \times (0,T]$ by extension of (2.22) with the plus sign choice. The problem (2.27) equipped with the matrix $\mathbf{n} \otimes \mathbf{n}$ indeed produces an *anisotropic* extension of the surface velocity w.

To derive the corresponding variational formulation for each *fixed* time $t \in [0,T]$ we define a proper function space that enforces the Dirichlet boundary condition

$$\mathcal{V}_w := \left\{ \mathbf{v} \in [\mathcal{H}^1(\bar{\Omega})]^d \mid \mathbf{v} = w\mathbf{n} \text{ on } \Gamma(t) \right\} \tag{2.28}$$

and the corresponding test function space

$$\mathcal{V}_0 := \left\{ \mathbf{v} \in [\mathcal{H}^1(\bar{\Omega})]^d \mid \mathbf{v} = \mathbf{0} \text{ on } \Gamma(t) \right\}. \tag{2.29}$$

[2] From here on, the term "properly contain" implies that a subdomain with its proper neighborhood is totally contained in a domain.

The PDE problem (2.27) can then be written in a weak sense:
To find $\mathbf{w} \in \mathcal{V}_w$ such that

$$\int_{\bar{\Omega}} (\mathbf{n} \otimes \mathbf{n}) \nabla \mathbf{w} \nabla \mathbf{v} \, d\mathbf{x} = 0 \qquad \forall \mathbf{v} \in \mathcal{V}_0. \tag{2.30}$$

For the existence of this weak solution, see [61, Section 6.2]. We will study this choice of velocity extension, among its alternatives, in the sense of computation in Section 5.1.

Now let us assume that the velocity field $\mathbf{w}$ has been obtained. Provided that $\mathbf{w} : \bar{\Omega} \to \mathbb{R}^d$ is properly given, the scalar-valued level set function $\phi : \bar{\Omega} \times [0,T] \to \mathbb{R}$ is governed by Equation 2.25 with the following initial and boundary conditions:

$$\partial_t \phi + \mathbf{w} \cdot \nabla \phi = 0 \qquad \text{in } \bar{\Omega} \times (0,T], \tag{2.31a}$$

$$\phi = \phi_0 \qquad \text{in } \bar{\Omega} \times \{0\}, \tag{2.31b}$$

$$\phi = \phi_{\bar{\Omega}} \qquad \text{on } \partial\bar{\Omega} \times [0,T], \tag{2.31c}$$

where the initial data $\phi_0(\mathbf{x})$ is prescribed to be a sufficiently smooth signed distance function in our model, which satisfies $\phi_0(\mathbf{x}) \neq 0$ for all $\mathbf{x} \in \partial\bar{\Omega}$. Since the level set function ϕ is an auxiliary function artificially constructed for describing the physical domain, it is free to be determined on the boundary of the background domain $\partial\bar{\Omega}$, which contains the inflow boundary $\partial\bar{\Omega}_-(t) := \{\mathbf{x} \in \partial\bar{\Omega} \mid \mathbf{w}(\mathbf{x},t) \cdot \mathbf{n}_{\bar{\Omega}}(\mathbf{x}) < 0\}$ for $\mathbf{n}_{\bar{\Omega}}$ the outward unit normal on the boundary, and the outflow boundary $\partial\bar{\Omega}_+(t) = \partial\bar{\Omega} \setminus \partial\bar{\Omega}_-(t)$. One choice of the boundary value $\phi_{\bar{\Omega}}(\mathbf{x},t)$ is that

$$\phi_{\bar{\Omega}}(\mathbf{x},t) = \begin{cases} \phi_0(\mathbf{x}) & \text{for } \mathbf{x} \in \partial\bar{\Omega}_-(t), \\ \lim_{\varepsilon \to 0} \phi(\mathbf{x} - \varepsilon \mathbf{w}, t) & \text{for } \mathbf{x} \in \partial\bar{\Omega}_+(t). \end{cases} \tag{2.32}$$

In other words, $\phi_{\bar{\Omega}}(\mathbf{x},t)$ takes value from the initial data on the inflow boundary and from the upwind neighborhood on the outflow boundary. This boundary condition ensures that there is no new zero level to be imported from the boundary. See [113, Section 3.3] for a detailed discussion about the boundary condition. For the wellposedness of the PDE problem (2.31), see [113, Theorem 3.4 in Section 3.1].

In contrast to Equation 2.24, this transport (advection) equation is linear and can be solved easily by some well-investigated numerical methods for hyperbolic conservation laws, which we will discuss in Section 5.2. From the solution $\phi(\mathbf{x},t)$ to the PDE problem (2.31), we have all the information about the bounding hypersurface $\Gamma(t) := \partial\Omega(t)$ along with the enclosed domain $\Omega(t)$ on which the PDEs of physical phenomena may

be posed. This hyperbolic approach facilitates the resolution to the geometric evolution compared to the parabolic approach.

2.3 PDEs on Evolving Domains

In this section, we discuss the sub-model of our geometrically coupled bulk-surface problem where PDEs are posed on time-dependent domains of which the evolution is *given in advance*. Due to the decoupling with the geometric evolution equation, though more complicated than stationary problems, it is relatively simple from a geometric perspective, and has been studied for many classes of PDEs, theoretically in [4, 28, 46] and numerically in [23, 33, 83, 102, 130, 157]. We begin with an advection-diffusion equation on a single domain, and then consider a non-stationary two-phase interface problem, and end up with a homogeneous diffusion equation used in the osmosis model.

2.3.1 Advection-diffusion equation

In order to describe physical phenomena where particles, density, energy, chemical concentration, or other scalar quantities are transported within a physical system through two processes: *advection* and *diffusion*, the advection-diffusion equation [3] arises. Due to the linearity and the hybrid phenomena, it is often employed as a basic model of many real-world applications.

We follow the similar lines in [102, Section 2] to build the mathematical model. Let $\Omega(t) \subset \mathbb{R}^d,\ d = 2,3$ be a time-dependent domain with Lipschitz boundary $\Gamma(t) = \partial\Omega(t)$ smoothly evolving in a time interval $t \in [0,T],\ T \in \mathbb{R}_+$, which is properly contained in a polygonal time-independent background domain $\bar{\Omega} \subset \mathbb{R}^d$ for all time $t \in [0,T]$. For the initial domain $\Omega(0) \in \mathbb{R}^d$ as a fixed reference we assume there exists a *diffeomorphism* describing the evolution such that

$$\psi(t) : \Omega(0) \to \Omega(t) \qquad \text{for } t \in [0,T] \tag{2.33}$$

with the additional regularity $\psi \in \mathcal{W}^1_\infty([0,T];\mathcal{W}^2_\infty(\Omega(0)))$, cf. [23, Section 2]. For the Bochner space we refer the reader to [61, Subsection 5.9.2]. Hence for each time t, the domain $\Omega(t)$ is a differentiable manifold. In practice, $\Omega(t)$ may be considered as a

[3] It is also called convection-diffusion equation in the literature. Although they are in general considered synonym to each other, technically speaking, advection is the movement of physical quantity transported by the velocity field of a fluid, whereas convection often applies to the movement of a fluid arising from thermal gradient. We therefore use the term "advection" in this thesis.

volume of fluid under motion and deformation, with a material velocity field $\mathbf{w} : \bar{\Omega} \to \mathbb{R}^d$ that has a proper meaning over the whole background domain. The diffeomorphism ψ can be regarded as a Lagrangian mapping from $\Omega(0)$ to $\Omega(t)$ for each $\mathbf{x}_0 \in \Omega(0)$ satisfying the dynamical system

$$\psi(0, \mathbf{x}_0) = \mathbf{x}_0, \qquad \partial_t \psi(t, \mathbf{x}_0) = \mathbf{w}(t, \psi(t, \mathbf{x}_0)) \quad \text{for } t \in [0, T]. \tag{2.34}$$

In the Eulerian framework, the conservation of a scalar quantity $u(\mathbf{x}, t)$ of the fluid with a diffusive flux is governed by the following advection-diffusion equation and Neumann boundary condition

$$\partial_t u + \nabla \cdot (u\mathbf{w} - \nu \nabla u) = g \qquad \text{in } \Omega(t),\ t \in (0, T], \tag{2.35a}$$

$$\nabla u \cdot \mathbf{n} = 0 \qquad \text{on } \Gamma(t),\ t \in (0, T], \tag{2.35b}$$

where $\nu \in \mathbb{R}_+$ denotes a constant diffusion coefficient, $g(\mathbf{x}, t)$ is a source term that we set zero for the time being, and $\mathbf{n}(\mathbf{x}, t)$ is the outward unit normal on $\Gamma(t)$. To solve this PDE problem we assume in addition a proper initial condition

$$u(\mathbf{x}, 0) = u_0(\mathbf{x}) \qquad \text{in } \Omega(0) \tag{2.36}$$

with given initial data $u_0(\mathbf{x})$. An illustration of this problem is given in Figure 2.4.

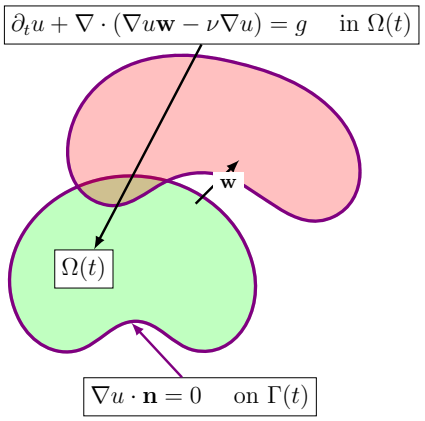

Fig. 2.4 The problem of advection-diffusion equation posed on single evolving domain. The domain $\Omega(t)$ is moving from the green region to the red region by a velocity field $\mathbf{w}$. The no-flux boundary condition imposed on the boundary of domain (in purple) guarantees the conservation of the physical quantity u.

By Reynolds transport theorem applied to the evolving domain $\Omega(t)$ we can verify that the no-flux boundary condition (2.35b) properly assures the conservation of $u(\mathbf{x},t)$

$$\frac{d}{dt}\int_{\Omega(t)} u \, d\mathbf{x} = \int_{\Omega(t)} \partial_t u \, d\mathbf{x} + \int_{\partial\Omega(t)} u(\mathbf{w}\cdot\mathbf{n}) \, ds = \int_{\Omega(t)} \partial_t u + \nabla\cdot(u\mathbf{w}) \, d\mathbf{x} \tag{2.37}$$
$$= \int_{\Omega(t)} \nabla\cdot(\nu\nabla u) \, d\mathbf{x} = \int_{\partial\Omega(t)} \nu\nabla u\cdot\mathbf{n} \, ds.$$

For wellposedness of the PDE problems above we refer to [61, Chapter 7]. In this thesis we will solve this problem numerically in Chapter 3.

2.3.2 Two-phase interface problem

Let us push forward the advection-diffusion equation further onto two subdomains separated by a sharp interface where the thickness is assumed to be zero, across which mass transport happens. This gives rise to the so-called *two-phase interface problem* (see Figure 2.5), cf. [98]. We discuss this problem here because it will be implemented as a numerical example in Subsection 3.3.2. In this thesis we only investigate the case of moving interface, while for the corresponding stationary problem as a foundation we refer the reader to [98, Chapter 2].

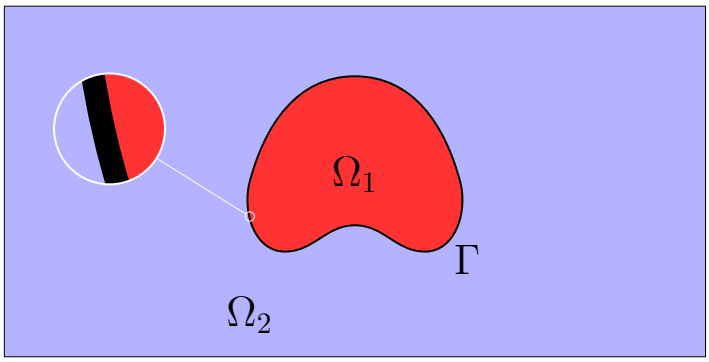

Fig. 2.5 A sketch of the two-phase interface problem. The disjoint subdomains Ω_1 and Ω_2 are separated by the sharp interface Γ, which is properly contained in a background domain.

Analogously to Subsection 2.3.1, we setup the geometry for the two-phase interface problem based on Theorem 1. Let $\Omega_i(t)$, $i=1,2$ be two disjoint subdomains of a background domain such that $\overline{\Omega}_1(t)\cap\overline{\Omega}_2(t)=\Gamma(t)\subset\bar{\Omega}$ and $\overline{\Omega}_1(t)\cup\overline{\Omega}_2(t)=\bar{\Omega}\subset\mathbb{R}^d$. The subdomains $\Omega_i(t)$ with their interface $\Gamma(t)$ are Lipschitz continuous and the evolution is smooth in a time interval $t\in[0,T]$, $T\in\mathbb{R}_+$. We consider the advection-diffusion

equation (2.35a) posed on the two subdomains

$$\partial_t u + \nabla \cdot (u\mathbf{w} - \nu \nabla u) = g \qquad \text{in } \Omega_i(t),\ i = 1,2,\ t \in (0,T] \tag{2.38}$$

and the Neumann boundary condition (2.35b) imposed on the interface in addition to a Henry interface condition

$$[\![-\nu \nabla u \cdot \mathbf{n}]\!] = 0 \qquad \text{on } \Gamma(t),\ t \in (0,T], \tag{2.39a}$$

$$[\![\gamma u]\!] = 0 \qquad \text{on } \Gamma(t),\ t \in (0,T], \tag{2.39b}$$

for $\nu_i,\ i = 1,2$ the diffusion coefficients and $\gamma_i,\ i = 1,2$ the Henry weights, cf. [98, Section 1.2]. Moreover, we prescribe the Dirichlet data on the boundary of the background domain, i.e., $\partial\bar{\Omega}$, and some proper initial conditions

$$u(\mathbf{x},t) = g_D \qquad \text{on } \partial\bar{\Omega},\ t \in (0,T], \tag{2.40}$$

$$u(\mathbf{x},0) = u_0(\mathbf{x}) \qquad \text{in } \Omega_i(0),\ i = 1,2. \tag{2.41}$$

For more details about this model please refer to [98, Chapter 3]. In this thesis we will employ this model and study the numerical solution in Subsection 3.3.2.

2.3.3 Homogeneous diffusion equation

To conclude this section, we propose a simpler case used in the osmosis model. Let us ignore the advection for the moment and consider a homogeneous diffusion equation posed on a single-phase domain, which is reduced from the inhomogeneous advection-diffusion equation (2.35a), with a proper Robin boundary condition and a prescribed initial data

$$\partial_t u - \nabla \cdot (\nu \nabla u) = 0 \qquad \text{in } \Omega(t),\ t \in (0,T], \tag{2.42a}$$

$$wu + \nu \nabla u \cdot \mathbf{n} = 0 \qquad \text{on } \Gamma(t),\ t \in (0,T], \tag{2.42b}$$

$$u = u_0 \qquad \text{in } \Omega(0). \tag{2.42c}$$

See Figure 2.6 for an illustration of this problem.

By following the same lines of (2.37), it can be verified that the boundary condition (2.42b) properly assures the conservation of the physical quantity $u(\mathbf{x},t)$.

The advection-diffusion problem (2.35) has a global velocity field $\mathbf{w}$ involved over $\bar{\Omega}$, but in the osmotic cell swelling problem the physical velocity absents apart from

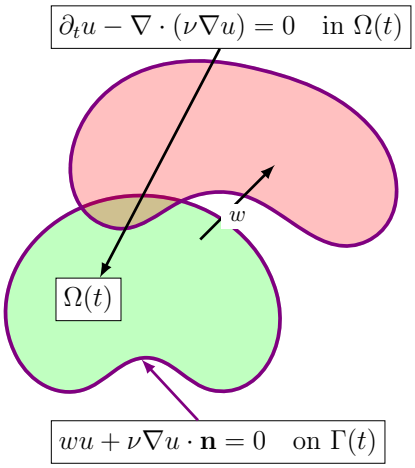

Fig. 2.6 The problem of diffusion equation posed on single evolving domain. The domain $\Omega(t)$ is moving from the green region to the red region by a surface velocity w. The no-flux boundary condition imposed on the boundary of domain (in purple) guarantees the conservation of the physical quantity u.

the membrane (i.e., the surface), which makes the global velocity field $\mathbf{w}$ in (2.35) meaningless. We therefore make use of this diffusion model (2.42) instead, where only the normal component of the surface velocity w is involved.

2.4 The Coupled Geometry-Physics System of PDEs

We have introduced all the sub-models that are united to unfold the geometrically coupled solution-curvature-driven moving FBP, cf. Section 1.2. In this section, we collect these sub-models towards a coupled system of physical and geometric equations. Due to the nonlinearity of coupling we will probe two linearization strategies in the sense of discrete solutions in Chapter 6.

Let us recall the equations we have discussed before. Altogether, (2.16), (2.2), (2.22), (2.27), (2.31), and (2.42) constitute the following coupled system of equations

$$\kappa\mathbf{n} = -\Delta_\Gamma \mathbf{x} \qquad \text{on } \Gamma(t),\ t\in[0,T], \tag{2.43a}$$
$$w = -\alpha\kappa + \beta u \qquad \text{on } \Gamma(t),\ t\in[0,T], \tag{2.43b}$$
$$\mathbf{w} = w\mathbf{n} \qquad \text{on } \Gamma(t),\ t\in[0,T], \tag{2.43c}$$
$$\nabla\cdot((\mathbf{n}\otimes\mathbf{n})\nabla\mathbf{w}) = 0 \qquad \text{in } \bar{\Omega}\times[0,T], \tag{2.43d}$$
$$\mathbf{n} = \nabla\phi/\|\nabla\phi\| \qquad \text{in } \bar{\Omega}\times[0,T], \tag{2.43e}$$
$$\partial_t\phi + \mathbf{w}\cdot\nabla\phi = 0 \qquad \text{in } \bar{\Omega}\times(0,T], \tag{2.43f}$$
$$\phi = \phi_0 \qquad \text{in } \bar{\Omega}\times\{0\}, \tag{2.43g}$$
$$\phi = \phi_{\bar{\Omega}} \qquad \text{on } \partial\bar{\Omega}\times[0,T], \tag{2.43h}$$
$$\partial_t u - \nabla\cdot(\nu\nabla u) = 0 \qquad \text{in } \Omega(t),\ t\in(0,T], \tag{2.43i}$$
$$wu + \nu\nabla u\cdot\mathbf{n} = 0 \qquad \text{on } \Gamma(t),\ t\in(0,T], \tag{2.43j}$$
$$u = u_0 \qquad \text{in } \Omega(0). \tag{2.43k}$$

There are eleven equations involved in the nonlinearly coupled system (2.43), among which three boundary conditions and two initial conditions present. The six unknowns in the system are the scalar-valued physical quantity u, the mean curvature κ, the unit normal $\mathbf{n}$, the surface velocity w, the velocity field $\mathbf{w}$, and the level set function ϕ.

We summarize step by step the idea to unravel the coupled system by the sub-models with introducing the related notation of operators:

1. Provided that the level set domain $\Omega(t_0) = \{\mathbf{x}\in\bar{\Omega} \mid \phi(\mathbf{x},t) < 0\}$ is prescribed at a *fixed* time $t_0\in[0,T]$, the mean curvature vector $\mathbf{H} := \kappa\mathbf{n}$ on the bounding hypersurface $\Gamma(t) = \{\mathbf{x}\in\bar{\Omega} \mid \phi(\mathbf{x},t) = 0\}$ can be determined by the geometric equation (2.43a). With the unit normal $\mathbf{n}(\mathbf{x},t_0)$ from (2.43e) it gives the scalar-valued mean curvature $\kappa(\mathbf{x},t_0)$. Hence the first *stationary* sub-problem is

$$\kappa\mathbf{n} = -\Delta_{\Gamma(\phi)}\mathbf{x} \qquad \text{on } \Gamma, \tag{2.44a}$$
$$\mathbf{n} = \nabla\phi/\|\nabla\phi\| \qquad \text{on } \Gamma, \tag{2.44b}$$

   for which an operator we denoted by

$$\kappa = \mathfrak{A}(\phi). \tag{2.45}$$

2. At the fixed time $t_0 \in [0,T]$, the mean curvature $\kappa(\mathbf{x},t_0)$ together with the PDE solution $u(\mathbf{x},t_0)$ defines the surface velocity $w(\mathbf{x},t_0)$ simply by the *algebraic* geometric evolution equation (2.43b)

$$w = -\alpha\kappa + \beta u \qquad \text{on } \Gamma, \tag{2.46}$$

which can be written in the operator form

$$w = \mathfrak{B}(\kappa, u). \tag{2.47}$$

3. At the fixed time $t_0 \in [0,T]$, with the consistency restriction (2.43c) from the surface velocity $w(\mathbf{x},t_0)$ and the unit normal $\mathbf{n}(\mathbf{x},t_0)$ from (2.43e), the extended velocity field $\mathbf{w}(\mathbf{x},t_0)$ on the background domain $\bar{\Omega}$ can be achieved by solving the elliptic diffusion equation (2.43d). It gives rise to the third *stationary* sub-problem

$$\begin{aligned} \mathbf{w} &= w\mathbf{n} && \text{on } \Gamma, && (2.48a)\\ \nabla\cdot((\mathbf{n}\otimes\mathbf{n})\nabla\mathbf{w}) &= 0 && \text{in } \bar{\Omega}, && (2.48b)\\ \mathbf{n} &= \nabla\phi/\|\nabla\phi\| && \text{in } \bar{\Omega}, && (2.48c) \end{aligned}$$

for which we denote

$$\mathbf{w} = \mathfrak{C}(w, \phi). \tag{2.49}$$

4. Once the velocity field $\mathbf{w}(\mathbf{x},t_0)$ is provided at the time $t_0 \in [0,T]$, the level set function $\phi(\mathbf{x},t)$ that represents the evolving domain $\Omega(t)$ can be transported in a time interval $(t_0, t_0+\Delta t]$, $\Delta t = T/N$, $N \in \mathbb{N}$ as a solution to the hyperbolic advection equation (2.43f) with the initial condition (2.43g) and the boundary condition (2.43h). Then the following *time-dependent* sub-problem arises

$$\begin{aligned} \partial_t\phi + \mathbf{w}\cdot\nabla\phi &= 0 && \text{in } \bar{\Omega}\times(t_0, t_0+\Delta t], && (2.50a)\\ \phi &= \phi_0 && \text{in } \bar{\Omega}\times\{t_0\}, && (2.50b)\\ \phi &= \phi_{\bar{\Omega}} && \text{on } \partial\bar{\Omega}\times[t_0, t_0+\Delta t], && (2.50c) \end{aligned}$$

which can be written as

$$\phi = \mathfrak{D}(\mathbf{w}, \phi_0, \phi_{\bar{\Omega}}). \tag{2.51}$$

5. Once the evolution of the level set domain $\Omega(t)$ is given in $[t_0, t_0+\Delta t]$, the diffusion equation (2.43i) posed on this evolving domain can be solved with the boundary condition (2.43j) and the initial data (2.43k). It models the diffusion phenomenon and results in the following sub-problem of PDEs on *moving* domain

$$\begin{aligned}
\partial_t u - \nabla\cdot(\nu\nabla u) &= 0 && \text{in } \Omega(t),\ t\in(t_0,t_0+\Delta t], && \text{(2.52a)}\\
wu + \nu\nabla u\cdot\mathbf{n} &= 0 && \text{on } \Gamma(t),\ t\in(t_0,t_0+\Delta t], && \text{(2.52b)}\\
\mathbf{n} &= \nabla\phi/\|\nabla\phi\| && \text{on } \Gamma(t),\ t\in(t_0,t_0+\Delta t], && \text{(2.52c)}\\
u &= u_0 && \text{in } \Omega(t_0), && \text{(2.52d)}
\end{aligned}$$

for the solution $u(\mathbf{x},t)$ as a physical quantity of conservation. We use the operator

$$u = \mathfrak{E}(\phi, w, u_0). \tag{2.53}$$

As we have seen, the strategy solves the nonlinearly coupled system in such a way that it confines the geometric evolution within a small time interval and then linearizes the sub-problems. Although every equation itself is linear, they are nonlinearly coupled in the system. This results from that we use the approach of the linear hyperbolic equation (2.31) to avoid the difficulties of solving the highly nonlinear, degenerate parabolic equation (2.24), cf. Subsection 2.2.2. As a consequence, the nonlinearity arises accordingly from the geometry-physics coupling as a cost we have to pay, which makes most of analytical tools impracticable. To this end, the numerical methods for the sub-models will be proposed in Chapter 3, Chapter 4, and Chapter 5, while a weak and a strong coupling models will be presented in Chapter 6.

To conclude this chapter, we summarize an overview of the problem in Figure 2.7, and rewrite the coupled system (2.43) in a compact form of equivalence

$$\partial_t \phi + \mathbf{w} \cdot \nabla \phi = 0 \qquad \text{in } \bar{\Omega} \times (0,T], \tag{2.54a}$$
$$\phi = \phi_0 \qquad \text{in } \bar{\Omega} \times \{0\}, \tag{2.54b}$$
$$\phi = \phi_{\bar{\Omega}} \qquad \text{on } \partial\bar{\Omega} \times [0,T], \tag{2.54c}$$
$$\nabla \cdot ((\mathbf{n} \otimes \mathbf{n}) \nabla \mathbf{w}) = 0 \qquad \text{in } \bar{\Omega} \times [0,T], \tag{2.54d}$$
$$\partial_t u - \nabla \cdot (\nu \nabla u) = 0 \qquad \text{in } \{\mathbf{x} \in \bar{\Omega}, t \in (0,T] \mid \phi(\mathbf{x},t) < 0\}, \tag{2.54e}$$
$$u(\mathbf{w} \cdot \mathbf{n}) + \nu \nabla u \cdot \mathbf{n} = 0 \qquad \text{on } \{\mathbf{x} \in \bar{\Omega}, t \in (0,T] \mid \phi(\mathbf{x},t) = 0\}, \tag{2.54f}$$
$$u = u_0 \qquad \text{in } \Omega(0), \tag{2.54g}$$
$$\mathbf{w} - \alpha \Delta_{\Gamma(\phi)} \mathbf{x} - \beta u \mathbf{n} = 0 \qquad \text{on } \{\mathbf{x} \in \bar{\Omega}, t \in (0,T] \mid \phi(\mathbf{x},t) = 0\}, \tag{2.54h}$$

in which the level set domain and hypersurface are presented implicitly, as well as the dependence of the unit normal on the level set function.

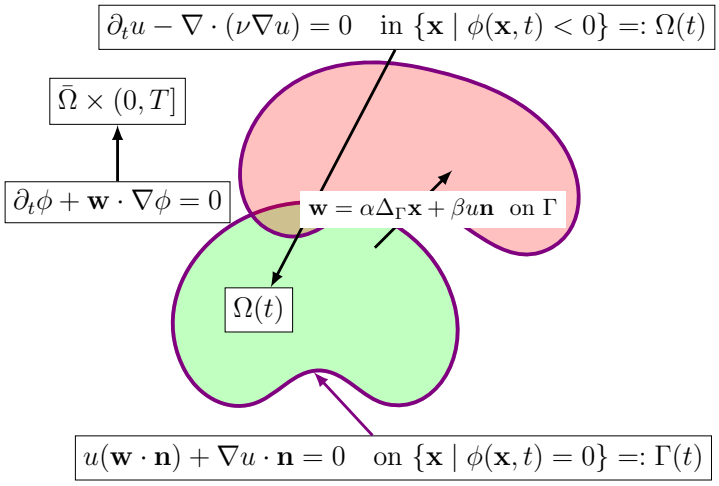

Fig. 2.7 The geometrically coupled bulk-surface moving FBP with a solution-curvature-driven boundary involves a nonlinearly coupled system of the diffusion equation posed on the time-dependent level set domain, the no-flux boundary condition imposed on the bounding hypersurface, the geometric evolution equation given by the mean curvature vector and the physical quantity, the velocity extension equation with the consistent surface condition, and the advection equation transporting the level set function.

Chapter 3

Numerical PDEs on Time-dependent Domains

Towards the coupled bulk-surface model proposed in Section 2.4, our strategy is based on decoupling and linearization. In this chapter, we will only consider the bulk model and discuss the numerical methods for solving *uncoupled* PDEs posed on time-varying bulk domains, of which the evolution is given independently and in advance. In other words, the involved PDEs do not affect the geometry on which they are posted, whereas the prescribed geometry has an influence on the quantities subject to the involved PDEs. A variety of methods have been developed to solve numerical PDEs on time-dependent domains in the past decades. Generally speaking, however, there are only two categories of these methods, namely *Eulerian* and *Lagrangian* frameworks. Discretizations based on a Lagrangian coordinate system work with an explicit description of geometry, in which the computational mesh is adapted to fit the boundary of domain. A popular approach of this sort is the so-called *Arbitrary-Lagrangian-Eulerian* (ALE) formulation, cf. [43, 56]. Although the Lagrangian methods offer a more natural way to deal with non-stationary geometry by tracking the boundary of domain, they are challenged by significant deformations or topological changes of the geometry. These issues, on the other hand, can be overcome by the Eulerian methods that work with the computational mesh unfitted to the boundary of domain, in which the geometry is represented implicitly, for example, by a level set function. In this thesis, we will focus on this family of the so-called *geometrically unfitted* FEM that captures the boundary (i.e., the interface or the hypersurface) by the level set method, cf. [29, 54, 126, 142–146]. This chapter is built substantially on the work of Lou and Lehrenfeld in [114].

3.1 Eulerian Finite Element Method

Recalling that in Subsection 2.3.1 an advection-diffusion equation posed on a space-time domain $\Xi := \bigcup_{t\in[0,T]} \Omega(t)\times\{t\} \subset \bar{\Omega}\times[0,T]$ is considered, i.e., for $t\in[0,T]$

$$\partial_t u + \nabla\cdot(u\mathbf{w} - \nu\nabla u) = g \text{ in } \Omega(t), \qquad \nabla u\cdot\mathbf{n} = 0 \text{ on } \Gamma(t), \quad u = u_0 \text{ on } \Omega(0). \tag{3.1}$$

There is a single domain $\Omega(t)$ on which the equation is posed, cf. Figure 3.1 for a sketch of the problem in the unfitted setting. While for the numerical tests we will also consider a two-phase moving interface problem where the equation is posed on both $\Omega_1(t)$ and $\Omega_2(t) := \bar{\Omega}\setminus\Omega_1(t)$ that is separated by a jump interface $\Gamma(t) := \overline{\Omega}_1\cap\overline{\Omega}_2$, cf. Subsection 2.3.2. Let $\Omega_\varepsilon(t) := \{\mathbf{x}\in\bar{\Omega} \mid \operatorname{dist}(\mathbf{x},\Omega(t)) < \varepsilon\}$ be an ε-neighborhood of the domain $\Omega(t)$ for some $\varepsilon\in\mathbb{R}_+$, with the corresponding space-time domain $\Xi_\varepsilon := \bigcup_{t\in[0,T]} \Omega_\varepsilon(t)\times\{t\} \subset \bar{\Omega}\times[0,T]$, which will be used in the analysis.

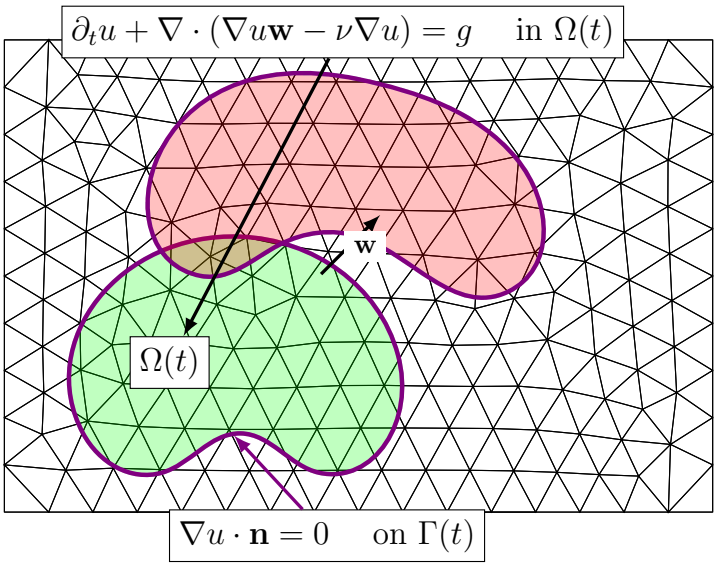

Fig. 3.1 The problem of an advection-diffusion equation with a no-flux Neumann boundary condition posed on a single evolving domain unfitted to the background mesh in the Eulerian framework.

In the Eulerian framework, a naive idea to solve this PDE problem follows the method of lines that combines a finite element discretization in space with a finite difference scheme for time marching. However, this is not directly applicable to problems with non-stationary geometry, as the domain of definition of the discrete solution evolves and the corresponding unfitted finite element space varies in time, and the degrees of freedom may get active or inactive across such a time-stepping stencil. In [102] this difficulty has been overcome by the so-called *Eulerian Finite Element*

Method (Eulerian FEM, the name due to the Eulerian framework and the implicit Euler scheme), which extends the discrete solution at every time step to a sufficiently large neighborhood in order to include all the degrees of freedom that are relevant at the next time step. To this end, a discrete extension based on the so-called *ghost penalty method* [21], is applied at every time step to make the solution still well-defined on the domain of the next time step. This method, however, performs a piecewise linear interpolation of the level set domain and the first-order backward Euler scheme for time stepping, which make it a method of low-order accuracy in both space and time. We therefore develop it into a higher-order method in space and time, based on a sequence of *isoparametric mappings* of the level set domain and the *backward differentiation formula* (BDF) [49] for time stepping, as we have proposed in [114].

In this section, we will first introduce some preliminaries and discrete notation, followed by the weak formulation of the low-order Eulerian FEM including the ghost penalty mechanism for stabilization and discrete extension, cf. [102]. We then give an introduction to the technique of isoparametric mappings for a high-order approximation of the geometry, cf. [99, 105], and design a mesh transfer operator that is required for projecting the solutions between differently deformed meshes. Based on a sequence of the isoparametric mappings in time, the mesh transfer operator, and the BDF time stencils, we derive the space and time discretizations of high-order accuracy. A comprehensive error analysis of this method will be conducted in the next section, followed by three numerical experiments.

3.1.1 Preliminaries and nomenclature

In order to introduce the numerical methods, we first define the discrete objects and their notation.

Discrete space and time

Let $\{\mathcal{T}_h\}_{h\in\mathbb{R}_+}$ be a family of consistent subdivisions of the background domain $\bar{\Omega}\subset\mathbb{R}^d,\ d=1,2,3$ into an admissible quasi-uniform triangulation $\mathcal{T}_h$ consisting of simplexes (i.e., elements) $\{\hat{T}\in\mathcal{T}_h\}$ with a characteristic diameter (mesh size) $h\in\mathbb{R}_+$. On each of these triangulations $\mathcal{T}_h$ we define a time-independent, finite-dimensional space of continuous piecewise polynomial functions of degree k, i.e., a finite element space, by

$$\mathcal{V}_h=\mathcal{V}_h^{(k)}:=\Big\{v_h\in\mathcal{C}(\bar{\Omega})\mid v_h|_{\hat{T}}\in\mathcal{P}^k(\hat{T}),\ \forall\hat{T}\in\mathcal{T}_h\Big\},\tag{3.2}$$

where the *bracketed* upper index (k) may be omitted below. We call $\mathcal{T}_h$ a background mesh.

Let $\Delta t := T/N,\ T \in \mathbb{R}_+, N \in \mathbb{N}$ be a uniform time step of an equally-spaced subdivision of the time interval $[0,T]$ under investigation. Let $t_n := n\Delta t,\ n = 0,1,...,N$ be time instances for which we denote by *unbracketed* upper index $(\cdot)^n := (\cdot)|_{t=t_n}$ the time-dependent objects restricted to $t = t_n$, e.g., $\Omega^n := \Omega(t_n),\ \Gamma^n := \Gamma(t_n)$, or $\phi^n := \phi(\cdot, t_n)$.

Geometric approximation

Let $\phi(\mathbf{x}, t_n)$ be a level set function whose negative level set represents a smooth domain $\Omega^n = \{\mathbf{x} \in \bar{\Omega} \mid \phi(\mathbf{x}, t_n) < 0\}$ exactly, with its zero level set for the boundary $\Gamma^n := \partial\Omega^n = \{\mathbf{x} \in \bar{\Omega} \mid \phi(\mathbf{x}, t_n) = 0\}$, for $n = 0, ..., N,\ N \in \mathbb{N}$. Let $\hat{\phi}_h^n := \mathcal{I}_h^n \phi$ be a piecewise linear interpolation of the level set function $\phi(\mathbf{x}, t_n)$ at second order of accuracy, where $\mathcal{I}_h^n$ is the corresponding nodal interpolation operator in the finite element space $\mathcal{V}_h^{(k)}$. Let ϕ_h^n be an abitrarily high-order piecewise polynomial appoximation to $\phi(\mathbf{x}, t_n)$. The discrete level set domains can be defined by the corresponding approximated level set functions

$$\hat{\Omega}_h^n := \left\{\mathbf{x} \in \bar{\Omega} \mid \hat{\phi}_h^n(\mathbf{x}) < 0\right\}, \qquad \tilde{\Omega}_h^n := \left\{\mathbf{x} \in \bar{\Omega} \mid \phi_h^n(\mathbf{x}) < 0\right\}. \tag{3.3}$$

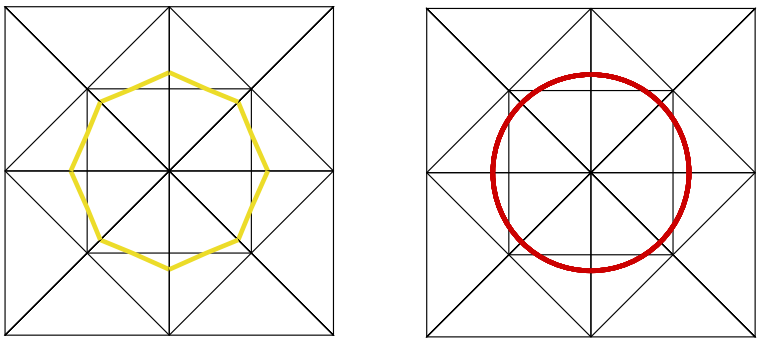

(a) $\hat{\Omega}_h^n$ (b) $\tilde{\Omega}_h^n$

Fig. 3.2 Left: the boundary (in yellow) of a second-order discrete level set domain $\hat{\Omega}_h^n$. Right: the boundary (in red) of a high-order discrete level set domain $\tilde{\Omega}_h^n$.

A sketch of the two approximations of the smooth domain Ω^n is given in Figure 3.2. We assume that the boundary $\partial\Omega^n$ is sufficiently smooth and has a proximity bound

$$\operatorname{dist}\left(\partial\Omega^n, \partial\tilde{\Omega}_h^n\right) \lesssim h^{q+1}, \qquad \forall t_n \in [0,T], \tag{3.4}$$

where $q \in \mathbb{N}$ is for the order of accuracy of ϕ_h^n.

Remark 7 (Inequalities up to constants)**.** *In order to simplify the inequalities that involve generic constants c independent of mesh size h, time step Δt, and time instance t_n, we introduce the signs $\lesssim$, $\gtrsim$, and $\simeq$. In particular, $x \lesssim y$ ($x \gtrsim y$) denotes $x \leq cy$ ($x \geq cy$), and $x \simeq y$ indicates $x \lesssim y$ and $x \gtrsim y$. The hidden constant c may be refered to by $c_{(\boldsymbol{x}.\boldsymbol{y})}$ where $(\boldsymbol{x}.\boldsymbol{y})$ is the label of the corresponding inequality using $\lesssim$, $\gtrsim$, or $\simeq$.*

Since the quadrature rules have difficulty in preserving the geometrical order of accuracy, in this thesis we consider the *isoparametric mappings* approach introduced in [99] to tackle this problem. The underlying idea of this technique is that the second-order approximation of the geometry $\hat{\Omega}_h^n$ based on the piecewise linear interpolation $\hat{\phi}_h^n$ serves as a *reference configuration* on which the quadrature rules can be constructed easily, e.g., by simple geometrical decomposition rules. To improve the accuracy of this low-order approximation, a polynomial function of degree q, denoted by $\Theta^n \in [\mathcal{V}_h^{(q)}]^d$, for transformation of the geometry is constructed at each time step n such that

$$\operatorname{dist}\Big(\partial\Omega^n, \Theta^n(\partial\hat{\Omega}_h^n)\Big) \lesssim \operatorname{dist}\Big(\partial\Omega^n, \partial\tilde{\Omega}_h^n\Big) + \operatorname{dist}\Big(\partial\tilde{\Omega}_h^n, \Theta^n(\partial\hat{\Omega}_h^n)\Big) \lesssim h^{q+1}. \tag{3.5}$$

This transformation is itself a finite element function with respect to the background mesh which renders the task of accurate numerical integration feasible. The mesh deformation is *local*, namely only in the vicinity of zero level set it deviates from the identity, and *small* everywhere in the sense that $\|\Theta^n\|_{\mathcal{L}^\infty(\bar{\Omega})} \lesssim h^2$, cf. Subsection 3.1.3. However, the fact that the deformed meshes and the properly adapted finite element spaces are in general time-dependent, results in the need of a *mesh transfer operator*, cf. Subsection 3.1.4 for details.

Based on this reference configuration, we define the *high-order* approximations of the domain and its boundary, the *deformed* background mesh, and the time-dependent *isoparametric* finite element spaces for $n = 1, ..., N$, respectively,

$$\Omega_h^n := \Theta^n(\hat{\Omega}_h^n), \qquad \Gamma_h^n := \partial\Omega_h^n, \qquad \mathcal{T}_h^n := \Theta^n(\mathcal{T}_h), \qquad \mathcal{V}_h^n := \mathcal{V}_h \circ \Theta^{-n}, \tag{3.6}$$

where the abbreviation denoted by $\Theta^{-n} := (\Theta^n)^{-1}$ is the inverse of the transformation. Please note that Ω_h^n is a good approximation to $\tilde{\Omega}_h^n$ but $\Omega_h^n \neq \tilde{\Omega}_h^n$. We call $\hat{T} \in \mathcal{T}_h$ an undeformed or straight element and $T^n \in \mathcal{T}_h^n$ a deformed or curved element from here on.

Discrete domains and active meshes

In unfitted finite element discretizations, only a part of the background mesh is involved in the computation at each time step, which we call *active* parts of domains, meshes and finite element spaces, as those parts correspond to the elements that overlap the physical domain Ω^n or its *discrete* neighborhoods. See Figure 3.3 for a sketch of the concepts and notation introduced hereafter.

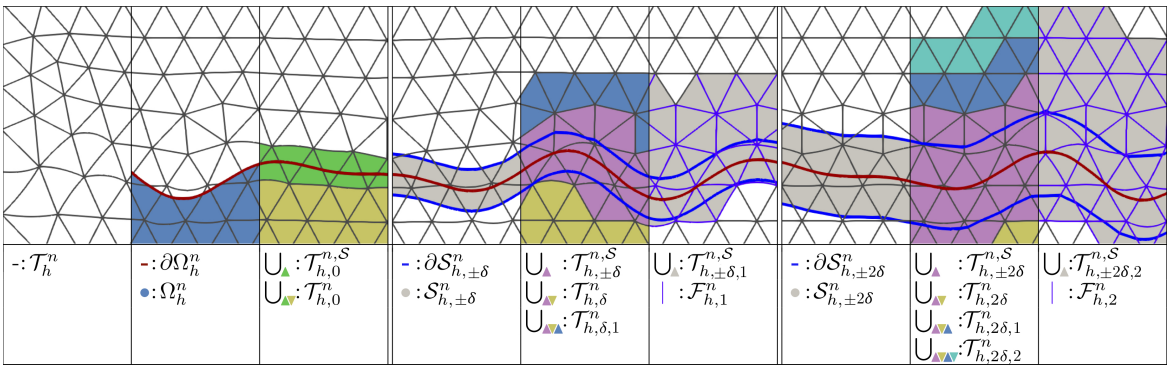

Fig. 3.3 The concepts of discrete domains, strips, and different selections of elements and facets. The first three columns display the mesh, the discrete domain Ω^n, and the set of active elements. The three columns in the middle display a strip domain related to an extension by $\pm\delta$ and a further extension by one element layer, with corresponding element and facet selections. While in the last three columns an extension by 2δ and two element layers is considered.

First of all, let us define an *inflated* level set domain and a *deflated* one based on (3.3) with a parameter $\delta \in \mathbb{R}_+$ as follows:

$$\hat{\Omega}_{h,\delta}^n := \left\{\mathbf{x} \in \bar{\Omega} \mid \hat{\phi}_h^n(\mathbf{x}) - \delta < 0\right\}, \qquad \hat{\Omega}_{h,-\delta}^n := \left\{\mathbf{x} \in \bar{\Omega} \mid \hat{\phi}_h^n(\mathbf{x}) + \delta < 0\right\}. \tag{3.7}$$

We assume the level set function $\phi(\mathbf{x}, t_n)$ is of *signed distance property* which guarantees the extent of domain changes to be scaled approximately to δ, cf. Subsection 2.1.3.

By the inflated and the deflated level set domains we can easily define a *discrete* mapped δ-strip for some $\delta \in \mathbb{R}_+$ as follows:

$$\mathcal{S}_{h,\pm\delta}^n := \Theta^n\left(\hat{\Omega}_{h,\delta}^n \setminus \hat{\Omega}_{h,-\delta}^n\right), \quad \mathcal{S}_{h,\delta}^n := \Theta^n\left(\hat{\Omega}_{h,\delta}^n \setminus \hat{\Omega}_h^n\right), \quad \mathcal{S}_{h,-\delta}^n := \Theta^n\left(\hat{\Omega}_h^n \setminus \hat{\Omega}_{h,-\delta}^n\right), \tag{3.8}$$

with the deformed mesh and the corresponding domain for $\mathcal{S}_{h,\pm\delta}^n$

$$\mathcal{T}_{h,\pm\delta}^{n,\mathcal{S}} := \left\{T^n \in \mathcal{T}_h^n \mid \mathrm{meas}_d(T^n \cap \mathcal{S}_{h,\pm\delta}^n) > 0\right\}, \qquad \mathcal{D}_{h,\pm\delta}^{n,\mathcal{S}} := \left\{\mathbf{x} \in \overline{T^n} \mid T^n \in \mathcal{T}_{h,\pm\delta}^{n,\mathcal{S}}\right\}, \tag{3.9}$$

and similarly for $\mathcal{S}^n_{h,+\delta}$ and $\mathcal{S}^n_{h,-\delta}$ we have $\mathcal{T}^{n,\mathcal{S}}_{h,\delta}$, $\mathcal{D}^{n,\mathcal{S}}_{h,\delta}$ and $\mathcal{T}^{n,\mathcal{S}}_{h,-\delta}$, $\mathcal{D}^{n,\mathcal{S}}_{h,-\delta}$, respectively. In addition, when $\delta \to 0$ we detain $\mathcal{S}^n_{h,0} := \Gamma^n_h$, hence denoted by $\mathcal{T}^{n,\mathcal{S}}_{h,0}$ and $\mathcal{D}^{n,\mathcal{S}}_{h,0}$ are the set of *cut elements* $\{T^n \in \mathcal{T}^n_h \mid \text{meas}_{d-1}(T^n \cap \Gamma^n_h) > 0\}$ and the corresponding domain, respectively, namely the set of elements that are cut by the discrete boundary.

For the discrete extension of the mapped domain that includes its *interior*, we specify

$$\Omega^n_{h,\delta} := \Theta^n\left(\hat{\Omega}^n_{h,\delta}\right) \tag{3.10}$$

with the corresponding active part of the deformed mesh and the domain

$$\mathcal{T}^n_{h,\delta} := \left\{T^n \in \mathcal{T}^n_h \mid \text{meas}_d(T^n \cap \Omega^n_{h,\delta}) > 0\right\}, \qquad \mathcal{D}^n_{h,\delta} := \left\{\mathbf{x} \in \overline{T^n} \mid T^n \in \mathcal{T}^n_{h,\delta}\right\}. \tag{3.11}$$

Corresponding to the *active meshes* $\mathcal{T}^n_{h,\delta}$ we define the time-dependent *isoparametric* finite element spaces restricted to $\mathcal{T}^n_{h,\delta}$, as function spaces of continuous, piecewise *mapped* polynomials of degree k for $n = 1, ..., N$, by

$$\mathcal{V}^n_{h,\delta} := \mathcal{V}^n_h|_{\mathcal{D}^n_{h,\delta}} = \left\{v_h \in \mathcal{C}(\mathcal{D}^n_{h,\delta}) \mid v_h|_{T^n} \in \mathcal{P}^k(\hat{T}) \circ \Theta^{-n},\ \forall T^n \in \mathcal{T}^n_{h,\delta}\right\}. \tag{3.12}$$

Please note that when $\delta \to \infty$ we have trivially $\mathcal{S}^n_{h,\pm\delta} = \mathcal{D}^{n,\mathcal{S}}_{h,\pm\delta} = \mathcal{D}^n_{h,\delta} = \Omega^n_{h,\delta} = \bar{\Omega}$, $\mathcal{T}^{n,\mathcal{S}}_{h,\pm\delta} = \mathcal{T}^n_{h,\delta} = \mathcal{T}^n_h$, and $\mathcal{V}^n_{h,\delta} = \mathcal{V}^n_h$.

Moreover, we add a subscript $r \in \mathbb{N}$ next to δ, to further expand a set of elements or domain by all neighboring elements [1] for r times, in addition to an extension of δ distance, for a sufficient extension to cover the possible mesh displacement at forward time steps, denoted by $(\cdot)_{h,\delta,r}$. For instance, the set of cut elements plus all their neighboring elements is denoted by $\mathcal{T}^{n,\mathcal{S}}_{h,0,1}$, and the active elements $\mathcal{T}^n_{h,\delta}$ plus two stacks of neighboring elements is denoted by $\mathcal{T}^n_{h,\delta,2}$ with the coresponding domain $\mathcal{D}^n_{h,\delta,2}$. From here on, unless otherwise stated, let us simplify the notation by a single subscript $(\cdot)_r$ to represent $(\cdot)_{h,r\delta,r}$, namely $(\cdot)_r$ for a discrete extension of $r\delta$ distance plus r stacks of neighboring elements, which will be most frequently used in this chapter. For example, $\mathcal{T}^n_r := \mathcal{T}^n_{h,r\delta,r}$, $\mathcal{T}^{n,\mathcal{S}}_{\pm r} := \mathcal{T}^{n,\mathcal{S}}_{h,\pm r\delta,r}$, $\mathcal{D}^n_r := \mathcal{D}^n_{h,r\delta,r}$, $\mathcal{D}^{n,\mathcal{S}}_{\pm r} := \mathcal{D}^{n,\mathcal{S}}_{h,\pm r\delta,r}$ and $\mathcal{V}^n_r := \mathcal{V}^n_{h,r\delta,r}$.

Remark 8 (Extension by neighboring elements)**.** *This extension by neighboring elements is involved only in the analysis for self-consistency, but not necessarily in the implementation where the desired inclusion properties can be ensured simply by choosing a sufficiently large δ.*

Remark 9 (Symbols with index h or r)**.** *It is important to distinguish the abbreviations Ω^n_r, $\mathcal{T}^n_r$ and $\mathcal{V}^n_r$ from their non-extended counterparts Ω^n_h, $\mathcal{T}^n_h$ and $\mathcal{V}^n_h$ by the parameter*

[1] An element is considered a neighbor to another element if they share at least one vertex.

$h \in \mathbb{R}_+$ or $r \in \mathbb{N}$. For the sake of notational simplicity, we hide the subscripts h and δ for these extended domains, meshes, and spaces that already have the subscript r to represent the discrete sense implicitly.

Obviously, there holds

$$\operatorname{dist}\left(\partial\mathcal{D}_r^n, \partial\mathcal{D}_0^n\right) \gtrsim r(h+\delta). \tag{3.13}$$

Next, from $\mathcal{F}_h^n$, which is the set of all facets involved in the mesh $\mathcal{T}_h^n$, we introduce a set of *active facets* that is later on used for stabilization and discrete extension purposes. To this end, we mark all facets between elements in the strip and those in the extended domain, as follows:

$$\mathcal{F}_{h,\delta}^n := \left\{\overline{T_1^n} \cap \overline{T_2^n} \mid T_1^n \in \mathcal{T}_{h,\delta}^n, T_2^n \in \mathcal{T}_{h,\delta}^{n,\mathcal{S}}, T_1^n \neq T_2^n\right\}, \tag{3.14a}$$

$$\mathcal{F}_r^n := \left\{\overline{T_1^n} \cap \overline{T_2^n} \mid T_1^n \in \mathcal{T}_r^n, T_2^n \in \mathcal{T}_r^{n,\mathcal{S}}, T_1^n \neq T_2^n\right\}. \tag{3.14b}$$

Please note that this selection of facets connects the domain interior of Ω_h^n with $\mathcal{D}_r^n$, i.e., the region obtained by applying an extension by $r\delta$ distance plus r neighboring element layers.

We further introduce a *patch* $\omega(\cdot) : \bar{\Omega} \cup \mathcal{F}_h^n \cup \mathcal{T}_h^n \to \mathcal{T}_h^n$ that maps a point, a facet, or an element to a set of neighboring elements such that

$$\omega(\mathbf{x}) := \{\cup_{T^n \in \mathcal{T}_h^n} T^n,\ \mathbf{x} \in \overline{T^n}\} \qquad \text{for a point } \mathbf{x} \in \bar{\Omega}, \tag{3.15a}$$

$$\omega(F^n) := \{\cup_{T^n \in \mathcal{T}_h^n} T^n,\ F^n \subset \overline{T^n}\} \qquad \text{for a facet } F^n \in \mathcal{F}_h^n, \tag{3.15b}$$

$$\omega(T^n) := \{\cup_{T' \in \mathcal{T}_h^n} T' \mid \operatorname{meas}_{d-1}(\overline{T'} \cap \overline{T^n}) > 0\} \qquad \text{for an element } T^n \in \mathcal{T}_h^n. \tag{3.15c}$$

We employ this symbol of patch $\omega(\cdot)$ also with respect to the *undeformed* mesh $\mathcal{T}_h$ in the same manner where the neighbors are picked from the straight facets $\mathcal{F}_h$ or elements $\mathcal{T}_h$. The patch may also be applied to a part of an element, e.g., $T_\Omega^n := T^n \cap \Omega_h^n$, by the same definition as (3.15c).

On top of all the *active* objects introduced above, we make use of the hat symbol $\hat{(\cdot)}$ with respect to *undeformed* mesh and *low-order* geometry, i.e., when $\Theta^n \equiv \mathrm{id}$. For instance, $\hat{\mathcal{F}}_{h,\delta}^n$, $\hat{\mathcal{T}}_{h,\delta}^n$, $\hat{\mathcal{D}}_{h,\delta}^n$ and $\hat{\mathcal{V}}_{h,\delta}^n$. The hat symbol is, however, not applied to the global [2] objects of low-order geometry, such as $\mathcal{F}_h$, $\mathcal{T}_h$ and $\mathcal{V}_h$, for the sake of simplicity.

We conclude this subsection with the following definition.

[2]The term "global" implies that an object acts over the whole background domain.

Definition 10 (Trivial finite element extension)**.** *We identify discrete functions on restricted meshes with functions on the whole background mesh by setting all degrees of freedom outside the restriction to zero, namely, e.g., there holds* $\mathcal{V}_{h,\delta}^n \subset \mathcal{V}_h^n$ *for any* $\delta \in \mathbb{R}_+$.

3.1.2 Variational formulation of low-order discretizations

First of all, we derive the weak formulation of the *original* Eulerian FEM of low-order accuracy, cf. [102], for an advection-diffusion equation posed on an evolving domain, cf. Subsection 2.3.1 for the problem (2.35) or this chapter for (3.1). Each time step in this low-order scheme consists of the following four parts:

1. The finite difference approximation of the time derivative through the implicit Euler time stencil $\frac{u_h^n - u_h^{n-1}}{\Delta t}$;
2. The spatially discrete bilinear form b_h^n for advection and diffusion;
3. A ghost-penalty-type bilinear form s_δ^n for discrete extension and stabilization;
4. The linear form f_h^n for a source term.

The weak formulation reads:
To find $u_h^n \in \hat{\mathcal{V}}_{h,\delta}^n,\ n = 1, ..., N$ for a given $u_h^0 \in \hat{\mathcal{V}}_{h,\delta}^0$ such that

$$\int_{\hat{\Omega}_h^n} \frac{u_h^n - u_h^{n-1}}{\Delta t} v_h d\mathbf{x} + b_h^n(u_h^n, v_h) + \gamma s_\delta^n(u_h^n, v_h) = f_h^n(v_h), \qquad \forall v_h \in \hat{\mathcal{V}}_{h,\delta}^n, \tag{3.16}$$

where the first integrand is the standard backward Euler scheme and the right-hand side linear form $f_h^n(v_h) := \int_{\hat{\Omega}_h^n} g v_h d\mathbf{x}$ exists for a source term g. The remaining terms are defined as follows.

Advection and diffusion

Here, the bilinear form for advection and diffusion makes use of a skew-symmetrized form for the convection part

$$\begin{aligned} b_h^n(u_h, v_h) := &\int_{\hat{\Omega}_h^n} \nu \nabla u_h \cdot \nabla v_h d\mathbf{x} + \frac{1}{2} \int_{\hat{\Omega}_h^n} \Big((\mathbf{w}^e \cdot \nabla u_h) v_h - (\mathbf{w}^e \cdot \nabla v_h) u_h \Big) d\mathbf{x} \\ &+ \frac{1}{2} \int_{\hat{\Omega}_h^n} (\nabla \cdot \mathbf{w}^e) u_h v_h d\mathbf{x} + \frac{1}{2} \int_{\hat{\Gamma}_h^n} (\mathbf{w}^e \cdot \mathbf{n}) u_h v_h ds, \qquad \forall u_h, v_h \in \mathcal{H}^1(\hat{\Omega}_h^n), \end{aligned} \tag{3.17}$$

where $(\cdot)^e$ denotes a smooth extension from Ω^n to $\hat{\Omega}_h^n$ that is presumed to exist.

If the time step is bounded by

$$\Delta t < \xi^{-1} := 2\Big(\|\nabla\cdot(\mathbf{w}^e)\|_{\mathcal{L}^\infty(\hat{\Omega}_h^n)} + \nu + c_{3.18}^2\|\mathbf{w}^e\cdot\mathbf{n}\|_{\mathcal{L}^\infty(\hat{\Omega}_h^n)}/4\nu\Big)^{-1}, \tag{3.18}$$

where $c_{3.18}$ is a constant of the multiplicative trace inequality, then b_h^n has a lower bound

$$b_h^n(v_h, v_h) \geq \frac{\nu}{2}\|\nabla v_h\|_{\hat{\Omega}_h^n}^2 - \xi\|v\|_{\hat{\Omega}_h^n}^2. \tag{3.19}$$

Here one assumes that the (extended) velocity $\mathbf{w}^e$ has bounded divergence and normal flux, cf. [102, Lemma 3.1 and Remark 4.1].

Ghost penalty

Another bilinear form $s_\delta^n(\cdot,\cdot)$ in (3.16) for discrete extension and stabilization comes with a parameter $\gamma(h,\delta)$, which is yet to be defined below. This term makes use of the so-called *ghost penalty* stabilization mechanism introduced in [21], where several variants to realize the same effects are available, cf. [102, Section 4.3]. The most well-known version is the classical *derivative jump* ghost penalty formulation proposed in [21] – the name due to penalizing jumps in directional derivatives across facets – which we will exploit in Chapter 4. For here, however, we rather employ the *direct* version of ghost penalty instead of the original version, due to the computational advantages of its direct implementation only implicitly depending on the polynomial degree, cf. [130, Lemma 3.1 and Remark 6], which takes the form

$$s_\delta^n(u_h, v_h) := \sum_{\hat{F}\in\hat{\mathcal{F}}_{h,\delta}^n} s_F^n(u_h, v_h), \text{ with } s_F^n(u_h, v_h) := \frac{1}{h^2}\int_{\omega(\hat{F})}(u_1 - u_2)(v_1 - v_2)d\mathbf{x}, \tag{3.20}$$

where $u_i = \mathcal{E}^{\mathcal{P}}(u_h|_{\hat{T}_i}), v_i = \mathcal{E}^{\mathcal{P}}(v_h|_{\hat{T}_i}),\ i = 1,2$ with $\mathcal{E}^{\mathcal{P}} : \mathcal{P}^k(\hat{T}_i) \to \mathcal{P}^k(\mathbb{R}^d)$ the canonical extensions of a polynomial function to $\mathbb{R}^d$, and the patch $\omega(\hat{F}) = \hat{T}_1 \cup \hat{T}_2$. See Figure 3.4b for an illustration of the facets where the ghost penalty applied.

The ghost penalty mechanism is responsible for two duties. On the one hand, it stabilizes the weak formulation to achieve robustness with respect to the cut position of the geometry within the elements, which further carries over to the conditioning of the linear system. On the other hand, it implicitly realizes a discrete extension from $\hat{\Omega}_h^n$ to $\hat{\mathcal{D}}_{h,\delta}^n \supset \mathcal{B}_\delta(\hat{\Omega}_h^n)$, which is required to make u_h^n well-defined on the domain $\hat{\Omega}_h^{n+1} \subset \mathcal{B}_\delta(\hat{\Omega}_h^n) \subset \hat{\mathcal{D}}_{h,\delta}^n$. To this end, we make the following assumption on the extended

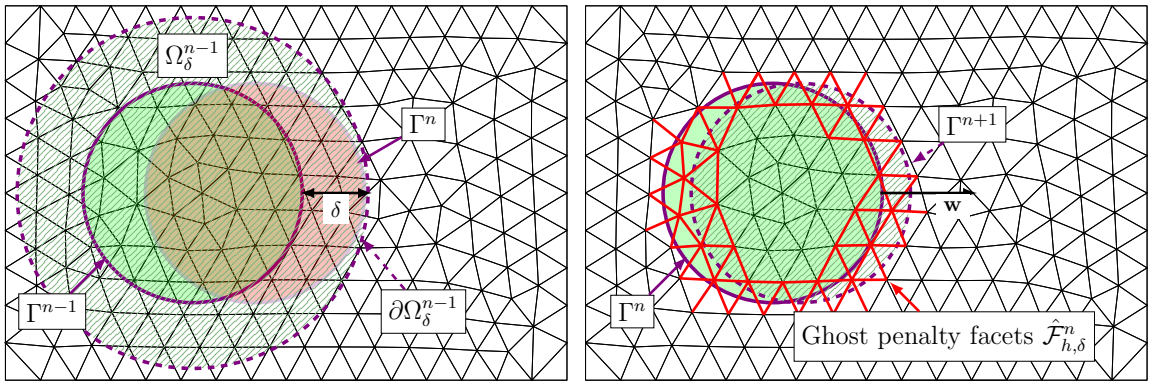

(a) Smooth extension (b) Discrete extension

Fig. 3.4 A comparison between smooth and discrete extensions: (a) A moving domain Ω^{n-1} extended by δ distance to cover Ω^n, cf. [102]; (b) A moving domain on a background mesh where the facets in red the ghost penalty acts on.

distance

$$\delta \geq \Delta t \|\mathbf{w}\|_{\mathcal{L}^\infty((0,T),\mathcal{L}^\infty(\bar{\Omega}))}. \tag{3.21}$$

Here, a global lower bound in space and time for δ is taken to keep the presentation feasible, but a local choice of an extension would be accessible by considering different values for δ in various time steps and spatial regions. Note that the solution is extended away from $\hat{\Omega}_h^n$ by at least one additional layer of elements, namely by at least a distance proportional to h such that for a constant $c > 0$ depending only on the shape regularity there holds

$$\operatorname{dist}(\partial\hat{\mathcal{D}}_{h,\delta}^n, \partial\hat{\Omega}_h^n) \geq \delta + ch \gtrsim \Delta t + h. \tag{3.22}$$

With $\Omega^{n+1} \subset \mathcal{B}_\delta(\Omega^n)$ and $\operatorname{dist}(\partial\hat{\Omega}_h^n, \partial\Omega^n) \lesssim h^2$ for all $n = 0, .., N$, the inclusion $\hat{\Omega}_h^{n+1} \subset \mathcal{B}_\delta(\hat{\Omega}_h^n) \subset \hat{\mathcal{D}}_{h,\delta}^n$ holds for sufficiently small h.

Finally, to specify the parameter $\gamma(h, \delta)$, we make the following assumption as in [102, Section 4.4].

Assumption 2 (Finite facets of paths)**.** *Recalling that $\mathcal{T}_r^{n,\mathcal{S}}$ denotes the "exterior" subset of the strip mesh $\mathcal{T}_{\pm r}^{n,\mathcal{S}}$ where for at least one point $\mathbf{x} \in T \in \mathcal{T}_r^{n,\mathcal{S}}$ there holds $\phi_h^n(\mathbf{x}) > 0$. To every element in $\mathcal{T}_r^{n,\mathcal{S}}$ we require an element in $\mathcal{T}_r^n \setminus \mathcal{T}_r^{n,\mathcal{S}}$ that can be reached by repeatedly passing through facets in $\mathcal{F}_r^n$. We assume that the number of facets passed through in this path is bounded by $K \lesssim (1 + \frac{\delta}{h})$. Moreover, every "interior" element in the active mesh, i.e., $T \in \mathcal{T}_r^n \setminus \mathcal{T}_r^{n,\mathcal{S}}$, provides at most M paths in which it serves as the terminal element of such paths, where M is a number that is bounded independently of h and Δt.*

With this definition of K, we specify – following the same lines in [102, Section 4.4] – $\gamma(h,\delta) := c_\gamma K \lesssim 1 + \frac{\delta}{h}$ for a constant c_γ independent of h and Δt. This completes the full discretization of the low-order Eulerian FEM.

Unique solvability

The coercivity of the overall left-hand side bilinear forms in (3.16) with respect to the norm

$$|||v_h|||_n := \Big(\frac{\nu}{2}\|\nabla v_h\|^2_{\hat{\Omega}_h^n} + \|v_h\|^2_{\hat{\Omega}_h^n} + \gamma s_h^n(v_h, v_h)\Big)^{\frac{1}{2}} \tag{3.23}$$

guarantees the unique solvability at each time step based on the Lax-Milgram theorem, cf. [96, Theorem 6 in Section 6.3] and [61, Subsection 6.2.1].

The Eulerian FEM aforementioned has a low order of accuracy in space and time. We have proposed in [114] an extension of this method to higher order of accuracy, based on the technique of isoparametric mappings, an accurate mesh transfer operator, and the BDF time stepping. Before discussing the corresponding weak formulation in Subsection 3.1.5 and Subsection 3.1.6, we introduce the properties of the parametric mappings in Subsection 3.1.3 as a function in space and in time, and then design a mesh transfer operator between differently mapped meshes in Subsection 3.1.4.

3.1.3 Introduction to isoparametric mapping

As discussed in Section 3.1.1 the piecewise linear approximation of the level set domain gives only second order of geometrical accuracy. In order to achieve higher-order approximations of the geometry, we introduce the technique of isoparametric mappings, cf. Figure 3.5 for a sketch of the idea on a stationary domain, as proposed in [99, 105].

Parametric mapping as a function in space

Let $\Theta^n : \bar{\Omega} \to \bar{\Omega}$ be a sequence of mappings for the time step $n = 0, ..., N$ based on the construction strategies for time-independent domain, cf. [99, 105]. The mappings are enable mainly on cut elements, i.e., on $\mathcal{T}_0^{n,\mathcal{S}}$, where the construction for each n ensures that the image of the zero level set of $\hat{\phi}_h^n$ under the mappings is close to the zero level set of ϕ_h^n in a high-order sense. In particular, the mapping is an identity on vertices and $\mathcal{O}(h^2)$ small elsewhere on cut elements, since the linearized level set function $\hat{\phi}_h^n$ is already exact on all vertices and second-order accurate elsewhere. Away from cut elements and their direct neighbors, i.e., on $\mathcal{T}_h \setminus \mathcal{T}_{h,0,1}^{n,\mathcal{S}}$, the mapping is an identity as well. On those elements adjacent to cut elements, i.e., on $\mathcal{T}_{h,0,1}^{n,\mathcal{S}} \setminus \mathcal{T}_0^{n,\mathcal{S}}$, a transition to

the identity is realized. Overall, for all $n = 0, ..., N$ the mappings Θ^n are $\mathcal{O}(h^2)$ small and local around the interface.

The idea of the isoparametric mappings for an explicit and high-order accurate representation of the geometry is to map the zero level set of $\hat{\phi}_h^n(\mathbf{x})$ towards that of ϕ_h^n as the target by the mapping Θ^n. The geometry described by the high-order approximation of the level set function ϕ_h^n is highly accurate but implicit. The zero level set of the piecewise linear interpolation $\{\mathbf{x} \in \bar{\Omega} \mid \hat{\phi}_h^n(\mathbf{x}) := \mathcal{I}_h^n \phi(t_n) = 0\}$, where $\mathcal{I}_h^n$ is the corresponding nodal interpolation operator, has an explicit representation but only second order of accuracy. By the mesh deformation under Θ^n, $\{\mathbf{x} \in \bar{\Omega} \mid \hat{\phi}_h^n(\mathbf{x}) = 0\}$ is mapped to $\{\mathbf{x} \in \bar{\Omega} \mid \phi_h^n(\mathbf{x}) = 0\}$ approximately, resulting in a high-order accurate and explicit description $\Gamma_h^n := \{\mathbf{x} \in \bar{\Omega} \mid \hat{\phi}_h^n \circ \Theta^{-n}(\mathbf{x}) = 0\}$. An illustration of the idea is shown in Figure 3.5.

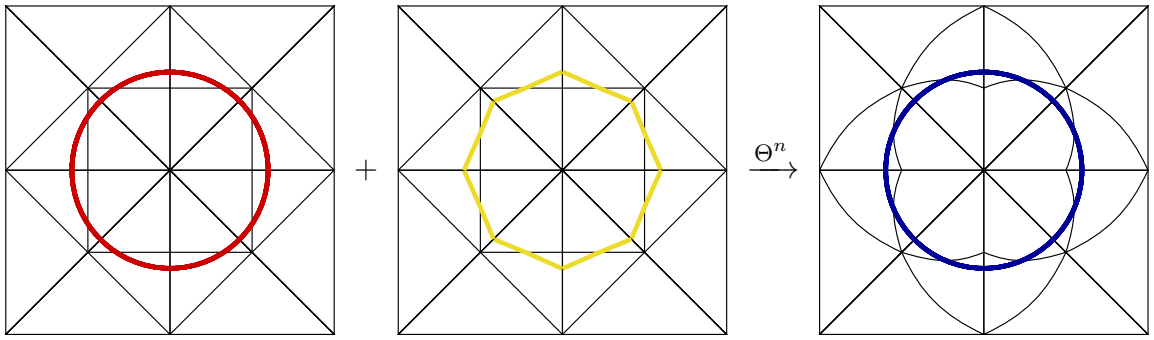

(a) ϕ_h^n (b) $\hat{\phi}_h^n := \mathcal{I}_h^n \phi(t_n)$ (c) $\hat{\phi}_h^n \circ (\Theta^n)^{-1}$

Fig. 3.5 The idea of isoparametric mappings to achieve high-order accurate and explicit representation of interface Γ_h^n: (a) The highly accurate but implicitly described interface by ϕ_h^n; (b) The explicit but only second-order accurate interface represented by $\hat{\phi}_h^n$; (c) The high-order accurate and explicitly described interface by the mesh deformation through Θ^n.

By $\Phi^n : \bar{\Omega} \to \bar{\Omega}$ a sequence of ideal mappings is denoted for each $n = 0, ..., N$ that projects the zero level set of $\hat{\phi}_h^n$ onto Γ^n exactly. In a similar manner to Θ^n, the ideal mappings Φ^n deviate from identity in $\mathcal{T}_{h,0,1}^{n,\mathcal{S}}$ only.

The following lemma concludes the accuracy of the isoparametric mappings as a sequence of functions in space

Lemma 2. *Let $n \in \{0,..,N\}$ be fixed and $\mathcal{D}^{n,\mathcal{S}}_{h,0,1}$ be the domain of cut elements with their direct neighbors. For a sufficiently small mesh size h, there holds*

$$\Theta^n(\mathbf{x}) = \mathbf{x}, \qquad \text{for } \mathbf{x} \text{ a vertex in } \mathcal{T}_h \text{ or } \mathbf{x} \in \bar{\Omega} \setminus \mathcal{D}^{n,\mathcal{S}}_{h,0,1}, \tag{3.24a}$$

$$\|\Theta^n - \mathrm{id}\|_{\mathcal{L}^\infty(\bar{\Omega})} \lesssim h^2, \qquad \|D\Theta^n(\mathbf{x}) - \mathbb{I}\|_{\mathcal{L}^\infty(\bar{\Omega})} \lesssim h, \tag{3.24b}$$

$$\|\Theta^n - \Phi^n\|_{\mathcal{L}^\infty(\bar{\Omega})} + h\|D(\Theta^n - \Phi^n)\|_{\mathcal{L}^\infty(\bar{\Omega})} \lesssim h^{q+1}, \tag{3.24c}$$

$$\text{where the latter implies} \qquad \mathrm{dist}(\partial\Omega(t), \partial\Omega_h(t)) \lesssim h^{q+1}. \tag{3.24d}$$

Proof. See [105, Lemmas 3.4, 3.6 and 3.7]. □

We further characterize the inclusion relations between the (slightly) inflated elements and the deflated ones by the following lemma, with a sketch in Figure 3.6.

Lemma 3. *Let $\hat{T} \in \mathcal{T}_h$ be an undeformed element, we define the corresponding inflated element $\hat{T}_\varepsilon := \{\mathbf{x} \in \bar{\Omega} \mid \mathrm{dist}(\mathbf{x}, \hat{T}) \le \varepsilon\}$ and deflated element $\hat{T}_{-\varepsilon} := \{\mathbf{x} \in \hat{T} \mid \mathrm{dist}(\mathbf{x}, \partial\hat{T}) \ge \varepsilon\}$ for some $\varepsilon > 0$. Furthermore, for $m = 0,..,N$ let $\Theta^{m*}_T : \hat{T}_\varepsilon \to \mathbb{R}^d$ denotes the canonical extension of the polynomial function $\Theta^m|_{\hat{T}}$ to $\hat{T}_\varepsilon$. For a sufficiently small mesh size h, there is a constant $c_{L3} > 0$ independent of h, $\hat{T}$ and m, n, such that with $\varepsilon = c_{L3}h^2$ the following inclusion properties hold for $m, n = 0, ..., N$ and $T^m_{\pm\varepsilon} := \Theta^{m*}_T(\hat{T}_{\pm\varepsilon})$*

$$T^n \subset \hat{T}_{\frac{\varepsilon}{2}} \subset T^m_\varepsilon, \qquad \hat{T}_{-\varepsilon} \subset T^n \cap T^m \text{ with } \mathrm{meas}_d\Big((T^n \cup T^m) \setminus \hat{T}_{-\varepsilon}\Big) \lesssim h^{d+1}. \tag{3.25}$$

Proof. Due to norm equivalences on the space of polynomials on a reference element and its extension, by standard scaling arguments, we have with $\varepsilon \simeq h^2 \lesssim 1$ that $\|\Theta^{m*}_T - \mathrm{id}\|_{\mathcal{L}^\infty(\hat{T}_\varepsilon)} \lesssim \|\Theta^m|_{\hat{T}} - \mathrm{id}\|_{\mathcal{L}^\infty(\hat{T})} \lesssim h^2$ and $\|D\Theta^{m*}_T - \mathbb{I}\|_{\mathcal{L}^\infty(\hat{T}_\varepsilon)} \lesssim \|D\Theta^m|_{\hat{T}} - \mathbb{I}\|_{\mathcal{L}^\infty(\hat{T})} \lesssim h$. Hence, the properties of (3.24b) carry over to the extended function Θ^{m*}_T which ensures the inclusion properties and the measure of the ε-band, i.e., $(T^n \cup T^m) \setminus \hat{T}_{-\varepsilon}$, with a bound εh^{d-1} where $\varepsilon \simeq h^2$. □

A direct corollary of the two previous lemmas can be concluded that for $\hat{T} \in \mathcal{T}_h$, $T^n = \Theta^n_T(\hat{T})$ and $\hat{v} \in \mathcal{P}^k(\hat{T})$ there hold the following norm equivalences

$$\begin{array}{ccccc} h^{\frac{d}{2}}\|\hat{v}\circ\Theta_T^{-n}\|_{\mathcal{L}^\infty(T^n)} & \simeq \|\hat{v}\circ\Theta_T^{-n}\|_{T^n} & \simeq \|\hat{v}\|_{\hat{T}} & \simeq \|\hat{v}\|_{\mathcal{L}^\infty(\hat{T})} \\ \wr & \wr & \wr & \wr \\ h^{\frac{d}{2}}\|\hat{v}\circ\Theta_T^{-n}\|_{\mathcal{L}^\infty(T^n_{\pm\varepsilon})} & \simeq \|\hat{v}\circ\Theta_T^{-n}\|_{T^n_{\pm\varepsilon}} & \simeq \|\hat{v}\|_{\hat{T}_{\pm\varepsilon}} & \simeq \|\hat{v}\|_{\mathcal{L}^\infty(\hat{T}_{\pm\varepsilon})}. \end{array} \tag{3.26}$$

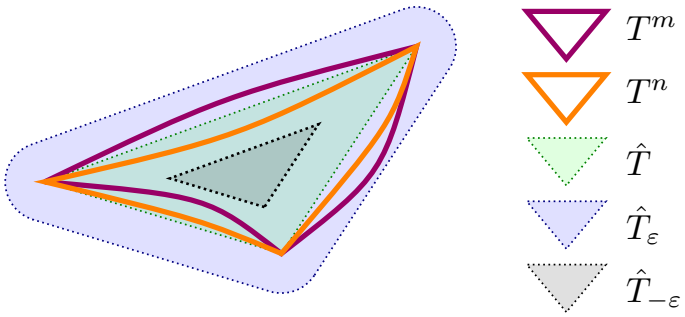

Fig. 3.6 An undeformed (straight) element $\hat{T}$ with its inflated element $\hat{T}_\varepsilon$ and deflated element $\hat{T}_{-\varepsilon}$, Θ^m-deformed (curved) element T^m and Θ^n-deformed (curved) element T^n, involved in Lemma 3.

Parametric mapping as a function in time

The isoparametric mappings are not only the functions in space but also a sequence in time. In contrast to the stationary problem, once the geometry is evolving in time, the cut elements change as well following the moving interface, hence the *mapped* meshes are slightly different between consecutive time steps, i.e., $\mathcal{T}_h^n \neq \mathcal{T}_h^{n-1}$. To do proper time stepping in such an unfitted setting, we need to project solutions from one deformed mesh to another. The projection will be investigated in detail later in the next subsection. As such a projection has to be applied at every time step, one may expect the projection errors accumulating with the increasing number of time steps $N \simeq \frac{1}{\Delta t}$. In order to show in the analysis that this is *not* true, we take a careful look at how the mesh deformation depends on time. More specifically, we characterize where and when the mesh deformation depends continuously on time and where and when not. This will then be exploited when we analyze the accumulation of the projection errors later in the next section.

Due to the properties of isoparametric mappings discussed in Section 3.1.3, for any fixed time t, there exist three different types of mapped elements: cut elements, transition elements (adjacent to cut elements) and undeformed elements. The cut elements are transformed based on the desired property $\hat{\phi}_h^n \approx \phi_h^n \circ \Theta^n$, while the undeformed elements sufficiently far away from the cut elements have $\Theta^n = \mathrm{id}$, and the remainders are the transition elements which realize a proper blending between these two zones. See Figure 3.7 for a sketch of these three element types in spatially one-dimensional case.

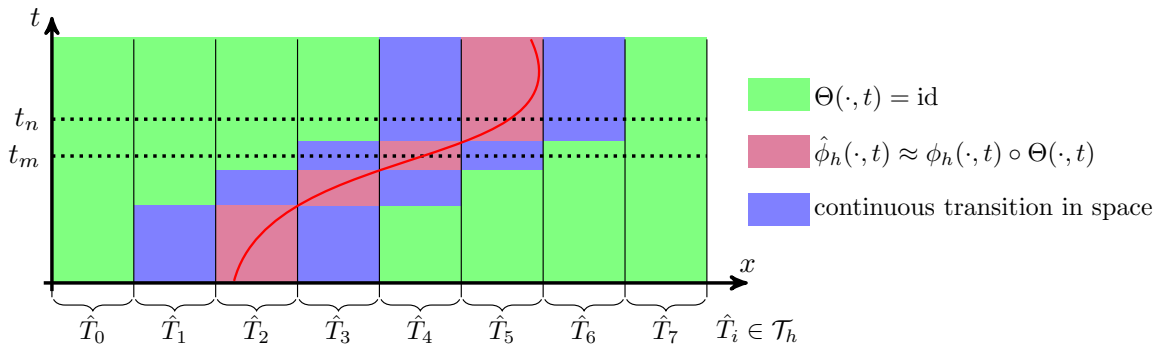

Fig. 3.7 Three regions of element types under mesh deformation. At any fixed time t an element is in exactly one of the three categories: cut (in purple), transition (in blue) or undeformed (in green). Between any two time instances $t_m < t_n$, for each fixed element two situations can be distinguished: the element and all its adjacent neighbors keep their own element types for all $t \in [t_m, t_n]$ *or not*.

Let us consider a fixed straight element $\hat{T} \in \mathcal{T}_h$ at two time instances $t_m < t_n$ and define a function (**C**ut **C**onfiguration **C**hanges) $\texttt{CCC} : \hat{T} \times [0,T] \times [0,T] \to \{\texttt{True}, \texttt{False}\}$ that allows to distinguish two cases:

- $\texttt{CCC}(\hat{T}, t_m, t_n) = \texttt{False}$: If the element $\hat{T}$ and all its adjacent neighbors keep their element types in the time interval $[t_m, t_n]$, then CCC evaluates to False. In this case the mesh deformation depends continuously on the change of the level set function, which is assumed to be Lipschitz-continuous in time, yielding the bound

$$\|\Theta^m - \Theta^n\|_{\mathcal{L}^\infty(\bar{\Omega})} \lesssim |t_n - t_m|. \tag{3.27a}$$

- $\texttt{CCC}(\hat{T}, t_m, t_n) = \texttt{True}$: If the type of the element $\hat{T}$ or any of its adjacent neighbors changes within the time interval $[t_m, t_n]$, then CCC evaluates to True. In this case the mesh deformation on $\hat{T}$ is not necessarily Lipschitz-continuous in time. However, due to (3.24b) the difference between Θ^m and Θ^n is still bounded by

$$\|\Theta^m - \Theta^n\|_{\mathcal{L}^\infty(\bar{\Omega})} \leq \|\Theta^m - \mathrm{id}\|_{\mathcal{L}^\infty(\bar{\Omega})} + \|\mathrm{id} - \Theta^n\|_{\mathcal{L}^\infty(\bar{\Omega})} \lesssim h^2. \tag{3.27b}$$

Recalling that $t_n = n\Delta t,\ n = 1, ..., N$ are the time instances of a partition in the time interval $[0,T]$. For every fixed straight element $\hat{T} \in \mathcal{T}_h$ we can define an integer $N_{\hat{T}} := \#\{n \in \{1,..,N\} \mid \texttt{CCC}(\hat{T}, t_{n-1}, t_n) = \texttt{True}\}$ that counts the number of time steps for the case True, and $N_{\texttt{C}} := \max_{\hat{T} \in \mathcal{T}_h} \{N_{\hat{T}}\}$ as the largest number of time steps among all $\hat{T} \in \mathcal{T}_h$ for the case True that has the mesh transformations *discontinuous* in time.

Assumption 3 (Boundedness of the discontinuous mesh transformations)**.** *In this thesis we assume that for a fixed time interval* $[0,T]$ *and a fixed computational mesh* $\mathcal{T}_h$*, the number* $N_{\mathcal{C}}$ *is bounded independent of the partition of the time interval, but only depends on the specific motion of the geometry.*

3.1.4 Transfer operator between mapped meshes

As aforementioned in Section 3.1.3 the sequence of isoparametric mappings in time makes the mapped meshes slightly different between consecutive time steps, and hence the solutions on the mapped meshes have to be projected from one mesh to another, in order to do proper time stepping. In this section, we therefore design a mesh transfer operator of finite element functions, denoted by $\Pi^n : \mathcal{V}_h^{n-1} \to \mathcal{V}_h^n$, which deviates from a direct $\mathcal{L}^2$ projection on account of locality and computational efficiency. The analysis of this mesh transfer projection will subsequently be conducted in Subsection 3.2.1.

Let $v_{\mathcal{T}_h^m} \in \mathcal{V}_h^m$, $m = n-1$ be a discrete function with respect to the deformed mesh $\mathcal{T}_h^m = \Theta^m(\mathcal{T}_h)$. We aim to approximate it on the differently deformed mesh $\mathcal{T}_h^n = \Theta^n(\mathcal{T}_h)$ with $v_{\mathcal{T}_h^n} := \Pi_m^n v_{\mathcal{T}_h^m} \in \mathcal{V}_h^n$, i.e., a discrete function with respect to the slightly different mesh $\mathcal{T}_h^n$. This projection is achieved in three steps:

1. By exploiting that $v_{T^m} := v_{\mathcal{T}_h^m}|_{T^m}$, i.e., the restriction of $v_{\mathcal{T}_h^m}$ to an element $T^m \in \mathcal{T}_h^m$, is smooth, we define and denote by $v_{T^m}^*$ an extension of v_{T^m} to a small neighborhood T_ε^m of T^m with $T^n \subset T_\varepsilon^m$, such that $v_{T^m}^* \in \mathcal{C}^\infty(T_\varepsilon^m)$;

2. We then project these extensions into $\bigoplus_{T^n \in \mathcal{T}_h^n} \mathcal{V}_h^n|_{T^n}$, i.e., the discontinuous (across element interfaces) version of $\mathcal{V}_h^n$, yielding $\tilde{v}_{\mathcal{T}_h^n}$;

3. An Oswald-type interpolation of $\tilde{v}_{\mathcal{T}_h^n}$ is then applied in order to obtain a continuous function $v_{\mathcal{T}_h^n} \in \mathcal{V}_h^n$.

The first two steps are completely element-local and allow for a trivial parallelization, especially since the access to neighboring elements is not required, whereas the third step is a highly efficient vector operation, namely averaging. This is in contrast to an only seemingly simpler approach such as a global $\mathcal{L}^2$ projection which would involve non-local operations.

Element-local extensions

For an undeformed element $\hat{T} \in \mathcal{T}_h$ we denote $T^i := \Theta_T^i(\hat{T}) \in \mathcal{T}_h^i$ with $\Theta_T^i := \Theta^i|_{\hat{T}} \in [\mathcal{P}^q(\hat{T})]^d$, $i \in \{m,n\}$ the parametric mapping restricted to local element. The restriction

of $v_{\mathcal{T}_h^m} \in \mathcal{V}_h^m$ to T^m, i.e., $v_{T^m} := v_{\mathcal{T}_h^m}|_{T^m}$, is a mapped polynomial and hence a smooth function, i.e., $v_{T^m} \in \mathcal{C}^\infty(T^m)$. We can map it back to the undeformed element $\hat{T} \in \mathcal{T}_h$ and realize a function $\hat{v}_T \in \mathcal{P}^k(\hat{T})$ such that $v_{T^m} = \hat{v}_T \circ \Theta_T^{-m}$.

Let $\hat{v}_T^* = \mathcal{E}^{\mathcal{P}}(\hat{v}_T) \in \mathcal{P}^k(\hat{T}_\varepsilon)$ and $\Theta_T^{m*} = \mathcal{E}^{\mathcal{P}}(\Theta_T^m) \in [\mathcal{P}^q(\hat{T}_\varepsilon)]^d$ be the canonical extension of this polynomial to the ε-neighborhood $\hat{T}_\varepsilon$ of $\hat{T}$. With $v_{T^m}^* := \hat{v}_T^* \circ \Theta_T^{-m*} = \mathcal{E}^{\mathcal{P}}(\hat{v}_T) \circ (\mathcal{E}^{\mathcal{P}}\Theta_T^m)^{-1}$ we have a smooth extension of v_{T^m} from T^m to $T_\varepsilon^m := \Theta_T^{m*}(\hat{T}_\varepsilon)$, such that $v_{T^m}^*|_{T^m} = v_{T^m}$ still holds and furthermore $T^n \subset T_\varepsilon^m$. An illustration of this extension is shown in Figure 3.8.

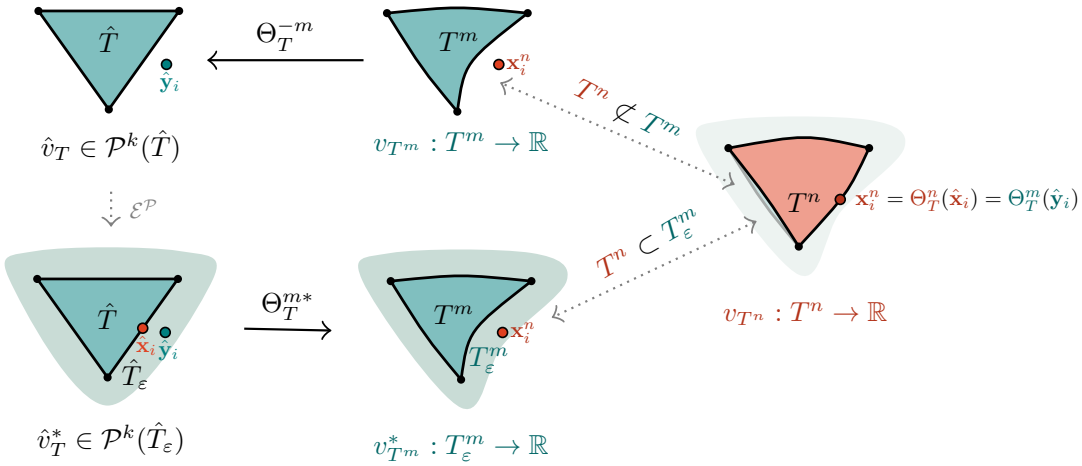

Fig. 3.8 Element-local extensions and interpolation. For a deformed element $T^m = \Theta_T^m(\hat{T}) \in \mathcal{T}_h^m$ the corresponding extension T_ε^m covers the differently deformed element $T^n = \Theta_T^n(\hat{T}) \in \mathcal{T}_h^n$. For a Lagrange node $\mathbf{x}_i^n$ in T^n the mappings Θ_T^{-n} and Θ_T^{-m*}, respectively, yield different points $\hat{\mathbf{x}}_i$ and $\hat{\mathbf{y}}_i$ in $\hat{T}_\varepsilon$.

Element-local interpolation

With $T^n \subset T_\varepsilon^m$ we can define the following element-local interpolation, for given $v_{T^m}^*$ as constructed above, yields $\tilde{v}_{T^n} \in \mathcal{P}^k(\hat{T}) \circ \Theta_T^{-n}$, or equivalently $\hat{v}_{T^n} \in \mathcal{P}^k(\hat{T})$ with $\hat{v}_{T^n} = \tilde{v}_{T^n} \circ \Theta_T^n$, by nodal interpolation.

Let $\mathrm{L}(\hat{T}) = \{\hat{\mathbf{x}}_i\}_{i=1,\dots,\#\mathrm{L}(\hat{T})}$ be the set of Lagrange nodes of $\mathcal{V}_h^n|_{\hat{T}} = \mathcal{P}^k(\hat{T})$ on $\hat{T}$ with corresponding set of Lagrange basis functions $\{\hat{\varphi}_i\}_{i=1,\dots,\#\mathrm{L}(\hat{T})}$, such that $\hat{\varphi}_i(\hat{\mathbf{x}}_j) = \delta_{ij},\ i,j \in \{1,..,\#\mathrm{L}(\hat{T})\}$. The correspondingly mapped nodes and basis functions are $\mathrm{L}(T^n) := \{\mathbf{x}_i^n\}_{i=1,\dots,\#\mathrm{L}(\hat{T})}$ and $\{\varphi_i^n\}_{i=1,\dots,\#\mathrm{L}(\hat{T})}$ with $\mathbf{x}_i^n = \Theta_T^n(\hat{\mathbf{x}}_i)$ and $\varphi_i^n = \hat{\varphi}_i \circ \Theta_T^{-n}$.

We define

$$\tilde{v}_{T^n}(\mathbf{x}) := \sum_{i=1}^{\#\mathrm{L}(\hat{T})} v^*_{T^m}(x_i^n)\varphi_i^n(\mathbf{x}), \qquad \forall \mathbf{x} \in T^n \tag{3.28a}$$

or equivalently, with $v^*_{T^m} = \hat{v}^*_T \circ \Theta_T^{-m*}$ and $\mathbf{x}_i^n = \Theta_T^n(\hat{\mathbf{x}}_i)$ we have

$$\hat{v}_T(\hat{\mathbf{x}}) := \sum_{i=1}^{\#\mathrm{L}(\hat{T})} \hat{v}^*_T \underbrace{\left(\Theta_T^{-m*}\left(\Theta_T^n(\hat{\mathbf{x}}_i)\right)\right)}_{\hat{\mathbf{y}}_i} \hat{\varphi}_i(\hat{\mathbf{x}}), \qquad \forall \hat{\mathbf{x}} \in \hat{T}. \tag{3.28b}$$

We stress that $\hat{\mathbf{x}}_i \neq \hat{\mathbf{y}}_i := \Theta_T^{-m*}(\mathbf{x}_i^n)$ and hence call this step *shifted evaluation*. See Figure 3.8 for a sketch of the relation between $\hat{\mathbf{x}}_i$ and $\hat{\mathbf{y}}_i$. By setting $\tilde{v}_{\mathcal{T}_h^n}|_{T^n} := \tilde{v}_{T^n}$ for all $T^n \in \mathcal{T}_h^n$ we obtain $\tilde{v}_{\mathcal{T}_h^n} \in \bigoplus_{T^n \in \mathcal{T}_h^n} \mathcal{V}_h^n|_{T^n}$.

Projection into the space of continuous functions

After the previous two steps, we obtain a discontinuous, element-wise, mapped polynomial approximation on $\mathcal{T}_h^n$. Finally, we apply an Oswald-type quasi-interpolation $P_h : \bigoplus_{T^n \in \mathcal{T}_h^n} \mathcal{C}(T^n) \to \mathcal{V}_h^n$ in order to arrive at a continuous function $v_{\mathcal{T}_h^n} \in \mathcal{V}_h^n$, namely $v_{\mathcal{T}_h^n} := \Pi_m^n v_{\mathcal{T}_h^m} := P_h(\tilde{v}_{\mathcal{T}_h^n} \circ \Theta^n) \circ \Theta^{-n}$.

Let $\mathrm{L}(\mathcal{T}_h^n) = \{\mathbf{x}_i^n\}$ be the set of Lagrange nodes of $\mathcal{V}_h^n$ on $\mathcal{T}_h^n$, and $\{\varphi_i^n\}$ the set of corresponding Lagrange basis functions. Let $\omega(\mathbf{x}_i^n)$ be the set of elements containing the Lagrange node $\mathbf{x}_i^n$. The Oswald-type projector P_h is the following generalization of the Lagrange interpolation for a discontinuous function v

$$P_h v := \sum_{\mathbf{x}_i^n \in \mathrm{L}(\mathcal{T}_h^n)} \Big(\#\omega(\mathbf{x}_i^n)^{-1} \sum_{T^n \in \omega(\mathbf{x}_i^n)} v|_{T^n}(\mathbf{x}_i^n)\Big)\varphi_i^n. \tag{3.29}$$

3.1.5 Isoparametric discretization in space

The low-order discretization introduced in Subsection 3.1.2 can be improved trivially to higher order of accuracy in space if exact geometry handling is assumed or sufficiently accurate quadrature on $\Omega^n_{\phi_h}$ is given. However, the former is typically not realistic and the latter is hard to secure, we therefore utilize the technique of isoparametric mappings to achieve high-order approximation of the geometry.

As the physical domain evolves and the cut elements change, the time-dependent deformation of the mesh based on a sequence of the parametric mappings $\{\Theta^n\}_{n=1,\dots,N}$ is realized, which implies $\mathcal{T}_h^{n-1} \neq \mathcal{T}_h^n$ and $u_h^{n-1} \notin \mathcal{V}_h^n$, hence a projection of the solution

onto slightly different mesh arises. Thanks to the mesh transfer operator Π_m^n, $m = n-1$ already prepared in Subsection 3.1.4, we make use of this *consecutive* transfer operator, denoted by $\Pi^n : \mathcal{V}_h^{n-1} \to \mathcal{V}_h^n$, to project initial data u_h^{n-1} from one time step to the next. Analogously to (3.16), the weak formulation of high-order accuracy in space reads: To find $u_h^n \in \mathcal{V}_1^n$, $n = 1, ..., N$ for a given $u_h^0 \in \mathcal{V}_1^0$, such that

$$\int_{\Omega_h^n} \frac{u_h^n - \Pi^n u_h^{n-1}}{\Delta t} v_h \, d\mathbf{x} + b_h^n(u_h^n, v_h) + \gamma s_1^n(u_h^n, v_h) = f_h^n(v_h), \qquad \forall v_h \in \mathcal{V}_1^n. \tag{3.30}$$

Note that here the *isoparametric* finite element space $\mathcal{V}_1^n$ deviates from $\hat{\mathcal{V}}_{h,\delta}^n$. Accordingly, s_1^n takes the form as in (3.20) but the set of active facets $\mathcal{F}_{h,\delta}^n$ is now replaced by $\mathcal{F}_1^n$, cf. (3.14b), for extension of an additional element layer in order to cover the deformed meshes at next time step. In particular, we define

$$s_1^n(u_h, v_h) := \sum_{\mathcal{F}^n \in \mathcal{F}_1^n} s_F^n(u_h, v_h), \text{ with } s_F^n(u_h, v_h) := \frac{1}{h^2} \int_{\omega(F^n)} (u_1 - u_2)(v_1 - v_2) d\mathbf{x}, \tag{3.31}$$

where u_i, v_i, $i = 1, 2$ are canonical extensions of the *mapped* functions, namely $u_i = (\mathcal{E}^{\mathcal{P}}(u_h|_{T_i^n} \circ \Theta_{T_i}^n)) \circ \Theta_{T_i}^{-n*}$ (and similarly for v_i) with $\Theta_{T_i}^{n*} = \mathcal{E}^{\mathcal{P}}(\Theta_{T_i}^n)$ and $\mathcal{E}^{\mathcal{P}} : \mathcal{P}^k(\hat{T}_i) \to \mathcal{P}^k(\mathbb{R}^d)$, $\hat{T}_i = \Theta_{T_i}^{-n}(T_i^n)$ the canonical extension of a polynomial to $\mathbb{R}^d$.

This discretization is considered an arbitrarily high-order method in space, as it makes use of the isoparametrically mapped domain Ω_h^n and the isoparametric finite element space $\mathcal{V}_1^n$, but it has only low order of accuracy in time since the time derivative is still approximated by the first-order time difference stencil, i.e., the backward Euler scheme. We will therefore improve the time accuracy towards higher order by the BDF schemes in the next subsection.

3.1.6 BDF discretization in time

The low-order discretization introduced in Subsection 3.1.2 employs a backward Euler scheme with a ghost penalty term for the solution to be extended and well-defined on the domain at next time step. For higher-order discretization in time, we apply the following *backward differentiation formula* (BDF) to the approximation of the time derivative. A further domain extension is required accordingly.

Let us introduce the symbol $\partial^r_{\Delta t}(...)$ for the BDF time stencils (for $r = 1, 2, 3$):

$$\partial_{\Delta t}(u_h^n, u_h^{n-1}) := \frac{u_h^n - u_h^{n-1}}{\Delta t}, \qquad r = 1; \tag{3.32a}$$

$$\partial^2_{\Delta t}(u_h^n, u_h^{n-1}, u_h^{n-2}) := \frac{3u_h^n - 4u_h^{n-1} + u_h^{n-2}}{2\Delta t}, \qquad r = 2; \tag{3.32b}$$

$$\partial^3_{\Delta t}(u_h^n, u_h^{n-1}, u_h^{n-2}, u_h^{n-3}) := \frac{11u_h^n - 18u_h^{n-1} + 9u_h^{n-2} - 2u_h^{n-3}}{6\Delta t}, \qquad r = 3. \tag{3.32c}$$

These time stencils, however, require multiple δ-extensions to make all the previous solutions well-defined on the current domain, and the mesh transfer operators across multiple time steps to project all the previous solutions onto the current deformed mesh. To this end, we define the following *consecutive* application of the mesh transfer operators over all intermediate time steps

$$\Pi^n_{n-r} : \mathcal{V}_h^{n-r} \to \mathcal{V}_h^n, \qquad v \mapsto \Pi^n \, \Pi^{n-1} \cdots \Pi^{n-r+1} v. \tag{3.33}$$

Armed with the BDF and the consecutive mesh transfer operators, in contrast to (3.30), the weak formulation of this completely high-order method reads:
To find $u_h^n \in \mathcal{V}_r^n$, $n = r, ..., N$ for given $u_h^0 \in \mathcal{V}_r^0, ..., u_h^{r-1} \in \mathcal{V}_r^{r-1}$, such that for any $v_h \in \mathcal{V}_r^n$

$$\int_{\Omega_h^n} \partial^r_{\Delta t}(u_h^n, ..., \Pi^n_{n-r} u_h^{n-r}) v_h \, d\mathbf{x} + b_h^n(u_h^n, v_h) + \gamma s_r^n(u_h^n, v_h) = f_h^n(v_h). \tag{3.34}$$

where s_r^n takes the form as in (3.31) but the set of active facets $\mathcal{F}_1^n$ is now replaced by $\mathcal{F}_r^n$, cf. (3.14b), for extension of $r\delta$ distance plus r additional element layers in order to cover all the deformed meshes involved in the rth-order BDF time stencils.

Remark 10 (Consecutive mesh transfers in implementation)**.** *It is not necessary to apply the whole chain of the projections Π^n_{n-r} in implementation as the terms involving Π^m, $m < n$ are already evaluated in previous time steps and can be reused. In fact, there is only the projection Π^n to be evaluated at each time step (on possibly several terms though).*

3.2 Error Analysis

In this section, we analyze the isoparametric BDF-Eulerian method to derive a priori error estimate. The analysis substantially follows the lines in [114] and in [102]. The extra work on top of [102] appears due to the mesh transfer operator Π^n_m and the BDF

time stencil $\partial^r_{\Delta t}$, cf. Subsection 3.1.6. Therefore, we will first carry out a comprehensive analysis of the mesh transfer operator, which is followed by a priori error analysis that is composed of error splitting equation, consistency and interpolation bounds, ghost penalty and stability analysis, and finally the error estimate. Without loss of generality, we will only analyze the case of BDF2 time discretization, i.e., when $r = 2$ is fixed, but an extension to higher order of accuracy in time is possible.

As a result of the errors induced by the mesh transfer operator, in the subsequent analysis, we make the following assumption on the ratio between space and time refinements.

Assumption 4 (Refinements in space and time)**.** *We assume that as mesh size h and time step Δt go to zero, $\frac{h^5}{\Delta t^2}$ converges to zero. Then, for any constant $c_{A4} > 0$ there is an $h_0 > 0$ such that for all meshes with mesh size $h < h_0$ we have $\frac{h^5}{\nu \Delta t^2} < c_{A4}$, which implies $\frac{h^4}{\nu \Delta t} < c_{A4}$ as well.*

Remark 11. *Assumption 4 is only a restriction on the efficiency for very high order in space. Suppose an $\mathcal{L}^2(0,T;\mathcal{H}^1(\Omega))$-error bound of the form [3] $\mathcal{O}(\Delta t^2 + h^k)$, then only for $k \geq 5$ a scaling $h \geq \Delta t^{\frac{2}{5}}$ would be benefitial for the efficiency of the scheme.*

Moreover, in the remainder we treat the asymptotic behavior $h, \Delta t \to 0$ only, i.e., we implicitly assume h and Δt *sufficiently small* at several occasions.

3.2.1 Analysis of the mesh transfer operator

As discussed in Section 3.1.3, the sequence of isoparametric mappings in time probably alters the deformed meshes between consecutive time steps, and thus the solutions on the deformed meshes have to be projected from one mesh to another, in order to do proper time stepping. We therefore proposed the mesh transfer operator of finite element functions $\Pi^n : \mathcal{V}_h^{n-1} \to \mathcal{V}_h^n$ in Subsection 3.1.4, which deviates from a direct $\mathcal{L}^2$ projection on account of locality and computational efficiency. As a consequence, this projection may induce some errors, and hence in this subsection, we analyze the mesh transfer operator by the following lemmas, with using the same notation aforementioned, cf. Subsection 3.1.1 and Subsection 3.1.4.

We start with a simple observation for the norm evaluation with respect to one mesh of a function defined on another (slightly different) mesh.

[3] See also the numerical examples for a motivation of this ansatz.

Lemma 4. *For $v_h \in \mathcal{V}_h^n$, $w_h \in \mathcal{V}_h^m$, $T_i = \Theta_T^i(\hat{T})$, $\hat{T} \in \mathcal{T}_h$, $i \in \{m,n\}$, there holds*

$$\|v_h + w_h\|_{T^n} \lesssim h^{\frac{d}{2}} \|v_h + w_h\|_{\mathcal{L}^\infty(T^n_{-\varepsilon})} + h^{\frac{5}{2}} \|\nabla v_h\|_{T^n} + h^{\frac{5}{2}} \|\nabla w_h\|_{\omega(T^m)}. \tag{3.35}$$

Proof. Obviously we have $\|v_h + w_h\|_{T^n} \lesssim \|v_h + w_h\|_{T^n_{-\varepsilon}} + \|v_h + w_h\|_{T^n \setminus T^n_{-\varepsilon}}$. The first term on the right-hand side is simply bounded by $h^{\frac{d}{2}} \|v_h + w_h\|_{\mathcal{L}^\infty(T^n_{-\varepsilon})}$. For the second term we use Lemma 3, i.e., $\text{meas}_d(T^n \setminus T^n_{-\varepsilon}) \lesssim h^{d+1}$, and that for $\mathbf{x} \in T^n \setminus T^n_{-\varepsilon}$ there is $\mathbf{y} \in \partial T^n_{-\varepsilon}$ and $\mathbf{z} \in \text{conv}\{\mathbf{x},\mathbf{y}\} \subset T \setminus T^n_{-\varepsilon}$ such that $|(v_h + w_h)(\mathbf{x})| \leq |(v_h + w_h)(\mathbf{y})| + |(\nabla(v_h + w_h))(\mathbf{z})|\ |\mathbf{y} - \mathbf{x}|$, and hence with $\varepsilon \lesssim h^2$ we obtain

$$\begin{aligned}
\|v_h + w_h\|_{T^n \setminus T^n_{-\varepsilon}} &\lesssim h^{\frac{d+1}{2}} \|v_h + w_h\|_{\mathcal{L}^\infty(T^n \setminus T^n_{-\varepsilon})} \\
&\lesssim h^{\frac{d+1}{2}} \left(\|v_h + w_h\|_{\mathcal{L}^\infty(T^n_{-\varepsilon})} + \varepsilon \|\nabla(v_h + w_h)\|_{\mathcal{L}^\infty(T^n \setminus T^n_{-\varepsilon})} \right) \\
&\lesssim h^{\frac{d+1}{2}} \left(\|v_h + w_h\|_{\mathcal{L}^\infty(T^n_{-\varepsilon})} + h^2 \|\nabla v_h\|_{\mathcal{L}^\infty(T^n)} + h^2 \|\nabla w_h\|_{\mathcal{L}^\infty(\omega(T^m))} \right) \\
&\lesssim h^{\frac{d+1}{2}} \|v_h + w_h\|_{\mathcal{L}^\infty(T^n_{-\varepsilon})} + h^{\frac{5}{2}} \|\nabla v_h\|_{T^n} + h^{\frac{5}{2}} \|\nabla w_h\|_{\omega(T^m)}.
\end{aligned}$$

In the last step we take advantage of the norm equivalences on a reference element after transformation. Please note that we cannot apply such a result directly for $v_h + w_h$ as w_h and v_h are not from the same (mapped) polynomial space. This completes the proof by adding up the two terms. □

In the next lemma, we claim that the $\mathcal{L}^2$-norm of a projected function (or its gradient) on one element can be bounded by the original function (or its gradient) on the corresponding element patch.

Lemma 5. *Let $\Pi^n : \mathcal{V}_h^m \to \mathcal{V}_h^n$, $m = n-1$ be the projection for a discrete function $v_h \in \mathcal{V}_h^m$ from the mesh $\mathcal{T}_h^m$ to the mesh $\mathcal{T}_h^n$. Furthermore, let $\tilde{\mathcal{T}}_h \subset \mathcal{T}_h$ be an arbitrary selection of straight elements and the corresponding deformed meshes $\tilde{\mathcal{T}}_h^m$, $\tilde{\mathcal{T}}_h^n$ with the corresponding domains $\tilde{\mathcal{D}}_h^m$, $\tilde{\mathcal{D}}_h^n$, respectively. For $c_{5a} > 0$ and $c_{5b} > 0$ independent of mesh size h and time step Δt, there holds for $\hat{T} \in \mathcal{T}_h$, $T^n = \Theta_T^n(\hat{T}), T^m = \Theta_T^m(\hat{T})$*

$$\|\Pi^n v_h\|^2_{T^n} \lesssim \|v_h\|^2_{\omega(T^m)}, \qquad \|\Pi^n v_h\|^2_{\tilde{\mathcal{D}}_h^n} \leq c_{5a} \|v_h\|^2_{\tilde{\mathcal{D}}^m_{h,0,1}}; \tag{3.36a}$$

$$\|\nabla \Pi^n v_h\|^2_{T^n} \lesssim \|\nabla v_h\|^2_{\omega(T^m)}, \qquad \|\nabla \Pi^n v_h\|^2_{\tilde{\mathcal{D}}_h^n} \leq c_{5b} \|\nabla v_h\|^2_{\tilde{\mathcal{D}}^m_{h,0,1}}. \tag{3.36b}$$

Proof. First of all, we have $\|\Pi^n v_h\|_{T^n} \simeq \|\Pi^n v_h\|_{T^n_{-\varepsilon}}$ by (3.26). For $\mathbf{x} \in T^n_{-\varepsilon}$ and $\hat{\mathbf{x}} = \Theta^{-n}(\mathbf{x}) \in \hat{T}_{-\varepsilon}$, with the notation introduced in Section 3.1.4, there holds by definition

$$\Pi^n v_h(\mathbf{x}) = \sum_{i=1}^{\#\mathrm{L}(T^n)} \Big(\#\hat{\omega}(\mathbf{x}_i^n)^{-1} \sum_{\tilde{T} \in \hat{\omega}(\mathbf{x}_i^n)} \hat{v}^*_{\tilde{T}}(\hat{\mathbf{y}}_i) \Big) \hat{\varphi}_i(\hat{\mathbf{x}})$$

where $\#\mathrm{L}(T^n) \lesssim 1$ is the number of Lagrange nodes on T^n and $\#\hat{\omega}(\mathbf{x}_i^n)$ is the number of elements in the patch set $\hat{\omega}(\mathbf{x}_i^n) = \Theta^{-n}(\omega(\mathbf{x}_i^n))$ with respect to the undeformed mesh $\mathcal{T}_h$. Thus we have $\|\Pi^n v_h\|_{T^n_{-\varepsilon}} \lesssim h^{\frac{d}{2}} \|v_h\|_{\mathcal{L}^\infty(\omega(T^m))} \lesssim \|v_h\|_{\omega(T^m)}$. Summing over all elements in $\tilde{\mathcal{T}}_h^n$ yields (3.36a). For (3.36b) we proceed with $\Pi^n \bar{v}_h = \bar{v}_h$ on $T^n_{-\varepsilon}$ similarly after introducing $\bar{v}_h = \frac{1}{|\omega(T^m)|} \int_{\omega(T^m)} v_h ds$, namely

$$\begin{aligned} \|\nabla \Pi^n v_h\|_{T^n_{-\varepsilon}} = \|\nabla \Pi^n (v_h - \bar{v}_h)\|_{T^n_{-\varepsilon}} &\lesssim h^{\frac{d}{2}} h^{-1} \|v_h - \bar{v}_h\|_{\mathcal{L}^\infty(\omega(T^m))} \\ &\lesssim h^{-1} \|v_h - \bar{v}_h\|_{\omega(T^m)} \lesssim \|\nabla v_h\|_{\omega(T^m)}. \end{aligned}$$

This completes the proof. □

Next, we estimate the bounds of the difference between original and projected functions in the following lemma.

Lemma 6. *Let $\Pi^n : \mathcal{V}_h^m \to \mathcal{V}_h^n$, $m = n-1$ be the projection for a discrete function $v_h \in \mathcal{V}_h^m$ from the mesh $\mathcal{T}_h^m$ to the mesh $\mathcal{T}_h^n$. There holds for $T^n \in \mathcal{T}_h^n$ and $T^m = \Theta^m(\Theta^{-n}(T^n)) \in \mathcal{T}_h^m$*

$$\|(\mathrm{id} - \Pi^n) v_h\|_{T^n} \lesssim h^2 \|\nabla v_h\|_{\omega(T^m)} \lesssim h \|v_h\|_{\omega(T^m)}. \tag{3.37a}$$

Moreover, for an arbitrary selection of straight elements $\tilde{\mathcal{T}}_h \subset \mathcal{T}_h$ and the corresponding deformed meshes $\tilde{\mathcal{T}}_h^m$, $\tilde{\mathcal{T}}_h^n$ with the corresponding domains $\tilde{\mathcal{D}}_h^m$, $\tilde{\mathcal{D}}_h^n$, respectively, there holds

$$\|(\mathrm{id} - \Pi^n) v_h\|_{\tilde{\mathcal{D}}_h^n} \lesssim h^2 \|\nabla v_h\|_{\tilde{\mathcal{D}}^m_{h,0,1}} \lesssim h \|v_h\|_{\tilde{\mathcal{D}}^m_{h,0,1}}. \tag{3.37b}$$

Proof. Let $T^n = \Theta_T^n(\hat{T}) \in \mathcal{T}_h^n$ and $T^m = \Theta_T^m(\hat{T}) \in \mathcal{T}_h^m$ be the deformed elements of $\hat{T} \in \mathcal{T}_h$. By Lemma 4 and Lemma 5 we obtain

$$\|(\mathrm{id} - \Pi^n) v_h\|_{T^n} \lesssim h^{\frac{d}{2}} \|(\mathrm{id} - \Pi^n) v_h\|_{\mathcal{L}^\infty(T^n_{-\varepsilon})} + h^{\frac{5}{2}} \|\nabla v_h\|_{\omega(T^m)}.$$

We then bound the first term with using the notation introduced in Section 3.1.4. For $\forall \mathbf{x} \in T^n_{-\varepsilon} \subset T^n \cap T^m$ and $\hat{\mathbf{x}} := \Theta_T^{-n}(\mathbf{x})$, we have by definition

$$(v_h - \Pi^n v_h)(\mathbf{x}) = \sum_{i=1}^{\#\mathrm{L}(T^n)} \Big(\#\hat{\omega}(\mathbf{x}_i^n)^{-1} \sum_{\tilde{T} \in \hat{\omega}(\mathbf{x}_i^n)} \big(\hat{v}^*_{\tilde{T}}(\hat{\mathbf{x}}_i) - \hat{v}^*_{\tilde{T}}(\hat{\mathbf{y}}_i) \big) \Big) \hat{\varphi}_i(\hat{\mathbf{x}})$$

for the number of Lagrange nodes $\#\mathrm{L}(T^n) \lesssim 1$ and the number of straight elements $\#\hat{\omega}(\mathbf{x}_i^n)$ in the patch $\hat{\omega}(\mathbf{x}_i^n) = \Theta^{-n}(\omega(\mathbf{x}_i^n)) \subset \mathcal{T}_h$ with respect to the undeformed mesh. With the second-order boundedness of Θ^i, $i \in \{m, n\}$, cf. Lemma 2, we have $|\hat{\mathbf{x}}_i - \hat{\mathbf{y}}_i| \lesssim h^2$ and hence for every $\tilde{T}$ in the element patch $\omega(\hat{T})$ there holds

$$|\hat{v}^*_{\tilde{T}}(\hat{\mathbf{x}}_i) - \hat{v}^*_{\tilde{T}}(\hat{\mathbf{y}}_i)| \lesssim h^2 \|\nabla \hat{v}^*_{\tilde{T}}\|_{\mathcal{L}^\infty(\hat{T}_\varepsilon)} \lesssim h^2 \|\nabla \hat{v}_{\tilde{T}}\|_{\mathcal{L}^\infty(\hat{T})} \lesssim h^{2-\frac{d}{2}} \|\nabla \hat{v}_{\tilde{T}}\|_{\hat{T}},$$

where we made use of the norm equivalence on finite dimensional spaces and scaling arguments. This yields (3.37a). Summing over $\tilde{\mathcal{T}}_h^n$ we obtain (3.37b) by using finite overlap. □

In the following lemma, we study how the projection acts on the ghost penalty terms, which bridges the ghost penalty terms at different time steps.

Lemma 7. *Let $\Pi^n : \mathcal{V}_h^m \to \mathcal{V}_h^n$, $m = n-1$ be the projection for a discrete function $v_h \in \mathcal{V}_h^m$ from the mesh $\mathcal{T}_h^m$ to the mesh $\mathcal{T}_h^n$. For constants c_{7a} and c_{7b} independent of mesh size h and time step Δt, there holds*

$$s_1^n(\Pi^n v_h, \Pi^n v_h) \leq c_{7a} s_2^m(v_h, v_h) + c_{7b} h^2 \|\nabla v_h\|^2_{\mathcal{D}_2^{m,\mathcal{S}}}. \tag{3.38}$$

Proof. Let us consider a curved facet $F^n \in \mathcal{F}_1^n$ with the corresponding straight facet $\hat{F} = \Theta^{-n}(F^n)$ and accordingly $F^m = \Theta^m(\hat{F}) \in \mathcal{F}_2^m$. Their adjacent elements of the patches are denoted by $\omega(F^n) = T_1^n \cup T_2^n$, $\omega(\hat{F}) = \hat{T}_1 \cup \hat{T}_2$, and $\omega(F^m) = T_1^m \cup T_2^m$, respectively. Note that $\Theta^m_{T_1}$, $\Theta^n_{T_1}$, $\Theta^m_{T_2}$ and $\Theta^n_{T_2}$ are involved here. Let $u_h = \Pi^n v_h \in \mathcal{V}_h^n$ be the discrete function after projection. Recalling the notation from (3.20) or (3.31), we define $u_i = \hat{u}_i \circ \Theta_{T_i}^{-n*}$, $i = 1, 2$ with $\hat{u}_i := \mathcal{E}^{\mathcal{P}}(u_h|_{T_i^n} \circ \Theta^n_{T_i})$ and $v_i = \hat{v}_i \circ \Theta_{T_i}^{-m*}$, $i = 1, 2$ with $\hat{v}_i := \mathcal{E}^{\mathcal{P}}(v_h|_{T_i^m} \circ \Theta^m_{T_i})$. We further introduce the symbols for the properly extended neighboring functions: $\hat{u}_j^* := \hat{u}_j \circ \Upsilon^n(\hat{\mathbf{x}})$ and $\hat{v}_j^* := \hat{v}_j \circ \Upsilon^m(\hat{\mathbf{x}})$ with $\Upsilon^n = \Theta_{T_j}^{-n*} \circ \Theta^n_{T_i}$ and $\Upsilon^m = \Theta_{T_j}^{-m*} \circ \Theta^m_{T_i}$. Importing the definition of the ghost penalty from (3.20) and exploiting the h^2-smallness of the deformations, we find after transformation to $\hat{T}_i$, $\hat{T}_j$

that

$$h^2 s_F^n(u_h,u_h) \le 2\sum_{i,j=1,2}\int_{\hat{T}_i}(\hat{u}_i-\hat{u}_j^*)^2 d\hat{\mathbf{x}} \quad \text{and} \quad \sum_{i,j=1,2}\int_{\hat{T}_i}(\hat{v}_i-\hat{v}_j^*)^2 d\hat{\mathbf{x}} \le 2h^2 s_F^m(v_h,v_h).$$

Let $a := \hat{u}_i - \hat{u}_j^*$ and $b := \hat{v}_i - \hat{v}_j^*$, then with $A := \hat{u}_i - \hat{v}_i$ and $B := \hat{u}_j^* - \hat{v}_j^*$ we have $a-b = A-B$, so that there holds

$$\begin{aligned} a^2-b^2 = \underbrace{(a-b)}_{(A-B)}(a+b) \le (A-B)^2 + \frac{1}{4}(a+b)^2 \le 2(A^2+B^2) + \frac{1}{2}(a^2+b^2) \\ \implies \frac{1}{2}a^2 - \frac{3}{2}b^2 \le 2(A^2+B^2) \implies a^2 \le 3b^2 + 4(A^2+B^2). \end{aligned}$$

Hence, we arrive at

$$s_F^n(u_h,u_h) \lesssim s_F^m(v_h,v_h) + h^{-2}\sum_{\substack{i,j=1,2\\ i\neq j}}\Big(\|\underbrace{\hat{u}_i-\hat{v}_i}_{=A}\|_{\hat{T}_i}^2 + \|\underbrace{\hat{u}_i^*-\hat{v}_i^*}_{=B}\|_{\hat{T}_i}^2\Big).$$

As a polynomial in $\mathcal{P}^k(\mathbb{R}^d)$ we can retreat $A(\hat{x})$ to $\hat{T}_{i,-\varepsilon}$ and find

$$\begin{aligned} \|A\|_{\hat{T}_i} \simeq \|A\|_{\hat{T}_{i,-\varepsilon}} &\lesssim \|v_h\circ\Theta_{T_i}^n - \overbrace{u_h\circ\Theta_{T_i}^n}^{\hat{u}_i}\|_{\hat{T}_{i,-\varepsilon}} + \|v_h\circ\Theta_{T_i}^n - \overbrace{v_h\circ\Theta_{T_i}^m}^{\hat{v}_i}\|_{\hat{T}_{i,-\varepsilon}} \\ &\lesssim \|(\mathrm{id}-\Pi^n)v_h\|_{T_i^n} + \|v_h\circ(\Theta_{T_i}^n-\Theta_{T_i}^m)\|_{\hat{T}_{i,-\varepsilon}} \lesssim h^2\|\nabla v_h\|_{\omega(T_i^m)} \end{aligned}$$

where in the last step we made use of Lemma 6 and the closeness of Θ_T^n and Θ_T^m. For $B(\hat{x})$ we first note that $\|\Upsilon^n-\Upsilon^m\|_{\mathcal{L}^\infty(\hat{T}_i)} \lesssim h^2$ and then recall $\hat{u}_j-\hat{v}_j \in \mathcal{P}^k(\mathbb{R}^d)$ such that with standard scaling arguments we have $\|\hat{u}_j-\hat{v}_j\|_{\Upsilon^n(\hat{T}_i)} \lesssim \|\hat{u}_j-\hat{v}_j\|_{\hat{T}_{j,-\varepsilon}}$ and

$$\begin{aligned} \|B\|_{\hat{T}_i} &\lesssim \|(\hat{u}_j-\hat{v}_j)\circ\Upsilon^n\|_{\hat{T}_i} + \|\hat{v}_j\circ\Upsilon^n - \hat{v}_j\circ\Upsilon^m\|_{\hat{T}_j} \lesssim \|\hat{u}_j-\hat{v}_j\|_{\Upsilon^n(\hat{T}_i)} + h^2\|\nabla v_h\|_{T_j^m} \\ &\lesssim \|u_h\circ\Theta_{T_j}^n - v_h\circ\Theta_{T_j}^m\|_{\hat{T}_{j,-\varepsilon}} + h^2\|\nabla v_h\|_{T_j^m} \\ &\lesssim \|(u_h-v_h)\circ\Theta_{T_j}^n\|_{\hat{T}_{j,-\varepsilon}} + \|v_h\circ\Theta_{T_j}^n - v_h\circ\Theta_{T_j}^m\|_{\hat{T}_{j,-\varepsilon}} + h^2\|\nabla v_h\|_{T_j^m} \\ &\lesssim \|\Pi^n u_h - v_h\|_{T_j^n} + h^2\|\nabla v_h\|_{T_j^m} \lesssim h^2\|\nabla v_h\|_{\omega(T_j^m)}. \end{aligned}$$

Putting all together completes the proof. □

The previous lemmas describe the scenarios of *the worst case* as v_h is allowed to be arbitrarily rough in $\mathcal{V}_h^m$. Assuming more smoothness helps to improve the bound.

Lemma 8. *Let $\Pi^n : \mathcal{V}_h^m \to \mathcal{V}_h^n$, $m = n-1$ be the projection for a discrete function $v_h \in \mathcal{V}_h^m$ from the mesh $\mathcal{T}_h^m$ to the mesh $\mathcal{T}_h^n$. For any $\hat{T} \in \mathcal{T}_h$ and $T^n = \Theta^n(\hat{T}) \in \mathcal{T}_h^n$,*

$v \in \mathcal{W}_\infty^{k+1}(T_\varepsilon^n) \cap C^0(\omega(T^n))$ and $\mathcal{I}_h^p$ the Lagrange interpolation operator with respect to $\mathcal{T}_h^p$, $p \in \{m,n\}$, there holds

$$\|(\mathcal{I}_h^n - \Pi^n \mathcal{I}_h^m)v\|_{T^n} \lesssim \|\Theta^n - \Theta^m\|_{\mathcal{L}^\infty(\hat{\omega}(\hat{T}))}\ h^{k+\frac{d}{2}} |v|_{\mathcal{W}_\infty^{k+1}(T_\varepsilon^n)}. \tag{3.39}$$

Proof. Let $\varphi_i^p := \hat{\varphi}_i \circ \Theta_T^{-p}$ be the Lagrange basis functions of $\mathcal{V}_h^p|_{T^p}$ with respect to the Lagrange nodes $\mathbf{x}_i^p := \Theta_T^p(\hat{\mathbf{x}}_i)$ on $T^p \in \mathcal{T}_h^p$ such that $\varphi_i^p(\mathbf{x}_j^p) = \delta_{ij},\ i,j = 1,...,\#\mathrm{L}(T^p)$. Analogously to the local interpolation operator $\mathcal{I}_{T^p}^p$ on T^p we define the nodal interpolation operator on the extension T_ε^p of T^p, namely for $p \in \{m,n\}$ such that

$$\mathcal{I}_{T^p}^p v(\mathbf{x}) := \sum_{i=1}^{\#\mathrm{L}(T^p)} v(\mathbf{x}_i^p)\varphi_i^p(\mathbf{x}) \quad \text{and} \quad \mathcal{I}_{T_\varepsilon^p}^p v(\mathbf{x}) := \sum_{i=1}^{\#\mathrm{L}(T^p)} v(\mathbf{x}_i^p)\varphi_i^{p*}(\mathbf{x}), \qquad v \in \mathcal{L}^\infty(T^p),$$

where $(\cdot)^* = \mathcal{E}^{\mathcal{P}}(\cdot)$ canonically extends the basis functions φ_i^p on $T^p \in \mathcal{T}_h^p$ to T_ε^p. With the definition of the projection Π^n, cf. Section 3.1.4, we have for $\mathbf{x} \in T^n$

$$(\mathcal{I}_h^n v - \Pi^n \mathcal{I}_h^m v)(\mathbf{x}) = \sum_{j=1}^{\#\mathrm{L}(T^n)} \Big(\#\omega(\mathbf{x}_i^m)^{-1} \sum_{\tilde{T}^m \in \omega(\mathbf{x}_i^m)} \big((v - \mathcal{I}_{\tilde{T}_\varepsilon^m}^m v)(\mathbf{x}_j^n) \big) \Big) \varphi_j^n(\mathbf{x})$$

for any $v \in C^0(\omega(T^m))$. Taking the $\mathcal{L}^2$-norm on $T^n \in \mathcal{T}_h^n$ we arrive at

$$\|\mathcal{I}_h^n v - \Pi^n \mathcal{I}_h^m v\|_{T^n} \lesssim h^{\frac{d}{2}} \max_{\tilde{T}^m \in \omega(T^m)} \|v - \mathcal{I}_{\tilde{T}_\varepsilon^m}^m v\|_{l_\infty(\mathrm{L}(T^n))},$$

where we made use of $\|\sum_{j=1}^{\#\mathrm{L}(T^n)} \varphi_j^n\|_{T^n} \lesssim h^{\frac{d}{2}}$. Let the Taylor polynomial of degree k be denoted by $\hat{\mathfrak{T}}_{\hat{x}_j^m}$ that expands a function $\hat{v}$ at node $\hat{x}_j^m$. We introduce the mapped Taylor polynomial to the element $\tilde{T}$ in the patch $\omega(T^m)$ by transformation to the undeformed element applying the Taylor expansion there and transforming back, i.e., $\mathfrak{T}_{\mathbf{x}_j^m} v := (\hat{\mathfrak{T}}_{\hat{x}_j^m}(v \circ \Theta_{\tilde{T}}^{m*})) \circ \Theta_{\tilde{T}}^{-m*}$ such that there holds $\mathfrak{T}_{\mathbf{x}_j^m} v = \mathcal{I}_{\tilde{T}_\varepsilon^m}^m \mathfrak{T}_{\mathbf{x}_j^m} v$. For $j = 1,...,\#\mathrm{L}(T^n)$ we then have

$$\begin{aligned} |(v - \mathcal{I}_{\tilde{T}_\varepsilon^m}^m v)(\mathbf{x}_j^n)| &= \big| (v - \mathfrak{T}_{\mathbf{x}_j^m} v)(\mathbf{x}_j^n) + (\mathfrak{T}_{\mathbf{x}_j^m} v - \mathcal{I}_{\tilde{T}_\varepsilon^m}^m v)(\mathbf{x}_j^n) \big| \\ &\le |(v - \mathfrak{T}_{\mathbf{x}_j^m} v)(\mathbf{x}_j^n)| + |\mathcal{I}_{\tilde{T}_\varepsilon^m}^m (\mathfrak{T}_{\mathbf{x}_j^m} v - v)(\mathbf{x}_j^n)|. \end{aligned}$$

For the first part we simply have with $\mathbf{x}_j^n = \Theta_{\tilde{T}}^n(\hat{\mathbf{x}}_j)$, $\mathbf{x}_j^m = \Theta_{\tilde{T}}^m(\hat{\mathbf{x}}_j)$ and $\mathbf{x}_j^n, \mathbf{x}_j^m \in T_\varepsilon^n$

$$|(v - \mathfrak{T}_{\mathbf{x}_j^m} v)(\mathbf{x}_j^n)| \lesssim |\mathbf{x}_j^n - \mathbf{x}_j^m|^{k+1} |v|_{\mathcal{W}_\infty^{k+1}(T_\varepsilon^n)} \lesssim \|\Theta_{\tilde{T}}^n - \Theta_{\tilde{T}}^m\|_{\mathcal{L}^\infty(\hat{T})}^{k+1} |v|_{\mathcal{W}_\infty^{k+1}(T_\varepsilon^n)}.$$

For the second part we exploit $(\mathfrak{T}_{\mathbf{x}_j^m} v - v)(\mathbf{x}_j^m) = 0$ to obtain

$$\begin{aligned}
|\mathcal{I}^m_{\tilde{T}^m_\varepsilon}(\mathfrak{T}_{\mathbf{x}_j^m} v - v)(\mathbf{x}_j^n)| &= \Big| \sum_{i=1}^{\#\mathrm{L}(T^n)} (\mathfrak{T}_{\mathbf{x}_j^m} v - v)(\mathbf{x}_i^m) \varphi_i^{m*}(\mathbf{x}_j^n) \Big| = \Big| \sum_{i \neq j} (\mathfrak{T}_{\mathbf{x}_j^m} v - v)(\mathbf{x}_i^m) \varphi_i^{m*}(\mathbf{x}_j^n) \Big| \\
&\lesssim \max_{i \neq j} |\varphi_i^{m*}(\mathbf{x}_j^n)| \ \max_{i \neq j} |(\mathfrak{T}_{\mathbf{x}_j^m} v - v)(\mathbf{x}_i^m)| \\
&\lesssim \max_{i \neq j} |\varphi_i^{m*}(\mathbf{x}_j^n)| \ \underbrace{|\mathbf{x}_i^m - \mathbf{x}_j^m|^{k+1}}_{\lesssim h^{k+1}} |v|_{\mathcal{W}^{k+1}_\infty(T^n_\varepsilon)}.
\end{aligned}$$

Finally, we bound $\left|\varphi_i^{m*}(\mathbf{x}_j^n)\right|$ for $i \neq j$ by using $\varphi_i^{m*}(\mathbf{x}_j^m) = 0$

$$|\varphi_i^{m*}(\mathbf{x}_j^n)| = |\varphi_i^{m*}(\mathbf{x}_j^n) - \varphi_i^{m*}(\mathbf{x}_j^m)| \lesssim \|\nabla \varphi_i^{m*}\|_{\mathcal{L}^\infty(\hat{T}_\varepsilon)} \|\mathbf{x}_j^n - \mathbf{x}_j^m\| \lesssim h^{-1} \|\Theta^n_{\tilde{T}} - \Theta^m_{\tilde{T}}\|_{\mathcal{L}^\infty(\hat{T})}.$$

Altogether, this completes the proof by summing over all $\tilde{T}^m$ in $\omega(T^m)$. □

3.2.2 Error splitting equation

In order to conduct a priori error analysis of the numerical method, we start with an error splitting into consistency and interpolation parts and estimate their error bounds.

Let u be the exact solution to the PDE problem (2.35) or (3.1). For $u^n := u(t_n)$, $n = 0, 1, ..., N \in \mathbb{N}$, we make use of the smooth extension operator $\mathcal{E} : \mathcal{L}^2(\Omega^n) \to \mathcal{L}^2(\Omega^n_\varepsilon)$ as introduced in [102, Section 3.2.1], such that $\mathcal{E}u^n$ is well-defined on $\Omega^n_\varepsilon \supset \Omega^{n+r}$ and $\mathcal{E}$ is uniformly continuous in standard Sobolev norms. In the remainder of this section, we assume that $\varepsilon \in \mathbb{R}_+$ can be chosen sufficiently large to ensure $\Omega^n_\varepsilon \supset \mathcal{D}^n_r$, and we identify $\mathcal{E}u^n$ with u^n for the sake of simplicity of the notation.

Let $u^n_I := \mathcal{I}^n_h u^n \in \mathcal{V}^n_h$ be the global Lagrange interpolant with respect to $\mathcal{T}^n_h$ such that the error can be split into

$$\mathbf{e}^n := u^n - u^n_h = \mathbf{e}^n_I + \mathbf{e}^n_h, \qquad \text{for} \quad \mathbf{e}^n_I := u^n - u^n_I, \ \mathbf{e}^n_h := u^n_I - u^n_h, \tag{3.40}$$

where $\mathbf{e}^n_I$ is the *interpolation error* and $\mathbf{e}^n_h$ is the *discrete error*. Furthermore, we split the error after mesh transfer from $\mathcal{V}^m_h$ to $\mathcal{V}^n_h$ in such a way that

$$\tilde{\mathbf{e}}^m := u^m - \Pi^n_m u^m_h = \tilde{\mathbf{e}}^m_I + \Pi^n_m \mathbf{e}^m_h, \qquad \text{for} \quad \tilde{\mathbf{e}}^m_I := u^m - \Pi^n_m u^m_I, \tag{3.41}$$

where $\tilde{\mathbf{e}}^m_I$ is the corresponding interpolation error after projection, and $\Pi^n_m \mathbf{e}^m_h$ is the projection of the corresponding discrete error.

We then introduce a lifting operator $(\cdot)^l : \mathcal{H}^1(\Omega_h^n) \to \mathcal{H}^1(\Omega^n),\ v_h \mapsto v_h \circ \Theta^n \circ \Psi^{-n}$ that maps a function from the approximated domain to the exact domain, and correspondingly $b^n(\cdot,\cdot)$ and $f^n(\cdot)$, in forms of the discrete bilinear form $b_h^n(\cdot,\cdot)$ and the linear one $f_h^n(\cdot)$ but in which Ω_h^n, Γ_h^n are now replaced by Ω^n, Γ^n of exact geometry.

For the exact solution u^n to (3.1) there holds for $n = 0, 1, ..., N$

$$\int_{\Omega_h^n} \partial_t u^n v \ d\mathbf{x} + b^n(u^n, v) = f^n(v) \qquad \forall v \in \mathcal{H}^1(\Omega_h^n), \tag{3.42}$$

from which we subtract (3.34) to obtain the equation of errors $\mathbf{e}^n, \tilde{\mathbf{e}}^{n-1}, ..., \tilde{\mathbf{e}}^{n-r}$

$$\int_{\Omega_h^n} \partial_{\Delta t}^2(\mathbf{e}^n, ..., \tilde{\mathbf{e}}^{n-r})\ v_h \ d\mathbf{x} + b_h^n(\mathbf{e}^n, v_h) + \gamma s_r^n(\mathbf{e}^n, v_h) = \mathbf{E}_C^n(v_h), \tag{3.43}$$

where the consistency error term can be decomposed into four contributions

$$\begin{aligned} \mathbf{E}_C^n(v_h) := & \overbrace{\int_{\Omega_h^n} \partial_{\Delta t}^2(u^n, ..., u^{n-r})\ v_h \ d\mathbf{x} - \int_{\Omega^n} \partial_t u^n v_h^l d\mathbf{x}}^{\mathbf{E}_{C1}^n(v_h)} \\ & + \underbrace{b_h^n(u^n, v_h) - b^n(u^n, v_h^l)}_{\mathbf{E}_{C2}^n(v_h)} + \underbrace{\gamma s_r^n(u^n, v_h)}_{\mathbf{E}_{C3}^n(v_h)} + \underbrace{f^n(v_h^l) - f_h^n(v_h)}_{\mathbf{E}_{C4}^n(v_h)}. \end{aligned} \tag{3.44}$$

Further splitting $\mathbf{e}^n$ and $\tilde{\mathbf{e}}^{n-1}, ..., \tilde{\mathbf{e}}^{n-r}$ in (3.43) yields

$$\int_{\Omega_h^n} \partial_{\Delta t}^2(\mathbf{e}_h^n, ..., \Pi_{n-r}^n \mathbf{e}_h^{n-r}) v_h d\mathbf{x} + b_h^n(\mathbf{e}_h^n, v_h) + \gamma s_r^n(\mathbf{e}_h^n, v_h) = \mathbf{E}_C^n(v_h) + \mathbf{E}_I^n(v_h), \tag{3.45}$$

for the interpolation error term of two contributions

$$\mathbf{E}_I^n(v_h) := \underbrace{-\int_{\Omega_h^n} \partial_{\Delta t}^2(\mathbf{e}_I^n, ..., \tilde{\mathbf{e}}_I^{n-r})\ v_h \ d\mathbf{x}}_{\mathbf{E}_{I1}^n(v_h)} \underbrace{- b_h^n(\mathbf{e}_I^n, v_h) - \gamma s_r^n(\mathbf{e}_I^n, v_h)}_{\mathbf{E}_{I2}^n(v_h)}. \tag{3.46}$$

In the following analysis, we will fix $r = 2$ for the BDF2 time stencil, however, an extension to higher order of accuracy in time (i.e., BDF-r) is accessible.

3.2.3 Consistency estimates

In this subsection, we estimate the consistency error bound.

Lemma 9. *Let $u \in \mathcal{W}_\infty^3(\Xi) \cap \mathcal{L}^\infty(0,T;\mathcal{H}^{k+1}(\Omega(t)))$ be the exact solution to (3.1) and let $g \in \mathcal{L}^\infty(0,T;\mathcal{W}_\infty^1(\Omega(t)))$, then the consistency error in (3.44) with $r = 2$ has the*

following bound for all $v_h \in \mathcal{V}_2^n$

$$|\mathbf{E}_C^n(v_h)| \lesssim (\Delta t^2 + h^q + h^k K^{\frac{1}{2}}) \mathcal{R}_9(u,g) |||v_h|||_n$$

with $\mathcal{R}_9(u,g) := \|u\|_{\mathcal{W}_\infty^3(\Xi)} + \|u\|_{\mathcal{L}^\infty(0,T;\mathcal{H}^{k+1}(\Omega(t)))} + \|g\|_{\mathcal{L}^\infty(0,T;\mathcal{W}_\infty^1(\Omega(t)))}$, *where the semi-norm* $|||v_h|||_n^2 = \|v_h\|_{\Omega_h^n}^2 + \frac{\nu}{2}\|\nabla v_h\|_{\Omega_h^n}^2 + \gamma s_2^n(v_h, v_h)$.

Proof. Recall (3.44), i.e., $\mathbf{E}_C^n(v_h) = \sum_{i=1}^4 \mathbf{E}_{Ci}(v_h)$. We start with $\mathbf{E}_{C1}^n(v_h)$ by the triangle inequality

$$|\mathbf{E}_{C1}^n(v_h)| \leq \underbrace{\left| \int_{\Omega_h^n} \left(\partial_{\Delta t}^2(u^n, u^{n-1}, u^{n-2}) - \partial_t u^n \right) v_h d\mathbf{x} \right|}_{\mathbf{E}_{C1a}^n} + \underbrace{\left| \int_{\Omega_h^n} \partial_t u^n v_h d\mathbf{x} - \int_{\Omega^n} \partial_t u^n v_h^l d\mathbf{x} \right|}_{\mathbf{E}_{C1b}^n}.$$

The first term is similar to the one in [102, Lemma 5.11] but differs due to the high-order time difference stencil. By elementary calculations based on integration by parts on $[t_{n-2}, t_{n-1}]$ and $[t_{n-1}, t_n]$ one obtains

$$\mathbf{E}_{C1a}^n = \int_{\Omega_h^n} \int_{t_{n-2}}^{t_n} z(t)\ \partial_t^3 u\ dt\ v_h d\mathbf{x}$$

for $z \in \mathcal{C}^1([t_{n-2}, t_n])$ satisfying $z(t)|_{[t_{n-2}, t_{n-1}]} = -\frac{1}{4\Delta t}(t - t_{n-2})^2$ and $z(t)|_{(t_{n-1}, t_n]} = \frac{1}{12\Delta t}((3t - 3t_{n-1} - \Delta t)^2 - 4\Delta t^2)$, which leads to $\|z\|_{\mathcal{L}^\infty([t_{n-2}, t_n])} \leq \frac{1}{3}\Delta t$. Thus we have the bound with $\|\partial_t^3 u\|_{\mathcal{L}^\infty(\Omega_h^n \times [t_{n-2}, t_n])} \leq \|\partial_t^3 u\|_{\mathcal{L}^\infty(\Xi_\varepsilon)} \lesssim \|\partial_t^3 u\|_{\mathcal{L}^\infty(\Xi)}$

$$|\mathbf{E}_{C1a}^n| \lesssim \Delta t^2 \|\partial_t^3 u\|_{\mathcal{L}^\infty(\Xi)} \|v_h\|_{\Omega_h^n}.$$

The second term $\mathbf{E}_{C1b}^n$ involves the high-order geometric approximation error, namely the error from $\Omega_h^n := \Theta(\hat{\Omega}_h^n)$ approximating Ω^n. By denoting $\Phi := \Psi \circ \Theta^{-1} : \Omega_h^n \to \Omega^n$, i.e., a mapping from the high-order approximated domain to the exact domain, and applying an integral transformation, one has

$$|\mathbf{E}_{C1b}^n| = \left| \int_{\Omega_h^n} \left(\partial_t u^n - (\partial_t u^n \circ \Phi) \det(D\Phi) \right) v_h d\mathbf{x} \right|$$

Splitting the integrand (apart from v_h) into the sum of $\partial_t u^n - (\partial_t u^n \circ \Phi)$ and $(\partial_t u^n \circ \Phi)(1 - \det(D\Phi))$ yields

$$\begin{aligned} |\mathbf{E}_{C1b}^n| &\leq \left| \int_{\Omega_h^n} |\mathrm{id} - \Phi|\ \|\nabla \partial_t u^n\|_{\mathcal{L}^\infty(\Omega_\varepsilon^n)} v_h d\mathbf{x} \right| + \left| \int_{\Omega_h^n} |1 - \det(D\Phi)|\ \|\partial_t u^n\|_{\mathcal{L}^\infty(\Omega_\varepsilon^n)} v_h d\mathbf{x} \right| \\ &\lesssim h^{q+1} \|u\|_{\mathcal{W}_\infty^2(\Xi)} \|v_h\|_{\mathcal{L}^1(\Omega_h^n)} + h^q \|u\|_{\mathcal{W}_\infty^1(\Xi)} \|v_h\|_{\mathcal{L}^1(\Omega_h^n)} \lesssim h^q \|u\|_{\mathcal{W}_\infty^2(\Xi)} \|v_h\|_{\Omega_h^n}, \end{aligned}$$

where we made use of

$$|\partial_t u^n(\mathbf{x}) - (\partial_t u^n \circ \Phi)(\mathbf{x})| \leq \|\nabla \partial_t u^n\|_{\mathcal{L}^\infty(\Omega_\varepsilon^n)} |\mathbf{x} - \Phi(\mathbf{x})| \qquad \forall \mathbf{x} \in \Omega_h^n$$

and Lemma 2 to bound the parametric mapping error.

The bound for the second part follows similar lines in [102, Lemma 5.11] and yields

$$|\mathbf{E}_{C2}^n(v_h)| = |b_h^n(u^n, v_h) - b^n(u^n, v_h^l)| \lesssim h^q \|u\|_{\mathcal{W}_\infty^2(\Xi)} \|v_h\|_{\mathcal{H}^1(\Omega_h^n)}.$$

The third part is bounded by Cauchy-Schwarz inequality and the estimate from [102, Lemma 5.8], which is still valid on deformed meshes, as follows:

$$\begin{aligned} |\mathbf{E}_{C3}^n(v_h)| &= \gamma s_2^n(u^n, v_h) \leq \gamma s_2^n(u^n, u^n)^{\frac{1}{2}} s_2^n(v_h, v_h)^{\frac{1}{2}} \\ &\lesssim \gamma h^k \|u^n\|_{\mathcal{H}^{k+1}(\mathcal{D}_2^n)} s_2^n(v_h, v_h)^{\frac{1}{2}} \lesssim K^{\frac{1}{2}} h^k \|u^n\|_{\mathcal{H}^{k+1}(\Omega^n)} \left(\gamma s_2^n(v_h, v_h)\right)^{\frac{1}{2}}, \end{aligned}$$

where for the last inequality we make use of $\mathcal{D}_2^n \subset \Omega_\varepsilon^n$ and continuity of the extension.

Finally, the fourth part is estimated analogously to $|\mathbf{E}_{C1b}^n|$ as follows:

$$\begin{aligned} &|\mathbf{E}_{C4}^n(v_h)| = \left| \int_{\Omega_h^n} ((g^n \circ \Phi) \det(D\Phi) - g^n) v_h d\mathbf{x} \right| \\ &\leq \|v_h\|_{\mathcal{L}^1(\Omega_h^n)} \left(\|1 - \det(D\Phi)\|_{\mathcal{L}^\infty(\Omega_\varepsilon^n)} \|g^n\|_{\mathcal{L}^\infty(\Omega_\varepsilon^n)} + \|\mathrm{id} - \Phi\|_{\mathcal{L}^\infty(\Omega_\varepsilon^n)} \|\nabla g^n\|_{\mathcal{L}^\infty(\Omega_\varepsilon^n)} \right) \\ &\lesssim \left(h^q \|g^n\|_{\mathcal{L}^\infty(\Omega_h^n)} + h^{q+1} \|g^n\|_{\mathcal{W}_\infty^1(\Omega_h^n)} \right) \|v_h\|_{\Omega_h^n} \lesssim \sup_{t \in [0,T]} h^q \|g\|_{\mathcal{W}_\infty^1(\Omega(t))} \|v_h\|_{\Omega_h^n}. \end{aligned}$$

This completes the proof. □

3.2.4 Interpolation estimates

In this subsection, we estimate the interpolation error bounds.

Lemma 10. *Let $u \in \mathcal{L}^\infty(0,T;\mathcal{W}_\infty^{k+1}(\Omega(t)))$ with $\partial_t u \in \mathcal{L}^\infty(0,T;\mathcal{H}^k(\Omega(t)))$ be the exact solution to (3.1), the interpolation errors in (3.46) have the following bound for all $v_h \in \mathcal{V}_2^n$*

$$\sum_{n=2}^{N} |\mathbf{E}_{I1}^n(v_h)| \lesssim N^{\frac{1}{2}} h^k \mathcal{R}_{10}(u) \|v_h\|_N, \qquad |\mathbf{E}_{I2}^n(v_h)| \lesssim K^{\frac{1}{2}} h^k \|u\|_{\mathcal{H}^{k+1}(\Omega_h^n)} |||v_h|||_n,$$

with $\mathcal{R}_{10}(u) := \|\partial_t u\|_{\mathcal{L}^\infty(0,T;\mathcal{H}^k(\Omega(t)))} + \|u\|_{\mathcal{L}^\infty(0,T;\mathcal{W}_\infty^{k+1}(\Omega(t)))}$ and $\|v_h\|_N^2 := \sum_{n=2}^N \|v_h\|_{\Omega_h^n}^2$, where the semi-norm $|||v_h|||_n^2 = \|v_h\|_{\Omega_h^n}^2 + \frac{\nu}{2} \|\nabla v_h\|_{\Omega_h^n}^2 + \gamma s_2^n(v_h, v_h)$.

Proof. We start with the first term $\mathbf{E}_{I1}^n(v_h)$ in (3.46) and sum it over all time steps from $n=2$ to N. Let $T_\Omega^n := T^n \cap \Omega_h^n$ be the intersection of the element and the domain, then by Cauchy-Schwarz inequality one obtains

$$\begin{aligned}\sum_{n=2}^{N} |\mathbf{E}_{I1}^n(v_h)| &= \sum_{n=2}^{N} \Big| \int_{\Omega_h^n} \underbrace{\partial_{\Delta t}^2(\mathbf{e}_I^n, \tilde{\mathbf{e}}_I^{n-1}, \tilde{\mathbf{e}}_I^{n-2})}_{=:\mathbf{z}^n} v_h d\mathbf{x} \Big| \leq \sum_{T^n \in \mathcal{T}_h^n} \sum_{n=2}^{N} \int_{T^n \cap \Omega_h^n} |\mathbf{z}^n||v_h| d\mathbf{x} \\ &\leq \sum_{T^n \in \mathcal{T}_h^n} \sum_{n=2}^{N} \|\mathbf{z}^n\|_{T_\Omega^n} \|v_h\|_{T_\Omega^n} \leq \sum_{T^n \in \mathcal{T}_h^n} \Big(\sum_{n=2}^{N} \|\mathbf{z}^n\|_{T_\Omega^n}^2 \Big)^{\frac{1}{2}} \Big(\sum_{n=2}^{N} \|v_h\|_{T_\Omega^n}^2 \Big)^{\frac{1}{2}}.\end{aligned}$$

Another triangle inequality yields the splitting

$$\begin{aligned}\sum_{n=2}^{N} \|\mathbf{z}^n\|_{T_\Omega^n}^2 \leq \; & \overbrace{\sum_{n=2}^{N} \Big\| \frac{3\mathbf{e}_I^n - 4\tilde{\mathbf{e}}_I^{n-1} + \tilde{\mathbf{e}}_I^{n-2}}{2\Delta t} \Big\|_{T_\Omega^n}^2}^{=:\mathbf{z}_1^n} \lesssim \Delta t^{-2} \sum_{n=2}^{N} \Big\| 3\mathbf{e}_I^n - 4\mathbf{e}_I^{n-1} + \mathbf{e}_I^{n-2} \Big\|_{T_\Omega^n}^2 \\ & \underbrace{+ \Delta t^{-2} \sum_{n=2}^{N} \Big\| 4(\mathcal{I}_h^n - \Pi_{n-1}^n \mathcal{I}_h^{n-1}) u^{n-1} - (\mathcal{I}_h^n - \Pi_{n-2}^n \mathcal{I}_h^{n-2}) u^{n-2} \Big\|_{T_\Omega^n}^2}_{=:\mathbf{z}_2^n}.\end{aligned}$$

With $\mathbf{e}_I(t) := u(t) - \mathcal{I}_h u(t)$ and the standard interpolation properties, the first part $\mathbf{z}_1^n$ can be estimated as follows:

$$\mathbf{z}_1^n = \Delta t^{-2} \sum_{n=2}^{N} \Big\| 3 \int_{t_{n-1}}^{t_n} \partial_t \mathbf{e}_I(t) dt - \int_{t_{n-2}}^{t_{n-1}} \partial_t \mathbf{e}_I(t) dt \Big\|_{T_\Omega^n}^2 \lesssim N h^{2k} \|\partial_t u\|_{\mathcal{L}^\infty(0,T;\mathcal{H}^k(T_\Omega^n))}^2.$$

For the second part $\mathbf{z}_2^n$ we split the expression into the following two terms by the triangle inequality

$$\Delta t^2 \mathbf{z}_2^n \leq \underbrace{\sum_{n=2}^{N} \Big\| (\mathcal{I}_h^n - \Pi^n \mathcal{I}_h^{n-1})(4u^{n-1} - u^{n-2}) \Big\|_{T_\Omega^n}^2}_{=:\Delta t^2 \mathbf{z}_{2a}^n} + \underbrace{\sum_{n=2}^{N} \Big\| \Pi^n (\mathcal{I}_h^{n-1} - \Pi^{n-1} \mathcal{I}_h^{n-2}) u^{n-2} \Big\|_{T_\Omega^n}^2}_{=:\Delta t^2 \mathbf{z}_{2b}^n}$$

We treat $\mathbf{z}_{2a}^n$ by applying Lemma 8 with using $T_{\Omega_\varepsilon}^n$ for the extended version of T_Ω^n

$$\begin{aligned}
\mathbf{z}_{2a}^n &\lesssim \Delta t^{-2} \sum_{n=2}^{N} \left\| (\mathcal{I}_h^n - \Pi^n \mathcal{I}_h^{n-1})(4u^{n-1} - u^{n-2}) \right\|_{T_\Omega^n}^2 \\
&\lesssim \Delta t^{-2} \sum_{n=2}^{N} \|\Theta^n - \Theta^{n-1}\|_{\mathcal{L}^\infty(\omega(\hat{T}))}^2 \; h^{2k+d} \|4u^{n-1} - u^{n-2}\|_{\mathcal{W}_\infty^{k+1}(T_{\Omega_\varepsilon}^n)}^2 \\
&\lesssim (N + N_{\mathtt{C}} \Delta t^{-2} h^4) h^{2k+d} \sup_{m,n=0,..,N} \|u^m\|_{\mathcal{W}_\infty^{k+1}(T_{\Omega_\varepsilon}^n)}^2
\end{aligned}$$

where by Assumption 3 for most of the time steps there holds $\|\Theta^n - \Theta^m\|_{\mathcal{L}^\infty(\bar{\Omega})} \lesssim \Delta t$, while for a bounded number of time steps $N_{\mathtt{C}}$ there holds $\|\Theta^n - \Theta^m\|_{\mathcal{L}^\infty(\bar{\Omega})} \lesssim h^2$. For $\mathbf{z}_{2b}^n$ we additionally make use of (3.36a) which extends the relevant region by one element layer, yielding

$$\begin{aligned}
\mathbf{z}_{2b}^n &\lesssim \Delta t^{-2} \sum_{n=2}^{N} \left\| (\mathcal{I}_h^{n-1} - \Pi^{n-1} \mathcal{I}_h^{n-2}) u^{n-2} \right\|_{\omega(T_\Omega^{n-1})}^2 \\
&\lesssim \Delta t^{-2} \sum_{n=2}^{N} \|\Theta^n - \Theta^{n-1}\|_{\mathcal{L}^\infty(\omega^2(\hat{T}_\Omega))}^2 \; h^{2k+d} \|u^{n-2}\|_{\mathcal{W}_\infty^{k+1}(\omega(T_{\Omega_\varepsilon}^{n-1}))}^2 \\
&\lesssim (N + N_{\mathtt{C}} \Delta t^{-2} h^4) h^{2k+d} \sup_{m,n=0,..,N} \|u^m\|_{\mathcal{W}_\infty^{k+1}(\omega(T_{\Omega_\varepsilon}^n))}^2
\end{aligned}$$

where $\omega^2(\hat{T}_\Omega) := \omega \circ \omega(\hat{T}_\Omega)$ is the patch of the element patch $\omega(\hat{T}_\Omega)$ for $\hat{T}_\Omega := \Theta_T^{-n}(T_\Omega^n)$. As a consequence, with $N_{\mathtt{C}} \lesssim N\Delta t$ and $\frac{h^4}{\Delta t} \lesssim 1$, cf. Assumption 4, we arrive at $(N + N_{\mathtt{C}} \Delta t^{-2} h^4) \lesssim N$ and hence by continuity, after summing over the mesh, the bound

$$\sum_{T^n \in \mathcal{T}_h^n} \sum_{n=2}^{N} \|\mathbf{z}^n\|_{T_\Omega^n}^2 \lesssim N h^{2k} \Big(\|\partial_t u\|_{\mathcal{L}^\infty(0,T;\mathcal{H}^k(\Omega(t)))}^2 + \underbrace{\mathrm{card}(\mathcal{T}_h^n) h^d}_{\lesssim 1} \|u\|_{\mathcal{L}^\infty(0,T;\mathcal{W}_\infty^{k+1}(\Omega(t)))}^2 \Big).$$

This concludes the first result.

Next, we bound the second term $\mathbf{E}_{I2}^n(v_h)$ in (3.46) by Cauchy-Schwarz inequality, interpolation estimates, and using the results from [102, Lemma 5.8] as follows:

$$\begin{aligned}
|b_h^n(\mathbf{e}_I^n, v_h)| &\leq \|\mathbf{e}_I^n\|_{\mathcal{H}^1(\Omega^n)} \|v_h\|_{\mathcal{H}^1(\Omega_h^n)} \lesssim h^k \|u^n\|_{\mathcal{H}^{k+1}(\Omega^n)} \Big(\|v_h\|_{\Omega_h^n} + \frac{\nu}{2} \|\nabla v_h\|_{\Omega_h^n} \Big), \\
\gamma s_2^n(\mathbf{e}_I^n, v_h) &\leq \gamma s_2^n(\mathbf{e}_I^n, \mathbf{e}_I^n)^{\frac{1}{2}} s_2^n(v_h, v_h)^{\frac{1}{2}} \lesssim K^{\frac{1}{2}} h^k \|u^n\|_{\mathcal{H}^{k+1}(\Omega^n)} \Big(\gamma s_2^n(v_h, v_h) \Big)^{\frac{1}{2}}.
\end{aligned}$$

Finally, we obtain the following bound for $\mathbf{E}_{I2}^n(v_h)$

$$|\mathbf{E}_{I2}^n(v_h)| \lesssim (1 + K^{\frac{1}{2}}) h^k \|u^n\|_{\mathcal{H}^{k+1}(\Omega^n)} \Big(\|v_h\|_{\Omega_h^n} + \frac{\nu}{2} \|\nabla v_h\|_{\Omega_h^n} + \gamma s_2^n(v_h, v_h)^{\frac{1}{2}} \Big).$$

This completes the proof. □

3.2.5 Ghost penalty and tuple norm estimates

In this subsection, we first introduce a generalization of an important result in [102] regarding the bound of the extensions obtained through the application of the ghost penalty mechanism.

Lemma 11. *Let $v_h \in \mathcal{V}_r^n$, $r \in \{1,2,3\}$ be a discrete function on $\mathcal{D}_r^n$. For any $\theta \in \mathbb{R}_+$ the following inequalities hold true:*

$$\|v_h\|_{\mathcal{D}_r^n}^2 \lesssim \|v_h\|_{\Omega_h^n}^2 + Kh^2 s_r^n(v_h, v_h) \tag{3.47a}$$

$$\|\nabla v_h\|_{\mathcal{D}_r^n}^2 \lesssim \|\nabla v_h\|_{\Omega_h^n}^2 + K s_r^n(v_h, v_h) \tag{3.47b}$$

$$\|v_h\|_{\mathcal{D}_r^n}^2 \leq (1 + c_{11a}\Delta t)\|v_h\|_{\Omega_h^n}^2 + c_{11b}\nu\Delta t\|\nabla v_h\|_{\Omega_h^n}^2 + c_{11c}\Delta t K s_r^n(v_h, v_h) \tag{3.47c}$$

where the constants $c_{11a} = c_{11}r(1+\theta^{-1})$, $c_{11b}(\theta) = c_{11}r\theta\nu^{-1}$, $c_{11c} = c_{11}r(\theta + h^2 + h^2\theta^{-1})$ for a constant $c_{11} \in \mathbb{R}_+$ independent of h and Δt.

Proof. The results follows from [102, Lemma 5.2, Lemma 5.5 and Lemma 5.7] with minor modification for an extended strip size (from $\mathcal{O}_\delta^n$ in [102] to $\mathcal{D}_r^n$ here). □

Remark 12. *We note that the constant c_{11b} can be decreased for the price of the constant c_{11a} to be increased by choosing θ accordingly. We will make use of this adjustment later in order to drive c_{11b} to be sufficiently small. In the remainder of this subsection, we will however only reflect that dependency on θ for c_{11b}.*

Lemma 12. *Let $v_h \in \mathcal{V}_r^n$, $r \in \{1,2,3\}$ be a discrete function on $\mathcal{D}_r^n$. For the interior strip $\mathcal{S}_{h,-\varepsilon}^n$, $\varepsilon \in \mathbb{R}_+$ defined by (3.8) there holds for any $\sigma \in \mathbb{R}_+$*

$$\|v_h\|_{\mathcal{S}_{h,-\varepsilon}^n}^2 \leq c_{12}\Big((1+\sigma^{-1})\varepsilon\|v_h\|_{\Omega_h^n}^2 + \sigma\varepsilon\|\nabla v_h\|_{\Omega_h^n}^2\Big). \tag{3.48}$$

Proof. The claim follows from [59, Lemma 4.10] with an additional scaling argument. □

To deal with the BDF2 time stencil in the following stability analysis, we define a proper norm and make a simple but useful observation, cf. [60, Lemma 6.33].

Definition 11. *Let $u_h, v_h, w_h \in \mathcal{V}_2^n$. For any subset $U \subseteq \mathcal{D}_2^n$ we define the following BDF2 tuple norm*

$$|||(w_h, v_h)|||_U^2 := \|w_h\|_U^2 + \|2w_h - v_h\|_U^2. \tag{3.49}$$

Lemma 13. *For $\partial^2_{\Delta t}$ as defined in Subsection 3.1.6 with the BDF2 tuple norm there holds*

$$\Big(4\Delta t\partial^2_{\Delta t}(w_h,v_h,u_h),w_h\Big)_{\Omega_h^n} \geq |||(w_h,v_h)|||^2_{\Omega_h^n} - |||(v_h,u_h)|||^2_{\Omega_h^n}. \tag{3.50}$$

Proof. Multiplying the terms out we find

$$\begin{aligned}\Big(4\Delta t\partial^2_{\Delta t}(w_h,v_h,u_h),w_h\Big)_{\Omega_h^n} = \;& \|w_h\|^2_{\Omega_h^n} + \|2w_h - v_h\|^2_{\Omega_h^n} \\ & - \|v_h\|^2_{\Omega_h^n} - \|2v_h - u_h\|^2_{\Omega_h^n} + \underbrace{\|w_h - 2v_h + u_h\|^2_{\Omega_h^n}}_{\geq 0}.\end{aligned}$$

See also [60, Lemma 6.33]. □

Let us stress that the similar tuple norms with the corresponding estimates can also be defined for BDF3 and BDF4, cf. [112, Section 2]. In an analogous manner, the analysis below can thus be extended to $r = 3$ and $r = 4$ as well. We will however discuss the case of $r = 2$ only, in order to keep the technicalities at a manageable level.

Next, we bound the BDF2 tuple norm by a tuple of functions transferred from Ω_h^{n-1} and Ω_h^{n-2} to Ω_h^n.

Lemma 14. *For all $c_{14b} > 0$ and sufficiently small h and Δt there holds for all $w_h \in \mathcal{V}_1^{n-1}$ and $v_h \in \mathcal{V}_2^{n-2}$*

$$\begin{aligned}|||(\Pi^n w_h, \Pi^n\Pi^{n-1} v_h)|||^2_{\Omega_h^n} \leq\; & (1 + c_{14a}\Delta t)|||(w_h,\Pi^{n-1}v_h)|||^2_{\Omega_h^{n-1}} \\ & + c_{14b}\nu\Delta t\Big(\|\nabla w_h\|^2_{\Omega_h^{n-1}} + \|\nabla v_h\|^2_{\Omega_h^{n-2}}\Big) \\ & + c_{14c}K\Delta t\Big(s_1^{n-1}(w_h,w_h) + s_2^{n-2}(v_h,v_h)\Big)\end{aligned}$$

for constants $c_{14a}, c_{14c} > 0$ independent of h, Δt and n.

Proof. Let $\hat{\mathcal{D}}^{n,\mathcal{S}}_{\pm 1} := \Theta^{-n}(\mathcal{D}^{n,\mathcal{S}}_{\pm 1})$ be the unmapped strip domain of undeformed elements. Let $\tilde{\mathcal{D}}^n := \Theta^n(\hat{\mathcal{D}}^{n-1,\mathcal{S}}_{\pm 1} \cup \hat{\mathcal{D}}^{n,\mathcal{S}}_{\pm 1})$ be the union of the strip domains mapped through Θ^n, on which the mesh deformation acts such that $\Pi^n \neq \mathrm{id}$, namely provided $w_h \in \mathcal{V}_h^{n-1}$ and $\Pi^n w_h \in \mathcal{V}_h^n$ we have trivially $w_h - \Pi^n w_h = 0$ on $\bar{\Omega}\setminus\tilde{\mathcal{D}}^n$. Let $\tilde{\mathcal{D}}_1^{n-1} \subset \mathcal{D}_1^{n-1}$ be the extension of the intersection $\Theta^{n-1}(\Theta^{-n}(\tilde{\mathcal{D}}^n \cap \mathcal{D}_0^n))$ by all direct neighbors (but no extension with δ) mapped through Θ^{n-1}. By the fact that

$$\begin{aligned}\|\Pi^n w_h\|^2_{\Omega_h^n} &= \|w_h\|^2_{\Omega_h^n} + \|w_h - \Pi^n w_h\|^2_{\Omega_h^n} + 2(w_h, w_h - \Pi^n w_h)_{\Omega_h^n} \\ &\leq \|w_h\|^2_{\Omega_h^n} + \mu\|w_h\|^2_{\Omega_h^n\cap\tilde{\mathcal{D}}^n} + (1+\mu^{-1})\|w_h - \Pi^n w_h\|^2_{\Omega_h^n\cap\tilde{\mathcal{D}}^n}\end{aligned}$$

for any $\mu \in \mathbb{R}_+$ and similarly for $2w_h - \Pi^{n-1}v_h$ substituting w_h that

$$\begin{aligned}\|\Pi^n(2w_h - \Pi^{n-1}v_h)\|^2_{\Omega_h^n} \leq \|2w_h - \Pi^{n-1}v_h\|^2_{\Omega_h^n} + \mu\|2w_h - \Pi^{n-1}v_h\|^2_{\Omega_h^n \cap \tilde{\mathcal{D}}^n} \\ + (1+\mu^{-1})\Big\|(2w_h - \Pi^{n-1}v_h) - \Pi^n(2w_h - \Pi^{n-1}v_h)\Big\|^2_{\Omega_h^n \cap \tilde{\mathcal{D}}^n}\end{aligned}$$

we exploit the Definiton Definition 11 to unroll the BDF2 tuple norm as follows:

$$\begin{aligned}|||(\Pi^n w_h, \Pi^n\Pi^{n-1}v_h)|||^2_{\Omega_h^n} \leq |||(w_h, \Pi^{n-1}v_h)|||^2_{\Omega_h^n} + \mu|||(w_h, \Pi^{n-1}v_h)|||^2_{\Omega_h^n \cap \tilde{\mathcal{D}}^n} \\ + (1+\mu^{-1})c^2_{3.37b}h^4|||(\nabla w_h, \nabla\Pi^{n-1}v_h)|||^2_{\tilde{\mathcal{D}}_1^{n-1}}\end{aligned} \tag{3.51}$$

where the estimate (3.37b) from Lemma 6 was applied to the last term with $\Omega_h^n \cap \tilde{\mathcal{D}}^n \subset \tilde{\mathcal{D}}^n \cap \mathcal{D}_0^n$. Let us estimate the righ-hand side term by term.

The first term on the right-hand side of (3.51) can be bounded by applying (3.47c) in Lemma 11 with $\Omega_h^n \subset \mathcal{D}_1^{n-1}$

$$\begin{aligned}|||(w_h, \Pi^{n-1}v_h)|||^2_{\Omega_h^n} \leq (1 + c_{11a}\Delta t)|||(w_h, \Pi^{n-1}v_h)|||^2_{\Omega_h^{n-1}} \\ + 6c_{11b}\nu\Delta t\Big(\|\nabla w_h\|^2_{\Omega_h^{n-1}} + \|\nabla\Pi^{n-1}v_h\|^2_{\Omega_h^{n-1}}\Big) \\ + c_{11c}K\Delta t\Big(9s_1^{n-1}(w_h, w_h) + 2s_1^{n-1}(\Pi^{n-1}v_h, \Pi^{n-1}v_h)\Big)\end{aligned}$$

where we made use of $|||(u,v)|||^2_{\Omega_h^{n-1}} \leq 6\|u\|^2_{\Omega_h^{n-1}} + 6\|v\|^2_{\Omega_h^{n-1}}$ and $s_1^{n-1}(2u - v, 2u - v) \leq 8s_1^{n-1}(u,u) + 2s_1^{n-1}(v,v)$ for $u, v \in \mathcal{V}_1^{n-1}$. We then estimate $\|\nabla\Pi^{n-1}v_h\|^2_{\Omega_h^{n-1}}$ by (3.36b) in Lemma 5 with $\Omega_h^{n-1} \subset \mathcal{D}_1^{n-1}$ and (3.47b) in Lemma 11

$$\|\nabla\Pi^{n-1}v_h\|^2_{\Omega_h^{n-1}} \leq c_{5b}\|\nabla v_h\|^2_{\mathcal{D}_2^{n-2}} \leq c_{5b}c_{3.47b}\Big(\|\nabla v_h\|^2_{\Omega_h^{n-2}} + Ks_2^{n-2}(v_h, v_h)\Big)$$

and estimate $s_1^{n-1}(\Pi^{n-1}v_h, \Pi^{n-1}v_h)$ by Lemma 7 with $\mathcal{D}_{\pm 2}^{n-2,\mathcal{S}} \subset \mathcal{D}_2^{n-2}$

$$\begin{aligned}s_1^{n-1}(\Pi^{n-1}v_h, \Pi^{n-1}v_h) \leq c_{7a}s_2^{n-2}(v_h, v_h) + c_{7b}h^2\|\nabla v_h\|^2_{\mathcal{D}_2^{n-2}} \\ \leq (c_{7a} + c_{7b}c_{3.47b}h^2K)s_2^{n-2}(v_h, v_h) + c_{7b}c_{3.47b}h^2\|\nabla v_h\|^2_{\Omega_h^{n-2}}\end{aligned}$$

where (3.47b) in Lemma 11 was again applied. In summary, we have for the first term

$$\begin{aligned}|||(w_h,\Pi^{n-1}v_h)|||^2_{\Omega_h^n} &\le (1+c_{11a}\Delta t)|||(w_h,\Pi^{n-1}v_h)|||^2_{\Omega_h^{n-1}} \\ &+6c_{11b}\nu\Delta t\Big(\|\nabla w_h\|^2_{\Omega_h^{n-1}}+c_{3.47b}(c_{5b}+c_{3.52a})\|\nabla v_h\|^2_{\Omega_h^{n-2}}\Big) \\ &+c_{11c}K\Delta t\Big(9s_1^{n-1}(w_h,w_h)+2(c_{7a}+c_{7b}c_{3.47b}h^2K+c_{3.52b})s_2^{n-2}(v_h,v_h)\Big)\end{aligned} \tag{3.52}$$

where we set the parameters $c_{3.52a}:=c_{11c}c_{7b}Kh^2/(3c_{11b}\nu)$ and $c_{3.52b}:=3c_{11b}c_{5b}c_{3.47b}\nu/c_{11c}$.

The second term on the right-hand side of (3.51) is estimated by using Lemma 12 with choosing $\sigma=c_{12}/(1-c_{12})$ and $\varepsilon=2(\delta+h)=\mu^{-1}\Delta t$ such that $\Omega_h^n\cap\tilde{\mathcal{D}}^n\subset\mathcal{S}^n_{h,-\varepsilon}$

$$\begin{aligned}\mu|||(w_h,\Pi^{n-1}v_h)|||^2_{\Omega_h^n\cap\tilde{\mathcal{D}}^n} &\le \mu|||(w_h,\Pi^{n-1}v_h)|||^2_{\mathcal{S}^n_{h,-\varepsilon}} \\ &\le \Delta t|||(w_h,\Pi^{n-1}v_h)|||^2_{\Omega_h^n}+\sigma\Delta t|||(\nabla w_h,\nabla\Pi^{n-1}v_h)|||^2_{\mathcal{D}_1^{n-1}}\end{aligned} \tag{3.53}$$

where we set $\mu=\frac{\Delta t}{2(\delta+h)}$ the parameter of the Young's inequality in (3.51) and applied the inclusion $\Omega_h^n\subset\mathcal{D}_1^{n-1}$. The first tuple norm is identical to (3.52) and can be bounded in the same form. The second tuple norm is identical to the following estimate.

The third term on the right-hand side of (3.51) is bounded with $\tilde{\mathcal{D}}_1^{n-1}\subset\mathcal{D}_1^{n-1}$ by applying (3.36b) in Lemma 5 and Lemma 7

$$\begin{aligned}|||(\nabla w_h,\nabla\Pi^{n-1}v_h)|||^2_{\tilde{\mathcal{D}}_1^{n-1}} &\le 6\|\nabla w_h\|^2_{\mathcal{D}_1^{n-1}}+6c_{7b}\|\nabla v_h\|^2_{\mathcal{D}_2^{n-2}} \\ &\le 6c_{3.47b}\Big(\|\nabla w_h\|^2_{\Omega_h^{n-1}}+c_{7b}\|\nabla v_h\|^2_{\Omega_h^{n-2}}+Ks_1^{n-1}(w_h,w_h)+c_{7b}Ks_2^{n-2}(v_h,v_h)\Big).\end{aligned} \tag{3.54}$$

To conclude the proof, we add up (3.52), (3.53), (3.54) and summarize the conditions for the involved constants as follows:

$$\begin{aligned}c_{14a} &\ge \sum\{c_{11a},1\};\\ c_{14b} &\ge \sum\{6c_{11b},6c_{11b}c_{3.47b}(c_{5b}+c_{3.52a}),6c_{3.47b}((1+\mu^{-1})c^2_{3.37b}h^4/\Delta t+\sigma)/\nu,\\ &\qquad 6c_{3.47b}c_{7b}((1+\mu^{-1})c^2_{3.37b}h^4/\Delta t+\sigma)/\nu\};\\ c_{14c} &\ge \sum\{9c_{11c},2c_{11c}(c_{7a}+c_{7b}c_{3.47b}h^2K+c_{3.52b}),6c_{3.47b}((1+\mu^{-1})c^2_{3.37b}h^4/\Delta t+\sigma),\\ &\qquad 6c_{3.47b}c_{7b}((1+\mu^{-1})c^2_{3.37b}h^4/\Delta t+\sigma)\}.\end{aligned}$$

If h is sufficiently small, by Assumption 4 $(1+\mu^{-1})h^4/\Delta t\lesssim\nu$ and $Kh^2\lesssim\nu$, then for any choice of c_{14b} that only depends on c_{11b} we have correspondingly a θ in Lemma 11, which gives the choice of c_{11c} and hence c_{14c}. This completes the proof.

□

3.2.6 Stability analysis

In this subsection, we analyze the stability bound.

Theorem 6 (Stability of the numerical solution)**.** *The numerical solution* $\{u_h^n\}_{n=2,\dots,N}$ *to* (3.34) *with* $r=2$ *satisfies the following stability bound*

$$|||(u_h^N,\Pi^N u_h^{N-1})|||_{\Omega_h^N}^2+\Delta t\sum_{n=2}^{N}\Big(\nu\|\nabla u_h^n\|_{\Omega_h^n}^2+2\gamma s_2^n(u_h^n,u_h^n)\Big)\lesssim \exp(c_6 t_N)\mathcal{R}_6^0$$

$$\text{with } \mathcal{R}_6^0:=|||(u_h^1,\Pi^1 u_h^0)|||_{\Omega_h^1}^2+\Delta t\Big(\sum_{n=2}^{N}\|g^n\|_{\Omega_h^n}^2+\sum_{n=0}^{1}\Big(\nu\|\nabla u_h^n\|_{\Omega_h^n}^2+Ks_2^n(u_h^n,u_h^n)\Big)\Big)$$

where $c_6:=c_{14a}+\frac{1}{2}+4\xi$ *for* ξ *as in* (3.18) *indepedent of* h, Δt *or* T.

Proof. We test (3.34) with $v_h=4\Delta t u_h^n$ and apply Lemma 13 which yields

$$\begin{aligned}|||(u_h^n,\Pi^n u_h^{n-1})|||_{\Omega_h^n}^2+4\Delta t b_h^n(u_h^n,u_h^n)+4\Delta t\gamma s_2^n(u_h^n,u_h^n)\\ \le |||(\Pi^n u_h^{n-1},\Pi^n\Pi^{n-1}u_h^{n-2})|||_{\Omega_h^n}^2+4\Delta t f_h^n(u_h^n).\end{aligned}$$

Recall the lower bound of $b_h^n(\cdot,\cdot)$ from (3.19). We apply Lemma 14 on the right-hand side followed by Young's inequality with $\beta>0$ and Cauchy-Schwarz applied to f_h^n

$$\begin{aligned}&(1-4\xi\Delta t)|||(u_h^n,\Pi^n u_h^{n-1})|||_{\Omega_h^n}^2+2\Delta t\nu\|\nabla u_h^n\|_{\Omega_h^n}^2+4\Delta t\gamma s_2^n(u_h^n,u_h^n)\\ &\le(1+c_{14a}\Delta t)|||(u_h^{n-1},\Pi^{n-1}u_h^{n-2})|||_{\Omega_h^{n-1}}^2+c_{14b}\nu\Delta t\Big(\|\nabla u_h^{n-1}\|_{\Omega_h^{n-1}}^2+\|\nabla u_h^{n-2}\|_{\Omega_h^{n-2}}^2\Big)\\ &\quad+c_{14c}K\Delta t\Big(s_1^{n-1}(u_h^{n-1},u_h^{n-1})+s_2^{n-2}(u_h^{n-2},u_h^{n-2})\Big)+2\Delta t\Big(\beta^{-1}\|g^n\|_{\Omega_h^n}^2+\beta\|u_h^n\|_{\Omega_h^n}^2\Big).\end{aligned}$$

Summing over $n=2,\dots,N\le N$, choosing $c_{14b}\le\frac{1}{2}$, and assuming $\gamma\ge c_{14c}K$ yields

$$\begin{aligned}&(1-4\xi\Delta t-2\beta\Delta t)|||(u_h^N,\Pi^N u_h^{N-1})|||_{\Omega_h^N}^2+\Delta t\sum_{n=2}^{N}\nu\|\nabla u_h^n\|_{\Omega_h^n}^2+2\Delta t\sum_{n=2}^{N}\gamma s_2^n(u_h^n,u_h^n)\\ &\le|||(u_h^1,\Pi^1 u_h^0)|||_{\Omega_h^1}^2+\Delta t\sum_{n=0}^{1}\Big(\nu\|\nabla u_h^n\|_{\Omega_h^n}^2+c_{14c}Ks_2^n(u_h^n,u_h^n)\Big)\\ &\quad+(c_{14a}+4\xi+2\beta)\Delta t\sum_{n=2}^{N}|||(u_h^{n-1},\Pi^{n-1}u_h^{n-2})|||_{\Omega_h^{n-1}}^2+2\Delta t\beta^{-1}\sum_{n=2}^{N}\|g^n\|_{\Omega_h^n}^2.\end{aligned}\tag{3.55}$$

Finally, by choosing $\beta=\frac{1}{4}$ and applying the discrete Grönwall's lemma with $\Delta t\xi\le\frac{1}{16}$, we obtain the result. □

Let us note that some parts of the stability analysis of the BDF2 scheme have been considerably simplified in [89, Section 5.2.1].

3.2.7 A priori error estimate

In this subsection, we are ready to conclude the following a priori error analysis based on all the results above.

Theorem 7 (Error estimate for the advection-diffusion equation on evolving domain)**.** *Let $u \in \mathcal{W}_\infty^3(\Xi) \cap \mathcal{L}^\infty(0,T;\mathcal{W}_\infty^{k+1}(\Omega(t)))$ with $\partial_t u \in \mathcal{L}^\infty(0,T;\mathcal{H}^k(\Omega(t)))$ be the exact solution to the PDE problem (2.35) or (3.1) with the source term $g \in \mathcal{L}^\infty(0,T;\mathcal{W}_\infty^1(\Omega(t)))$. For $N = T/\Delta t$ the numerical solution $\{u_h^n\}_{n=2,\dots,N}$ to (3.34) with $r = 2$ fulfills the following error estimate for $\mathbf{e}^n := |u(t_n) - u_h^n|$*

$$\|\mathbf{e}^N\|_{\Omega_h^N}^2 + \Delta t \sum_{n=2}^{N} \left(\frac{\nu}{2} \|\nabla \mathbf{e}^n\|_{\Omega_h^n}^2 + \gamma s_2^n(\mathbf{e}^n, \mathbf{e}^n) \right) \lesssim \exp(cT) \Big((\Delta t^4 + K h^{2k} + h^{2q}) \, \mathcal{R}_9^2(u,g) + h^{2k} \mathcal{R}_{10}^2(u) \Big)$$

with $c := c_{14a} + 4\xi + 4$ independent of the mesh size h, the time step Δt, or the terminal time T.

Proof. By the error splitting in (3.40) we have with the standard interpolation estimate

$$\|\mathbf{e}^N\|_{\Omega_h^N}^2 \lesssim \|\mathbf{e}_I^N\|_{\Omega_h^N}^2 + \|\mathbf{e}_h^N\|_{\Omega_h^N}^2 \lesssim h^{2k} \|u^N\|_{\mathcal{H}^{k+1}(\Omega^N)}^2 + \|\mathbf{e}_h^N\|_{\Omega_h^N}^2$$

and by the result from [102, Lemma 5.8] for the ghost penalty of interpolation error

$$\Delta t \sum_{n=2}^{N} \left(\frac{\nu}{2} \|\nabla \mathbf{e}_I^n\|_{\Omega_h^n}^2 + \gamma s_2^n(\mathbf{e}_I^n, \mathbf{e}_I^n) \right) \lesssim T \sup_{n=2,\dots,N} K h^{2k} \|u^n\|_{\mathcal{H}^{k+1}(\Omega^n)}^2 \lesssim \exp(cT) K h^{2k} \mathcal{R}_9^2,$$

where the continuity property is employed, cf. [102, Lemma 3.4]. Hence only the discrete error terms need to be bounded yet. Based on the observation that (3.45) for $\mathbf{e}_h^n$ is identical to (3.34) if u_h^n is replaced by $\mathbf{e}_h^n$ and $f_h^n(v_h)$ by $\mathbf{E}_C^n(v_h) + \mathbf{E}_I^n(v_h)$, we proceed with the proof as in Theorem 6 but the additional source term.

Recalling Lemma 9 and Lemma 10, we test the consistency and interpolation error terms with $\mathbf{e}_h^n$ and sum up

$$\begin{aligned}\sum_{n=2}^{N}\left(\mathbf{E}_C^n(\mathbf{e}_h^n)+\mathbf{E}_I^n(\mathbf{e}_h^n)\right) &\lesssim (\Delta t^2+K^{\frac{1}{2}}h^k+h^q)\mathcal{R}_9\sum_{n=2}^{N}|||\mathbf{e}_h^n||| + N^{\frac{1}{2}}h^k\mathcal{R}_{10}\|\mathbf{e}_h^n\|_N \\ &\lesssim N(\Delta t^4+Kh^{2k}+h^{2q})\mathcal{R}_9^2+Nh^{2k}\mathcal{R}_{10}^2 \\ &\quad+\sum_{n=2}^{N}\left(|||(\mathbf{e}_h^n,\Pi^n\mathbf{e}_h^{n-1})|||_{\Omega_h^n}^2+\frac{\nu}{2}\|\nabla\mathbf{e}_h^n\|_{\Omega_h^n}^2+\gamma s_2^n(\mathbf{e}_h^n,\mathbf{e}_h^n)\right)\end{aligned}$$

Analogously to (3.55) we then arrive at

$$\begin{aligned}&(1-4\xi\Delta t-4\Delta t)|||(\mathbf{e}_h^N,\Pi^N\mathbf{e}_h^{N-1})|||_{\Omega_h^N}^2+\Delta t\sum_{n=2}^{N}\frac{\nu}{2}\|\nabla\mathbf{e}_h^n\|_{\Omega_h^n}^2+\Delta t\sum_{n=2}^{N}\gamma s_2^n(\mathbf{e}_h^n,\mathbf{e}_h^n)\\ &\quad\lesssim |||(\mathbf{e}_h^1,\Pi^1\mathbf{e}_h^0)|||_{\Omega_h^1}^2+\Delta t\sum_{n=0}^{1}\left(\nu\|\nabla\mathbf{e}_h^n\|_{\Omega_h^n}^2+\gamma s_2^n(\mathbf{e}_h^n,\mathbf{e}_h^n)\right)+Th^{2k}\mathcal{R}_{10}^2\\ &\qquad+T(\Delta t^4+Kh^{2k}+h^{2q})\mathcal{R}_9^2+(c_{14a}+4\xi+4)\,\Delta t\sum_{n=2}^{N}|||(\mathbf{e}_h^{n-1},\Pi^{n-1}\mathbf{e}_h^{n-2})|||_{\Omega_h^{n-1}}^2\end{aligned}$$

where we applied the discrete Grönwall's inequality with $(1+\xi)\Delta t\leq\frac{1}{8}$ and made use of $\|\mathbf{e}_h^n\|_{\Omega_h^n}\leq|||(\mathbf{e}_h^n,\Pi^n\mathbf{e}_h^{n-1})|||_{\Omega_h^n}$. This completes the proof by setting $c:=c_{14a}+4\xi+4$. □

Remark 13 (Impact of the anisotropy factor K)**.** *The error bound above involves the factor $Kh^{2k}\lesssim h^{2k}+\Delta t\ h^{2k-1}$. Hence, at first glance it seems that an anisotropy between space and time refinements, i.e., when $\frac{\Delta t}{h}\to\infty$ for $h,\Delta t\to 0$, may have a negative impact on the convergence rate. For $k>1$ one can estimate $\Delta t\ h^{2k-1}\leq\Delta t^2h^k+h^{3k-2}\lesssim\Delta t^4+h^{2k}$ and thereby conclude that the factor K has no influence on the convergence rate. For $k=1$, however, one indeed has that $\Delta t\ h$ converges slower than Δt^4+h^2 for $\frac{\Delta t}{h}\to\infty$ for $h,\Delta t\to 0$.*

3.3 Numerical Experiments

In this section, we present three numerical examples for the higher-order Eulerian FEM proposed in Section 3.1. The convergence study of the numerical results is in agreement with the order of accuracy predicted by Theorem 7 in Section 3.2. The numerical results also verify the stability with respect to the variation of discretization parameters, and demonstrate the robustness of the method to handle evolving geometry

even in complicated configurations such as topological changes. The following three geometrical configurations are considered:

- A domain of disk shape transforming towards a kite;
- A circular moving interface separating two phases with interface jump condition;
- Two disconnected domains merging, separating, and transforming their shapes.

All the numerical experiments in this thesis are implemented with the finite element package `NGSolve` [141] and its Add-on `ngsxfem` [101]. All the numerical examples in this chapter are contributed from [114, Section 7]. For reproducibility we provide the generating codes and instructions on the repository https://gitlab.gwdg.de/lehrenfeld/repro-isop-unf-bdf-fem. See also Section 1.5.

In contrast to the analysis, we make two minor changes in the discretization. Firstly, instead of the skew-symmetrized form (3.17), the following bilinear form is applied:

$$b_h^n(u_h, v_h) = \int_{\Omega_h^n} \nu \nabla u_h \cdot \nabla v_h d\mathbf{x} + \int_{\Omega_h^n} (\mathbf{w}^e \cdot \nabla u_h) v_h d\mathbf{x} + \int_{\Omega_h^n} (\nabla \cdot \mathbf{w}^e) u_h v_h d\mathbf{x}. \tag{3.56}$$

Secondly, we do not include the additional neighboring elements in the extension, namely, we still have $r\delta$ distance extension but skip the r element layers in $(\cdot)_{h,r\delta,r}$, cf. Subsection 3.1.1. However, in all the subsequent numerical tests we have ensured that the desired inclusion properties hold.

In some examples we construct a source term in order to obtain the corresponding manufactured solutions, by which we meassure the numerical error $\mathbf{e} := |u - u_h|$ in terms of the following discrete space-time norms:

$$\|\mathbf{e}\|^2_{\mathcal{L}^2(\mathcal{H}^1)} := \sum_{n=1}^{N} \Delta t \|\nabla \mathbf{e}\|^2_{\mathcal{L}^2(\Omega_h^n)}, \qquad \|\mathbf{e}\|_{\mathcal{L}^\infty(\mathcal{L}^2)} := \max_{n=1,\dots,N} \|\mathbf{e}\|_{\mathcal{L}^2(\Omega_h^n)}, \tag{3.57}$$

where we recall that u is identified with its extension $u^e := \mathcal{E}u$ to the proper neighborhood. For the first two examples we start with an initial (quasi-uniform) spatial and (uniform) temporal mesh with initial mesh sizes h_0 and Δt_0, respectively, and then apply successive regular refinements in space and time. We denote the corresponding refinement levels in space by L_x, and in time by L_t, such that $h = 2^{-L_x} h_0$ and $\Delta t = 2^{-L_t} \Delta t_0$.

3.3.1 Kite transformation

In the first numerical example, we consider a domain of disk shape transforming towards a kite shape. See Figure 3.9 for an illustration of this example.

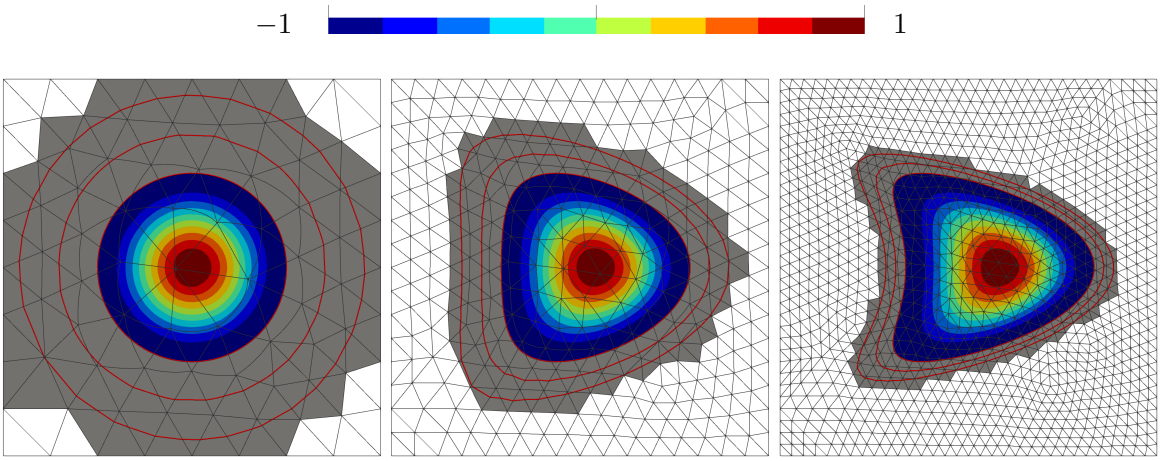

(a) $t = 0$ (b) $t = T/2$ (c) $t = T$

Fig. 3.9 Numerical example from Subsection 3.3.1 with $k = q = 3$ and $r = 2$ (BDF2): Mesh, active mesh (in grey), neighborhood extension (red line) and discrete solutions on $\Omega(t)$ for (a) $L_x = 0$, $L_t = 3$, $t = 0$; for (b) $L_x = 1$, $L_t = 4$, $t = T/2$; and for (c) $L_x = 2$, $L_t = 5$, $t = T$.

The background domain is fixed to $\bar{\Omega} = (-1,1)^2$ and the time interval $[0,T]$ is set for a terminal time $T = 1$. The evolution of the geometry is represented by the following level set function

$$\phi(\mathbf{x},t) = \|\mathbf{x} - \mathbf{c}(\mathbf{x},t)\|_2 - \frac{1}{2} \qquad \text{for } \mathbf{c}(\mathbf{x},t) = \mathbf{w}(\mathbf{x})\,t \text{ and } \mathbf{w}(\mathbf{x}) = \left(\frac{1}{6} - \frac{5}{3}x_2^2, 0\right)$$

where $\mathbf{x} := (x_1, x_2)$ denotes the standard Cartesian coordinate system. Note that ϕ may not be a signed distance function for $t \in (0,T]$, i.e., it may not preserve the signed distance properties. The source term function g is designed such that $u(\mathbf{x},t) = \cos\frac{\pi}{R}\|\mathbf{x} - \mathbf{c}\|_2$, which satisfies $-\nabla u \cdot \mathbf{n} = 0$, on $\Gamma(t)$, $t \in [0,T]$, solves (3.1) exactly. The initial spatial and temporal resolutions are $h_0 = 0.25$ and $\Delta t_0 = T$.

In Figure 3.10 the convergence of the errors in $\mathcal{L}^\infty(\mathcal{L}^2)$ and $\mathcal{L}^2(\mathcal{H}^1)$ norms are displayed for $r = k = q = 2$. We observe that the convergence rates in time are $\mathcal{O}(\Delta t^2)$ in both norms, whereas the convergence rates in space are $\mathcal{O}(h^2)$ in $\mathcal{L}^2(\mathcal{H}^1)$ norm and $\mathcal{O}(h^3)$ in $\mathcal{L}^\infty(\mathcal{L}^2)$ norm. These numerical results are in agreement with the prediction of Theorem 7, except for the $\mathcal{O}(h^3)$-convergence in $\mathcal{L}^\infty(\mathcal{L}^2)$ norm which is even one order better than the prediction.

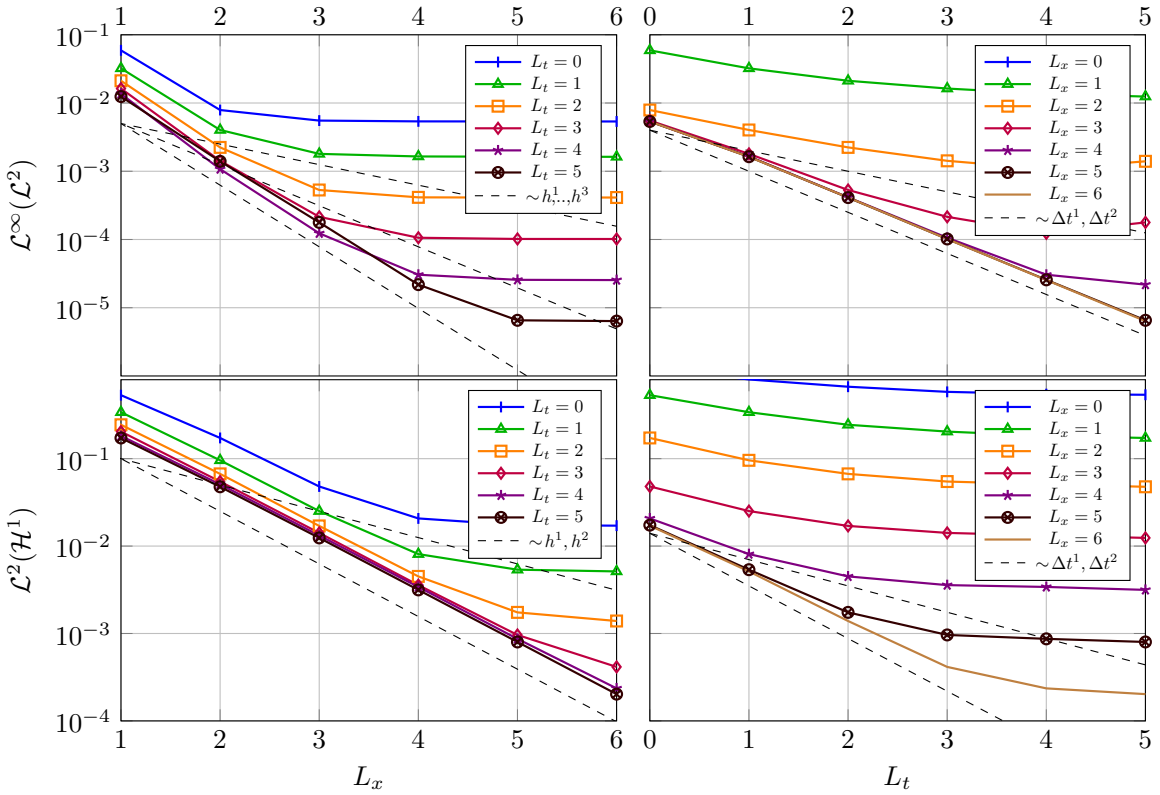

Fig. 3.10 $\mathcal{L}^\infty(\mathcal{L}^2)$- and $\mathcal{L}^2(\mathcal{H}^1)$-errors of the isoparametric unfitted BDF2-FEM discretization for $k = q = 2$ and $c_\gamma = 0.1$ for several levels of space and time refinements in the example from Subsection 3.3.1.

3.3.2 Two-phase mass transport

In the second example, we consider a two-phase moving interface problem as depicted in Subsection 2.3.2, cf. [98], of which the complexity and the third order of accuracy in space and time are beyond the scope of the previous analysis. A circular interface that separates two materials is moving within the background domain $\bar{\Omega} = (0,2)^2$ and the time interval $[0,T]$ for a final time $T = \frac{1}{2}$. The interface is described by the following level set function

$$\phi(\mathbf{x},t) = \|\mathbf{x} - \mathbf{c}(t)\|_2 - \frac{1}{3} \qquad \text{for } \mathbf{c}(t) = \left(\frac{1}{2} + \frac{1}{4\pi}\sin(2\pi t), 1\right),$$

of which the zero level set represents a circle moving with time-dependent velocity in the horizontal direction. We then define the two subdomains

$$\Omega_1(t) = \{\mathbf{x} \in \bar{\Omega} \mid \phi(\mathbf{x},t) < 0\}, \qquad \Omega_2(t) = \{\mathbf{x} \in \bar{\Omega} \mid \phi(\mathbf{x},t) > 0\},$$

on which the advection-diffusion equation $\partial_t u + \nabla \cdot (u\mathbf{w} - \nu_i \nabla u) = g$ is posed for $i = 1,2$ where $\mathbf{w}(t) = \partial_t \mathbf{c}(t)$ is given, as described in (2.38). We prescribe the Dirichlet data on $\partial\bar{\Omega}$ as in (2.40), and impose the jump interface conditions $[\![-\nu \nabla u \cdot n]\!] = 0, [\![\beta u]\!] = 0$ on $\Gamma(t) = \overline{\Omega}_1(t) \cap \overline{\Omega}_2(t)$ as in (2.39), for the diffusion coefficients ν_i, $i = 1,2$ and the Henry weights γ_i, $i = 1,2$ in the Henry interface condition, cf. [98, Section 1.2]. More specifically, we choose $(\nu_1, \nu_2) = (10, 20)$ and $(\beta_1, \beta_2) = (2, 1)$ in this example. The corresponding boundary data and source term function g are prescribed such that $u(\mathbf{x}, t) = \sin(\pi t) u_i(\|\mathbf{x} - \mathbf{c}(t)\|)$ with $u_1(z) = a + bz^2$ and $u_2(z) = \cos(\pi z)$, $a \approx 1.1569$, $b \approx -8.1621$, is the unique manufactured solution.

For the discretization we make use of a geometrically unfitted setting similar to (3.34), but for both subdomains a Nitsche formulation is applied for the coupling through the interface conditions. The discretization takes the following form:
To find $\mathbf{u}_h^n = (u_1^n, u_2^n) \in \mathcal{V}_r^n \times \mathcal{V}_r^n$, $n = r, ..., N$ for given $\mathbf{u}_h^0, ..., \mathbf{u}_h^{r-1}$, such that for all $\mathbf{v}_h = (v_1, v_2) \in \mathcal{V}_r^n \times \mathcal{V}_r^n$ there holds

$$\begin{aligned}
\sum_{i=1,2} \beta_i \Big(\int_{\Omega_{h,i}^n} \partial_{\Delta t}^r (u_i^n, ..., \Pi_{n-r}^n u_i^{n-r}) v_i \, d\mathbf{x} + b_{h,i}^n(\mathbf{u}_h^n, \mathbf{v}_h) + \gamma s_{r,i}^n(\mathbf{u}_h^n, \mathbf{v}_h) \Big) \\
+ \int_{\Gamma_h^n} -\{\!\{\nu \nabla \mathbf{u}_h \cdot \mathbf{n}\}\!\} [\![\beta \mathbf{v}_h]\!] - \{\!\{\nu \nabla \mathbf{v}_h \cdot \mathbf{n}\}\!\} [\![\beta \mathbf{u}_h]\!] + \frac{\{\!\{\nu\}\!\} \lambda_N}{h} [\![\beta \mathbf{u}_h]\!] [\![\beta \mathbf{v}_h]\!] \, ds \\
= \sum_{i=1,2} \beta_i \int_{\Omega_{h,i}^n} g_i v_i \, d\mathbf{x},
\end{aligned}$$

where $\Omega_{h,i}^n$, $i = 1,2$ and Γ_h^n are the discrete subdomains and the interface approximations to $\Omega_i(t_n)$ and $\Gamma(t_n)$, respectively. The discrete bilinear forms $b_{h,i}^n(\cdot,\cdot)$ and $s_{r,i}^n(\cdot,\cdot)$ are analogously to Section 3.1 but acting on $\Omega_{h,i}^n$ or on a corresponding set of facets $\mathcal{F}_{r,i}^n$, respectively. In the Nitsche terms we choose $\lambda_N = 40$. On the right-hand side g_i is a proper extension of $g|_{\Omega_i(t)}$ to $\Omega_{h,i}^n$. The spatial and temporal resolution are $h_0 = 0.5$ and $\Delta t_0 = T$ initially.

In Figure 3.11 the convergence of the errors in $\mathcal{L}^\infty(\mathcal{L}^2)$ and $\mathcal{L}^2(\mathcal{H}^1)$ norms, which are composed as the summation of the corresponding norms on the subdomains $\Omega_{h,i}^n, i = 1,2$, are displayed for $r = k = q = 3$ and we observe that the convergence rates in time are $\mathcal{O}(\Delta t^3)$ in both norms, whereas the convergence rates in space are $\mathcal{O}(h^3)$, and even higher in $\mathcal{L}^\infty(\mathcal{L}^2)$ norm. These numerical results are again in agreement with the expectations from the case of single domain predicted by Theorem 7.

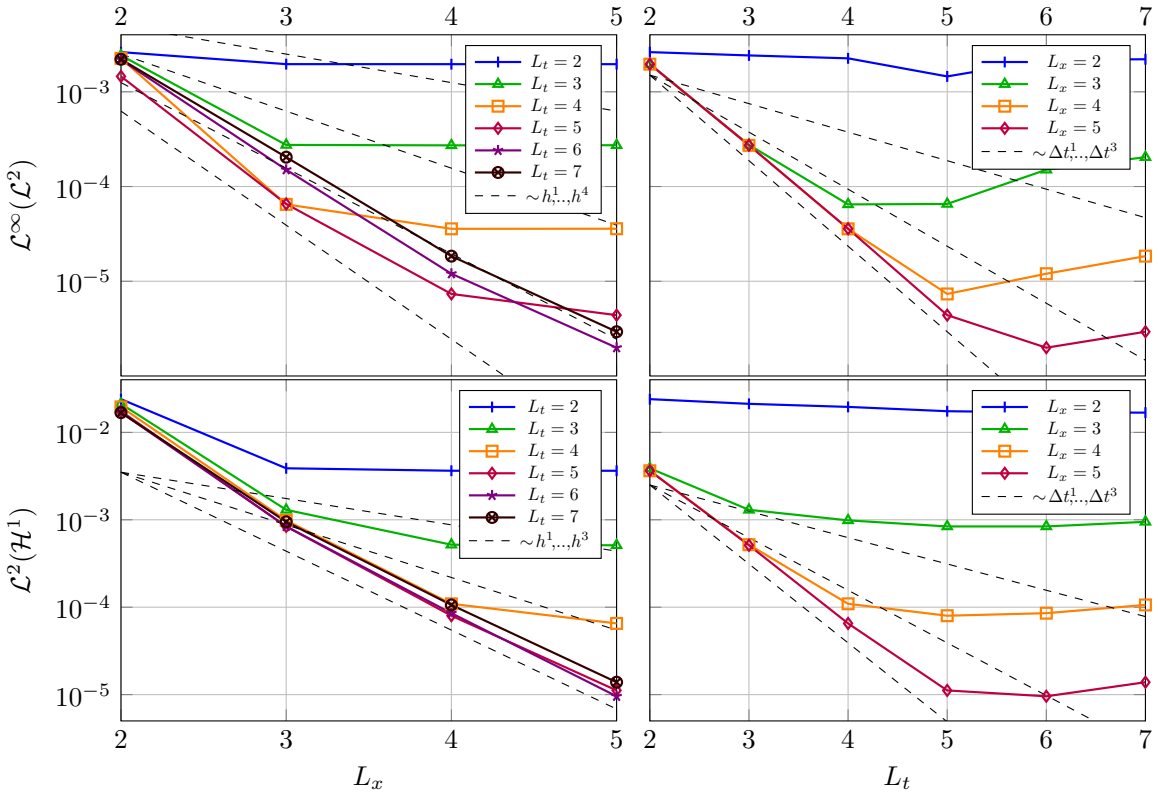

Fig. 3.11 $\mathcal{L}^\infty(\mathcal{L}^2)$- and $\mathcal{L}^2(\mathcal{H}^1)$-errors of the isoparametric unfitted BDF3-FEM discretization for $k = q = 3$ and $c_\gamma = 10$ for several levels of mesh and time refinements in the example from Subsection 3.3.2.

3.3.3 Topological changes

In the third example, we consider a geometrically singular configuration with topological changes, in order to test the robustness of the method. Two disjoint domains merge together and separate afterwards while their topology changes, and continuously transform their shapes between kites and disks while they are moving. The evolution of the geometry is represented by the following level set function

$$\phi(\mathbf{x},t) = \min\Big(\|\mathbf{x}-\mathbf{c}_-\|_2, \|\mathbf{x}-\mathbf{c}_+\|_2\Big) - \frac{1}{2}, \quad \text{for } \mathbf{c}_\pm(t) = \Big(\pm(1+\operatorname{sgn}(1-t)2x_2^2)(1-t), 0\Big).$$

The background domain is fixed to $\bar{\Omega} = (-2,2)\times(-1,1)$ and the time interval $[0,T]$ is set for a terminal time $T = 2$. The corresponding velocity field is discontinuous at $x_1 = 0$ and $t = 1$ such that

$$\mathbf{w}(\mathbf{x},t) = -\operatorname{sgn}(x_1)\operatorname{sgn}(1-t)\ (1,0).$$

The advection-diffusion equation (3.1) is posed on each disjoint domain or the merged domain, with initial data $u_0 = -1$ on the left side and $u_0 = 1$ on the right side, respectively.

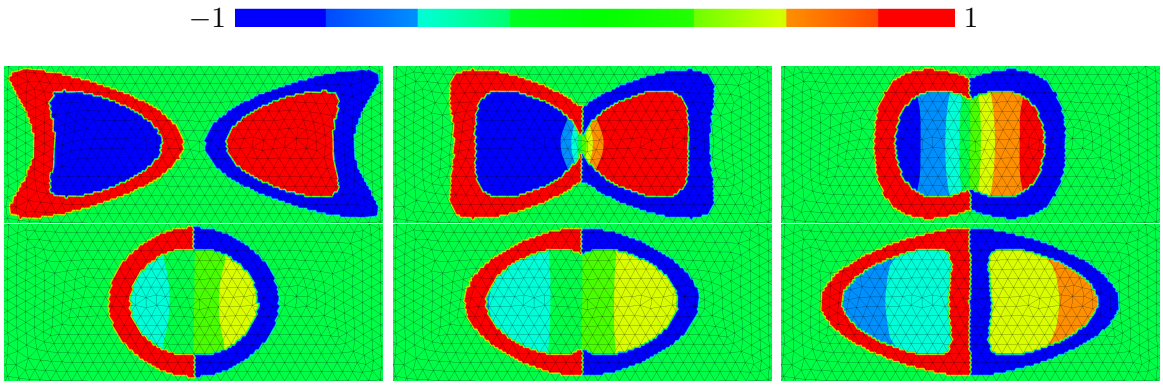

Fig. 3.12 Numerical example from Subsection 3.3.3 with $k = q = 2$ and $r = 2$ (BDF2): Mesh, evolving domain, boundary (in yellow), 2δ-extension (in red or blue), and discrete solutions on $\Omega(t)$. A series of snapshots with a time interval $\frac{3}{20}T$ in-between.

As the method is not able to maintain high order of accuracy under topological changes that cause non-smooth boundaries, we do not study the error convergence for this special example. As a bottom line, however, this topology changing experiment demonstrates the robustness of the method. Visit https://gitlab.gwdg.de/lehrenfeld/repro-isop-unf-bdf-fem/-/blob/master/solver/demo.ipynb for a tutorial of this example, and see Figure 3.12 for a series of the resulting snapshots.

3.4 Summary

In this chapter, we have developed the Eulerian FEM from [102] for solving PDEs on evolving domains towards *provably* higher order of accuracy in space and time. The contributions of this work in contrast to [102] include the high-order isoparametric method in space and the corresponding analysis on the one hand, and the analysis of the time stepping method from an implicit Euler to a higher-order BDF scheme on the other hand. The a priori error estimate of this isoparametric unfitted BDF-FEM yields arbitrarily high order of accuracy in space and up to second-order convergence in time. The construction, the analysis, and the implementation of the mesh transfer operator for mesh deformations changing in time with respect to the isoparametric unfitted discretization play a major part of this chapter, which are valuable not only for the numerical methods considered in this thesis. The numerical experiments have verified the convergence rates predicted by the analysis, the robustness of handling topological

changes of complex geometry, and the capability towards further applications beyond the scope of this thesis.

The isoparametric unfitted BDF-FEM shows several advantages over its competitors. In comparison to the isoparametric unfitted space-time FEM in [130], the proposed method based on the standard isoparametric unfitted discretization involves only spatial integrals and finite element spaces, which results in an implementational and computational complexity comparable to stationary unfitted problems. While compared to the characteristic Galerkin fictitious-domain method in [33], it trades the extra cost and complexity of the Lagrangian tracking of the geometry (to high-order accuracy) with a comparably simple ghost-penalty-based discrete extension. Moreover, as mentioned in [102], this approach waives the reconstruction of a physical domain on each time slab, but only approximates the domain at time instances. The avoidance of reconstruction by a Lagrangian or an arbitrary mapping from a reference domain makes the method especially promising for the applications in which the evolution of the geometry is described by a sequence of snapshots without further details about the continuous motion. One important application is the numerical simulation of cardiac hemodynamics where the blood flow through a heart is recovered based on a series of medical images, cf. [116, 153].

Chapter 4

Discrete Mean Curvature on Hypersurfaces

In Chapter 3 we have developed the higher-order Eulerian FEM for solving PDEs on a time-varying geometry of which the evolution is given in advance and decoupled with the involved PDEs, while for the geometrically coupled solution-curvature-driven moving *free boundary problem* (FBP) proposed in Section 2.4 the evolution of the geometry depends on the mean curvature of the geometry itself and the solution to the diffusion equation. In order to solve such a coupled bulk-surface problem, i.e., PDEs on the bulk coupled with a geometric flow of the surface, our strategy is to decouple it into three sub-models, cf. Section 1.2. In this chapter, we will take the mean curvature sub-model forward, to compute the mean curvature vector of the surface at each time step as a stationary problem, for which we develop a stabilized isoparametric *Trace Finite Element Method* (TraceFEM) to solve the geometric equation of mean curvature vector of manifolds numerically at arbitrarily high order of accuracy. The method is stabilized by using volumetric normal diffusion from [74] and ghost penalty mechanism from [82] as a whole. As discussed in Section 1.3 the discrete hypersurface may be represented either explicitly by fitted mesh or implicitly by unfitted approaches, we will however only consider the unfitted hypersurface cut by the zero level set of a level set function, on account of the coupling with the geometrically unfitted Eulerian FEM in Chapter 3 to solve the diffusion equation on the domain enclosed by the hypersurface. The discrete mean curvature vector (together with the PDE solution) gives the surface velocity to be extended onto the background domain for a velocity field, based on which we are able to solve the level set transport equation for the evolution of the geometry, cf. Subsection 2.2.2.

4.1 Stabilized Isoparametric Trace Finite Element Method

The *Trace Finite Element Method* (TraceFEM) firstly introduced in [122] for elliptic PDEs posted on stationary manifolds is particularly suitable for problems in which the hypersurface is given implicitly by a level set function, and in which there is a coupling with another PDE problem on a bulk domain that contains the surface, e.g., two-phase interface problem or the bulk-surface model we proposed in Section 2.4. We therefore utilize the TraceFEM for the geometric PDE in order to compute the discrete mean curvature vector of the hypersurface. The TraceFEM for PDEs posed on piecewise linear surfaces, i.e., surface PDEs, has been well investigated, for instance, in [26, 120, 124] for stationary surfaces and in [73, 75, 121, 123] for evolving surfaces. Towards high-order TraceFEM for PDEs on isoparametrically mapped hypersurfaces, however, there does not exist a comparably adequate literature. A recent work of Grande et al. in [74], where a unified framework for the analysis of various stabilizations has been presented, shows that only the so-called *normal derivative volume stabilization* is compatible for high-order TraceFEM. To couple with the unfitted isoparametric BDF-FEM developed in Chapter 3, we accordingly demand the discrete mean curvature vector on a high-order approximation of the hypersurface. Consequently, we take advantage of the high-order isoparametric TraceFEM with using both ghost penalty and normal derivative volume stabilizations, and the later is called *normal diffusion* in this thesis. In contrast to the surface PDEs of physical phenomena, the geometric PDE of mean curvature has its own issue about stability that we will discuss in Subsection 4.1.2. To this end, we make use of the both stabilization mechanisms and call the method *stabilized isoparametric TraceFEM* for solving the geometric equation of mean curvature vector.

4.1.1 Preliminaries and nomenclature

In a similar manner to Subsection 3.1.1, we first prepare the notation for the discrete objects but all time-independent in this subsection.

Finite element spaces and level set hypersurfaces

Let $\{\mathcal{T}_h\}_{h\in\mathbb{R}_+}$ be a family of consistent subdivisions of the background domain $\bar{\Omega}\subset\mathbb{R}^d,\ d=2,3$ into an admissible quasi-uniform triangulation $\mathcal{T}_h$ consisting of simplexes (elements) $\{\hat{T}\in\mathcal{T}_h\}$ with the interior facets $\mathcal{F}_h := \{\overline{T}_1\cap\overline{T}_2 \,|\, T_1,T_2\in\mathcal{T}_h,\ T_1\neq T_2\}$ and a characteristic diameter (mesh size) $h\in\mathbb{R}_+$. On each of these triangulations $\mathcal{T}_h$ we

define a time-independent, finite-dimensional function space of polynomials of order k, i.e., a finite element space, by

$$\mathcal{V}_h = \mathcal{V}_h^{(k)} := \left\{ \hat{v}_h \in \mathcal{C}(\bar{\Omega}) \mid \hat{v}_h|_T \in \mathcal{P}^k(T),\ \forall \hat{T} \in \mathcal{T}_h \right\}, \tag{4.1}$$

where the bracketed upper index (k) may be omitted below.

Let $\Gamma \subset \bar{\Omega} \subset \mathbb{R}^d$, $d = 2,3$ be a smooth hypersurface. Let $\hat{\Gamma}_h \subset \Gamma_\delta = \mathcal{B}_\delta(\Gamma)$, $h < \delta \in \mathbb{R}_+$ be a connected piecewise linear hypersurface, which gives a second-order approximation to Γ, such that $\hat{\Gamma}_h \cap \hat{T}$ is a closed subset of a hyperplane $\hat{\mathcal{G}}_h := \{\hat{\Gamma}_h \cap \hat{T} \mid \forall \hat{T} \in \mathcal{T}_h\}$ in which $\hat{\mathcal{E}}_h := \{\hat{G}_1 \cap \hat{G}_2 \mid \hat{G}_1, \hat{G}_2 \in \hat{\mathcal{G}}_h,\ \hat{G}_1 \neq \hat{G}_2\}$ is the set of edges. Let $\hat{\mathcal{F}}_h^\Gamma = \{\hat{F} \in \mathcal{F}_h \mid \mathrm{meas}_{d-2}(\hat{F} \cap \hat{\Gamma}_h) > 0\}$ be the set of facets and $\hat{\mathcal{T}}_h^\Gamma = \{\hat{T} \in \mathcal{T}_h \mid \mathrm{meas}_{d-1}(\hat{T} \cap \hat{\Gamma}_h) > 0\}$ be the set of elements cut by the hypersurface $\hat{\Gamma}_h$.

In order to represent Γ and $\hat{\Gamma}_h$ implicitly within an unfitted discretization, we design a level set function ϕ that matches the signed distance function ρ as introduced in Subsection 2.1.3, such that for all time $t \in [0,T]$ there holds

$$\phi(\mathbf{x},t) = \rho(\mathbf{x}) \qquad \text{in } \Gamma_\delta. \tag{4.2}$$

Remark 14 (Signed distance properties)**.** *Equation 4.2 implies the assumption of signed distance properties on the level set function, cf. Corollary 1. It considerably simplifies the error analysis in this chapter, but it is not crucial (and thus may not be strictly preserved) to the implementation of the numerical methods.*

The zero level set of ϕ is utilized to describe the exact hypersurface by

$$\Gamma = \{\mathbf{x} \in \bar{\Omega} \subset \mathbb{R}^d \mid \phi(\mathbf{x},\cdot) = 0\}. \tag{4.3}$$

We then apply a piecewise linear interpolation of the level set function for a fixed time $t \in [0,T]$, i.e., $\hat{\phi}_h(\mathbf{x},t) := I_h \phi(\mathbf{x},t)$ by the nodal interpolation operator I_h, such that the linearized level set hypersurface is represented by

$$\hat{\Gamma}_h = \{\mathbf{x} \in \bar{\Omega} \subset \mathbb{R}^d \mid \hat{\phi}_h(\mathbf{x},\cdot) = 0\}. \tag{4.4}$$

Let Θ be the isoparametric mapping which is a q^{th}-order finite element function constructed such that $\Gamma_h := \Theta(\hat{\Gamma}_h)$ gives a high-order approximation to Γ, cf. Subsection 3.1.1 and Subsection 3.1.3. On the deformed cut elements $\mathcal{T}_h^\Gamma := \Theta(\hat{\mathcal{T}}_h^\Gamma)$ we define the *isoparametric trace* finite element space of polynomial degree k by

$$\mathcal{V}_h^\Gamma := \left\{ v_h \in \mathcal{C}(\mathcal{T}_h^\Gamma) \mid v_h = \hat{v}_h|_{\hat{\Gamma}_h} \circ \Theta^{-1},\ \hat{v}_h \in \mathcal{V}_h^{(k)} \right\}. \tag{4.5}$$

Correspondingly, we have the partition of the isoparametrically mapped hypersurface and the edges within it, as well as the sets of deformed cut facets and cut elements, respectively,

$$\mathcal{G}_h := \Theta(\hat{\mathcal{G}}_h), \qquad \mathcal{E}_h := \Theta(\hat{\mathcal{E}}_h), \qquad \mathcal{F}_h^\Gamma := \Theta(\hat{\mathcal{F}}_h^\Gamma), \qquad \mathcal{T}_h^\Gamma := \Theta(\hat{\mathcal{T}}_h^\Gamma). \tag{4.6}$$

Geometric approximation

We begin this section with the *closest point projector* that connects the points between the hypersurface Γ and its open tubular neighborhood $\Gamma_\delta := \{\mathbf{x} \in \bar{\Omega} \subset \mathbb{R}^d \mid |\rho(\mathbf{x})| < \delta\}$ for some finite $\delta > h$ depending on the smoothness of Γ. See also Subsection 2.1.3.

Definition 12 (Closest point projector)**.** *Let $p : \Gamma_\delta \to \Gamma$ be the closest point projector such that*

$$p(\mathbf{x}) := \mathbf{x} - \rho(\mathbf{x})(\mathbf{n} \circ p(\mathbf{x})) \qquad \forall \mathbf{x} \in \Gamma_\delta$$

which assigns precisely one $\mathbf{x}$ on the exact hypersurface Γ to each $\mathbf{x}$ in the open tubular neighborhood Γ_δ.

In Subsection 2.1.2 we have introduced the oriented and compact $\mathcal{C}^2$-hypersurfaces on which we may define the mean curvature vector. In Assumption 1 we have assumed the hypersurfaces to be $\mathcal{C}^\infty$-smooth, but to analyze the discrete mean curvature of arbitrarily high order of accuracy, the requirement of geometric regularity depends on the approximation order, i.e., the hypersurface needs to be sufficiently smooth up to a certain degree. We hence make the following assumption.

Assumption 5 (Geometric regularity)**.** *In this chapter we assume the hypersurface $\Gamma \in \mathcal{C}^{k+3}(\mathbb{R}^d)$ on which the mean curvature vector $\mathbf{H}$ satisfies*

$$\|\mathbf{H}\|_{\mathcal{W}_\infty^{k+1}(\Gamma)} \lesssim 1$$

where $k \geq 1$ is set to match the polynomial degree of the finite element space $\mathcal{V}_h^{(k)}$. By the Sobolev embedding theorem (See [61, Section 5.6]), $\mathbf{H} \in \mathcal{C}(\Gamma)$ follows.

Provided that by the Sobolev extension theorem (See [61, Section 5.4]) the mean curvature vector $\mathbf{H}$ can be continuously extended onto the open tubular neighborhood Γ_δ, $\delta > h$ with the closest point projector p in Definition 12, we have in addition the stability of the extension

$$\|\mathbf{H} \circ p\|_{\mathcal{W}_\infty^{k+1}(\Gamma_\delta)} \lesssim 1.$$

Next, we relate the signed distance function to the unit normals on the hypersurfaces, and carry out the estimates for the signed distance function and the unit normals. We

emphasize that many of the following results hold based on the assumption of *signed distance property*, which simplifies the analysis but is not necessary to be preserved in numerical implementation, cf. Corollary 1 and Remark 14.

Lemma 15 (Unit normal vectors)**.** *Let $\rho : \bar{\Omega} \to \mathbb{R}$ be the signed distance function satisfying (4.2). By definition of the $\mathcal{C}^2$-hypersurface Γ, the tangent space $\mathsf{T}_{\mathbf{x}}\Gamma$ is orthogonal to $\nabla\rho(\mathbf{x})$, hence the unit normal $\mathbf{n}$ on Γ satisfies*

$$\mathbf{n} = \frac{\nabla\rho}{\|\nabla\rho\|_2}.$$

With the piecewise linear interpolation operator $\mathcal{I}_h$ the unit normal $\hat{\mathbf{n}}_h$ on linearized hypersurface $\hat{\Gamma}_h$ satisfies

$$\hat{\mathbf{n}}_h = \frac{\nabla(\mathcal{I}_h\rho)}{\|\nabla(\mathcal{I}_h\rho)\|_2}.$$

With the isoparametric mapping Θ the unit normal $\mathbf{n}_h$ on the mapped hypersurface $\Gamma_h := \Theta(\hat{\Gamma}_h)$ satisfies

$$\mathbf{n}_h = \frac{\nabla(\mathcal{I}_h\rho \circ \Theta^{-1})}{\|\nabla(\mathcal{I}_h\rho \circ \Theta^{-1})\|_2} = \frac{(D\Theta)^{-\mathrm{T}}\hat{\mathbf{n}}_h}{\|(D\Theta)^{-\mathrm{T}}\hat{\mathbf{n}}_h\|_2}.$$

Note that $\|\cdot\|_2$ is the standard Euclidean norm.

Proof. See [74, Lemma 3.3].

□

Next, we estimate the distances between the exact and the approximated hypersurfaces, as well as the distances between their unit normals.

Lemma 16 (Discrete hypersurface estimates)**.** *Let $\hat{\mathbf{n}}_h$ be the unit normal on $\hat{\Gamma}_h$ and $\mathbf{n}_h$ be the unit normal on $\Gamma_h := \Theta(\hat{\Gamma}_h)$. By the construction of $\hat{\Gamma}_h$ and Γ_h the following estimates hold true:*

$$\|\rho\|_{\mathcal{L}^\infty(\hat{\Gamma}_h)} \lesssim h^2, \qquad \|\mathbf{n} \circ p - \hat{\mathbf{n}}_h\|_{\mathcal{L}^\infty(\hat{\Gamma}_h)} \lesssim h \tag{4.7}$$

for linearized cut hypersurface $\hat{\Gamma}_h$ and

$$\|\rho\|_{\mathcal{L}^\infty(\Gamma_h)} \lesssim h^{q+1}, \qquad \|\mathbf{n} \circ p - \mathbf{n}_h\|_{\mathcal{L}^\infty(\Gamma_h)} \lesssim h^q \tag{4.8}$$

for mapped cut hypersurface Γ_h with Θ of polynomial degree $q \geq 1$.

Proof. See [105, Corollary 3.2 and Lemma 3.6] for the first result of (4.8). See [74, Lemma 3.3] for the second result of (4.8). The linearized case (4.7) follows directly when $q = 1$.

□

By the two lemmas above we have the following corollary.

Corollary 2. *The unit normal* $\mathbf{n}$ *and the discrete unit normals* $\hat{\mathbf{n}}_h, \mathbf{n}_h$ *have the stability bounds*

$$\|\mathbf{n} \circ p\|_{\mathcal{L}^\infty(\Gamma_\delta)} \lesssim 1, \qquad \|\hat{\mathbf{n}}_h\|_{\mathcal{L}^\infty(\hat{\Gamma}_h)} \lesssim 1, \qquad \|\mathbf{n}_h\|_{\mathcal{L}^\infty(\Gamma_h)} \lesssim 1. \tag{4.9}$$

In addition, for the tensor product of the unit normals there hold

$$\|(\mathbf{n} \circ p) \otimes (\mathbf{n} \circ p) - \hat{\mathbf{n}}_h \otimes \hat{\mathbf{n}}_h\|_{\mathcal{L}^\infty(\hat{\Gamma}_h)} \lesssim h, \tag{4.10}$$

$$\|(\mathbf{n} \circ p) \otimes (\mathbf{n} \circ p) - \mathbf{n}_h \otimes \mathbf{n}_h\|_{\mathcal{L}^\infty(\Gamma_h)} \lesssim h^q. \tag{4.11}$$

Proof. The stability bounds (4.9) obviously hold based on Lemma 15 and Lemma 16. We prove (4.11) as follows:

$$\begin{aligned}
\|(\mathbf{n} \circ p) \otimes (\mathbf{n} \circ p) - \mathbf{n}_h \otimes \mathbf{n}_h\|_{\mathcal{L}^\infty(\Gamma_h)} &= \|(\mathbf{n} \circ p - \mathbf{n}_h)(\mathbf{n} \circ p)^{\mathrm{T}} + \mathbf{n}_h(\mathbf{n} \circ p - \mathbf{n}_h)^{\mathrm{T}}\|_{\mathcal{L}^\infty(\Gamma_h)} \\
&\leq \|(\mathbf{n} \circ p - \mathbf{n}_h)\|_{\mathcal{L}^\infty(\Gamma_h)} + \|(\mathbf{n} \circ p - \mathbf{n}_h)^{\mathrm{T}}\|_{\mathcal{L}^\infty(\Gamma_h)} \\
&\lesssim h^q + h^q \lesssim h^q,
\end{aligned}$$

where we made use of the triangle inequality, normal estimates (4.9) and (4.8). The linearized case (4.10) follows the similar lines when $q = 1$.

□

Recalling the tangential projection $P_\Gamma := \mathbb{I} - \mathbf{n} \otimes \mathbf{n}$ we have introduced in Section 2.1. Obviously, it is an identity in the tangent space $\mathsf{T}_{\mathbf{x}}\Gamma$ because

$$P_\Gamma P_\Gamma = (\mathbb{I} - \mathbf{n} \otimes \mathbf{n})^2 = \mathbb{I}^2 - \mathbf{n}\mathbf{n}^{\mathrm{T}}\mathbb{I} - \mathbb{I}\mathbf{n}\mathbf{n}^{\mathrm{T}} + (\mathbf{n}\mathbf{n}^{\mathrm{T}})^2 = \mathbb{I} - 2\,\mathbf{n}\mathbf{n}^{\mathrm{T}} + \mathbf{n}\mathbf{n}^{\mathrm{T}} = P_\Gamma. \tag{4.12}$$

Analogously, we can define the tangential projections to the tangent space of the linearized hypersurface and to that of the mapped hypersurface, as follows:

Definition 13 (Tangential projections)**.** *Let* $P_{\hat{\Gamma}_h}$ *be the tangential projection to* $\mathsf{T}_{p(\mathbf{x})}\hat{\Gamma}_h$*, and* P_{Γ_h} *be the tangential projection to* $\mathsf{T}_{p(\mathbf{x})}\Gamma_h$*, such that*

$$P_{\hat{\Gamma}_h} := \mathbb{I} - \hat{\mathbf{n}}_h \otimes \hat{\mathbf{n}}_h, \qquad P_{\Gamma_h} := \mathbb{I} - \mathbf{n}_h \otimes \mathbf{n}_h.$$

The corresponding tangential gradients are defined by

$$\nabla_{\hat{\Gamma}_h} := P_{\hat{\Gamma}_h}\nabla, \qquad \nabla_{\Gamma_h} := P_{\Gamma_h}\nabla.$$

Similarly, they are identities in the corresponding tangent spaces as well. Furthermore, we have the following lemma for the tangential projections.

Lemma 17 (Tangential projection bounds)**.** *The tangential projections have the stability bounds*

$$\|P_\Gamma\|_{\mathcal{L}^\infty(\Gamma)} \leq 1, \qquad \|P_{\hat{\Gamma}_h}\|_{\mathcal{L}^\infty(\hat{\Gamma}_h)} \leq 1, \qquad \|P_{\Gamma_h}\|_{\mathcal{L}^\infty(\Gamma_h)} \leq 1. \tag{4.13}$$

In addition, there hold for the distance between the tangential projections

$$\|P_\Gamma \circ p - P_{\hat{\Gamma}_h}\|_{\mathcal{L}^\infty(\hat{\Gamma}_h)} \lesssim h, \qquad \|P_\Gamma \circ p - P_{\Gamma_h}\|_{\mathcal{L}^\infty(\Gamma_h)} \lesssim h^q. \tag{4.14}$$

Proof. The stability bounds (4.13) hold directly by Definition 13. The estimates for projection distances (4.14) are based on Definition 13 with the normal estimates (4.9), (4.10) and (4.11).

□

4.1.2 Variational formulations

By geometric equation (2.16) in Subsection 2.1.4, we have defined the mean curvature vector $\mathbf{H}$ and derived the corresponding weak formulation (2.17). However, this weak form is *not* wellposed. We start this section with an investigation on the issue of wellposedness, and then propose the stabilized discretizations of the weak form for both piecewisely linearized and isoparametrically mapped hypersurfaces.

Wellposedness

Recall the variational formulation of the geometric equation (2.17):
To find $\mathbf{H} \in [\mathcal{H}^1(\Gamma)]^d$ such that

$$B(\mathbf{H}, \mathbf{v}) = L(\mathbf{v}) \qquad \forall \mathbf{v} \in [\mathcal{H}^1(\Gamma)]^d \tag{4.15}$$

where

$$B(\mathbf{H}, \mathbf{v}) = \int_\Gamma \mathbf{H} \cdot \mathbf{v} \; ds \qquad \text{and} \qquad L(\mathbf{v}) = \int_\Gamma \nabla_\Gamma \mathbf{x} : \nabla_\Gamma \mathbf{v} \; ds. \tag{4.16}$$

As we discussed in Remark 2, by the Lax-Milgram theorem, cf. [96, Theorem 6 in Section 6.3] and [61, Subsection 6.2.1], the problem is wellposed, provided that coercivity and continuity of the bilinear form $B(\cdot,\cdot)$ hold in addition to the bounded linear functional $L(\cdot)$ in a Hilbert space. However, the challenge arises from the absence of the ellipticity of $B(\cdot,\cdot)$ in $\mathcal{H}^1$ space, while in $\mathcal{L}^2$ space it is indeed coercive but $L(\cdot)$ is not continuous.

More specifically, let us consider the Ritz-Galerkin discretization on a proper fitted mesh $\mathbf{T}_h$ with the characteristic length h, and assume a meshed hypersurface $\Gamma = \bigcup_{\mathbf{T}\in\mathbf{T}_h} \overline{\mathbf{T}}$ for the conforming triangulation $\mathbf{T}_h$, which is a special case of the unfitted setting in an ideal condition. The Ritz-Galerkin method reads:
To find $\mathbf{u}_h \in [\mathcal{V}_h(\Gamma)]^d \subset [\mathcal{H}^1(\Gamma)]^d$ such that

$$B(\mathbf{u}_h, \mathbf{v}_h) = L(\mathbf{v}_h) \qquad \forall \mathbf{v}_h \in [\mathcal{V}_h(\Gamma)]^d. \tag{4.17}$$

The Lax-Milgram theorem is applicable since $\mathcal{V}_h$ is a finite dimensional subspace of $\mathcal{H}^1$. The bilinear form $B(\cdot,\cdot)$ is then elliptic for a constant c_1 in this problem

$$B(\mathbf{v}_h, \mathbf{v}_h) = \|\mathbf{v}_h\|^2_{\mathcal{L}^2(\Gamma)} \geq c_1 h^2 \|\mathbf{v}_h\|^2_{\mathcal{H}^1(\Gamma)} \qquad \forall \mathbf{v}_h \in [\mathcal{V}_h(\Gamma)]^d \tag{4.18}$$

where the inverse inequality holds only in finite dimensional spaces. Hence a unique solution exists. Suppose $\mathbf{u}$ is the exact solution to (4.17) and $\mathbf{u}_h$ is the corresponding discrete solution in the finite dimensional subspace $[\mathcal{V}_h(\Gamma)]^d \subset [\mathcal{H}^1(\Gamma)]^d$. With Galerkin orthogonality and boundedness of $B(\cdot,\cdot)$ we have for all $\mathbf{v}_h \in [\mathcal{V}_h(\Gamma)]^d$

$$\begin{aligned} c_1 h^2 \|\mathbf{u}-\mathbf{u}_h\|^2_{\mathcal{H}^1(\Gamma)} &\leq B(\mathbf{u}-\mathbf{u}_h, \mathbf{u}-\mathbf{u}_h) = B(\mathbf{u}-\mathbf{u}_h, \mathbf{u}-\mathbf{v}_h) + \underbrace{B(\mathbf{u}-\mathbf{u}_h, \mathbf{v}_h-\mathbf{u}_h)}_{=0} \\ &\leq c_2 \|\mathbf{u}-\mathbf{u}_h\|_{\mathcal{H}^1(\Gamma)} \|\mathbf{u}-\mathbf{v}_h\|_{\mathcal{H}^1(\Gamma)} \end{aligned}$$

where c_2 is a constant independent of h. Hence we arrive at the Céa's lemma

$$\|\mathbf{u}-\mathbf{u}_h\|_{\mathcal{L}^2(\Gamma)} \leq \|\mathbf{u}-\mathbf{u}_h\|_{\mathcal{H}^1(\Gamma)} \leq \frac{c_2}{c_1}\, h^{-2} \inf_{\mathbf{v}_h\in[\mathcal{V}_h(\Gamma)]^d} \|\mathbf{u}-\mathbf{v}_h\|_{\mathcal{H}^1(\Gamma)}$$

which indicates $\|\mathbf{u}-\mathbf{u}_h\|_{\mathcal{L}^2(\Gamma)}$ loses two orders of accuracy with respect to the quasi-optimal error estimate. It therefore motivates us to look for a stabilization of the $\mathcal{L}^2$-orthogonal projection.

Stabilized discretization for linearized hypersurface

In [82] Hansbo et al. propose a stabilized approximation of the mean curvature vector $\hat{\mathbf{H}}_h$, defined as follows:
To find $\hat{\mathbf{H}}_h \in [\mathcal{V}_h|_{\hat{\mathcal{T}}_h^\Gamma}]^d$ such that for all $\mathbf{v}_h \in [\mathcal{V}_h|_{\hat{\mathcal{T}}_h^\Gamma}]^d$

$$\hat{B}_h(\hat{\mathbf{H}}_h, \mathbf{v}_h) + \hat{S}_h(\hat{\mathbf{H}}_h, \mathbf{v}_h) = \hat{L}_h(\mathbf{v}_h), \tag{4.19}$$

where the original bilinear and linear forms

$$\hat{B}_h(\hat{\mathbf{H}}_h, \mathbf{v}_h) := \int_{\hat{\Gamma}_h} \hat{\mathbf{H}}_h \cdot \mathbf{v}_h \, ds, \qquad \hat{L}_h(\mathbf{v}_h) = \int_{\hat{\Gamma}_h} \nabla_{\hat{\Gamma}_h} \mathbf{x} : \nabla_{\hat{\Gamma}_h} \mathbf{v}_h \, ds, \tag{4.20}$$

and the additional stabilization term of ghost penalty

$$\begin{aligned} \hat{S}_h(\hat{\mathbf{H}}_h, \mathbf{v}_h) := & \overbrace{\gamma_{\hat{F}} \sum_{\hat{F} \in \hat{\mathcal{F}}_h^\Gamma} \int_F [\![\nabla \hat{\mathbf{H}}_h \cdot \mathbf{n}_{\hat{F}}]\!][\![\nabla \mathbf{v}_h \cdot \mathbf{n}_{\hat{F}}]\!] ds}^{\text{Facet stabilization}} \\ & \underbrace{+ \gamma_{\hat{E}} h \sum_{\hat{E} \in \hat{\mathcal{E}}_h} \int_{\hat{E}} [\![\nabla_{\hat{\Gamma}_h} \hat{\mathbf{H}}_h \cdot \mathbf{n}_{\hat{E}}]\!][\![\nabla_{\hat{\Gamma}_h} \mathbf{v}_h \cdot \mathbf{n}_{\hat{E}}]\!] ds}_{\text{Edge stabilization}}, \end{aligned} \tag{4.21}$$

where $\hat{\mathcal{F}}_h^\Gamma$ is the set of cut facets and $\hat{\mathcal{E}}_h$ is the set of edges in the partition of the hypersurface $\hat{\mathcal{G}}_h$, and the two parameters $\gamma_{\hat{\mathcal{F}}}, \gamma_{\hat{\mathcal{E}}} \in \mathbb{R}$. Note that $\mathbf{n}_{\hat{F}}$ is the outward unit normal to the facet $\hat{F}$, and $\mathbf{n}_{\hat{E}}$ is the outward co-normal orthogonal to the edge $\hat{E}$ and tangent to the hypersurface piece $\hat{G} \in \hat{\mathcal{G}}_h$ such that $\forall \hat{E} \in \{\partial \hat{G}\}_{\hat{G} \in \hat{\mathcal{G}}_h}$. More specifically, we define the jumps

$$[\![\nabla \mathbf{v}_h \cdot \mathbf{n}_{\hat{F}}]\!] := \nabla \mathbf{v}_h|_{\hat{T}_1} \cdot \mathbf{n}_{\hat{F},\hat{T}_1} + \nabla \mathbf{v}_h|_{\hat{T}_2} \cdot \mathbf{n}_{\hat{F},\hat{T}_2}, \tag{4.22a}$$

$$[\![\nabla_{\hat{\Gamma}_h} \mathbf{v}_h \cdot \mathbf{n}_{\hat{E}}]\!] := \nabla_{\hat{\Gamma}_h} \mathbf{v}_h|_{\hat{G}_1} \cdot \mathbf{n}_{\hat{E},\hat{G}_1} + \nabla_{\hat{\Gamma}_h} \mathbf{v}_h|_{\hat{G}_2} \cdot \mathbf{n}_{\hat{E},\hat{G}_2}, \tag{4.22b}$$

where $\mathbf{v}_h|_{\hat{T}_i}$, $i = 1, 2$ are for the facet jump and $\mathbf{v}_h|_{\hat{G}_i}$ for the edge jump, and correspondingly $\mathbf{n}_{\hat{F},\hat{T}_i}$ are the unit normals to the facet $\hat{F} = \overline{\hat{T}_1} \cap \overline{\hat{T}_2}$ and outward to the element $\hat{T}_i$, whereas $\mathbf{n}_{\hat{E},\hat{G}_i}$ are the co-normals orthogonal to the edge $\hat{E} = \overline{\hat{G}_1} \cap \overline{\hat{G}_2}$ and tangent to the hypersurface piece $\hat{G}_i$.

Remark 15 (Edge stabilization)**.** *The edge stabilization has been proven crucial for meshed hypersurfaces but unnecessary for cut hypersurfaces by Hansbo et al., cf. [82, Theorem 4.2]. Hence in this thesis we will not apply this stabilization term in our*

numerical method. However, we display it here because the edge-related objects will be used in the error analysis.

Higher-order discretization for isoparametrically mapped hypersurface

We define the stabilized discrete mean curvature vector $\mathbf{H}_h$ on the high-order isoparametrically mapped cut hypersurface Γ_h by a weak formulation based on the isoparametric TraceFEM discretization, and then estimate the numerical error.

To compute the stabilized discrete mean curvature vector $\mathbf{H}_h$ that is sufficiently accurate in the $\mathcal{H}^1$ norm, we utilize the *ghost penalty mechanism* to regulate the geometry, cf. [82]. Moreover, for high order of accuracy we make use of the normal diffusion mechanism to stabilize the method, so-called *normal derivative volume stabilization* in [74], on top of the high-order ghost penalty stabilization.

Given the discrete coordinate map $\mathbf{x}_{\Gamma_h} : \Gamma_h \ni \mathbf{x} \to \mathbf{x} \in \mathbb{R}^d$, we define the stabilized discrete mean curvature vector $\mathbf{H}_h$ by the following weak formulation:
To find $\mathbf{H}_h \in [\mathcal{V}_h^\Gamma]^d$ such that for all $\mathbf{v}_h \in [\mathcal{V}_h^\Gamma]^d$

$$B_h(\mathbf{H}_h, \mathbf{v}_h) + S_h(\mathbf{H}_h, \mathbf{v}_h) = L_h(\mathbf{v}_h) \tag{4.23}$$

where the original bilinear and linear forms

$$B_h(\mathbf{H}_h, \mathbf{v}_h) = \int_{\Gamma_h} \mathbf{H}_h \cdot \mathbf{v}_h \, ds, \qquad L_h(\mathbf{v}_h) = \int_{\Gamma_h} \nabla_{\Gamma_h} \mathbf{x} : \nabla_{\Gamma_h} \mathbf{v}_h \, ds, \tag{4.24}$$

and the additional stabilization term of ghost penalty and normal diffusion

$$\begin{aligned} S_h(\mathbf{H}_h, \mathbf{v}_h) = \overbrace{\gamma_{\mathcal{F}} h^\lambda \sum_{F \in \mathcal{F}_h^\Gamma} \sum_{j=1}^{k} h^{2j-1} \int_F [\![\partial_{\mathbf{n}_F}^j \mathbf{H}_h]\!] [\![\partial_{\mathbf{n}_F}^j \mathbf{v}_h]\!] ds}^{\text{Ghost penalty}} \\ \underbrace{+ \gamma_{\mathcal{T}} h \int_{\mathcal{T}_h^\Gamma} (\nabla \mathbf{H}_h \cdot \mathbf{n}_h)(\nabla \mathbf{v}_h \cdot \mathbf{n}_h) d\mathbf{x}}_{\text{Normal diffusion}} \end{aligned} \tag{4.25}$$

where $\mathcal{F}_h^\Gamma$ is the set of cut facets and $\mathcal{T}_h^\Gamma$ is the set of cut elements, which are all deformed through the isoparametric mapping Θ of polynomial degree q, with the two parameters $\gamma_{\mathcal{F}}, \gamma_{\mathcal{T}} \in \mathbb{R}$ and the mesh size scaling parameter $\lambda \in \mathbb{R}$ to be determined yet. Note that here we use the k^{th}-order *derivative jump* ghost penalty formulation where the jump is defined analogously to (4.22a) but the gradients are replaced by the high-order directional derivatives.

Remark 16 ($\mathcal{L}^2$-scale and $\mathcal{H}^1$-scale)**.** *The mesh size scaling parameter $\lambda \in \mathbb{R}$ typically chosen 1 or -1 corresponds to $\mathcal{L}^2$- or $\mathcal{H}^1$-scale, respectively. In [82] Hansbo et al. select $\lambda = -1$ for $\mathcal{H}^1$-scale in the facet-based ghost penalty term. We however reserve the flexibility of λ choices at this point, and will investigate how the different choices of λ affect the results in the error analysis in Section 4.2 and in the numerical experiments in Section 4.3.*

In order to conduct the error analysis below we define the following semi-norms for the edge ghost penalty, the high-order facet ghost penalty and the normal diffusion for all $\mathbf{v}_h \in [\mathcal{V}_h^\Gamma]^d$ based on the jumps similar to (4.22)

$$|||\mathbf{v}_h|||_{\mathcal{E}_h}^2 := h \|[\![\nabla_{\Gamma_h} \mathbf{v}_h \cdot \mathbf{n}_E]\!]\|_{\mathcal{E}_h}^2, \tag{4.26a}$$

$$|||\mathbf{v}_h|||_{\mathcal{F}_h^\Gamma}^2 := \sum_{j=1}^{k} h^{2j-1} \|[\![\partial_{\mathbf{n}_F}^j \mathbf{v}_h]\!]\|_{\mathcal{F}_h^\Gamma}^2, \tag{4.26b}$$

$$|||\mathbf{v}_h|||_{\mathcal{T}_h^\Gamma}^2 := \|\nabla \mathbf{v}_h \cdot \mathbf{n}_h\|_{\mathcal{T}_h^\Gamma}^2. \tag{4.26c}$$

Remark 17 (Edge semi-norm)**.** *We eliminate the edge ghost penalty stabilization term in (4.25) that has been proven not required for cut surfaces, cf. [82, Theorem 4.2], but we reserve the corresponding edge semi-norm defined by (4.26a) that will be exploited in the error analysis, particularly in Lemma 24.*

4.2 Error Analysis

In this section, we aim at a priori error estimate for the discrete mean curvature vector of the high-order isoparametrically mapped hypersurfaces. Hansbo et al. have carried out a priori error analysis for the low-order case of piecewise linear surfaces by a quite technical way in [82]. At first, we will not follow the same lines but a more unified framework of error analysis by error splitting and the Strang's lemma, which is considered a simplified proof and easier to discuss the effect of the mesh size scaling h^λ. After achieving an order of convergence in this approach, we will then turn to Hansbo's outlines towards an optimal order of convergence, and compare the cases to explain where difficulties arise. This section is organized along the similar lines in [82] as follows: Firstly, in Subsection 4.2.1 two operators for extending and lifting of functions are introduced, and some estimates for the Hessian of the signed distance function; Secondly, a mapping between tangent spaces and its properties are investigated in Subsection 4.2.2; Thirdly, we probe the errors induced by the coordinate embedding in Subsection 4.2.3, and prepare several trace and inverse inequalities in Subsection 4.2.4

that are preliminaries for the error estimates; Fourthly, in order to analyze through error splitting we conduct the interpolation estimates in Subsection 4.2.5 and the consistency estimates in Subsection 4.2.6; Next, the stability analysis is studied in Subsection 4.2.7; Finally, the a priori error analysis based on the consistency and the interpolation errors is performed in Subsection 4.2.8, followed by the alternative a priori error estimate based on the proof of the low-order case in [82]. We will focus on the high-order case of isoparametrically mapped hypersurface in the following analysis, while the linearized hypersurface may be considered a reduced case of our results that has been well-investigated in [82].

4.2.1 Extension and projections

Extending and lifting of functions

In order to carry out the analysis we first introduce two operators that map a function onto or off from the exact hypersurface Γ.

Definition 14 (Extending operator)**.** *Any function* $\mathbf{u}:\Gamma\to\mathbb{R}^d$ *defined on* Γ *can be extended to* Γ_δ *for a finite* $\delta>h$*, denoted by* $(\cdot)^e:\Gamma\to\Gamma_\delta$*, using the pull back*

$$\mathbf{u}^e(\mathbf{x})=\mathbf{u}\circ p(\mathbf{x})\qquad\forall\mathbf{x}\in\Gamma_\delta,$$

where $p:\Gamma_\delta\to\Gamma$ *is the closest point projector by Definition 12.*

By the Sobolev extension theorem, cf. [61, Section 5.4] and [82, Subsection 4.1], the following stability estimate holds true:

$$\|\mathbf{u}^e\|_{\mathcal{W}_\infty^{k+1}(\Gamma_\delta)}\lesssim\|\mathbf{u}\|_{\mathcal{W}_\infty^{k+1}(\Gamma)}\qquad\forall\mathbf{u}\in\mathcal{W}_\infty^{k+1}(\Gamma).\tag{4.27}$$

Definition 15 (Lifting operator)**.** *As* $\hat\Gamma_h\subset\Gamma_\delta$ *and* $\Gamma_h:=\Theta(\hat\Gamma_h)\subset\Gamma_\delta$*, the closest point projector* $p:\Gamma_\delta\to\Gamma$ *projects each* $\mathbf{x}\in\hat\Gamma_h\cup\Gamma_h$ *onto* Γ*. Hence, any function* $\mathbf{v}:\hat\Gamma_h\cup\Gamma_h\to\mathbb{R}^d$ *defined on* $\hat\Gamma_h$ *or* Γ_h *can be lifted to* Γ*, denoted by* $(\cdot)^l:\hat\Gamma_h\cup\Gamma_h\to\Gamma$*, using the push forward*

$$(\mathbf{v}^l)^e(\mathbf{x})=\mathbf{v}^l\circ p(\mathbf{x})=\mathbf{v}(\mathbf{x})\qquad\forall\mathbf{x}\in\hat\Gamma_h\cup\Gamma_h.$$

The Hessian of the signed distance function

Recalling the Hessian of the signed distance function $\mathbb{H}(\mathbf{x}) = \nabla \otimes \nabla \rho(\mathbf{x})$ introduced in Subsection 2.1.4 we have

$$\mathbb{H}(\mathbf{x}) = \sum_{i=1}^{2} \frac{\kappa_i^e}{1+\rho\kappa_i^e} \mathbf{v}_i^e \otimes \mathbf{v}_i^e \qquad \forall \mathbf{x} \in \Gamma_\delta, \tag{4.28}$$

which projects any vector to be parallel to $\mathbf{v}_i^e$, i.e., into $\mathsf{T}_{p(\mathbf{x})}\Gamma$, cf. [70, Lemma 14.7]. Thus one has the identity

$$\mathbb{H} = \mathbb{H} P_\Gamma^e. \tag{4.29}$$

In addition, the Hessian has the stability bound

$$\|\mathbb{H}\|_{\mathcal{L}^\infty(\Gamma_\delta)} \lesssim 1. \tag{4.30}$$

To conclude this subsection, we derive an identity for the derivative of the closest point projector.

Lemma 18. *For the closest point projector p in Γ_δ there holds*

$$Dp = P_\Gamma^e - \rho\mathbb{H}.$$

Proof. For any point $\mathbf{x} \in \Gamma_\delta$ we have

$$\begin{aligned} Dp(\mathbf{x}) &= D\Big(\mathbf{x} - \rho(\mathbf{x})(\mathbf{n} \circ p(\mathbf{x}))\Big) = D\mathbf{x} - \mathbf{n}(p(\mathbf{x}))D\rho(\mathbf{x}) - \rho(\mathbf{x})D\mathbf{n}(p(\mathbf{x})) \\ &= \mathbb{I} - \mathbf{n}(p(\mathbf{x})) \otimes \mathbf{n}(p(\mathbf{x})) - \rho(\mathbf{x})\Big(\nabla \otimes \nabla \rho(\mathbf{x})\Big)^{\mathrm{T}} = (P_\Gamma^e - \rho\mathbb{H})(\mathbf{x}), \end{aligned}$$

where we made use of (2.9) and (2.10).

□

4.2.2 Mapping between tangent spaces

In this subsection, we introduce a mapping from the tangent space of the approximated hypersurface to that of the exact hypersurface, and then carry out some estimates for the mapping, cf. [82].

Definition 16 (The mapping between tangent spaces)**.** *Let $M : \mathsf{T}_{\mathbf{x}}\Gamma_h \to \mathsf{T}_{p(\mathbf{x})}\Gamma$ be a mapping from the tangent space of Γ_h to the tangent space of Γ such that*

$$M := P_\Gamma^e(\mathbb{I} - \rho\mathbb{H})P_{\Gamma_h}. \tag{4.31}$$

M is an invertible matrix. To simplify the notation, we omit the extending operator $(\cdot)^e$ or the lifting operator $(\cdot)^l$ from $M, M^{-1}, M^{\mathrm{T}}, M^{-\mathrm{T}}$ that are extended or lifted implicitly.

By this mapping we can bridge the tangential gradients of any smooth functions on the two tangent spaces, as shown in the following lemma.

Lemma 19. *Let $\mathbf{u} : \Gamma \to \mathbb{R}^d$ be any smooth function defined on Γ, and $\mathbf{v} : \Gamma_h \to \mathbb{R}^d$ be any smooth function defined on Γ_h. For the tangential gradients of $\mathbf{u}$ and $\mathbf{v}$ there hold*

$$\nabla_\Gamma \mathbf{u} = M^{-\mathrm{T}} \nabla_{\Gamma_h} \mathbf{u}^e, \qquad \nabla_{\Gamma_h} \mathbf{v} = M^{\mathrm{T}} \nabla_\Gamma \mathbf{v}^l,$$

where the invertible matrix $M : \mathsf{T}_{\mathbf{x}} \Gamma_h \to \mathsf{T}_{p(\mathbf{x})} \Gamma$ is defined by (4.31).

Proof. We make use of Lemma 18 and (4.29) to obtain

$$\begin{aligned} \nabla_{\Gamma_h} \mathbf{u}^e &= P_{\Gamma_h} \nabla (\mathbf{u} \circ p) = P_{\Gamma_h} (Dp)^{\mathrm{T}} (P_\Gamma^e)^{-1} \nabla_\Gamma \mathbf{u} = P_{\Gamma_h} (P_\Gamma^e - \rho \mathbb{H}) (P_\Gamma^e)^{-1} P_\Gamma \nabla_\Gamma \mathbf{u} \\ &= P_{\Gamma_h} (\mathbb{I} - \rho \mathbb{H}) P_\Gamma \nabla_\Gamma \mathbf{u} = M^{\mathrm{T}} \nabla_\Gamma \mathbf{u}. \end{aligned}$$

This gives the first result. The second one is reached directly by setting $\mathbf{u} = \mathbf{v}^l$ and $\mathbf{u}^e = \mathbf{v}$.

□

We summarize in the following lemma the equivalences of $\mathcal{L}^p$ norms on Γ and Γ_h.

Lemma 20 (Norm equivalences)**.** *For any functions $\mathbf{u}$ on Γ and $\mathbf{v}$ on Γ_h the following norm equivalences hold for $p \in [1, \infty]$*

$$\|\mathbf{u}\|_{\mathcal{L}^p(\Gamma)} \simeq \|\mathbf{u}^e\|_{\mathcal{L}^p(\Gamma_h)}, \qquad \|\mathbf{v}\|_{\mathcal{L}^p(\Gamma_h)} \simeq \|\mathbf{v}^l\|_{\mathcal{L}^p(\Gamma)}.$$

In addition, if $\mathbf{u}, \mathbf{v}$ are sufficiently smooth there hold

$$\|\nabla_\Gamma \mathbf{u}\|_{\mathcal{L}^p(\Gamma)} \simeq \|\nabla_{\Gamma_h} \mathbf{u}^e\|_{\mathcal{L}^p(\Gamma_h)}, \qquad \|\nabla_{\Gamma_h} \mathbf{v}\|_{\mathcal{L}^p(\Gamma_h)} \simeq \|\nabla_\Gamma \mathbf{v}^l\|_{\mathcal{L}^p(\Gamma)}.$$

Proof. See [82, Subsection 4.1].

□

To conclude this subsection, we estimate some important bounds for the mapping.

Lemma 21. *Let M be the mapping between the tangent spaces defined by Equation 4.31. The following estimates hold true:*

$$\|M\|_{\mathcal{L}^\infty(\Gamma_h)} \lesssim 1, \qquad \|M^{-1}\|_{\mathcal{L}^\infty(\Gamma)} \lesssim 1, \qquad \|P_\Gamma - M M^{\mathrm{T}}\|_{\mathcal{L}^\infty(\Gamma)} \lesssim h^{q+1}.$$

Proof. The first two bounds follow the same lines in [25, Section 3] but with the high-order estimates in Lemma 16. In order to prove the third result, we start with the norm equivalence

$$\|P_\Gamma - MM^{\mathrm{T}}\|_{\mathcal{L}^\infty(\Gamma)} \simeq \|P_\Gamma^e - MM^{\mathrm{T}}\|_{\mathcal{L}^\infty(\Gamma_h)}$$

due to Lemma 20. By inserting the definition of M and multiplying out the brackets, we have

$$\begin{aligned}
\|P_\Gamma^e - MM^{\mathrm{T}}\|_{\mathcal{L}^\infty(\Gamma_h)} &= \|P_\Gamma^e - (P_\Gamma^e(\mathbb{I}-\rho\mathbb{H})P_{\Gamma_h})(P_\Gamma^e(\mathbb{I}-\rho\mathbb{H})P_{\Gamma_h})^{\mathrm{T}}\|_{\mathcal{L}^\infty(\Gamma_h)} \\
&= \|P_\Gamma^e - P_\Gamma^e(\mathbb{I}-\rho\mathbb{H})P_{\Gamma_h}(\mathbb{I}-\rho\mathbb{H})P_\Gamma^e\|_{\mathcal{L}^\infty(\Gamma_h)} \\
&= \|P_\Gamma^e - P_\Gamma^e(P_{\Gamma_h} - \rho\mathbb{H}P_{\Gamma_h} - P_{\Gamma_h}\rho\mathbb{H} + \rho\mathbb{H}P_{\Gamma_h}\rho\mathbb{H})P_\Gamma^e\|_{\mathcal{L}^\infty(\Gamma_h)} \\
&\leq \|P_\Gamma^e - P_\Gamma^e P_{\Gamma_h} P_\Gamma^e\|_{\mathcal{L}^\infty(\Gamma)} + \|P_\Gamma^e(\rho\mathbb{H}P_{\Gamma_h} + P_{\Gamma_h}\rho\mathbb{H})P_\Gamma^e\|_{\mathcal{L}^\infty(\Gamma_h)} \\
&\qquad + \|P_\Gamma^e\rho\mathbb{H}P_{\Gamma_h}\rho\mathbb{H}P_\Gamma^e\|_{\mathcal{L}^\infty(\Gamma_h)},
\end{aligned}$$

where we applied the triangle inequality in the last step. With using the stability bounds (4.30), (4.13) and the second estimate of (4.14) in Lemma 17, the first term above is bounded by

$$\begin{aligned}
\|P_\Gamma^e - P_\Gamma^e P_{\Gamma_h} P_\Gamma^e\|_{\mathcal{L}^\infty(\Gamma)} &\lesssim \|P_\Gamma^e(P_\Gamma^e - P_{\Gamma_h})(P_\Gamma^e - P_{\Gamma_h})P_\Gamma^e\|_{\mathcal{L}^\infty(\Gamma_h)} \\
&\lesssim \|P_\Gamma^e - P_{\Gamma_h}\|^2_{\mathcal{L}^\infty(\Gamma_h)} \lesssim h^{2q},
\end{aligned}$$

while the second and the third terms are bounded by

$$\begin{aligned}
\|P_\Gamma^e(\rho\mathbb{H}P_{\Gamma_h} + P_{\Gamma_h}\rho\mathbb{H})P_\Gamma^e\|_{\mathcal{L}^\infty(\Gamma_h)} &\lesssim \|\rho\|_{\mathcal{L}^\infty(\Gamma_h)} \lesssim h^{q+1}, \\
\|P_\Gamma^e\rho\mathbb{H}P_{\Gamma_h}\rho\mathbb{H}P_\Gamma^e\|_{\mathcal{L}^\infty(\Gamma_h)} &\lesssim \|\rho\|^2_{\mathcal{L}^\infty(\Gamma_h)} \lesssim h^{2q+2},
\end{aligned}$$

where the first estimate of (4.8) in Lemma 16 was applied. Hence for $q \geq 1$ we arrive at

$$\|P_\Gamma^e - MM^{\mathrm{T}}\|_{\mathcal{L}^\infty(\Gamma_h)} \lesssim h^{q+1},$$

which completes the proof.

□

Lemma 22. *Let M be the mapping between the tangent spaces defined by Equation 4.31 and $|M|$ be the determinant of M such that the surface measure*

$$d\Gamma = |M| d\Gamma_h, \tag{4.32}$$

which is given as in [25, Section 3.3] but the unit normals in Lemma 15. The following estimates hold true:

$$\||M|\|_{\mathcal{L}^\infty(\Gamma_h)} \lesssim 1, \qquad \||M|^{-1}\|_{\mathcal{L}^\infty(\Gamma_h)} \lesssim 1, \qquad \|1-|M|\|_{\mathcal{L}^\infty(\Gamma_h)} \lesssim h^{q+1}.$$

Proof. The results follow the same lines in [25, Section 3.3] but with the high-order estimates in Lemma 16.

□

4.2.3 Coordinate embedding

The exact and the approximated hypersurfaces are both embedded in the $\mathbb{R}^d$ Euclidean space, the difference between their coordinates however exists. In this subsection, we estimate the distance between the embeddings of the exact and the approximated hypersurfaces.

Lemma 23 (Coordinate embedding)**.** *With Lemma 16 the following estimate holds for the exact hypersurface Γ and the q^{th}-order mapped hypersurface Γ_h embedded in the $\mathbb{R}^d$ Euclidean space*

$$\|\mathbf{x}_\Gamma^e - \mathbf{x}_{\Gamma_h}\|^2_{\mathcal{L}^\infty(\Gamma_h)} + h^2\|\nabla_{\Gamma_h}(\mathbf{x}_\Gamma^e - \mathbf{x}_{\Gamma_h})\|^2_{\mathcal{L}^\infty(\Gamma_h)} \lesssim h^{2q+2}. \tag{4.33}$$

As a consequence, in $\mathcal{L}^2$ norm there holds

$$\|\mathbf{x}_\Gamma^e - \mathbf{x}_{\Gamma_h}\|^2_{\Gamma_h} + h^2\|\nabla_{\Gamma_h}(\mathbf{x}_\Gamma^e - \mathbf{x}_{\Gamma_h})\|^2_{\Gamma_h} \lesssim h^{2q+2}. \tag{4.34}$$

Proof. The first term on the left-hand side of (4.33) is bounded by using (4.8), namely

$$\|\mathbf{x}_\Gamma^e - \mathbf{x}_{\Gamma_h}\|_{\mathcal{L}^\infty(\Gamma_h)} = \|\rho\|_{\mathcal{L}^\infty(\Gamma_h)} \lesssim h^{q+1}.$$

The second term on the left-hand side of (4.33) can be estimated with using the chain rule followed by Lemma 18, namely

$$\begin{aligned}
\|\nabla_{\Gamma_h}(\mathbf{x}_\Gamma^e - \mathbf{x}_{\Gamma_h})\|_{\mathcal{L}^\infty(\Gamma_h)} &\leq \|P_{\Gamma_h} Dp^{\mathrm{T}} - P_{\Gamma_h}\|_{\mathcal{L}^\infty(\Gamma_h)} \\
&= \|(P_\Gamma^e - \rho\mathbb{H})P_{\Gamma_h} - P_{\Gamma_h}\|_{\mathcal{L}^\infty(\Gamma_h)} \\
&\leq \|(P_\Gamma^e - P_{\Gamma_h})P_{\Gamma_h}\|_{\mathcal{L}^\infty(\Gamma_h)} + \|\rho\mathbb{H}P_{\Gamma_h}\|_{\mathcal{L}^\infty(\Gamma_h)} \\
&\lesssim \|P_\Gamma^e - P_{\Gamma_h}\|_{\mathcal{L}^\infty(\Gamma_h)} + \|\rho\|_{\mathcal{L}^\infty(\Gamma_h)} \\
&\lesssim h^q + h^{q+1} \lesssim h^q,
\end{aligned}$$

where we made use of the identity (4.29), the stability bounds (4.30), (4.13) and the second estimate of (4.14) in Lemma 17. This completes the proof of (4.33). The second result (4.34) follows correspondingly with $\mathrm{meas}(\Gamma_h) \simeq 1$.

□

4.2.4 Trace and inverse estimates

In this subsection, we formulate several inequalities that will be used in the a priori error analysis. The first lemma gives an upper bound for the edge stabilization term in the isoparametric case.

Lemma 24 (Edge estimate)**.** *The semi-norm of edge ghost penalty defined by* (4.26a) *satisfies the following stability estimate for any function* $\mathbf{u} \in \mathcal{W}^1_\infty(\Gamma)$

$$|||\mathbf{u}^e|||^2_{\mathcal{E}_h} \lesssim h^{2q} \|\mathbf{u}\|^2_{\mathcal{W}^1_\infty(\Gamma)}.$$

Proof. Analogously to [82, Lemma 4.5], let $\mathbf{t}_E$ be the unit vector parallel to the edge $E \in \mathcal{E}_h$ at each point $\mathbf{x} \in E$ such that $\mathbf{n}_{E,G_1}(\mathbf{x}) = \mathbf{n}_{h,G_1}(\mathbf{x}) \times \mathbf{t}_E(\mathbf{x})$ and $\mathbf{n}_{E,G_2}(\mathbf{x}) = -\mathbf{n}_{h,G_2}(\mathbf{x}) \times \mathbf{t}_E(\mathbf{x})$. For $\mathbf{t}_\Gamma := (\mathbf{n}^e \times \mathbf{t}_E)^l$ and $\mathbf{t}_\mathcal{F} := \mathbf{t}_\Gamma \times \mathbf{n}$ such that $\mathrm{span}\{\mathbf{t}_\Gamma, \mathbf{t}_\mathcal{F}\} = \mathsf{T}_{p(\mathbf{x})}\Gamma$ for $\mathbf{x} \in E$, we have by the triangle inequality combined with the Young's inequality

$$\begin{aligned}
|||\mathbf{u}^e|||^2_{\mathcal{E}_h} &= \sum_{E\in\mathcal{E}_h} h\|\nabla_{\Gamma_h}\mathbf{u}^e \cdot (\mathbf{n}_{E,G_1} - \mathbf{n}_{E,G_2})\|^2_E \\
&\lesssim \sum_{E\in\mathcal{E}_h} h\Big(\|\mathbf{n}_{E,G_1} - \mathbf{t}_\Gamma)\|^2_{\mathcal{L}^\infty(E)} + \|\mathbf{t}_\Gamma - \mathbf{n}_{E,G_2}\|^2_{\mathcal{L}^\infty(E)}\Big)\|\nabla_{\Gamma_h}\mathbf{u}^e\|^2_E \\
&= \sum_{E\in\mathcal{E}_h} h\Big(\|(\mathbf{n}_{h,G_1} - \mathbf{n}^e) \times \mathbf{t}_E\|^2_{\mathcal{L}^\infty(E)} + \|(\mathbf{n}^e - \mathbf{n}_{h,G_2}) \times \mathbf{t}_E\|^2_{\mathcal{L}^\infty(E)}\Big)\|\nabla_{\Gamma_h}\mathbf{u}^e\|^2_E \\
&\lesssim \sum_{E\in\mathcal{E}_h} h\|\mathbf{n}^e - \mathbf{n}_h\|^2_{\mathcal{L}^\infty(E)}\|\mathbf{t}_E\|^2_{\mathcal{L}^\infty(E)}\mathrm{meas}(E)\|\mathbf{u}^e\|^2_{\mathcal{W}^1_\infty(E)} \\
&\lesssim \mathrm{card}(\mathcal{E}_h)\ \mathrm{meas}(E)\ h^{2q+1}\|\mathbf{u}\|^2_{\mathcal{W}^1_\infty(\Gamma)} \simeq h^{2q}\|\mathbf{u}\|^2_{\mathcal{W}^1_\infty(\Gamma)},
\end{aligned}$$

where we made use of the second estimate of (4.8) in Lemma 16, and the extension stability (4.27), with $\mathrm{card}(\mathcal{E}_h) \simeq h^{1-d}$, $\mathrm{meas}(E) \simeq h^{d-2}$. This completes the proof.

□

The following trace inequality bounds the facet norm by the corresponding volume norms.

Lemma 25 (Facet trace inequality). *For $\mathbf{v}_h \in \mathcal{V}_h^\Gamma$ and h sufficiently small there holds*

$$\|\mathbf{v}_h\|^2_{\mathcal{F}_h^\Gamma} \lesssim h^{-1}\|\mathbf{v}_h\|^2_{\mathcal{T}_h^\Gamma} + h\|\nabla \mathbf{v}_h\|^2_{\mathcal{T}_h^\Gamma}.$$

Proof. See [81] and [74, Subsection 5.1].

□

The high-order facet ghost penalty term is estimated by the following lemma.

Lemma 26 (Facet ghost penalty inequality). *The semi-norm of high-order facet ghost penalty defined by (4.26b) satisfies the following estimate for any function $\mathbf{u} \in \mathcal{W}_\infty^{k+1}(\Gamma)$*

$$|||\mathbf{u}^e|||^2_{\mathcal{F}_h^\Gamma} \lesssim \sum_{j=1}^{k} h^{2j-2}\|\nabla^j \mathbf{u}^e\|^2_{\mathcal{T}_h^\Gamma} + h^{2j}\|\nabla^{j+1}\mathbf{u}^e\|^2_{\mathcal{T}_h^\Gamma}.$$

Proof. With using Lemma 25 after unrolling the ghost penalty semi-norm, the result follows directly. See also [100].

□

The following inverse inequality bounds the volume norm by the corresponding semi-norm with the $\mathcal{L}^2$ norm on the hypersurface.

Lemma 27 (Volume inverse inequality). *For $\mathbf{v}_h \in \mathcal{V}_h^\Gamma$ and h sufficiently small there holds*

$$\|\mathbf{v}_h\|^2_{\mathcal{T}_h^\Gamma} \lesssim h\|\mathbf{v}_h\|^2_{\Gamma_h} + h^2|||\mathbf{v}_h|||^2_{\mathcal{T}_h^\Gamma}.$$

Proof. See [74, Lemma 7.10].

□

Next, we derive two important estimates in the following lemma that bound the tangential gradients of discrete functions on the hypersurfaces by the normal diffusion semi-norms of the functions.

Lemma 28 (Tangential gradient inverse inequality). *For $\mathbf{v}_h \in \mathcal{V}_h^\Gamma$ and h sufficiently small there holds eq:volume semi norm*

$$\|\nabla_{\Gamma_h}\mathbf{v}_h\|^2_{\Gamma_h} \lesssim h^{-2}\|\mathbf{v}_h\|^2_{\Gamma_h} + h^{-1}|||\mathbf{v}_h|||^2_{\mathcal{T}_h^\Gamma}. \tag{4.35}$$

Furthermore, for the lifted function $\mathbf{v}_h^l$ on Γ there holds

$$\|\nabla_\Gamma \mathbf{v}_h^l\|^2_{\Gamma} \lesssim h^{-2}\|\mathbf{v}_h\|^2_{\Gamma_h} + h^{-1}|||\mathbf{v}_h|||^2_{\mathcal{T}_h^\Gamma}. \tag{4.36}$$

Proof. The first result (4.35) can be bounded with using the projection stability estimates (4.13), the standard inverse inequalities and Lemma 27 such that

$$\begin{aligned}\|\nabla_{\Gamma_h}\mathbf{v}_h\|_{\Gamma_h}^2 &\lesssim \|P_{\Gamma_h}\|_{\mathcal{L}^\infty(\Gamma_h)}^2\|\nabla\mathbf{v}_h\|_{\Gamma_h}^2 \lesssim h^{-1}\|\nabla\mathbf{v}_h\|_{\mathcal{T}_h^\Gamma}^2 \lesssim h^{-3}\|\mathbf{v}_h\|_{\mathcal{T}_h^\Gamma}^2 \\ &\lesssim h^{-2}\|\mathbf{v}_h\|_{\Gamma_h}^2 + h^{-1}|||\mathbf{v}_h|||_{\mathcal{T}_h^\Gamma}^2.\end{aligned}$$

The second result (4.36) follows directly by Lemma 20 the norm equivalence

$$\|\nabla_\Gamma \mathbf{v}_h^l\|_\Gamma \simeq \|\nabla_{\Gamma_h}\mathbf{v}_h\|_{\Gamma_h}.$$

This completes the proof.

□

4.2.5 Interpolation estimates

In this subsection, we introduce the interpolation operators and the corresponding error estimates, cf. [82, Subsection 4.6] and [74, Subsection 5.1].

Definition 17 (Interpolation operators)**.** *Let $\mathcal{I}_h^\Theta : \mathcal{C}(\mathcal{T}_h^\Gamma) \to \mathcal{V}_h^\Gamma$ be the isoparametric trace interpolation operator such that*

$$(\mathcal{I}_h^\Theta \mathbf{v}) \circ \Theta = \mathcal{I}_h^{\mathrm{id}}(\mathbf{v}\circ\Theta) \qquad \forall \mathbf{v} \in \mathcal{C}(\mathcal{T}_h^\Gamma),$$

where $\mathcal{I}_h^{\mathrm{id}}$ is the nodal interpolation operator in the standard finite element space $\mathcal{V}_h^{(k)}$ of continuous piecewise polynomials up to degree k, i.e., when $\Theta = \mathrm{id}$. We define a new interpolation operator $\mathcal{I}_h : \mathcal{C}(\Gamma) \to \mathcal{V}_h^\Gamma$ by

$$\mathcal{I}_h : \mathbf{u} \mapsto \mathcal{I}_h^\Theta \mathbf{u}^e \qquad \forall \mathbf{u} \in \mathcal{C}(\Gamma)$$

and the corresponding lifting interpolation operator $\mathcal{I}_h^l : \mathcal{C}(\Gamma) \to \mathcal{V}_h^\Gamma|_\Gamma$ by

$$\mathcal{I}_h^l : \mathbf{u} \mapsto (\mathcal{I}_h^\Theta \mathbf{u}^e)^l \qquad \forall \mathbf{u} \in \mathcal{C}(\Gamma).$$

Lemma 29 (Interpolation estimate)**.** *Let $\mathcal{I}_h^l$ be the lifting interpolation operator in Definition 17. For $\mathbf{u} \in \mathcal{H}^{k+1}(\Gamma) \subset \mathcal{C}(\Gamma)$ the following interpolation error estimate holds true:*

$$\|\mathbf{u} - \mathcal{I}_h^l \mathbf{u}\|_{\mathcal{H}^s(\Gamma)} \lesssim h^{r-s}\|\mathbf{u}\|_{\mathcal{H}^r(\Gamma)}, \qquad 0 \le s \le r \le k+1. \tag{4.37}$$

In addition, for the extension of $\mathbf{u}$ *to the bulk* $\mathcal{T}_h^\Gamma$ *there holds*

$$\|\mathbf{u}^e - \mathcal{I}_h \mathbf{u}\|_{\mathcal{H}^s(\mathcal{T}_h^\Gamma)} \lesssim h^{r-s} \|\mathbf{u}^e\|_{\mathcal{H}^r(\mathcal{T}_h^\Gamma)}, \qquad 0 \le s \le r \le k+1. \tag{4.38}$$

Proof. See [74, Lemma 5.3] for the isoparametric case, [27] and [53] for the piecewise linear counterpart. See also [106].

□

Next, we estimate the approximation error with respect to the interpolation as a preparation for the a priori error analysis. We first derive a result with $\mathcal{L}^2$-scale ghost penalty, i.e., the mesh size scaling $\lambda = 1$ in the lemma, and subsequently another result with $\mathcal{H}^1$-scale, i.e., $\lambda = -1$ in the corollary. See the high-order ghost penalty term in (4.25) and Remark 16 for details.

Lemma 30 ($\mathcal{L}^2$-scale approximation error estimate)**.** *Let* $\mathbf{H} \in [\mathcal{H}^{k+1}(\Gamma) \cap \mathcal{W}_\infty^{k+1}(\Gamma)]^d$ *be the mean curvature vector of the oriented compact hypersurface* $\Gamma \in \mathcal{C}^{k+3}(\mathbb{R}^d), d = 2, 3$*, which is defined by* (2.16) *and is the weak solution to* (4.15) *under the geometric regularity Assumption 5. For the discrete hypersurface* Γ_h *the interpolation error satisfies*

$$\|\mathbf{H}^e - \mathcal{I}_h \mathbf{H}\|_{\Gamma_h} + h^{\frac{1}{2}} |||\mathbf{H}^e - \mathcal{I}_h \mathbf{H}|||_{\mathcal{F}_h^\Gamma} + h^{\frac{1}{2}} |||\mathbf{H}^e - \mathcal{I}_h \mathbf{H}|||_{\mathcal{T}_h^\Gamma} \lesssim h^{k+1},$$

where $\mathbf{H}^e$ *is the extension of* $\mathbf{H}$ *by Definition 14,* $\mathcal{I}_h$ *is the interpolation operator by Definition 17, and the semi-norms are given by* (4.26)*.*

Proof. The first term on the left-hand side can be lifted by Lemma 20, and subsequently bounded by the interpolation estimate (4.37) in Lemma 29 with $r = k+1$ and $s = 0$, namely

$$\|\mathbf{H}^e - \mathcal{I}_h \mathbf{H}\|_{\Gamma_h} \simeq \|\mathbf{H} - \mathcal{I}_h^l \mathbf{H}\|_\Gamma \lesssim h^{k+1} \|\mathbf{H}\|_{\mathcal{H}^{k+1}(\Gamma)} \lesssim h^{k+1},$$

where the geometric regularity Assumption 5 was realized in the last step.

For the second term, we apply Lemma 25 to each term of the high-order ghost penalty semi-norm, or use Lemma 26 directly, followed by the interpolation estimate

(4.38), namely

$$
\begin{aligned}
|||\mathbf{H}^e-\mathcal{I}_h\mathbf{H}|||_{\mathcal{F}_h^\Gamma}^2 &= \sum_{F\in\mathcal{F}_h^\Gamma}\sum_{j=1}^{k} h^{2j-1}\left\|[\![\partial_{\mathbf{n}_F}^j(\mathbf{H}^e-\mathcal{I}_h\mathbf{H})]\!]\right\|_F^2\\
&\lesssim \sum_{\tilde{T}\in\mathcal{T}_h^\Gamma}\sum_{j=1}^{k} h^{2j-2}\left\|\nabla^j(\mathbf{H}^e-\mathcal{I}_h\mathbf{H})\right\|_{\tilde{T}}^2+h^{2j}\left\|\nabla^{j+1}(\mathbf{H}^e-\mathcal{I}_h\mathbf{H})\right\|_{\tilde{T}}^2\\
&\leq \sum_{\tilde{T}\in\mathcal{T}_h^\Gamma}\sum_{j=1}^{k} h^{2j-2}\|\mathbf{H}^e-\mathcal{I}_h\mathbf{H}\|_{\mathcal{H}^j(\tilde{T})}^2+h^{2j}\|\mathbf{H}^e-\mathcal{I}_h\mathbf{H}\|_{\mathcal{H}^{j+1}(\tilde{T})}^2\\
&\lesssim \sum_{\tilde{T}\in\mathcal{T}_h^\Gamma}\sum_{j=1}^{k} h^{2j-2}h^{2k-2j+2}\|\mathbf{H}^e\|_{\mathcal{H}^{k+1}(\tilde{T})}^2+h^{2j}h^{2k-2j}\|\mathbf{H}^e\|_{\mathcal{H}^{k+1}(\tilde{T})}^2\\
&\lesssim \sum_{\tilde{T}\in\mathcal{T}_h^\Gamma}\sum_{j=1}^{k} h^{2k}\|\mathbf{H}^e\|_{\mathcal{H}^{k+1}(\tilde{T})}^2\lesssim \mathrm{card}(\mathcal{T}_h^\Gamma)\ \mathrm{meas}(\tilde{T})\ h^{2k}\|\mathbf{H}^e\|_{\mathcal{W}_\infty^{k+1}(\tilde{T})}^2\\
&\lesssim h^{2k+1},
\end{aligned}
$$

where in the last step we realized the fact that $\mathrm{card}(\mathcal{T}_h^\Gamma)\simeq h^{1-d}$ and $\mathrm{meas}(\tilde{T})\simeq h^d$ for any $\tilde{T}\in\mathcal{T}_h^\Gamma$, together with the geometric regularity Assumption 5 for $h<\delta<\infty$.

For the third term with the normal stability $\|\mathbf{n}_h\|_{\mathcal{L}^\infty(\mathcal{T}_h^\Gamma)}\lesssim 1$ the interpolation estimate (4.38) gives

$$
\begin{aligned}
|||\mathbf{H}^e-\mathcal{I}_h\mathbf{H}|||_{\mathcal{T}_h^\Gamma}^2 &= \|\nabla(\mathbf{H}^e-\mathcal{I}_h\mathbf{H})\cdot\mathbf{n}_h\|_{\mathcal{T}_h^\Gamma}^2\lesssim\|\mathbf{H}^e-\mathcal{I}_h\mathbf{H}\|_{\mathcal{H}^1(\mathcal{T}_h^\Gamma)}^2\\
&\lesssim h^{2k}\|\mathbf{H}^e\|_{\mathcal{H}^{k+1}(\mathcal{T}_h^\Gamma)}^2\lesssim h^{2k+1}\|\mathbf{H}^e\|_{\mathcal{W}_\infty^{k+1}(\mathcal{T}_h^\Gamma)}^2\lesssim h^{2k+1}
\end{aligned}
$$

where the fact that $\mathrm{meas}(\mathcal{T}_h^\Gamma)\simeq h$ and the geometric regularity Assumption 5 for $h<\delta<\infty$ are employed.

This completes the proof.

□

Corollary 3 ($\mathcal{H}^1$-scale approximation error estimate)**.** *Let* $\mathbf{H}\in[\mathcal{H}^{k+1}(\Gamma)\cap\mathcal{W}_\infty^{k+1}(\Gamma)]^d$ *be the mean curvature vector of the oriented compact hypersurface* $\Gamma\in\mathcal{C}^{k+3}(\mathbb{R}^d), d=2,3$, *which is defined by* (2.16) *and is the weak solution to* (4.15) *under the geometric regularity Assumption 5. For the discrete hypersurface* Γ_h *the interpolation error satisfies*

$$
\|\mathbf{H}^e-\mathcal{I}_h\mathbf{H}\|_{\Gamma_h}+h^{-\frac{1}{2}}|||\mathbf{H}^e-\mathcal{I}_h\mathbf{H}|||_{\mathcal{F}_h^\Gamma}+h^{\frac{1}{2}}|||\mathbf{H}^e-\mathcal{I}_h\mathbf{H}|||_{\mathcal{T}_h^\Gamma}\lesssim h^k,
$$

where $\mathbf{H}^e$ *is the extension of* $\mathbf{H}$ *by Definition 14,* $\mathcal{I}_h$ *is the interpolation operator by Definition 17, and the semi-norms are given by* (4.26).

Proof. The result follows directly by adding an h^{-1} to the ghost penalty semi-norm in Lemma 30.

□

4.2.6 Consistency estimates

In preparation of the a priori error analysis, we estimate the consistency error for both $\mathcal{L}^2$-scale and $\mathcal{H}^1$-scale in the following lemma and corollary. See also the high-order ghost penalty term in (4.25) and Remark 16 for the mesh size scaling.

Lemma 31 ($\mathcal{L}^2$-scale consistency error estimate)**.** *Let* $\mathbf{H}_h \in [\mathcal{V}_h^\Gamma]^d$, $d = 2,3$ *be the discrete mean curvature vector of* k^{th}*-order finite element function on the* q^{th}*-order isoparametrically mapped hypersurface* $\Gamma_h \hookrightarrow \mathbb{R}^d$, $k,q \geq 1$, *defined by* (4.23). *The consistency error of* $\mathbf{H}_h$ *satisfies*

$$\|\mathbf{H}_h - \mathcal{I}_h\mathbf{H}\|_{\Gamma_h} + h^{\frac{1}{2}}|||\mathbf{H}_h - \mathcal{I}_h\mathbf{H}|||_{\mathcal{F}_h^\Gamma} + h^{\frac{1}{2}}|||\mathbf{H}_h - \mathcal{I}_h\mathbf{H}|||_{\mathcal{T}_h^\Gamma} \lesssim h^{k+1} + h^{q-1}$$

where $\mathcal{I}_h$ *is the interpolation operator by Definition 17 and the semi-norms are given by* (4.26).

Proof. Let us first define a discrete bilinear form for $\mathbf{v}_h, \mathbf{w}_h \in [\mathcal{V}_h^\Gamma]^d$ such that

$$A_h(\mathbf{v}_h, \mathbf{w}_h) := B_h(\mathbf{v}_h, \mathbf{w}_h) + S_h(\mathbf{v}_h, \mathbf{w}_h)$$

with the corresponding semi-norm

$$|||\mathbf{v}_h|||_A^2 := A_h(\mathbf{v}_h, \mathbf{v}_h) = \|\mathbf{v}_h\|_{\Gamma_h}^2 + h|||\mathbf{v}_h|||_{\mathcal{F}_h^\Gamma}^2 + h|||\mathbf{v}_h|||_{\mathcal{T}_h^\Gamma}^2.$$

With the identities (4.15) and (4.23) we apply the Cauchy-Schwarz inequality to obtain

$$\begin{aligned}
|||\mathbf{H}_h - \mathcal{I}_h\mathbf{H}|||_A^2 &= A_h(\mathbf{H}_h - \mathcal{I}_h\mathbf{H}, \mathbf{H}_h - \mathcal{I}_h\mathbf{H}) \\
&= A_h(\mathbf{H}_h - \mathbf{H}^e, \mathbf{H}_h - \mathcal{I}_h\mathbf{H}) + A_h(\mathbf{H}^e - \mathcal{I}_h\mathbf{H}, \mathbf{H}_h - \mathcal{I}_h\mathbf{H}) \\
&= A_h(\mathbf{H}_h, \mathbf{H}_h - \mathcal{I}_h\mathbf{H}) - A_h(\mathbf{H}^e, \mathbf{H}_h - \mathcal{I}_h\mathbf{H}) + A_h(\mathbf{H}^e - \mathcal{I}_h\mathbf{H}, \mathbf{H}_h - \mathcal{I}_h\mathbf{H}) \\
&= L_h(\mathbf{H}_h - \mathcal{I}_h\mathbf{H}) - L(\mathbf{H}_h^l - \mathcal{I}_h^l\mathbf{H}) + B(\mathbf{H}, \mathbf{H}_h^l - \mathcal{I}_h^l\mathbf{H}) \\
&\qquad - A_h(\mathbf{H}^e, \mathbf{H}_h - \mathcal{I}_h\mathbf{H}) + A_h(\mathbf{H}^e - \mathcal{I}_h\mathbf{H}, \mathbf{H}_h - \mathcal{I}_h\mathbf{H}) \\
&\lesssim |||\mathbf{H}^e - \mathcal{I}_h\mathbf{H}|||_A |||\mathbf{H}_h - \mathcal{I}_h\mathbf{H}|||_A + \left| L_h(\mathbf{H}_h - \mathcal{I}_h\mathbf{H}) - L(\mathbf{H}_h^l - \mathcal{I}_h^l\mathbf{H}) \right| \\
&\qquad + \left| A_h(\mathbf{H}^e, \mathbf{H}_h - \mathcal{I}_h\mathbf{H}) - B(\mathbf{H}, \mathbf{H}_h^l - \mathcal{I}_h^l\mathbf{H}) \right|.
\end{aligned}$$

Dividing both sides by $|||\mathbf{H}_h - \mathcal{I}_h\mathbf{H}|||_A$ it follows for $\mathbf{w}_h = \mathbf{H}_h - \mathcal{I}_h\mathbf{H}$ that

$$\begin{aligned}
|||\mathbf{H}_h - \mathcal{I}_h\mathbf{H}|||_A \lesssim |||\mathbf{H}^e - \mathcal{I}_h\mathbf{H}|||_A &+ \sup_{\mathbf{w}_h \in [\mathcal{V}_h^\Gamma]^d} \frac{\left| A_h(\mathbf{H}^e, \mathbf{H}_h - \mathcal{I}_h\mathbf{H}) - B(\mathbf{H}, \mathbf{H}_h^l - \mathcal{I}_h^l\mathbf{H}) \right|}{|||\mathbf{H}_h - \mathcal{I}_h\mathbf{H}|||_A} \\
&+ \sup_{\mathbf{w}_h \in [\mathcal{V}_h^\Gamma]^d} \frac{\left| L_h(\mathbf{H}_h - \mathcal{I}_h\mathbf{H}) - L(\mathbf{H}_h^l - \mathcal{I}_h^l\mathbf{H}) \right|}{|||\mathbf{H}_h - \mathcal{I}_h\mathbf{H}|||_A}
\end{aligned}$$

in the form analogously to the first Strang lemma, cf. [151, Theorem 8.2].

The first term is identical to the approximation error estimated by Lemma 30 with the norm equivalence $\|\mathbf{H} - \mathcal{I}_h^l\mathbf{H}\|_\Gamma \simeq \|\mathbf{H}^e - \mathcal{I}_h\mathbf{H}\|_{\Gamma_h}$ by Lemma 20, which gives

$$\mathrm{I} := |||\mathbf{H}^e - \mathcal{I}_h\mathbf{H}|||_A \lesssim h^{k+1}. \tag{4.39}$$

For the second term, we take advantage of the trivial identities $[\![\nabla\mathbf{H}^e \cdot \mathbf{n}_F]\!] = 0$ on $\mathcal{F}_h^\Gamma$ and $\nabla\mathbf{H}^e \cdot \mathbf{n} = 0$ on $\mathcal{T}_h^\Gamma$, with using (4.32) to change domain of integration from Γ

to Γ_h, followed by the Cauchy-Schwarz inequality, yielding

$$\begin{aligned}
\mathrm{II} :&= \left|A_h(\mathbf{H}^e, \mathbf{H}_h - \mathcal{I}_h\mathbf{H}) - B(\mathbf{H}, \mathbf{H}_h^l - \mathcal{I}_h^l\mathbf{H})\right| \\
&= \left|B_h(\mathbf{H}^e, \mathbf{H}_h - \mathcal{I}_h\mathbf{H}) - B(\mathbf{H}, \mathbf{H}_h^l - \mathcal{I}_h^l\mathbf{H}) + S_h(\mathbf{H}^e, \mathbf{H}_h - \mathcal{I}_h\mathbf{H})\right| \\
&= \left|(\mathbf{H}^e, \mathbf{H}_h - \mathcal{I}_h\mathbf{H})_{\Gamma_h} - (\mathbf{H}, \mathbf{H}_h^l - \mathcal{I}_h^l\mathbf{H})_{\Gamma} + \left(\nabla\mathbf{H}^e \cdot \mathbf{n}_h, \nabla(\mathbf{H}_h - \mathcal{I}_h\mathbf{H}) \cdot \mathbf{n}_h\right)_{\mathcal{T}_h^\Gamma}\right| \\
&= \left|\left((1-|M|)\mathbf{H}^e, \mathbf{H}_h - \mathcal{I}_h\mathbf{H}\right)_{\Gamma_h} + \left(\nabla\mathbf{H}^e \cdot (\mathbf{n}_h - \mathbf{n}), \nabla(\mathbf{H}_h - \mathcal{I}_h\mathbf{H}) \cdot \mathbf{n}_h\right)_{\mathcal{T}_h^\Gamma}\right| \\
&\lesssim \left(\|1-|M|\|_{\mathcal{L}^\infty(\Gamma_h)}\|\mathbf{H}^e\|_{\Gamma_h} + \|\mathbf{n}_h - \mathbf{n}\|_{\mathcal{L}^\infty(\mathcal{T}_h^\Gamma)}\|\nabla\mathbf{H}^e\|_{\mathcal{T}_h^\Gamma} h^{-\frac{1}{2}}\right)|||\mathbf{H}_h - \mathcal{I}_h\mathbf{H}|||_A \\
&\lesssim \left(h^{q+1}\|\mathbf{H}^e\|_{\Gamma_h} + h^q\|\mathbf{H}^e\|_{\mathcal{W}^1_\infty(\mathcal{T}_h^\Gamma)}\right)|||\mathbf{H}_h - \mathcal{I}_h\mathbf{H}|||_A \\
&\lesssim h^q|||\mathbf{H}_h - \mathcal{I}_h\mathbf{H}|||_A
\end{aligned}$$

where we made use of the third result in Lemma 22, the second estimate in (4.8), and the geometric regularity Assumption 5 for $h < \delta$.

For the third term, we have with (4.32) to change domain of integration from Γ_h to Γ and the Cauchy-Schwarz inequality that

$$\begin{aligned}
\mathrm{III} :&= \left|L_h(\mathbf{H}_h - \mathcal{I}_h\mathbf{H}) - L(\mathbf{H}_h^l - \mathcal{I}_h^l\mathbf{H})\right| \\
&= \left|\left(\nabla_{\Gamma_h}\mathbf{x}_{\Gamma_h}, \nabla_{\Gamma_h}(\mathbf{H}_h - \mathcal{I}_h\mathbf{H})\right)_{\Gamma_h} - \left(\nabla_\Gamma\mathbf{x}_\Gamma, \nabla_\Gamma(\mathbf{H}_h^l - \mathcal{I}_h^l\mathbf{H})\right)_\Gamma\right| \\
&= \left|\left(|M|^{-1}M^{\mathrm{T}}\nabla_\Gamma\mathbf{x}_{\Gamma_h}^l, M^{\mathrm{T}}\nabla_\Gamma(\mathbf{H}_h^l - \mathcal{I}_h^l\mathbf{H})\right)_\Gamma - \left(\nabla_\Gamma\mathbf{x}_\Gamma, \nabla_\Gamma(\mathbf{H}_h^l - \mathcal{I}_h^l\mathbf{H})\right)_\Gamma\right| \\
&= \left|\left(|M|^{-1}MM^{\mathrm{T}}\nabla_\Gamma\mathbf{x}_{\Gamma_h}^l - \nabla_\Gamma\mathbf{x}_\Gamma, \nabla_\Gamma(\mathbf{H}_h^l - \mathcal{I}_h^l\mathbf{H})\right)_\Gamma\right| \\
&\leq \left\||M|^{-1}MM^{\mathrm{T}}\nabla_\Gamma\mathbf{x}_{\Gamma_h}^l - \nabla_\Gamma\mathbf{x}_\Gamma\right\|_\Gamma \left\|\nabla_\Gamma(\mathbf{H}_h^l - \mathcal{I}_h^l\mathbf{H})\right\|_\Gamma \\
&\lesssim \left\||M|^{-1}MM^{\mathrm{T}}\nabla_\Gamma\mathbf{x}_{\Gamma_h}^l - \nabla_\Gamma\mathbf{x}_\Gamma\right\|_\Gamma \left(h^{-1}\|\mathbf{H}_h - \mathcal{I}_h\mathbf{H}\|_{\Gamma_h} + h^{-\frac{1}{2}}|||\mathbf{H}_h - \mathcal{I}_h\mathbf{H}|||_{\mathcal{T}_h^\Gamma}\right) \\
&\lesssim h^{q-1}|||\mathbf{H}_h - \mathcal{I}_h\mathbf{H}|||_A
\end{aligned}$$

where we applied (4.36) from Lemma 28 to the second last step, and bounded the geometric error by the triangle inequality and the coordinate embedding estimate (4.34) with the norm equivalences by Lemma 20 in the last step, namely,

$$\begin{aligned}
\left\||M|^{-1}MM^{\mathrm{T}}\nabla_\Gamma\mathbf{x}_{\Gamma_h}^l - \nabla_\Gamma\mathbf{x}_\Gamma\right\|_\Gamma &\leq \left\|(|M|^{-1}MM^{\mathrm{T}} - P_\Gamma)\nabla_\Gamma\mathbf{x}_{\Gamma_h}^l\right\|_\Gamma + \left\|\nabla_\Gamma(\mathbf{x}_{\Gamma_h}^l - \mathbf{x}_\Gamma)\right\|_\Gamma \\
&\lesssim \|(|M|^{-1}MM^{\mathrm{T}} - P_\Gamma)\|_{\mathcal{L}^\infty(\Gamma)}\|\nabla_{\Gamma_h}\mathbf{x}_{\Gamma_h}\|_{\Gamma_h} + \|\nabla_{\Gamma_h}(\mathbf{x}_{\Gamma_h} - \mathbf{x}_\Gamma^e)\|_{\Gamma_h} \\
&\lesssim h^{q+1}\left(\|\nabla_{\Gamma_h}(\mathbf{x}_{\Gamma_h} - \mathbf{x}_\Gamma^e)\|_{\Gamma_h} + \|\nabla_\Gamma\mathbf{x}_\Gamma\|_\Gamma\right) + h^q \\
&\lesssim h^{q+1}(h^q + 1) + h^q \lesssim h^q.
\end{aligned}$$

We notice that this $\mathcal{O}(h^q)$ error is one order larger than what we expected.

Collecting all three terms together, we arrive at

$$|||\mathbf{H}_h - \mathcal{I}_h\mathbf{H}|||_A \lesssim \mathrm{I} + (\mathrm{II} + \mathrm{III})\ |||\mathbf{H}_h - \mathcal{I}_h\mathbf{H}|||_A^{-1} \lesssim h^{k+1} + h^{q-1}.$$

This completes the proof.

□

Corollary 4 ($\mathcal{H}^1$-scale consistency error estimate)**.** *Let $\mathbf{H}_h \in [\mathcal{V}_h^\Gamma]^d$, $d = 2,3$ be the discrete mean curvature vector of k^{th}-order finite element function on the q^{th}-order isoparametrically mapped hypersurface $\Gamma_h \hookrightarrow \mathbb{R}^d$, $k, q \geq 1$, defined by (4.23). The consistency error of $\mathbf{H}_h$ satisfies*

$$\|\mathbf{H}_h - \mathcal{I}_h\mathbf{H}\|_{\Gamma_h} + h^{-\frac{1}{2}}|||\mathbf{H}_h - \mathcal{I}_h\mathbf{H}|||_{\mathcal{F}_h^\Gamma} + h^{\frac{1}{2}}|||\mathbf{H}_h - \mathcal{I}_h\mathbf{H}|||_{\mathcal{T}_h^\Gamma} \lesssim h^k + h^{q-1}$$

where $\mathcal{I}_h$ is the interpolation operator by Definition 17 and the semi-norms are given by (4.26).

Proof. The result follows directly when Corollary 3 is applied to the first term I with the corresponding norm $|||\cdot|||_A$ in (4.39).

□

Remark 18 (Coordinate embedding error)**.** *We observe that in the third term* III *in the proof of Lemma 31, the coordinate embedding estimate induces a considerable error $\mathcal{O}(h^q)$, which eventually leads to an $\mathcal{O}(h^{q-1})$ convergence one order lower than our expectation of $\mathcal{O}(h^q)$.*

4.2.7 Stability analysis

In this subsection, we formulate a stability estimate for the discrete mean curvature vector.

Theorem 8 (Stability of the discrete mean curvature vector)**.** *The discrete mean curvature vector $\mathbf{H}_h \in [\mathcal{V}_h^\Gamma]^d$, $d = 2,3$ of k^{th}-order finite element function on the q^{th}-order isoparametrically mapped hypersurface $\Gamma_h \hookrightarrow \mathbb{R}^d$, $k, q \geq 1$, defined by (4.23), satisfies*

$$\|\mathbf{H}_h\|_{\Gamma_h}^2 + h^\lambda|||\mathbf{H}_h|||_{\mathcal{F}_h^\Gamma}^2 + h|||\mathbf{H}_h|||_{\mathcal{T}_h^\Gamma}^2 \lesssim 1$$

for the mesh size $h \in \mathbb{R}_+$ and the scaling $\lambda \in \mathbb{R}$.

Proof. By testing (4.23) with $\mathbf{v}_h = \mathbf{H}_h$ and using the triangle inequality it follows

$$\begin{aligned}\|\mathbf{H}_h\|^2_{\Gamma_h} + h^\lambda |||\mathbf{H}_h|||^2_{\mathcal{F}_h^\Gamma} + h|||\mathbf{H}_h|||^2_{\mathcal{T}_h^\Gamma} &= (\nabla_{\Gamma_h}\mathbf{x}, \nabla_{\Gamma_h}\mathbf{H}_h)_{\Gamma_h} \\ &\leq \left(\nabla_{\Gamma_h}(\mathbf{x}-\mathbf{x}^e_\Gamma), \nabla_{\Gamma_h}\mathbf{H}_h\right)_{\Gamma_h} + \left(\nabla_{\Gamma_h}\mathbf{x}^e_\Gamma, \nabla_{\Gamma_h}\mathbf{H}_h\right)_{\Gamma_h}.\end{aligned}$$

The first term on the right-hand side can be estimated by using the Cauchy-Schwarz and the Young's inequality for any $\varepsilon \in \mathbb{R}_+$, followed by Lemma 23 for discrete embedding error and Lemma 28 for the gradient of mean curvature

$$\begin{aligned}\left|\left(\nabla_{\Gamma_h}(\mathbf{x}-\mathbf{x}^e_\Gamma), \nabla_{\Gamma_h}\mathbf{H}_h\right)_{\Gamma_h}\right| &\leq \|\nabla_{\Gamma_h}(\mathbf{x}-\mathbf{x}^e_\Gamma)\|_{\Gamma_h}\|\nabla_{\Gamma_h}\mathbf{H}_h\|_{\Gamma_h} \\ &\lesssim \varepsilon^{-1}h^{-2}\|\nabla_{\Gamma_h}(\mathbf{x}-\mathbf{x}^e_\Gamma)\|^2_{\Gamma_h} + \varepsilon h^2\|\nabla_{\Gamma_h}\mathbf{H}_h\|^2_{\Gamma_h} \\ &\lesssim \varepsilon^{-1}h^{2q-2} + \varepsilon\left(\|\mathbf{H}_h\|^2_{\Gamma_h} + h|||\mathbf{H}_h|||^2_{\mathcal{T}_h^\Gamma}\right).\end{aligned}$$

For the second term, we take integration by parts first, and then apply the Cauchy-Schwarz and the Young's inequalities for any $\varepsilon \in \mathbb{R}_+$, with Lemma 20 for norm equivalences, yielding

$$\begin{aligned}\left|\left(\nabla_{\Gamma_h}\mathbf{x}^e_\Gamma, \nabla_{\Gamma_h}\mathbf{H}_h\right)_{\Gamma_h}\right| &= \left|\sum_{G\in\mathcal{G}_h}\left(\nabla_{\Gamma_h}\mathbf{x}^e_\Gamma, \nabla_{\Gamma_h}\mathbf{H}_h\right)_G\right| \\ &= \left|\sum_{E\in\mathcal{E}_h}\left([\![\nabla_{\Gamma_h}\mathbf{x}^e_\Gamma\cdot\mathbf{n}_E]\!], \mathbf{H}_h\right)_E - \sum_{G\in\mathcal{G}_h}\left(\Delta_{\Gamma_h}\mathbf{x}^e_\Gamma, \mathbf{H}_h\right)_G\right| \\ &\leq \sum_{E\in\mathcal{E}_h}\|[\![\nabla_{\Gamma_h}\mathbf{x}^e_\Gamma\cdot\mathbf{n}_E]\!]\|_E\|\mathbf{H}_h\|_E + \|\Delta_{\Gamma_h}\mathbf{x}^e_\Gamma\|_{\Gamma_h}\|\mathbf{H}_h\|_{\Gamma_h} \\ &\lesssim \varepsilon^{-1}h^{-2}|||\mathbf{x}^e_\Gamma|||^2_{\mathcal{E}_h} + \varepsilon h\sum_{E\in\mathcal{E}_h}\|\mathbf{H}_h\|^2_E + \varepsilon^{-1}\|\Delta_\Gamma\mathbf{x}_\Gamma\|^2_\Gamma + \varepsilon\|\mathbf{H}_h\|^2_{\Gamma_h},\end{aligned}$$

where for the first part Lemma 24 for edge stability gives

$$|||\mathbf{x}^e_\Gamma|||^2_{\mathcal{E}_h} \lesssim h^{2q}\|\mathbf{x}_\Gamma\|_{\mathcal{W}^1_\infty(\Gamma)} \lesssim h^{2q},$$

and for the second part the trace inequalities $\|\mathbf{H}_h\|^2_E \lesssim h^{-1}\|\mathbf{H}_h\|^2_{F(E)} \lesssim h^{-2}\|\mathbf{H}_h\|^2_{T(F)}$ yields

$$h\sum_{E\in\mathcal{E}_h}\|\mathbf{H}_h\|^2_E \lesssim h^{-1}\sum_{T\in\mathcal{T}_h^\Gamma}\|\mathbf{H}_h\|^2_T = h^{-1}\|\mathbf{H}_h\|^2_{\mathcal{T}_h^\Gamma} \lesssim \|\mathbf{H}_h\|^2_{\Gamma_h} + h|||\mathbf{H}_h|||^2_{\mathcal{T}_h^\Gamma},$$

where Lemma 27 was applied to the last step. Together with the remainder estimated by using (2.16) and $\mathbf{H} \in \mathcal{L}^2(\Gamma)$ that

$$\varepsilon^{-1}\|\Delta_\Gamma \mathbf{x}_\Gamma\|_\Gamma^2 + \varepsilon\|\mathbf{H}_h\|_{\Gamma_h}^2 = \varepsilon^{-1}\|\mathbf{H}\|_\Gamma^2 + \varepsilon\|\mathbf{H}_h\|_{\Gamma_h}^2 \lesssim \varepsilon^{-1} + \varepsilon\|\mathbf{H}_h\|_{\Gamma_h}^2,$$

we collect all the terms and make use of the kickback argument for a sufficiently small $0 < \varepsilon \lesssim 1$ to obtain

$$\|\mathbf{H}_h\|_{\Gamma_h}^2 + h^\lambda |||\mathbf{H}_h|||_{\mathcal{F}_h^\Gamma}^2 + h|||\mathbf{H}_h|||_{\mathcal{T}_h^\Gamma}^2 \lesssim \varepsilon^{-1} + \varepsilon^{-1}h^{2q-2} + \varepsilon\Big(\|\mathbf{H}_h\|_{\Gamma_h}^2 + h|||\mathbf{H}_h|||_{\mathcal{T}_h^\Gamma}^2\Big).$$

This completes the proof.

□

Remark 19 (Normal diffusion stability)**.** *The Theorem 8 implies that the discrete mean curvature vector is stable with the normal diffusion stabilization only, in which the ghost penalty is not present on the right-hand side. We will however observe that for higher order of accuracy the ghost penalty stabilization is required.*

4.2.8 A priori error estimate

In this subsection, we first collect the results from the approximation error estimate in Subsection 4.2.5 and the consistency error estimate in Subsection 4.2.6, in order to conduct the a priori error analysis of the discrete mean curvature vector of the isoparametrically mapped hypersurface. This result has provable arbitrarily high order of accuracy, however, it seems not optimal in comparison to the low-order result proved by Hansbo et al. in [82, Theorem 4.2]. Therefore, we subsequently follow the similar lines in [82, Theorem 4.1] to present an alternative proof and investigate the problem.

Theorem 9 (Error estimate of the discrete mean curvature vector)**.** *Let* $\mathbf{H} \in [\mathcal{H}^{k+1}(\Gamma) \cap \mathcal{W}_\infty^{k+1}(\Gamma)]^d$ *be the mean curvature vector of the oriented compact hypersurface* $\Gamma \in \mathcal{C}^{k+3}(\mathbb{R}^d), d = 2,3$*, which is defined by* (2.16) *and is the weak solution to* (4.15) *under the geometric regularity Assumption 5. Let* $\mathbf{H}_h \in [\mathcal{V}_h^\Gamma]^d$ *be the discrete mean curvature vector of* k^{th}*-order finite element function on the* q^{th}*-order isoparametrically mapped hypersurface* $\Gamma_h \hookrightarrow \mathbb{R}^d$*, defined by* (4.23) *with* $\mathcal{L}^2$*-scale* $\lambda = 1$ *in* (4.25)*. For any* $k, q \geq 1$ *the following error estimate holds true:*

$$\|\mathbf{H} - \mathbf{H}_h^l\|_\Gamma^2 + h|||\mathbf{H}^e - \mathbf{H}_h|||_{\mathcal{F}_h^\Gamma}^2 + h|||\mathbf{H}^e - \mathbf{H}_h|||_{\mathcal{T}_h^\Gamma}^2 \lesssim h^{2k+2} + h^{2q-2}.$$

Alternatively, if $\mathcal{H}^1$-scale $\lambda = -1$ is chosen in (4.25), it satisfies the estimate

$$\|\mathbf{H} - \mathbf{H}_h^l\|_\Gamma^2 + h^{-1}|||\mathbf{H}^e - \mathbf{H}_h|||_{\mathcal{F}_h^\Gamma}^2 + h|||\mathbf{H}^e - \mathbf{H}_h|||_{\mathcal{T}_h^\Gamma}^2 \lesssim h^{2k} + h^{2q-2}$$

for any $k, q \geq 1$.

Proof. Let us estimate each term on the left-hand side. By the triangle inequality for error splitting one has

$$|||\mathbf{H}^e - \mathbf{H}_h|||_{\mathcal{F}_h^\Gamma} \leq |||\mathbf{H}^e - \mathcal{I}_h\mathbf{H}|||_{\mathcal{F}_h^\Gamma} + |||\mathcal{I}_h\mathbf{H} - \mathbf{H}_h|||_{\mathcal{F}_h^\Gamma},$$
$$|||\mathbf{H}^e - \mathbf{H}_h|||_{\mathcal{T}_h^\Gamma} \leq |||\mathbf{H}^e - \mathcal{I}_h\mathbf{H}|||_{\mathcal{T}_h^\Gamma} + |||\mathcal{I}_h\mathbf{H} - \mathbf{H}_h|||_{\mathcal{T}_h^\Gamma},$$

and with the norm equivalences due to Lemma 20 it follows that

$$\|\mathbf{H} - \mathbf{H}_h^l\|_\Gamma \leq \|\mathbf{H} - \mathcal{I}_h^l\mathbf{H}\|_\Gamma + \|\mathcal{I}_h^l\mathbf{H} - \mathbf{H}_h^l\|_\Gamma \simeq \|\mathbf{H}^e - \mathcal{I}_h\mathbf{H}\|_{\Gamma_h} + \|\mathcal{I}_h\mathbf{H} - \mathbf{H}_h\|_{\Gamma_h}.$$

The Lemma 30 for approximation error gives

$$\|\mathbf{H}^e - \mathcal{I}_h\mathbf{H}\|_{\Gamma_h} + h^{\frac{1}{2}}|||\mathbf{H}^e - \mathcal{I}_h\mathbf{H}|||_{\mathcal{F}_h^\Gamma} + h^{\frac{1}{2}}|||\mathbf{H}^e - \mathcal{I}_h\mathbf{H}|||_{\mathcal{T}_h^\Gamma} \lesssim h^{k+1}.$$

The Lemma 31 for consistency error yields

$$\|\mathbf{H}_h - \mathcal{I}_h\mathbf{H}\|_{\Gamma_h} + h^{\frac{1}{2}}|||\mathbf{H}_h - \mathcal{I}_h\mathbf{H}|||_{\mathcal{F}_h^\Gamma} + h^{\frac{1}{2}}|||\mathbf{H}_h - \mathcal{I}_h\mathbf{H}|||_{\mathcal{T}_h^\Gamma} \lesssim h^{k+1} + h^{q-1}.$$

Summing up with using the Young's inequality leads to the first result. The second result follows directly by taking Corollary 3 and Corollary 4 instead of Lemma 30 and Lemma 31. This completes the proof.

□

This result shows arbitrarily high order of accuracy, however, it is not reduced to the result of the linearized case in [82, Theorem 4.1] when we choose $k = 1$ and $q = 1$. The geometrical error $\mathcal{O}(h^{q-1})$ is one order larger than our expectation. Towards an optimal order of convergence, next, we follow the similar lines in the proof by Hansbo et al. in [82, Theorem 4.1] but to pursue an arbitrarily high order of accuracy based on increasing the polynomial degrees of the finite element discretization and the isoparametric mapping.

Alternative proof. We begin with an error splitting into the following four terms:

$$
\begin{aligned}
&\|\mathbf{H}-\mathbf{H}_h^l\|_\Gamma^2 + h|||\mathbf{H}^e-\mathbf{H}_h|||_{\mathcal{F}_h^\Gamma}^2 + h|||\mathbf{H}^e-\mathbf{H}_h|||_{\mathcal{T}_h^\Gamma}^2 \\
&= B(\mathbf{H}-\mathbf{H}_h^l, \mathbf{H}-\mathbf{H}_h^l) + S_h(\mathbf{H}^e-\mathbf{H}_h, \mathbf{H}^e-\mathbf{H}_h) \\
&= B(\mathbf{H}-\mathbf{H}_h^l, \mathbf{H}-\mathcal{I}_h^l\mathbf{H}) + B(\mathbf{H}-\mathbf{H}_h^l, \mathcal{I}_h^l\mathbf{H}-\mathbf{H}_h^l) + S_h(\mathbf{H}^e-\mathbf{H}_h, \mathbf{H}^e-\mathbf{H}_h) \\
&= B(\mathbf{H}-\mathbf{H}_h^l, \mathbf{H}-\mathcal{I}_h^l\mathbf{H}) + L(\mathcal{I}_h^l\mathbf{H}-\mathbf{H}_h^l) - B(\mathbf{H}_h^l, \mathcal{I}_h^l\mathbf{H}-\mathbf{H}_h^l) + S_h(\mathbf{H}^e-\mathbf{H}_h, \mathbf{H}^e-\mathbf{H}_h) \\
&= \overbrace{B(\mathbf{H}-\mathbf{H}_h^l, \mathbf{H}-\mathcal{I}_h^l\mathbf{H})}^{\mathrm{I}} + \overbrace{B_h(\mathbf{H}_h, \mathcal{I}_h\mathbf{H}-\mathbf{H}_h) - B(\mathbf{H}_h^l, \mathcal{I}_h^l\mathbf{H}-\mathbf{H}_h^l)}^{\mathrm{II}} \\
&\quad + \underbrace{S_h(\mathbf{H}_h, \mathcal{I}_h\mathbf{H}-\mathbf{H}_h) + S_h(\mathbf{H}^e-\mathbf{H}_h, \mathbf{H}^e-\mathbf{H}_h)}_{\mathrm{III}} + \underbrace{L(\mathcal{I}_h^l\mathbf{H}-\mathbf{H}_h^l) - L_h(\mathcal{I}_h\mathbf{H}-\mathbf{H}_h)}_{\mathrm{IV}}
\end{aligned}
$$

where we used the identities $B(\mathbf{H}, \mathcal{I}_h^l\mathbf{H}-\mathbf{H}_h^l) = L(\mathcal{I}_h^l\mathbf{H}-\mathbf{H}_h^l)$ and $B_h(\mathbf{H}_h, \mathcal{I}_h\mathbf{H}-\mathbf{H}_h) + S_h(\mathbf{H}_h, \mathcal{I}_h\mathbf{H}-\mathbf{H}_h) = L_h(\mathcal{I}_h\mathbf{H}-\mathbf{H}_h)$. Let us look into each terms.

Term I:

Term I is estimated by using the Cauchy-Schwarz and the Young's inequality for any $\varepsilon \in \mathbb{R}_+$ as follows:

$$
\begin{aligned}
|\mathrm{I}| := \left|B(\mathbf{H}-\mathbf{H}_h^l, \mathbf{H}-\mathcal{I}_h^l\mathbf{H})\right| &\le \|\mathbf{H}-\mathbf{H}_h^l\|_\Gamma \|\mathbf{H}-\mathcal{I}_h^l\mathbf{H}\|_\Gamma \\
&\lesssim \varepsilon\|\mathbf{H}-\mathbf{H}_h^l\|_\Gamma^2 + \varepsilon^{-1}\|\mathbf{H}-\mathcal{I}_h^l\mathbf{H}\|_\Gamma^2 \lesssim \varepsilon\|\mathbf{H}-\mathbf{H}_h^l\|_\Gamma^2 + \varepsilon^{-1}h^{2k+2}\|\mathbf{H}\|_{\mathcal{H}^{k+1}(\Gamma)}^2 \\
&\lesssim \varepsilon^{-1}h^{2k+2} + \varepsilon\|\mathbf{H}-\mathbf{H}_h^l\|_\Gamma^2, \qquad (4.40)
\end{aligned}
$$

where we bound the last term by the interpolation estimate from Lemma 29 with the geometric regularity Assumption 5.

Term II:

Term II is estimated with using (4.32) to change domain of integration from Γ to Γ_h, followed by the Cauchy-Schwarz and the Young's inequalities for any $\varepsilon \in \mathbb{R}_+$, as

follows:

$$
\begin{aligned}
|\mathrm{II}| :&= \left|B_h(\mathbf{H}_h, \mathcal{I}_h\mathbf{H} - \mathbf{H}_h) - B(\mathbf{H}_h^l, \mathcal{I}_h^l\mathbf{H} - \mathbf{H}_h^l)\right| \\
&= \left|\left(\mathbf{H}_h, \mathcal{I}_h\mathbf{H} - \mathbf{H}_h\right)_{\Gamma_h} - \left(\mathbf{H}_h^l, \mathcal{I}_h^l\mathbf{H} - \mathbf{H}_h^l\right)_{\Gamma}\right| \\
&= \left|\left((1-|M|)\mathbf{H}_h, \mathcal{I}_h\mathbf{H} - \mathbf{H}_h\right)_{\Gamma_h}\right| \leq \|1-|M|\|_{\mathcal{L}^\infty(\Gamma_h)}\|\mathbf{H}_h\|_{\Gamma_h}\|\mathcal{I}_h\mathbf{H} - \mathbf{H}_h\|_{\Gamma_h} \\
&\lesssim \varepsilon^{-1}\|1-|M|\|^2_{\mathcal{L}^\infty(\Gamma_h)}\|\mathbf{H}_h\|^2_{\Gamma_h} + \varepsilon\|\mathcal{I}_h\mathbf{H} - \mathbf{H}_h\|^2_{\Gamma_h} \\
&\lesssim \varepsilon^{-1}h^{2q+2}\|\mathbf{H}_h\|^2_{\Gamma_h} + \varepsilon\|\mathbf{H} - \mathcal{I}_h^l\mathbf{H}\|^2_{\Gamma} + \varepsilon\|\mathbf{H} - \mathbf{H}_h^l\|^2_{\Gamma} \\
&\lesssim \varepsilon^{-1}h^{2q+2} + \varepsilon h^{2k+2}\|\mathbf{H}\|^2_{\mathcal{H}^{k+1}(\Gamma)} + \varepsilon\|\mathbf{H} - \mathbf{H}_h^l\|^2_{\Gamma} \\
&\lesssim \varepsilon h^{2k+2} + \varepsilon^{-1}h^{2q+2} + \varepsilon\|\mathbf{H} - \mathbf{H}_h^l\|^2_{\Gamma},
\end{aligned} \tag{4.41}
$$

where we made use of the third result in Lemma 22 to bound the $|M|$ term, Theorem 8 for the stability of $\mathbf{H}_h$, the norm equivalence due to Lemma 20, and the interpolation estimate from Lemma 29 with the geometric regularity Assumption 5.

Term III:

Term III is related to the stabilizations. Provided that a semi-norm for S_h involving both ghost penalty and normal diffusion is defined for $\mathbf{v}_h \in \mathcal{V}_h^\Gamma$ such that

$$
|||\mathbf{v}_h|||_S^2 := S_h(\mathbf{v}_h, \mathbf{v}_h) = h|||\mathbf{v}_h|||^2_{\mathcal{F}_h^\Gamma} + h|||\mathbf{v}_h|||^2_{\mathcal{T}_h^\Gamma}, \tag{4.42}
$$

we make use of the Cauchy-Schwarz and the Young's inequalities for any $\varepsilon \in \mathbb{R}_+$ to obtain

$$
\begin{aligned}
|\mathrm{III}| :&= \left|S_h(\mathbf{H}_h, \mathcal{I}_h\mathbf{H} - \mathbf{H}_h) + S_h(\mathbf{H}^e - \mathbf{H}_h, \mathbf{H}^e - \mathbf{H}_h)\right| \\
&= \left|S_h(\mathbf{H}_h, \mathcal{I}_h\mathbf{H} - \mathbf{H}^e) + S_h(\mathbf{H}_h, \mathbf{H}^e - \mathbf{H}_h) + S_h(\mathbf{H}^e, \mathbf{H}^e - \mathbf{H}_h) - S_h(\mathbf{H}_h, \mathbf{H}^e - \mathbf{H}_h)\right| \\
&= \left|S_h(\mathbf{H}_h - \mathbf{H}^e, \mathcal{I}_h\mathbf{H} - \mathbf{H}^e) + S_h(\mathbf{H}^e, \mathcal{I}_h\mathbf{H} - \mathbf{H}^e) + S_h(\mathbf{H}^e, \mathbf{H}^e - \mathbf{H}_h)\right| \\
&\leq |||\mathbf{H}_h - \mathbf{H}^e|||_S|||\mathcal{I}_h\mathbf{H} - \mathbf{H}^e|||_S + |||\mathbf{H}^e|||_S|||\mathcal{I}_h\mathbf{H} - \mathbf{H}^e|||_S + |||\mathbf{H}^e|||_S|||\mathbf{H}^e - \mathbf{H}_h|||_S \\
&\lesssim \varepsilon^{-1}|||\mathbf{H}^e|||^2_S + |||\mathcal{I}_h\mathbf{H} - \mathbf{H}^e|||^2_S + \varepsilon|||\mathbf{H}^e - \mathbf{H}_h|||^2_S.
\end{aligned}
$$

Now let us estimate each terms above. For the first term with the trivial identities $[\![\nabla \mathbf{H}^e \cdot \mathbf{n}_F]\!] = 0$ on $\mathcal{F}_h^\Gamma$ and $\nabla \mathbf{H}^e \cdot \mathbf{n} = 0$ on $\mathcal{T}_h^\Gamma$ it follows that

$$\begin{aligned}
|||\mathbf{H}^e|||_S^2 &= h|||\mathbf{H}^e|||_{\mathcal{F}_h^\Gamma}^2 + h|||\mathbf{H}^e|||_{\mathcal{T}_h^\Gamma}^2 = h|||\mathbf{H}^e|||_{\mathcal{T}_h^\Gamma}^2 = \|\nabla \mathbf{H}^e \cdot (\mathbf{n}_h - \mathbf{n})\|_{\mathcal{T}_h^\Gamma}^2 \\
&\leq \|\mathbf{n}_h - \mathbf{n}\|_{\mathcal{L}^\infty(\mathcal{T}_h^\Gamma)}^2 \|\nabla \mathbf{H}^e\|_{\mathcal{T}_h^\Gamma}^2 \lesssim h^{2q} \|\mathbf{H}^e\|_{\mathcal{H}^1(\mathcal{T}_h^\Gamma)}^2 \lesssim h^{2q+1} \|\mathbf{H}^e\|_{\mathcal{W}_\infty^1(\mathcal{T}_h^\Gamma)}^2 \lesssim h^{2q+1},
\end{aligned}$$

where we utilized the second estimate in (4.8), $\mathrm{meas}(\mathcal{T}_h^\Gamma) \simeq h$, and the geometric regularity Assumption 5 for $h < \delta$. The second term is composed of the interpolation errors in the semi-norms of ghost penaly and normal diffusion. With using Lemma 30 for approximation error estimate it follows directly that

$$|||\mathcal{I}_h \mathbf{H} - \mathbf{H}^e|||_S^2 = h|||\mathcal{I}_h \mathbf{H} - \mathbf{H}^e|||_{\mathcal{F}_h^\Gamma}^2 + h|||\mathcal{I}_h \mathbf{H} - \mathbf{H}^e|||_{\mathcal{T}_h^\Gamma}^2 \lesssim h^{2k+2}. \tag{4.43}$$

Hence, with adding the third term, one has for any $\varepsilon \in \mathbb{R}_+$ that

$$|\mathrm{III}| \lesssim h^{2k+2} + \varepsilon^{-1} h^{2q+1} + \varepsilon \Big(h|||\mathbf{H}^e - \mathbf{H}_h|||_{\mathcal{F}_h^\Gamma}^2 + h|||\mathbf{H}^e - \mathbf{H}_h|||_{\mathcal{T}_h^\Gamma}^2 \Big). \tag{4.44}$$

Term IV:

Term IV can be further split into two parts as follows:

$$\begin{aligned}
\mathrm{IV} :&= L(\mathcal{I}_h^l \mathbf{H} - \mathbf{H}_h^l) - L_h(\mathcal{I}_h \mathbf{H} - \mathbf{H}_h) \\
&= \underbrace{L(\mathcal{I}_h^l \mathbf{H} - \mathbf{H}) - L_h(\mathcal{I}_h \mathbf{H} - \mathbf{H}^e)}_{\mathrm{IV}_1} + \underbrace{L(\mathbf{H} - \mathbf{H}_h^l) - L_h(\mathbf{H}^e - \mathbf{H}_h)}_{\mathrm{IV}_2}.
\end{aligned}$$

The first part IV_1 is bounded by changing domain of integration from Γ_h to Γ with surface measure (4.32), followed by the Cauchy-Schwarz and the Young's inequality

$$\begin{aligned}
\mathrm{IV}_1 &= \Big(\nabla_\Gamma \mathbf{x}_\Gamma, \nabla_\Gamma (\mathcal{I}_h^l \mathbf{H} - \mathbf{H}) \Big)_\Gamma - \Big(\nabla_{\Gamma_h} \mathbf{x}_{\Gamma_h}, \nabla_{\Gamma_h} (\mathcal{I}_h \mathbf{H} - \mathbf{H}^e) \Big)_{\Gamma_h} \\
&= \Big(\nabla_\Gamma \mathbf{x}_\Gamma, \nabla_\Gamma (\mathcal{I}_h^l \mathbf{H} - \mathbf{H}) \Big)_\Gamma - \Big(|M|^{-1} M^{\mathrm{T}} \nabla_\Gamma \mathbf{x}_{\Gamma_h}^l, M^{\mathrm{T}} \nabla_\Gamma (\mathcal{I}_h^l \mathbf{H} - \mathbf{H}) \Big)_\Gamma \\
&= \Big(\nabla_\Gamma \mathbf{x}_\Gamma - |M|^{-1} M M^{\mathrm{T}} \nabla_\Gamma \mathbf{x}_{\Gamma_h}^l, \nabla_\Gamma (\mathcal{I}_h^l \mathbf{H} - \mathbf{H}) \Big)_\Gamma \\
&\leq \Big\| \nabla_\Gamma \mathbf{x}_\Gamma - |M|^{-1} M M^{\mathrm{T}} \nabla_\Gamma \mathbf{x}_{\Gamma_h}^l \Big\|_\Gamma \Big\| \nabla_\Gamma (\mathcal{I}_h^l \mathbf{H} - \mathbf{H}) \Big\|_\Gamma \\
&\leq h^{-2} \Big\| \nabla_\Gamma \mathbf{x}_\Gamma - |M|^{-1} M M^{\mathrm{T}} \nabla_\Gamma \mathbf{x}_{\Gamma_h}^l \Big\|_\Gamma^2 + h^2 \Big\| \nabla_\Gamma (\mathcal{I}_h^l \mathbf{H} - \mathbf{H}) \Big\|_\Gamma^2,
\end{aligned} \tag{4.45}$$

where for the first norm we use the triangle inequality combined with the Young's inequality, and the norm equivalence due to Lemma 20 to estimate the coordinate

embedding error by (4.34) in Lemma 23 for the first part

$$\begin{aligned}\left\|\nabla_\Gamma \mathbf{x}_\Gamma - |M|^{-1}MM^{\mathrm{T}}\nabla_\Gamma \mathbf{x}^l_{\Gamma_h}\right\|^2_\Gamma &\lesssim \left\|\nabla_\Gamma(\mathbf{x}_\Gamma - \mathbf{x}^l_{\Gamma_h})\right\|^2_\Gamma + \left\|(P_\Gamma - |M|^{-1}MM^{\mathrm{T}})\nabla_\Gamma \mathbf{x}^l_{\Gamma_h}\right\|^2_\Gamma \\ &\lesssim \underbrace{\left\|\nabla_{\Gamma_h}(\mathbf{x}^e_\Gamma - \mathbf{x}_{\Gamma_h})\right\|^2_{\Gamma_h}}_{\lesssim h^{2q}} + \underbrace{\left\|P_\Gamma - |M|^{-1}MM^{\mathrm{T}}\right\|^2_{\mathcal{L}^\infty(\Gamma)}}_{\lesssim h^{2q+2}}\end{aligned}$$

and the second part followed by applying the tangent mapping estimates from Lemma 21 and Lemma 22

$$\begin{aligned}\left\|P_\Gamma - |M|^{-1}MM^{\mathrm{T}}\right\|_{\mathcal{L}^\infty(\Gamma)} &\leq \left\||M|^{-1}(1-|M|)P_\Gamma\right\|_{\mathcal{L}^\infty(\Gamma)} + \left\||M|^{-1}(P_\Gamma - MM^{\mathrm{T}})\right\|_{\mathcal{L}^\infty(\Gamma)} \\ &\lesssim h^{q+1} + h^{q+1} \lesssim h^{q+1} \end{aligned} \tag{4.46}$$

and realizing the last term again by the norm equivalences due to Lemma 20

$$\|\nabla_\Gamma \mathbf{x}^l_{\Gamma_h}\|_\Gamma \lesssim \|\nabla_{\Gamma_h}(\mathbf{x}_{\Gamma_h} - \mathbf{x}^e_\Gamma)\|_{\Gamma_h} + \|\nabla_\Gamma \mathbf{x}_\Gamma\|_\Gamma \lesssim h^q + 1 \lesssim 1.$$

The second norm is also handled with the interpolation estimate and the geometric regularity Assumption 5 as follows:

$$\left\|\nabla_\Gamma(\mathcal{I}^l_h\mathbf{H} - \mathbf{H})\right\|_\Gamma \leq \|\mathcal{I}^l_h\mathbf{H} - \mathbf{H}\|_{\mathcal{H}^1(\Gamma)} \lesssim h^k \|\mathbf{H}\|_{\mathcal{H}^{k+1}(\Gamma)} \lesssim h^k. \tag{4.47}$$

Hence we arrive at

$$\mathrm{IV}_1 \lesssim h^{2k+2} + h^{2q-2}. \tag{4.48}$$

The second part IV_2 is further split into two parts, where the first part (4.49) can be treated analogously to the part IV_1 (4.45), but now $\mathbf{x}_{\Gamma_h}$ is replaced by $\mathbf{x}^e_\Gamma$ that eliminates the coordinate embedding error, hence only the geometric approximation error (4.46) is left, and $\mathcal{I}^l_h\mathbf{H}$ is replaced by $\mathbf{H}^l_h$, with the Young's inequality for any $\varepsilon \in \mathbb{R}_+$, yielding

$$\begin{aligned}\mathrm{IV}_2 &= \left(\nabla_\Gamma \mathbf{x}_\Gamma, \nabla_\Gamma(\mathbf{H} - \mathbf{H}^l_h)\right)_\Gamma - \left(\nabla_{\Gamma_h}\mathbf{x}_{\Gamma_h}, \nabla_{\Gamma_h}(\mathbf{H}^e - \mathbf{H}_h)\right)_{\Gamma_h} \\ &= \left(\nabla_\Gamma \mathbf{x}_\Gamma, \nabla_\Gamma(\mathbf{H} - \mathbf{H}^l_h)\right)_\Gamma - \left(\nabla_{\Gamma_h}\mathbf{x}^e_\Gamma, \nabla_{\Gamma_h}(\mathbf{H}^e - \mathbf{H}_h)\right)_{\Gamma_h} && (4.49) \\ &\quad + \left(\nabla_{\Gamma_h}(\mathbf{x}^e_\Gamma - \mathbf{x}_{\Gamma_h}), \nabla_{\Gamma_h}(\mathbf{H}^e - \mathbf{H}_h)\right)_{\Gamma_h} && (4.50) \\ &\lesssim \varepsilon^{-1}h^{2q} + \varepsilon h^2 \left\|\nabla_\Gamma(\mathbf{H} - \mathbf{H}^l_h)\right\|^2_\Gamma + \left\|\nabla_{\Gamma_h}(\mathbf{x}^e_\Gamma - \mathbf{x}_{\Gamma_h})\right\|_{\Gamma_h} \left\|\nabla_{\Gamma_h}(\mathbf{H}^e - \mathbf{H}_h)\right\|_{\Gamma_h} \\ &\lesssim \varepsilon^{-1}h^{2q} + 2\varepsilon h^2 \left\|\nabla_\Gamma(\mathbf{H} - \mathbf{H}^l_h)\right\|^2_\Gamma + \varepsilon^{-1}h^{-2}\left\|\nabla_{\Gamma_h}(\mathbf{x}^e_\Gamma - \mathbf{x}_{\Gamma_h})\right\|^2_{\Gamma_h}, && (4.51)\end{aligned}$$

where the second part (4.50) followed by the Cauchy-Schwarz and the Young's inequality for any $\varepsilon \in \mathbb{R}_+$, and by the norm equivalences due to Lemma 20 the mean curvature vector term was combined into the second term of (4.51). To this end, we split the error with using the Young's inequality, and then bound each part by the interpolation estimate (4.47) and the second result (4.36) in Lemma 28 to obtain

$$\begin{aligned}
\left\|\nabla_\Gamma(\mathbf{H}-\mathbf{H}_h^l)\right\|_\Gamma^2 &\lesssim \left\|\nabla_\Gamma(\mathbf{H}-\mathcal{I}_h^l\mathbf{H})\right\|_\Gamma^2 + \left\|\nabla_\Gamma(\mathcal{I}_h^l\mathbf{H}-\mathbf{H}_h^l)\right\|_\Gamma^2 \\
&\lesssim \|\mathbf{H}-\mathcal{I}_h^l\mathbf{H}\|_{\mathcal{H}^1(\Gamma)}^2 + h^{-2}\|\mathcal{I}_h^l\mathbf{H}-\mathbf{H}_h^l\|_\Gamma^2 + h^{-1}|||\mathcal{I}_h\mathbf{H}-\mathbf{H}_h|||_{\mathcal{T}_h^\Gamma}^2 \\
&\lesssim h^{2k}\|\mathbf{H}\|_{\mathcal{H}^{k+1}(\Gamma)}^2 + h^{-2}\Big(\|\mathbf{H}-\mathcal{I}_h^l\mathbf{H}\|_\Gamma^2 + \|\mathbf{H}-\mathbf{H}_h^l\|_\Gamma^2\Big) \\
&\qquad + h^{-1}\Big(|||\mathbf{H}^e-\mathcal{I}_h\mathbf{H}|||_{\mathcal{T}_h^\Gamma}^2 + |||\mathbf{H}^e-\mathbf{H}_h|||_{\mathcal{T}_h^\Gamma}^2\Big) \\
&\lesssim h^{2k} + h^{-2}\Big(\|\mathbf{H}-\mathbf{H}_h^l\|_\Gamma^2 + h|||\mathbf{H}^e-\mathbf{H}_h|||_{\mathcal{T}_h^\Gamma}^2\Big),
\end{aligned}$$

where we eliminate the interpolation error in the normal diffusion semi-norm by Lemma 30 for the approximation error estimate

$$|||\mathbf{H}^e-\mathcal{I}_h\mathbf{H}|||_{\mathcal{T}_h^\Gamma}^2 \lesssim h^{2k+1}.$$

The last term of (4.51) is simply the coordinate embedding error (4.34) bounded by

$$\left\|\nabla_{\Gamma_h}(\mathbf{x}_\Gamma^e-\mathbf{x}_{\Gamma_h})\right\|_{\Gamma_h}^2 \lesssim h^{2q}.$$

Hence, we arrive at for any $\varepsilon \in \mathbb{R}_+$

$$\mathrm{IV}_2 \lesssim \varepsilon^{-1}h^{2q-2} + \varepsilon h^{2k+2} + \varepsilon\Big(\|\mathbf{H}-\mathbf{H}_h^l\|_\Gamma^2 + h|||\mathbf{H}^e-\mathbf{H}_h|||_{\mathcal{T}_h^\Gamma}^2\Big). \tag{4.52}$$

Together with the first part IV_1 (4.48) we have for any $\varepsilon \in \mathbb{R}_+$ that

$$\begin{aligned}
\mathrm{IV} &= \mathrm{IV}_1 + \mathrm{IV}_2 \\
&\lesssim (1+\varepsilon)h^{2k+2} + (1+\varepsilon^{-1})h^{2q-2} + \varepsilon\Big(\|\mathbf{H}-\mathbf{H}_h^l\|_\Gamma^2 + h|||\mathbf{H}^e-\mathbf{H}_h|||_{\mathcal{T}_h^\Gamma}^2\Big).
\end{aligned} \tag{4.53}$$

Conclusion:

To conclude the proof, summing up the estimates (4.40), (4.41), (4.44), (4.53) of the Term I-IV, it follows that

$$\mathrm{I}+\mathrm{II}+\mathrm{III}+\mathrm{IV} \lesssim h^{2k+2} + h^{2q-2} + \epsilon\Big(\|\mathbf{H}-\mathbf{H}_h^l\|_\Gamma^2 + h|||\mathbf{H}^e-\mathbf{H}_h|||_{\mathcal{F}_h^\Gamma}^2 + h|||\mathbf{H}^e-\mathbf{H}_h|||_{\mathcal{T}_h^\Gamma}^2\Big)$$

for any $0 < \epsilon \lesssim 1$, which can be chosen sufficiently small, and by using the kickback argument we arrive at the first result.

Towards the second result, we change the mesh size scaling from h to h^{-1} in front of the high-order ghost penalty semi-norm in (4.42), and then rather use Corollary 3 to achieve an $\mathcal{O}(h^{2k})$ error in (4.43), which modifies the bound accordingly in (4.44). As a consequence, we obtain the second result.

This completes the proof.

□

Remark 20 (Optimal order of convergence)**.** *In the low-order case of piecewise linear surface, Hansbo et al. estimate* (4.50) *by partial integration and eliminate* $\Delta_{\hat{G}}\hat{\mathbf{H}}_h = 0$ *on the flat piece* $\hat{G}$ *due to the linear* $\hat{\mathbf{H}}_h$*. If we follow the same lines, it gives*

$$\begin{aligned}
\Big(\nabla_{\Gamma_h}(\mathbf{x}_\Gamma^e - \mathbf{x}_{\Gamma_h}), \nabla_{\Gamma_h}(\mathbf{H}^e - \mathbf{H}_h)\Big)_{\Gamma_h} &= \sum_{E\in\mathcal{E}_h} \Big(\mathbf{x}_\Gamma^e - \mathbf{x}_{\Gamma_h}, \nabla_{\Gamma_h}(\mathbf{H}^e - \mathbf{H}_h)\cdot\mathbf{n}_E\Big)_E \\
&\quad - \sum_{G\in\mathcal{G}_h} \Big(\mathbf{x}_\Gamma^e - \mathbf{x}_{\Gamma_h}, \Delta_G(\mathbf{H}^e - \mathbf{H}_h)\Big)_G \\
&\lesssim \varepsilon^{-1} \sum_{E\in\mathcal{E}_h} h^{-1}\|\mathbf{x}_\Gamma^e - \mathbf{x}_{\Gamma_h}\|_E^2 + \varepsilon|||\mathbf{H}^e - \mathbf{H}_h|||_{\mathcal{E}_h}^2 \\
&\quad + \sum_{G\in\mathcal{G}_h} \|\mathbf{x}_\Gamma^e - \mathbf{x}_{\Gamma_h}\|_G \|\Delta_G(\mathbf{H}^e - \mathbf{H}_h)\|_G \\
&\lesssim (1+\varepsilon^{-1})h^{2q} + \varepsilon|||\mathbf{H}^e - \mathbf{H}_h|||_{\mathcal{E}_h}^2 \\
&\qquad + h^2 \sum_{G\in\mathcal{G}_h} \|\Delta_G(\mathbf{H}^e - \mathbf{H}_h)\|_G^2,
\end{aligned}$$

where we have the last term $\Delta_G(\mathbf{H}^e - \mathbf{H}_h)$ *needs to be estimated yet. If this term could be bounded by* $\mathcal{O}(h^k)$*, the* $\mathcal{L}^2$*-error of the discrete mean curvature vector would be bounded at an optimal order of* $(h^{k+1} + h^q)$ *that made the Hansbo's result a reduced case when* $k = q = 1$*. Unfortunately, however, this seems not the case due to the curved piece* $\mathcal{G}$ *by the isoparametric mapping. We leave the improvement to the optimal order of convergence in the future work.*

Remark 21 (Interchangeable ghost penalty)**.** *As we have introduced in Section 3.1.2, multiple versions of the ghost penalty stabilization exist, cf. [102, Subsection 4.3]. Recall the stabilization bilinear form* (4.25) *in which we make use of the original version, i.e., high-order derivative jump ghost penalty*

$$S_h(\mathbf{H}_h, \mathbf{v}_h) = \gamma_{\mathcal{F}} h^\lambda \sum_{F\in\mathcal{F}_h^\Gamma} \sum_{j=1}^{k} h^{2j-1} \int_F [\![\partial_{\mathbf{n}_F}^j \mathbf{H}_h]\!][\![\partial_{\mathbf{n}_F}^j \mathbf{v}_h]\!] ds. \tag{4.54}$$

The mesh size scaling is yet to be chosen between $\mathcal{L}^2$-scale $\lambda = 1$ and $\mathcal{H}^1$-scale $\lambda = -1$. Recall the ghost penalty bilinear form (3.31) that we have exploited for discrete extension and stabilization in the isoparametric BDF-FEM, analogously we can use the direct version of ghost penalty

$$s_h(\mathbf{H}_h, \mathbf{v}_h) = \gamma_{\mathcal{F}} h^{\lambda-2} \sum_{F \in \mathcal{F}_h^\Gamma} \int_{\omega(F)} (\mathbf{H}_1 - \mathbf{H}_2)(\mathbf{v}_1 - \mathbf{v}_2) d\mathbf{x} \tag{4.55}$$

where $\lambda = \pm 1$ corresponds to $\mathcal{L}^2$-scale or $\mathcal{H}^1$-scale in the same manner, and $\mathbf{H}_i, \mathbf{v}_i$, $i = 1, 2$ are canonical extensions of the mapped polynomials. Indeed, it has been proven in [130, Lemma 3.1 and Remark 6] that the direct version is bounded by the derivative jump ghost penalty, namely, for any $\mathbf{v}_h \in [\mathcal{V}_h^\Gamma]^d$ there holds

$$s_h(\mathbf{v}_h, \mathbf{v}_h) \lesssim S_h(\mathbf{v}_h, \mathbf{v}_h). \tag{4.56}$$

As a consequence, the stability result of Theorem 8 and the error estimates in Theorem 9 still hold true if the semi-norm for derivative jump ghost penalty (4.26b) is replaced by the one corresponding to the direct version, and the stabilized isoparametric TraceFEM still works with the direct version of ghost penalty in (4.25).

In [130, Remark 6] the author has discussed the computational advantages the direct version of ghost penalty has for higher-order methods. We will take advantage of the direct version in the following numerical experiments, not only because it is more efficient in computation and easier for implementation, but also due to a precision limit around 10^{-7} when we use the add-on library `ngsxfem` *[101] to the finite element package* `NGSolve` *[141] to compute the derivative jumps in the ghost penalty term.*

4.3 Numerical Experiments

In this section, we test the stabilized isoparametric TraceFEM by two numerical examples for computing the discrete mean curvature vector fields on:

1. a unit circle in two dimensions;
2. a torus in three dimensions.

We investigate the experimental order of convergence (EOC) in order to verify the a priori error estimated in Subsection 4.2.8.

4.3.1 Unit circle

Let us first perform a concrete convergence study for the discrete mean curvature vector of a unit circle with radius $R = 1$, on which the exact mean curvature vector has a simple expression

$$\mathbf{H} = \frac{1}{R}\,\mathbf{x} = (x_1, x_2) \tag{4.57}$$

for $\mathbf{x} = (x_1, x_2)$ the standard Cartesian coordinate system. Based on the extension of this exact mean curvature vector, we measure the following $\mathcal{L}^2$-error for the discrete mean curvature vector $\mathbf{H}_h$ on the isoparametrically mapped hypersurface:

$$\|\mathbf{H}^e - \mathbf{H}_h\|_{\mathcal{L}^2(\Gamma_h)} = \left(\int_{\Gamma_h} |\mathbf{H}^e - \mathbf{H}_h|^2 ds\right)^{\frac{1}{2}}. \tag{4.58}$$

To implement the stabilized isoparametric TraceFEM, we generate an unstructured mesh $\mathcal{T}_h$ consisting of triangles with an initial mesh size $h_0 = 0.6$ in a background square domain $(-1.2, 1.2)^2$. The unit circle centered on the origin can be described by the signed distance function

$$\rho = x_1^2 + x_2^2 - 1. \tag{4.59}$$

We construct a high-order approximation of the signed distance function by using the isoparametric interpolation $\rho_h = \mathcal{I}_h \rho$, cf. Definition 17, such that Γ_h is the zero level set of ρ_h. The mesh refinement is applied in such a way that the mesh size $h = 2^{-L}\, h_0$ for the refinement level $L = 0, ..., 6$.

We will present the numerical results computed with the direct version of ghost penalty (4.55) applied into (4.25), in addition to the ones with the original version of derivative jump ghost penalty. See Remark 21 for details. Next, we will begin with the cases when $k = q$, i.e., uniform orders of the finite element discretization k and the isoparametric mapping q, for different mesh size scalings, i.e., $\mathcal{L}^2$-scale $\lambda = 1$ and $\mathcal{H}^1$-scale $\lambda = -1$. We will subsequently investigate the cases when $k \neq q$, which is suggested by Theorem 9.

Cases when $k = q$

The following cases of stabilization are considered:

- $\mathcal{L}^2$-scale derivative jump ghost penalty with normal diffusion;
- $\mathcal{H}^1$-scale derivative jump ghost penalty with normal diffusion;
- $\mathcal{L}^2$-scale direct version of ghost penalty with normal diffusion;

- $\mathcal{H}^1$-scale direct version of ghost penalty with normal diffusion.

With choosing the stabilization parameters $\gamma_{\mathcal{F}} = \gamma_{\mathcal{T}} = 1$, the stabilized isoparametric TraceFEM gives the numerical results in Figure 4.1 and Figure 4.2.

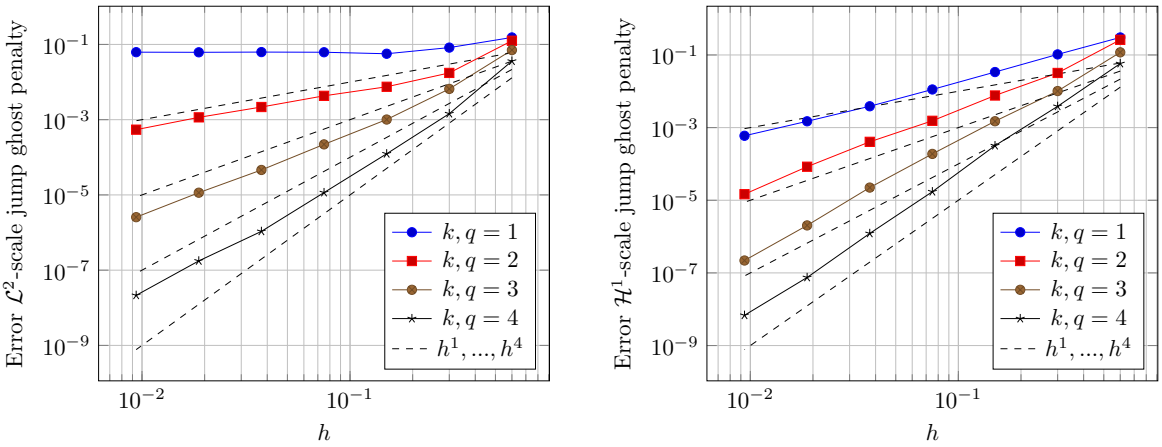

Fig. 4.1 $\mathcal{L}^2$-error of the discrete mean curvature vector of the unit circle for $k = q = 1, 2, 3, 4$, computed by the stabilized isoparametric TraceFEM with the derivative jump ghost penalty and the normal diffusion stabilization. Left: $\mathcal{L}^2$-scale $\lambda = 1$; Right: H^1-scale $\lambda = -1$.

In Figure 4.1 we show the $\mathcal{L}^2$-error convergence curves of the discrete mean curvature vector of the unit circle for $k = q = 1, 2, 3, 4$, which are computed by the stabilized isoparametric TraceFEM with the *derivative jump* ghost penalty and the normal diffusion stabilization, but different mesh size scalings are used for the ghost penalty term. To produce the left data we set $\mathcal{L}^2$-scale $\lambda = 1$, while for the right data $\mathcal{H}^1$-scale $\lambda = -1$. We observe that with $\mathcal{L}^2$-scale $\lambda = 1$ each convergence rate is approximately one order lower than k, q, which is in agreement with the prediction of Theorem 9, i.e., $\mathcal{O}(h^{k+1} + h^{q-1})$. However, with $\mathcal{H}^1$-scale $\lambda = -1$ each convergence rate is significantly higher than its left counterpart, and almost the same as k, q, which implies that Theorem 9 gives a suboptimal a priori error estimate, i.e., $\mathcal{O}(h^k + h^{q-1})$.

Let us further investigate the EOC with $\mathcal{H}^1$-scale $\lambda = -1$ *derivative jump* ghost penalty by specific numbers in Table 4.1. From Table 4.1 we observe that the EOC for $k = q = 1, 2, 3$ are approximately equivalent to (or even an half order higher than) k, q, while for $k = q = 4$ the EOC are downgraded to k, q, especially the last one loses an half order perhaps due to the precision limit from the add-on library `ngsxfem` [101] to the finite element package `NGSolve` [141] when we compute the derivative jumps in the ghost penalty term. Overall, we have realized that the $\mathcal{H}^1$-scale $\lambda = -1$ gives rise to a

Table 4.1 $\mathcal{L}^2$-error of the discrete mean curvature vector of the unit circle for $k = q = 1, 2, 3, 4$, computed by the stabilized isoparametric TraceFEM with the $\mathcal{H}^1$-scale $\lambda = -1$ derivative jump ghost penalty and the normal diffusion stabilization. The numbers are truncated to two decimal places without rounding, but the EOC in round brackets are computed based on double precision and then truncated to two decimal places without rounding.

L	$k = q = 1$	$k = q = 2$	$k = q = 3$	$k = q = 4$
0	$3.03 \cdot 10^{-1}$	$2.61 \cdot 10^{-1}$	$1.18 \cdot 10^{-1}$	$5.79 \cdot 10^{-2}$
1	$1.03 \cdot 10^{-1}$ (**1.55**)	$3.19 \cdot 10^{-2}$ (**3.03**)	$1.01 \cdot 10^{-2}$ (**3.54**)	$3.85 \cdot 10^{-3}$ (**3.91**)
2	$3.38 \cdot 10^{-2}$ (**1.61**)	$7.65 \cdot 10^{-3}$ (**2.06**)	$1.49 \cdot 10^{-3}$ (**2.76**)	$3.18 \cdot 10^{-4}$ (**3.59**)
3	$1.12 \cdot 10^{-2}$ (**1.59**)	$1.54 \cdot 10^{-3}$ (**2.31**)	$1.88 \cdot 10^{-4}$ (**2.98**)	$1.71 \cdot 10^{-5}$ (**4.21**)
4	$3.86 \cdot 10^{-3}$ (**1.53**)	$4.06 \cdot 10^{-4}$ (**1.92**)	$2.23 \cdot 10^{-5}$ (**3.07**)	$1.22 \cdot 10^{-6}$ (**3.81**)
5	$1.49 \cdot 10^{-3}$ (**1.37**)	$8.38 \cdot 10^{-5}$ (**2.27**)	$2.02 \cdot 10^{-6}$ (**3.46**)	$7.48 \cdot 10^{-8}$ (**4.02**)
6	$5.95 \cdot 10^{-4}$ (**1.32**)	$1.46 \cdot 10^{-5}$ (**2.51**)	$2.19 \cdot 10^{-7}$ (**3.20**)	$6.81 \cdot 10^{-9}$ (**3.45**)

better convergence rate, despite the suboptimal a priori error estimates in Theorem 9 predict that $\mathcal{L}^2$-scale $\lambda = 1$ would result in a sharper bound with respect to k.

The numerical results of the stabilized isoparametric TraceFEM with the *direct* version of ghost penalty and the normal diffusion stabilization are shown in Figure 4.2.

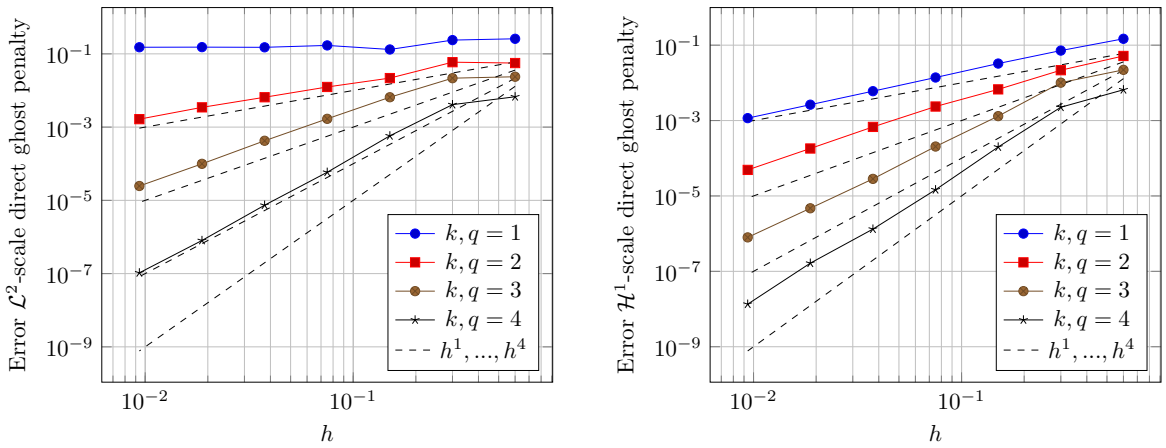

Fig. 4.2 $\mathcal{L}^2$-error of the discrete mean curvature vector of the unit circle for $k = q = 1, 2, 3, 4$, computed by the stabilized isoparametric TraceFEM with the direct version of ghost penalty and the normal diffusion stabilization. Left: $\mathcal{L}^2$-scale $\lambda = 1$; Right: H^1-scale $\lambda = -1$.

In Figure 4.2 we present the $\mathcal{L}^2$-error convergence curves of the discrete mean curvature vector of the unit circle for $k = q = 1, 2, 3, 4$ computed by the stabilized isoparametric TraceFEM with the *direct* version of ghost penalty and the normal

diffusion stabilization. Different mesh size scalings are applied into the ghost penalty term in such a way that we choose $\mathcal{L}^2$-scale $\lambda = 1$ for the left result and $\mathcal{H}^1$-scale $\lambda = -1$ for the right one. Again, we recognize that the convergence rates with $\mathcal{H}^1$-scale $\lambda = -1$ on the right side are considerably better than the ones with $\mathcal{L}^2$-scale $\lambda = 1$ on the left side. The right data surpasses the suboptimal a priori error estimate $\mathcal{O}(h^k + h^{q-1})$ by an half order, and has no significant difference from (a little bit worse than) the former result produced with the derivative jump ghost penalty, while the left data still follows the prediction of Theorem 9, i.e., $\mathcal{O}(h^{k+1} + h^{q-1})$. To summarize, the ghost penalty version does not matter, but the mesh size scaling matters.

Apart from that, we have also tested the cases with only one stabilization type, either the ghost penalty or the normal diffusion. We observe that without the ghost penalty the convergence behavior is similar to the cases of $\mathcal{L}^2$-scale $\lambda = 1$ ghost penalty. As a consequence, if the ghost penalty is not applied in the low-order case when $k = q = 1$ the error does not converge, which is in agreement with the result in [82]. On the other hand, when $k = q = 1, 2$ the ghost penalty itself shows sufficient capability to stabilize the discrete mean curvature vector, but higher-order convergence rate is not possible without the normal diffusion, which has been concluded in [74] where the normal diffusion is called *normal derivative volume stabilization*. For ease of presentation we do not plot these numerical results here, but the reader can feel free to replicate them with using our software and code provided on the `GitLab` repository, cf. Section 1.5.

Cases when $k \neq q$

The a priori error estimates in Theorem 9 suggest that one should choose the order of isoparametric mapping q higher than the order of finite element discretization k to optimize the error bounds, which motivates us to investigate the numerical results if $k \neq q$, especially when $k < q$. To this end, we fix $q = 3$ with varying $k = 1, 2, 3, 4$, and subsequently change $q = 2, 3, 4, 5$ with a fixed $k = 3$. Since we have realized the fact that $\mathcal{H}^1$-scale $\lambda = -1$ gives rise to better convergence behaviors, here we study only with this mesh size scaling. The numerical results come with the *derivative jump* ghost penalty in Figure 4.3. With the *direct* version of ghost penalty the numerical results are shown in Figure 4.4.

As we expected, the difference of ghost penalty versions does not impact on the convergence behavior in general. The numerical results above demonstrate that either k or q would limit the error convergence rates. On the left side when $q = 3$ is fixed, the maximum convergence rate is restricted below $\mathcal{O}(h^3)$ even though k goes to 4. The situation is much better on the right side with a fixed $k = 3$, since the maximum

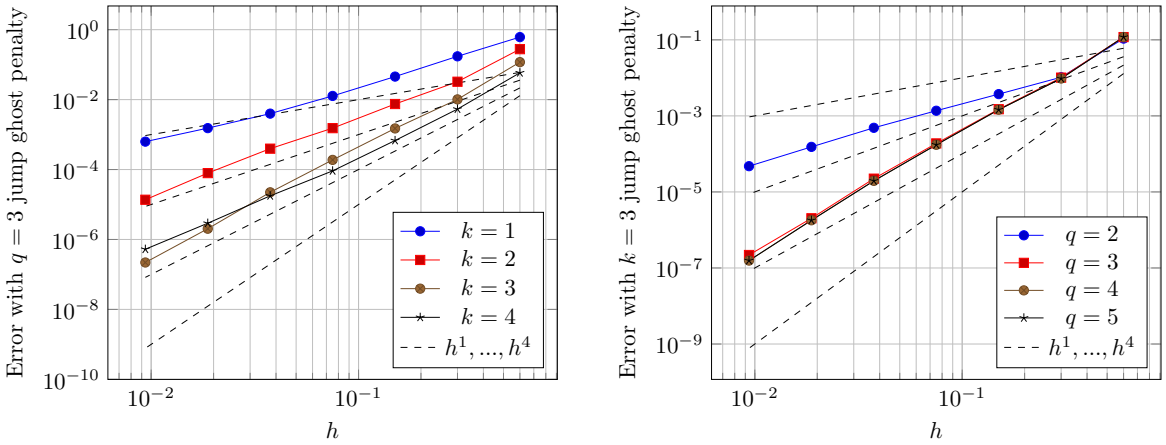

Fig. 4.3 $\mathcal{L}^2$-errors of the discrete mean curvature vector of the unit circle, computed by using the stabilized isoparametric TraceFEM with the $\mathcal{H}^1$-scale $\lambda = -1$ derivative jump ghost penalty and the normal diffusion stabilization. Left: The fixed $q = 3$ and the varied $k = 1,2,3,4$. Right: The fixed $k = 3$ and the varied $q = 2,3,4,5$.

convergence rate exceeds $\mathcal{O}(h^3)$ and approaches to $\mathcal{O}(h^4)$ when q goes up. Overall, based on Figure 4.3 and Figure 4.4 we conclude that the convergence rates are bounded approximately by $\mathcal{O}(h^{k+\frac{1}{2}} + h^{q-\frac{1}{2}})$. This observation on the convergence behavior has an half order better than the suboptimal a priori error estimate $\mathcal{O}(h^k + h^{q-1})$ predicted by Theorem 9. As a bottom line, one can optimize the choices of k and q by the criterion $q - k = 1$, which is in agreement with Theorem 9.

4.3.2 Torus

In the second numerical example, we consider the mean curvature vector of a torus in three spatial dimensions, which can be represent by the following signed distance function

$$\rho = \left(\left((x_1^2 + x_2^2)^{\frac{1}{2}} - R \right)^2 + x_3^2 \right)^{\frac{1}{2}} - r \tag{4.60}$$

with the parameters $R = 1.0$ and $r = 0.5$. This torus is embedded in the Euclidean space $\mathbb{R}^3$ with $\mathbf{x} = (x_1, x_2, x_3)$ the standard Cartesian coordinate system. Provided that the signed distance function ρ is given, the exact mean curvature vector of the torus can be computed by

$$\mathbf{H} = (\Delta\rho)\nabla\rho. \tag{4.61}$$

See [82, Subsection 5.1.2] for details of this formula. Based on the extension of this exact mean curvature vector, we measure the following $\mathcal{L}^2$-error for the discrete mean

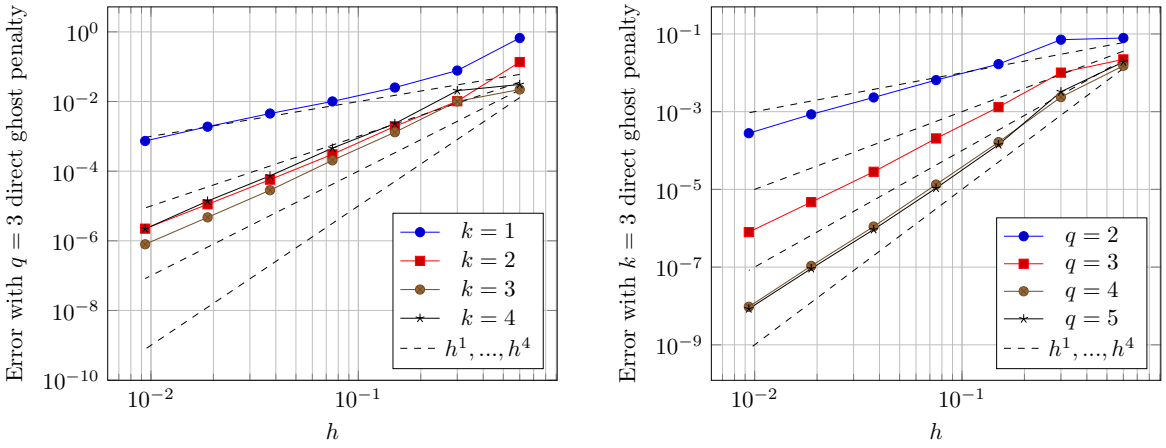

Fig. 4.4 $\mathcal{L}^2$-errors of the discrete mean curvature vector of the unit circle, computed by using the stabilized isoparametric TraceFEM with the $\mathcal{H}^1$-scale $\lambda = -1$ direct version of ghost penalty and the normal diffusion stabilization. Left: The fixed $q = 3$ and the varied $k = 1, 2, 3, 4$. Right: The fixed $k = 3$ and the varied $q = 2, 3, 4, 5$.

curvature vector $\mathbf{H}_h$ on the isoparametrically mapped hypersurface Γ_h:

$$\|\mathbf{H}^e - \mathbf{H}_h\|_{\mathcal{L}^2(\Gamma_h)} = \left(\int_{\Gamma_h} |\mathbf{H}^e - \mathbf{H}_h|^2 ds \right)^{\frac{1}{2}}. \tag{4.62}$$

Analogously, we generate an unstructured mesh $\mathcal{T}_h$ in three dimensions consisting of tetrahedrons with an initial mesh size $h_0 = 1.0$ in a background cube domain $[-2, 2] \times [-2, 2] \times [-2, 2]$. Again, we construct a high-order approximation of the signed distance function in the same manner by the isoparametric interpolation $\rho_h = \mathcal{I}_h \rho$ whose zero level set represents Γ_h. The mesh refinement is applied in such a way that $h = 2^{-L} h_0$ for the refinement level $L = 0, ..., 4$.

As we have discovered that H^1-scale $\lambda = -1$ enjoys the better convergence behavior, and the different versions of ghost penalty do not matter, we only investigate the H^1-scale derivative jump ghost penalty in this example. Both the standard $k = q$ and the optimal $k = q - 1$ cases are considered.

From Figure 4.5 we observe that convergence rates are approximately equal to k and q when $k = q$ on the left side, which are better than the $\mathcal{O}(h^k + h^{q-1})$-convergence predicted by Theorem 9. But on the right we do not see the expected improvement when we lift q by one order. These results might not be illustrative, because we take the maximum mesh refinement level only $L = 4$, and we cannot afford the expensive computational cost of the three-dimensional example on a finer mesh.

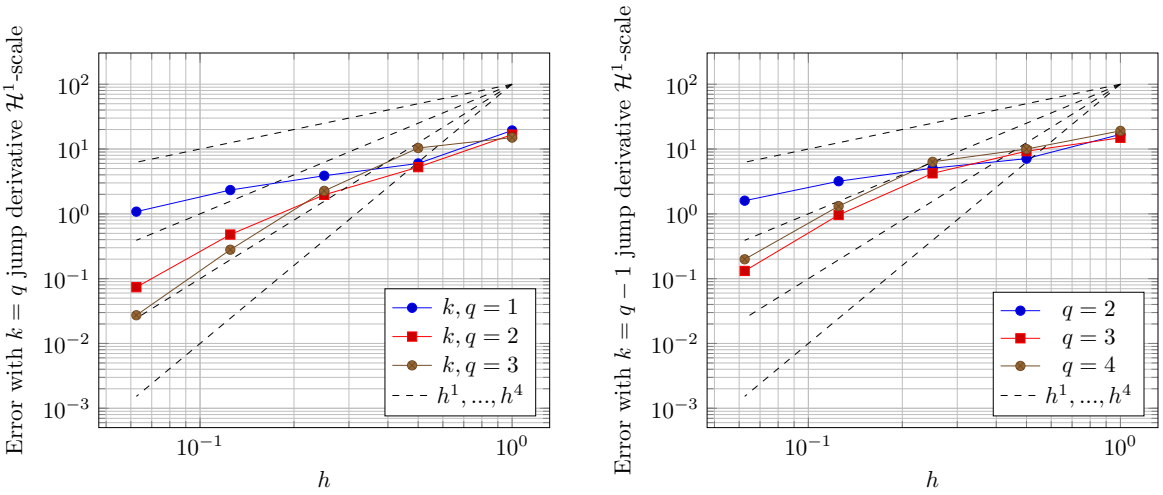

Fig. 4.5 $\mathcal{L}^2$-errors of the discrete mean curvature vector of the torus, computed by using the stabilized isoparametric TraceFEM with the $\mathcal{H}^1$-scale $\lambda = -1$ derivative jump ghost penalty and the normal diffusion stabilization. Left: The uniform orders $k = q = 1, 2, 3$. Right: The optimal orders $k = 1, 2, 3$ and $q = k + 1 = 2, 3, 4$.

Figure 4.6 shows how we generate the background cube domain and unfitted mesh containing the torus by using the GUI of `Netgen/NGSolve` [141]. The exact level set torus and the discrete mean curvature vectors around the torus are displayed.

Figure 4.7 shows the discrete level set torus we created and the unfitted mesh cut by the surface. The discrete mean curvature vectors are presented on the surface, with the color indicating the magnitude of them.

4.4 Summary

In this chapter, we have developed the stabilized isoparametric TraceFEM for solving the geometric equation of the discrete mean curvature vector of hypersurfaces. We have proved in the error analysis that the isoparametric TraceFEM working with the ghost penalty and normal diffusion stabilization gives rise to arbitrarily high order of accuracy. The numerical experiments we presented have verified the predicted convergence rates, and shown the effects of the different stabilizations and mesh size scalings. Moreover, the convergence study of the first example provides a remarkable suggestion on the optimal choice of the orders of finite element discretization and isoparametric mapping. The second example demonstrates the capability of our method to handle more flexible two-dimensional surfaces embedded in three spatial dimensions.

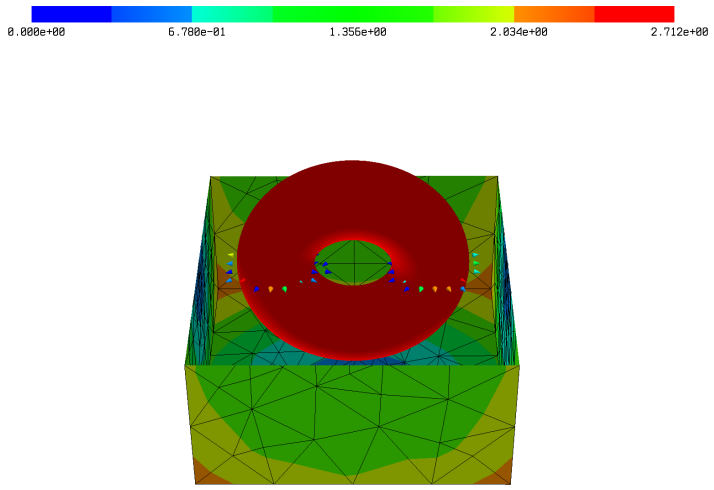

Fig. 4.6 The torus contained in the background cube domain, with the unstructured computational mesh, the exact level set surface, and some discrete mean curvature vectors intersected by a clipping plane.

This chapter is considered as the core of this thesis, which is not only a building block for the geometrically coupled bulk-surface problem, but it also plays an important role independently. In computer graphics and computational geometry, solving the high accurate mean curvature vector of a discrete surface is an active topic, cf. [17, 55]. The geometrically unfitted setting of this method gives the largest flexibility to the related applications. Furthermore, the method serves as a piece of puzzle towards the mean curvature flow.

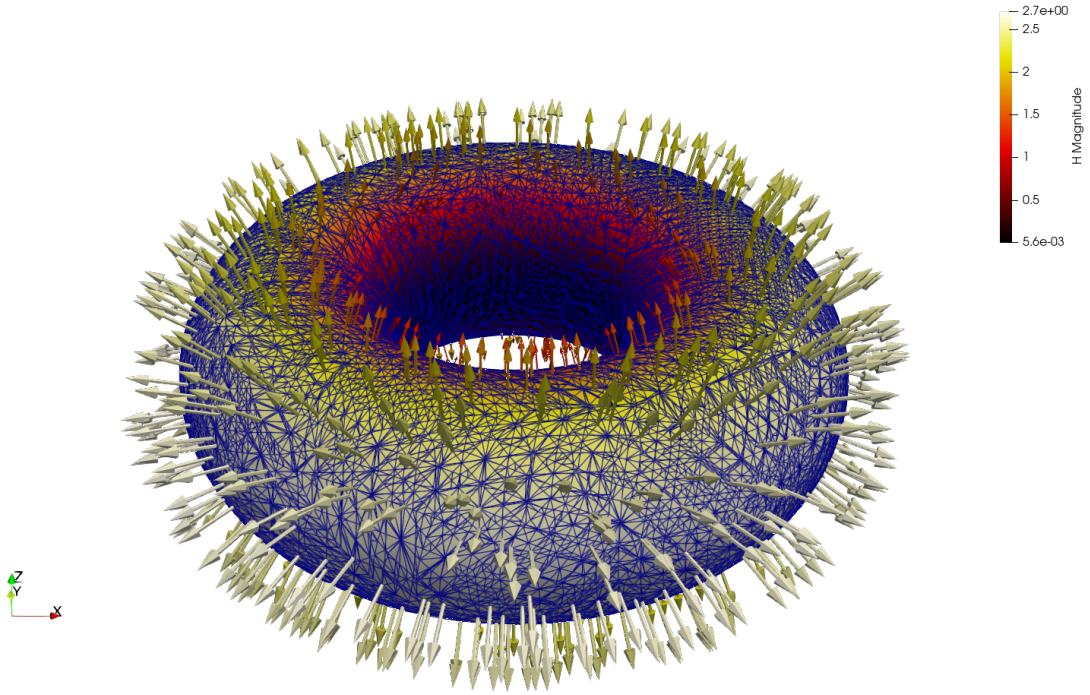

Fig. 4.7 The discrete level set torus with the cut element facets, and some discrete mean curvature vectors sampled on the surface, with the magnitude by color.

Chapter 5

Evolution of Level Set Geometry

As discussed in Subsection 2.2.2, there are two different approaches to figure out the evolution of a level set geometry. We do not choose to solve the highly nonlinear, degenerate, parabolic equation, but rather to solve the linear hyperbolic transport equation of the level set function, which additionally requires a velocity field well-defined on the whole background domain. To this end, the velocity field can be obtained through a variety of extension methods, e.g., the *Fast Marching Method* [1, 143–146], based on the surface velocity arising from the mean curvature vector and the PDE solution. We have developed the high-order numerical methods in Chapter 3 for the advection-diffusion equation on an evolving domain and in Chapter 4 for the geometric equation of mean curvature vector of the bounding hypersurface, hence we are ready to compute the surface velocity on the boundary of the domain. In this chapter, we present two methods for extending the surface velocity from the bounding hypersurface onto the background domain. One of these extension methods works by solving a normal diffusion equation of the velocity field over the background domain with an interface condition consistent with the surface velocity. Another method is the ghost-penalty-based discrete extension, as we have seen in Section 3.1.2. With this extended velocity field well-defined on the background domain and linearized with respect to the geometric evolution at each time step, we are able to solve the transport equation by a variety of standard schemes for hyperbolic PDEs. We briefly introduce the discontinuous Galerkin (DG) finite element discretization in space combined with the explicit Runge–Kutta (RK) schemes for time stepping, i.e., the RKDG methods developed in [36–38, 42, 40], which is popular and robust to solve hyperbolic system of conservation laws at high order of accuracy. For the corresponding error analysis, we collect some notable results from the established literature [35, 154, 164, 168–170]. A numerical experiment of the level set transport problem concludes this chapter.

5.1 Extension of Velocity Field

There are multiple approaches to construct the velocity field for evolving the level sets on the whole background domain. Once the surface velocity is determined, the only restriction is that the velocity field on the surface must be consistent with the surface velocity. Apart from that, the construction still has considerable degrees of freedom. The optimal choice indeed depends on the specific problem. For instance, in two-phase interface flow problem, an intrinsic velocity field of physics exists over the whole region, which can be utilized to solve the level set transport equation. In single-domain problem, however, the artificial background domain has no such a natural velocity outside of the physical domain, hence we have to take care of the manufacture of a velocity field. The simplest idea is extrapolation from the closest point on the boundary, but it may not preserve the signed distance property and give rise to a smooth velocity field that is desired when we continue updating the level sets. Another popular approach to build a distance-preserving extension of the velocity field is to solve the eikonal equation in front of the propagating interface, which is called *Fast Marching Method*, cf. [1, 143–146]. For the geometrically coupled solution-curvature-driven moving FBP we proposed in Section 2.4, a more convenient way is to extend the surface velocity by solving an elliptic diffusion equation over the whole background domain, with the interface condition for the compatibility with the surface velocity, on account of that we have employed the normal diffusion mechanism on cut elements for stabilizing the discrete mean curvature vector. Another on-hand approach of velocity extension is based on the ghost penalty formulations that we have exploited in Chapter 3. In this section, we introduce these two methods and implement them for some numerical examples. As the velocity extension is a stationary problem to be solved at each time step, the variable of time dependence is omitted in the notation.

5.1.1 Normal diffusion extension method

Recall the normal velocity on the bounding hypersurface Γ defined by (2.2) in Subsection 2.1.1 that

$$w := -\alpha\kappa + \beta u_\Gamma \tag{5.1}$$

for the mean curvature κ and the trace of the solution u_Γ to PDEs on the bounded domain, and some parameters $\alpha, \beta \in \mathbb{R}_+$. With the unit normal $\mathbf{n}$ of the hypersurface Γ we have the surface velocity *vector*

$$\mathbf{w}_\Gamma := w\mathbf{n} = (-\alpha\kappa + \beta u_\Gamma)\mathbf{n} = -\alpha\mathbf{H} + \beta u_\Gamma \mathbf{n} \qquad \text{on } \Gamma, \tag{5.2}$$

where $\mathbf{H}$ is the mean curvature vector of the hypersurface Γ.

In Subsection 2.2.2 we have introduced by Definition 9 the velocity extension operator $\mathcal{E} : \mathcal{C}^2(\Gamma) \to [\mathcal{C}^2(\bar{\Omega})]^d$ for the surface velocity w such that the restriction of consistency $(\mathcal{E}w)|_\Gamma = \mathbf{w}_\Gamma$ holds. A compatible velocity extension operator such that $\mathbf{w} := \mathcal{E}w$ defined on the background domain $\bar{\Omega}$ can be obtained by solving the following elliptic diffusion equation with the interface condition for the compatibility with the surface velocity vector:

$$\nabla \cdot (\mathbb{T}\nabla \mathbf{w}) = 0 \qquad \text{in } \bar{\Omega}, \tag{5.3a}$$

$$\mathbf{w} = \mathbf{w}_\Gamma \qquad \text{on } \Gamma, \tag{5.3b}$$

where for the diffusion coefficient $\mathbb{T}$ one has two choices:

$$\mathbb{T} := \begin{cases} \mathbb{I}, & \text{(isotropic)} \\ \mathbf{n} \otimes \mathbf{n}, & \text{(anisotropic)} \end{cases} \tag{5.4}$$

for the identity matrix $\mathbb{I}$ and a tensor-valued coefficient $\mathbf{n} \otimes \mathbf{n} = \mathbf{n}\mathbf{n}^{\mathrm{T}}$. Here $\mathbf{n} = \frac{\nabla \phi}{\|\nabla \phi\|}$ is well-defined over the background domain $\bar{\Omega}$ by extension of (2.22) with the plus sign choice, even if the level set function $\phi : \bar{\Omega} \to \mathbb{R}$ does not preserve the signed distance properties. The identity diffusion coefficient is called *isotropic* since it reduces (5.3a) to a Laplace equation that would smear out the values from (5.3b), namely, $\mathbf{w}|_\Gamma$ is to be distributed with the same magnitude in every direction from the hypersurface to the background domain. This is however not a preferred result. Alternatively, we make use of the *anisotropic* option which adds the diffusion only in those directions normal to the hypersurface. This aims to generate a velocity distribution that preserves the signed distance properties as much as possible for the level set function when it is being updated by solving the transport equation.

Let us recall the weak form (2.30) with the Sobolev spaces (2.28) and (2.29) in Subsection 2.2.2. For such a stationary diffusion problem in a simple polygon domain, the standard finite element discretization follows directly.

However, we have an idea to solve this PDE problem more efficiently. If we divide the computational domain into a partition of strips, and then we can solve the problem by element layers, in order to save computational cost. Recalling the notation for discrete domains and meshes in Section 3.1.1, we use the similar symbols but omit the time dependence n and choose $\delta = 0$ in this section. For example, the cut elements and the corresponding domain are denoted by $\mathcal{T}_0^{\mathcal{S}}$ and $\mathcal{D}_0^{\mathcal{S}}$, to which all the direct neighboring elements added are denoted by $\mathcal{T}_{\pm 1}^{\mathcal{S}}$ and $\mathcal{D}_{\pm 1}^{\mathcal{S}}$ (i.e., one element layer

extension in both directions), and so on. In addition, we define a strip domain $\tilde{\mathcal{D}}_r^{\mathcal{S}}$ such that

$$\tilde{\mathcal{D}}_0^{\mathcal{S}} := \overline{\mathcal{D}_0^{\mathcal{S}}} \qquad \text{and} \qquad \tilde{\mathcal{D}}_r^{\mathcal{S}} := \overline{\mathcal{D}_{\pm r}^{\mathcal{S}}} \setminus \mathcal{D}_{\pm(r-1)}^{\mathcal{S}} \qquad \text{for } r \in \mathbb{N}_+, \tag{5.5}$$

which is the set difference of two consecutive strip domains. It can be considered as two separate concentric strips, each of which has a single element layer away from the cut elements. Upon this relative complement of consecutive strip domains, we setup the following Dirichlet and Neumann boundary conditions:

$$\mathbf{w} = \mathbf{w}_\Gamma \qquad \text{on } \Gamma_h,\ i = 0, \tag{5.6a}$$

$$\mathbf{w} = \mathbf{w}_{\mathcal{D}_{i-1}} \qquad \text{on } \partial\overline{\tilde{\mathcal{D}}_{i-1}^{\mathcal{S}}} \cap \partial\overline{\tilde{\mathcal{D}}_i^{\mathcal{S}}},\ i = 1, ..., j, \tag{5.6b}$$

$$(\mathbf{n} \otimes \mathbf{n})\nabla\mathbf{w} \cdot \mathbf{n} = 0 \qquad \text{on } \partial\overline{\tilde{\mathcal{D}}_i^{\mathcal{S}}} \cap \partial\overline{\tilde{\mathcal{D}}_{i+1}^{\mathcal{S}}},\ i = 0, ..., j \tag{5.6c}$$

where $\mathbf{w}_{\mathcal{D}_{i-1}}$ denotes the Dirichlet data from the solution on $\tilde{\mathcal{D}}_{i-1}^{\mathcal{S}}$, and $\tilde{\mathcal{D}}_j^{\mathcal{S}}$ is the furthest element strip inward or outward from the hypersurface, with the frontier defined by $\partial\overline{\tilde{\mathcal{D}}_{j+1}^{\mathcal{S}}} := \partial\bar{\Omega}$ or by $\partial\overline{\tilde{\mathcal{D}}_{j+1}^{\mathcal{S}}} := \emptyset$ if the inward direction is further. Now we aim to find $\mathbf{w}_h \in [\mathcal{V}_h(\tilde{\mathcal{D}}_i^{\mathcal{S}})]^d$ such that

$$\int_{\bar{\Omega}} (\mathbf{n}_h \otimes \mathbf{n}_h)\nabla\mathbf{w}_h \nabla\mathbf{v}_h \, d\mathbf{x} = 0 \qquad \forall \mathbf{v}_h \in [\mathcal{V}_h(\tilde{\mathcal{D}}_i^{\mathcal{S}})]^d \tag{5.7}$$

for $i = 0, 1, ..., j$. This procedure is to be implemented as follows: When $i = 0$, (5.6a) and (5.6c) are applied; When $0 < i \leq j$, (5.6b) and (5.6c) are applied; When $i > j$ there is no further element strip to be solved.

Please note this is just an idea of solving the PDE problem with more efficient algorithm, but we do not bring it into practice yet.

5.1.2 Ghost penalty extension method

As we have seen in Section 3.1.2, one effect of the ghost penalty mechanism is the discrete extension of a domain along with the functions defined on the domain. Hence it can be utilized for velocity extension as well. Due to the variants of the ghost penalty formulation, we have accordingly various ghost-penalty-based extension methods with the same effect.

Recall the stabilization bilinear form (4.25) where we take the most well-known version, i.e., high-order derivative *jump* ghost penalty

$$S_h(\mathbf{u}_h, \mathbf{v}_h) = \gamma_{\mathcal{F}} h^{-1} \sum_{F \in \mathcal{F}_h^\Gamma} \sum_{j=1}^{k} h^{2j-1} \int_F [\![\partial_{\mathbf{n}_F}^j \mathbf{u}_h]\!][\![\partial_{\mathbf{n}_F}^j \mathbf{v}_h]\!] ds. \tag{5.8}$$

Recall the ghost penalty bilinear form (3.31) that we used for a discrete extension in the isoparametric unfitted BDF-FEM. Analogously, we carry out the *direct* version of the ghost penalty

$$s_h(\mathbf{u}_h, \mathbf{v}_h) = \gamma_{\mathcal{F}} \sum_{F \in \mathcal{F}_h^\Gamma} \frac{1}{h^3} \int_{\omega(F)} (\mathbf{u}_1 - \mathbf{u}_2)(\mathbf{v}_1 - \mathbf{v}_2) d\mathbf{x} \tag{5.9}$$

where $\mathbf{u}_i, \mathbf{v}_i,\ i = 1, 2$ are canonical extensions of mapped polynomials.

We prefer the direct version which is simpler in the sense of computation, since the high-order derivative jumps are involved implicitly, cf. [130, Remark 6]. But in Chapter 6 we will bring both velocity extension methods into implementation.

Numerical test

In this subsection, we present a simple example to test the velocity extension by normal diffusion. See Figure 5.1 for an illustration of the implementation.

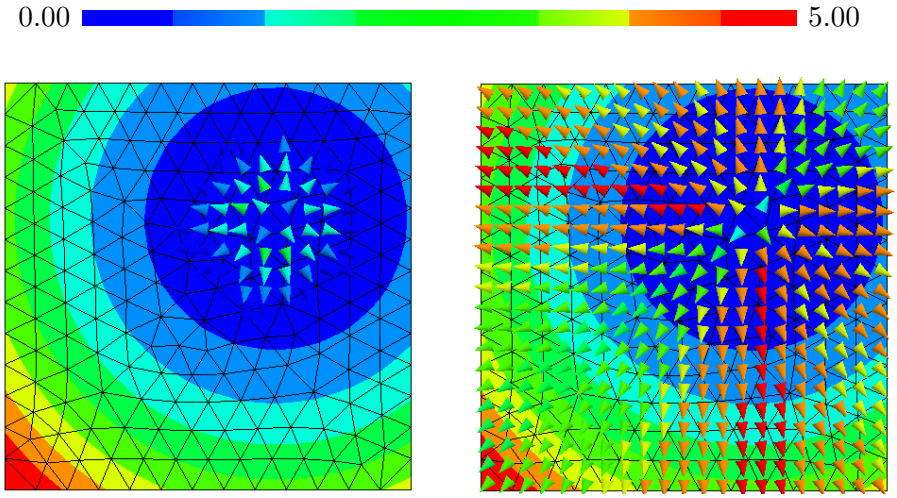

Fig. 5.1 An implementation example of velocity extension from the cut elements to the background mesh by anisotropic normal diffusion. The background color indicates a level set function and the vectors for a velocity field with the magnitude by color.

Figure 5.1 shows the velocity properly extended from the cut elements onto the background domain by anisotropic normal diffusion. To get it, we solve the stationary diffusion equation (5.3a) over the background domain with applying the restriction (5.3b) by using the standard FEM.

5.2 Runge–Kutta Discontinuous Galerkin Methods

As we have discussed in Section 2.2, for the level set method a real-valued auxiliary function $\phi : \bar{\Omega} \to \mathbb{R}$ is defined over the background domain, of which the zero level set is exploited to represent the boundary Γ of a physical domain $\Omega \subset \bar{\Omega}$. This level set function is time-dependent, i.e., $\phi : \bar{\Omega} \times [0,T] \to \mathbb{R}$, if the physical domain is moving with a surface velocity w in the background domain. Provided that a velocity field $\mathbf{w} : \bar{\Omega} \to \mathbb{R}^d$ is well-defined by extension from w, cf. Section 5.1, the level set function $\phi(\mathbf{x},t)$ can be considered as a solution to the corresponding advection equation on $\bar{\Omega}$, cf. Subsection 2.2.2. This hyperbolic PDE can be solved numerically by a variety of upwind schemes in order to track the evolution of the physical domain. In this section, we will briefly introduce the method of lines approach that combines the discontinuous Galerkin (DG) finite element discretization in space with the explicit Runge–Kutta (RK) methods for time stepping. The resulting *Runge–Kutta discontinuous Galerkin* (RKDG) methods have been developed by Cockburn et al. in a series of literature, cf. [36–38, 40, 42], which are robust and high-order accurate for advection-dominated problems, and found their way into the mainstream of computational fluid dynamics (CFD) by a wide range of real-world applications, cf. [41]. Next, we discuss in detail the RKDG methods applied to the linear hyperbolic transport equation of level set geometry.

5.2.1 Discontinuous Galerkin discretization in space

Recall the level set transport problem (2.31) in Subsection 2.2.2. Let $\phi : \bar{\Omega} \times [0,T] \to \mathbb{R}$ be a real-valued function for a scalar quantity transported in time by a solution-independent velocity field $\mathbf{w} : \bar{\Omega} \to \mathbb{R}^d$. It is considered a level set function governed by the following linear advection equation with proper initial and boundary conditions:

$$\partial_t \phi + \mathbf{w} \cdot \nabla \phi = 0 \qquad \text{in } \bar{\Omega} \times (0,T], \tag{5.10a}$$

$$\phi = \phi_0 \qquad \text{in } \bar{\Omega} \times \{0\}, \tag{5.10b}$$

$$\phi = \phi_{\bar{\Omega}} \qquad \text{on } \partial\bar{\Omega} \times [0,T], \tag{5.10c}$$

where the smooth initial data $\phi_0(\mathbf{x})$ is given such that $\phi_0(\mathbf{x}) \neq 0$ for all $\mathbf{x} \in \partial\bar{\Omega}$. The boundary value $\phi_{\bar{\Omega}}(\mathbf{x},t)$ can be prescribed such that $\phi_{\bar{\Omega}}(\mathbf{x},t) = \phi_0(\mathbf{x})$ for all $t \in [0,T]$ on the inflow boundary $\partial\bar{\Omega}_-(t) := \{\mathbf{x} \in \partial\bar{\Omega} \mid \mathbf{w}(\mathbf{x},t) \cdot \mathbf{n}_{\bar{\Omega}}(\mathbf{x}) < 0\}$ where $\mathbf{n}_{\bar{\Omega}}$ is the outward unit normal on the boundary, and it simply takes value from the upwind neighborhood on the outflow boundary $\partial\bar{\Omega}_+(t) = \partial\bar{\Omega} \setminus \partial\bar{\Omega}_-(t)$. This boundary condition ensures that no new zero level is to be imported from the boundary. The hyperbolic PDE problem (5.10) is wellposed and has a unique weak solution in the corresponding Sobolev space, cf. [113, Theorem 3.4 in Section 3.1].

Next, let us derive the weak formulation corresponding to DG-FEM. In the spirit of relaxing the $\mathcal{H}^1$-conformity of the standard FEM, we introduce the broken Sobolev space for a consistent subdivision $\mathcal{T}_h$ of the background domain $\bar{\Omega} \subseteq \mathbb{R}^d$, $d = 1,2,3$ (e.g., an admissible quasi-uniform triangulation)

$$\mathcal{H}^1_{\hat{T}}(\bar{\Omega}) := \left\{ v \in \mathcal{L}^2(\bar{\Omega}) \;\mid\; v|_{\hat{T}} \in \mathcal{H}^1(\hat{T}),\ \forall \hat{T} \in \mathcal{T}_h \right\}. \tag{5.11}$$

Towards the non-conforming DG finite element discretization, a finite-dimensional broken Sobolev space of piecewise polynomials of degree k is defined by

$$\ddot{\mathcal{V}}_h(\bar{\Omega}) := \left\{ v \in \mathcal{L}^2(\bar{\Omega}) \;\mid\; v|_{\hat{T}} \in \mathcal{P}^k(\hat{T}),\ \forall \hat{T} \in \mathcal{T}_h \right\}. \tag{5.12}$$

By multiplying a test function $v_h \in \ddot{\mathcal{V}}_h(\mathcal{T}_h)$ on both sides of Equation 5.10a, and using integration by parts, the weak formulation reads:
To find $\phi_h \in \ddot{\mathcal{V}}_h(\mathcal{T}_h)$ such that for all $v_h \in \ddot{\mathcal{V}}_h(\mathcal{T}_h)$

$$\sum_{\hat{T} \in \mathcal{T}_h} \left(\partial_t \int_{\hat{T}} \phi_h v_h d\mathbf{x} - \int_{\hat{T}} \phi_h \mathbf{w} \cdot \nabla v_h d\mathbf{x} + \int_{\partial\hat{T}} \ddot{\phi}_h (\mathbf{w} \cdot \mathbf{n}_{\hat{T}}) v_h ds \right) = 0 \tag{5.13}$$

where the value on the boundary of each element $\hat{T}$, denoted by $\ddot{\phi}_h$, allows multiple choices resulting in various DG schemes, for which the upwind direction of wave propagation is preferred. If the hyperbolic equation is nonlinear, typically one needs to solve a Riemann problem (either exactly or approximately) to find the proper intermediate state, but here for the linear problem we can simply define

$$\ddot{\phi}_h := \begin{cases} \phi_h|_{\hat{T}} & \text{if } \ \mathbf{w} \cdot \mathbf{n}_{\hat{T}} \geq 0, \\ \phi_0 & \text{if } \ \mathbf{x} \in \partial\bar{\Omega}_-, \\ \phi_h|_{\check{T}} & \text{if } \ \mathbf{w} \cdot \mathbf{n}_{\hat{T}} < 0 \ \text{ and } \ \mathbf{x} \notin \partial\bar{\Omega}_-, \end{cases} \tag{5.14}$$

where the inflow boundary condition on $\partial\bar{\Omega}_-$ has been enforced, and $\check{T}$ denotes the element neighboring to $\hat{T}$ with whom it shares the interface $\partial\hat{T}$ equipped with the outward unit normal $\mathbf{n}_{\hat{T}}$ pointing from $\hat{T}$ to $\check{T}$. The resulting choice of $\mathbf{F}(\ddot{\phi}_h)$ in (2.26) is known as an upwind numerical flux.

The DG-FEM weak formulation (5.13) is a semi-discretization for the time being, i.e., $\phi_h(t)$ is the semi-discrete solution as an unknown function of time t, and we have the time derivative to be discretized yet.

5.2.2 Explicit Runge–Kutta discretization in time

Let $\mathfrak{L} := \sum_{|\alpha|\leq m} a_\alpha(\mathbf{x}) D^\alpha$ be an m^{th}-order differential operator, such that a linear time-dependent PDE (e.g., Equation 5.10a) can be written as

$$\partial_t \phi(\mathbf{x}, t) = \mathfrak{L}\phi(\mathbf{x}, t). \tag{5.15}$$

Let $\mathfrak{L}_h(\cdot,\cdot)$ be a spatial discretization of the differential operator $\mathfrak{L}$, in particular the discontinuous Galerkin discretization introduced in Subsection 5.2.1, then the DG-FEM semi-discrete form (5.13) can be considered as an ODE problem

$$\frac{d}{dt}\phi_h(t) = \mathfrak{L}_h(\phi_h, t), \qquad \phi_h(0) = \phi_0, \tag{5.16}$$

which is known as a scheme of the method of lines yet to be discretized with a time integrator.

Let $\Delta t := T/N,\ T \in \mathbb{R}_+, N \in \mathbb{N}$ be a uniform time step of an equally-spaced subdivision of the time interval $[0, T]$ of interest. Let $t_n := n\Delta t,\ n = 0, 1, ..., N$ be time instances for which we denote by upper index $(\cdot)^n := (\cdot)|_{t=t_n}$ the time-dependent objects restricted to $t = t_n$, e.g., $\phi_h^n := \phi_h(t_n)$ for the semi-discrete solution ϕ_h as a function continuous in time and the fully discrete solution ϕ_h^n at time t_n.

For higher order of accuracy in time, other than multi-step methods like BDF, we can solve (5.16) by multi-stage methods that use temporary in-between states on way from t_n to t_{n+1}. Among the multi-stage methods the explicit Runge–Kutta schemes are the most popular. The classical 2^{nd}-order and 4^{th}-order RK schemes can be formulated as follows:

- The 2^{nd}-order RK2 scheme:

$$\phi_h^{n+1} = \phi_h^n + \Delta t\, R_2; \tag{5.17}$$

- The 4^{th}-order RK4 scheme:

$$\phi_h^{n+1} = \phi_h^n + \frac{1}{6}\Delta t(R_1 + 2R_2 + 2R_3 + R_4); \tag{5.18}$$

where the intermediate stages

$$R_1 = \mathfrak{L}_h(\phi_h^n,\ t_n), \qquad R_2 = \mathfrak{L}_h\Big(\phi_h^n + \frac{1}{2}\Delta t\, R_1,\ t_n + \frac{1}{2}\Delta t\Big), \tag{5.19a}$$

$$R_3 = \mathfrak{L}_h\Big(\phi_h^n + \frac{1}{2}\Delta t\, R_2,\ t_n + \frac{1}{2}\Delta t\Big), \quad R_4 = \mathfrak{L}_h(\phi_h^n + \Delta t\, R_3,\ t_n + \Delta t). \tag{5.19b}$$

Although even higher orders are possible, the RK4 scheme is sufficiently accurate and will be employed in the implementations.

Remark 22 (CFL condition and TVD property)**.** *It is well-known that the Courant-Friedrichs-Lewy (CFL) condition has to be satisfied such that the Courant number* $\|\mathbf{w}\|_\infty \frac{\Delta t}{h} \leq c_{CFL}$ *for a certain (maximum allowed) constant* c_{CFL} *for linear stability and consequently (with consistency by the Lax equivalence theorem) convergence of an explicit time stepping scheme, cf. [108]. Although this sub-model for level set transport is a linear hyperbolic problem starting with smooth initial data that is assumed not to develop discontinuities, the level set function solved within each time step in the geometrically coupled problem may contain kinks or even discontinuities. In order to achieve nonlinear stability, the total variation diminishing (TVD) schemes are suggested for discontinuous solutions to hyperbolic conservation laws, for example, the TVD Runge–Kutta schemes proposed in [72, 149, 150]. The classical RK2 and RK4 schemes above-mentioned are of the TVD property under certain CFL condition with* $c_{CFL} = 1$ *and* $c_{CFL} = \frac{2}{3}$*, respectively, for one-dimensional problems and divided by* d *for problems in* d *spatial dimensions, according to the results in [150]. In practice, we will set sufficiently small Courant numbers to ensure the CFL condition and the TVD property to be fulfilled.*

5.2.3 Error analysis and numerical experiment

Although the RKDG methods have been widely used by the CFD community, the theoretical analysis is lagging behind the applications. The error estimates of the RK and the DG schemes are both well-investigated, but it is not straightforward to derive the order of convergence for the fully discrete RKDG methods. To the best of our knowledge, most a priori error analyses exist for either semi-discrete or space-time DG methods only, provided that the exact solutions are sufficiently smooth. For example,

in [7] the authors show that the error bound of $\mathcal{O}(h^{k+\frac{1}{2}})$ holds for advection-dominated problems, whereas $\mathcal{O}(h^k)$ for diffusion-dominated and $\mathcal{O}(h^{k+1})$ for reaction-dominated problems, in which the $\mathcal{L}^2$ norms of the distances between DG solutions of piecewise polynomials of degree k and smooth exact solutions to stationary advection-diffusion-reaction problems are estimated, cf. [113, Section 7.1]. In [148], Shu concludes that the DG methods have at least $(k+\frac{1}{2})^{\text{-th}}$ order of accuracy, and often optimal $(k+1)^{\text{-th}}$ order, for smooth solutions regardless of the mesh structures, and possibly $(2k+1)^{\text{-th}}$ order super-convergence in negative norm and in strong $\mathcal{L}^2$ norm for post-processed solutions, cf. [39, 90, 95].

As for the error estimates of the RKDG methods, one challenge lies ahead of them beyond the method of lines that the fully discrete $\mathcal{L}^2$ stability is hard to be established with explicit Runge–Kutta time discretizations, as well as another difficulty sits on finding appropriate projection operators for the analysis, according to the discussion in [154]. In spite of these issues, some creative works of analyzing the RKDG methods for hyperbolic conservation laws have been presented in the past decades, e.g., in [35, 164, 168–170]. In this subsection, we collect several important results of error estimate from the established literature, and subsequently provide a numerical example to verify the order of convergence they predicted.

Selected error estimates

First of all, we begin with an analysis of the Crank–Nicolson DG method presented in [113, Chapter 7], which does not utilize the explicit Runge–Kutta time stepping but the well-known implicit Crank–Nicolson scheme in time combined with the discontinuous Galerkin discretization in space. However, the application in [113] is the same as ours and the idea in the proof may be useful. We therefore introduce the main result of error estimate in [113].

Theorem 10 (Error estimate of the Crank–Nicolson DG method for level set transport)**.** *Let $\phi \in \mathcal{C}^2([0,T];\mathcal{H}^1(\bar{\Omega})) \cap \mathcal{C}^1([0,T];\mathcal{H}^{k+1}(\bar{\Omega}))$ be the exact solution to the PDE problem (2.31) or (5.10). Let $\{\phi_h^n\}_{n=0,\ldots,N}$ be the numerical solution to the fully discrete form of the Crank–Nicolson DG scheme, cf. [113, Equation 4.47]. For constants $c(\phi,\mathbf{w},t^n)$ and $C(\phi,\mathbf{w},t^n)$ independent of the mesh size h and the time step Δt, the following error estimate holds true:*

$$\|\phi(\mathbf{x},t_n)-\phi_h^n\|_{\mathcal{L}^2(\bar{\Omega})} \leq c(\phi,\mathbf{w},t^n)h^{k+\frac{1}{2}} + C(\phi,\mathbf{w},t^n)\Delta t^2,$$

where k is the piecewise polynomial degree of the DG finite element space.

Proof. See [113, Theorem 7.19].

□

Remark 23. *This result gives the error bounds $\mathcal{O}(h^{k+\frac{1}{2}})$ in space and $\mathcal{O}(\Delta t^2)$ in time in the $\mathcal{L}^2$ norm. It is well-known that the Crank–Nicolson scheme is 2^{nd}-order accurate, thus the order of convergence in time is optimal. While the convergence rate in space may be not optimal, but expected according to the prior predictions, e.g., in [7], since the level set transport is a purely advection-dominated problem. We emphasize that the result holds only for smooth solution, under the assumption of a time-independent, divergence-free, globally Lipschitz-continuous velocity field without any closed curves or stationary points.*

Next, let us turn to the error estimates of the RKDG methods. The following result is presented by Zhang and Shu in [169] for the 2nd-order total variation diminishing (TVD) Runge–Kutta discontinuous Galerkin method for sufficiently smooth solutions to scalar conservation laws.

Theorem 11 (Error estimate of the 2nd-order TVD RKDG method)**.** *Let $\phi(\mathbf{x},t)$ be the sufficiently smooth exact solution to the linear scalar hyperbolic conservation law (2.26) posed on $\bar{\Omega}\times[0,T]$, which is periodic or compactly supported and whose derivatives are bounded. Let $\{\phi_h^n\}_{n=0,\dots,N}$ be the numerical solution to the fully discrete form of the 2^{nd}-order TVD RKDG method, cf. [169, Equation 2.4]. If an upwind numerical flux is used, then for sufficiently small mesh size h and time step Δt the following error estimate holds true:*

$$\max_{0\leq n\leq N}\|\phi(\mathbf{x},t_n)-\phi_h^n\|_{\mathcal{L}^2(\bar{\Omega})}\leq C(h^{k+1}+\Delta t^2),$$

where the constant C is independent of h, Δt, n and N. The result holds for the piecewise polynomials of degree $k=1$ under the CFL condition $\Delta t\leq c_{CFL}h$ or $k\geq 2$ under $\Delta t\leq c_{CFL}h^{\frac{4}{3}}$ with a properly given Courant number c_{CFL}. Moreover, the result still holds for nonlinear problems if $k>\frac{d+1}{2}$ and thus $\|\phi(\mathbf{x},t_n)-\phi_h^n\|_{\mathcal{L}^2(\bar{\Omega})}\leq h$ is assumed to be true.

Proof. See [169, Theorem 3.1 and Remark 5.2].

□

Remark 24. *This result gives optimal orders of convergence $\mathcal{O}(h^{k+1})$ in space and $\mathcal{O}(\Delta t^2)$ in time, provided that the exact solution is sufficiently smooth and an upwind numerical flux is chosen, otherwise quasi-optimal $\mathcal{O}(h^{k+\frac{1}{2}})$ in space for a general monotone numerical flux. The original Theorem 3.1 in [169] holds only for one-dimensional*

scalar conservation laws, but the result has been extended to multi-dimensional linear and nonlinear problems according to Remark 5.2 in [169]. We stress that the authors do not consider specific boundary conditions. Similar result but quasi-optimal $\mathcal{O}(h^{k+\frac{1}{2}})$ *convergence rate in space is given in [168, Theorem 2.1] for symmetrizable systems of conservation laws. In [170, Theorem 5.1] the result is further extended to the* 3^{rd}*-order TVD RKDG method which remains the same order of convergence in space but rises to* $\mathcal{O}(\Delta t^3)$ *in time.*

All the error estimates above are for sufficiently smooth exact solutions, which become invalid when the solutions contain discontinuities. In practice, discontinuous solutions may be developed from smooth initial data through nonlinear hyperbolic equations, or retained from discontinuous initial data in linear problems. It is therefore worth mentioning the following result by the work of Cockburn and Guzmán in [35].

Theorem 12 (Error estimate of non-smooth solution to 1d linear transport equation)**.** *Let* $\phi(x,t)$ *be the exact solution to the hyperbolic conservation law* (2.26) *posed on* $\mathbb{R}\times[0,T]$ *with* $\mathbf{w}=1$*, and the compactly supported initial data is discontinuous at* $x=0$ *but smooth everywhere else. Let* $\{\phi_h^n\}_{n=0,\dots,N}$ *be the numerical solution to the fully discrete form of the* 2^{nd}*-order TVD RKDG method, cf. [35, Equation 2.1]. Provided that* $\frac{\Delta t}{h}\le\frac{\alpha}{3}$ *for some fixed* $\alpha\in(0,\frac{1}{3})$*, then for any* $\beta\ge 4$ *and a constant* $C>0$ *independent of* h*,* Δt*,* T*, and* α*, the following error estimate holds true:*

$$\|\phi(x,T)-\phi_h^N\|_{\mathcal{L}^2(\mathbb{R}\setminus\mathcal{R}_D)}\le CTh^2\left(1+\left(\frac{\Delta t}{\alpha T}\right)^{\frac{1}{2}}\right)+Ch^\beta+\|\phi(x,T)-P(\phi(x,T))\|_{\mathcal{L}^2(\mathbb{R}\setminus\mathcal{R}_D)}$$

where the region containing the discontinuity denoted by $\mathcal{R}_D$ *is given by*

$$\mathcal{R}_D=T+\alpha^{-1}\beta\gamma\log(h^{-1})\left(-(\Delta t/h)^{-\frac{7}{3}}T^{\frac{1}{3}}h^{\frac{2}{3}},\ (\Delta t/h)^{-\frac{1}{2}}T^{\frac{1}{2}}h^{\frac{1}{2}}\right)$$

where the constant $\gamma>0$*, and the projection* $P(v)$ *of a function* $v\in\mathcal{H}^1_{\hat{T}}(\mathbb{R})$ *is in the finite-dimensional broken Sobolev space* $\ddot{\mathcal{V}}_h(\mathbb{R})$ *of piecewise polynomials of degree* 1*, cf.* (5.11) *and* (5.12)*, such that on each interval* $\hat{T}(j):=(x_{j-1/2},x_{j+1/2})$*,* $j\in\mathbb{Z}$ *there hold* $(P(v),1)_j=(v,1)_j$ *and* $P(v)(x^-_{j+1/2})=v(x^-_{j+1/2})$ *for* $\{\hat{T}(j)\}_{j\in\mathbb{Z}}$ *a uniform partition of* $\mathbb{R}$*.*

Proof. See [35, Theorem 2.1].

□

Remark 25. *This result is an extension of and can be reduced to Theorem 11 with* $k=1$*, when the initial data is sufficiently smooth. The error bound* $\mathcal{O}(h^2)$ *at time*

T in the $\mathcal{L}^2(\mathbb{R}\setminus\mathcal{R}_D)$ norm shows optimal order of convergence in space. This error estimate of non-smooth solutions is considered a milestone towards the goal of solving nonlinear hyperbolic conservation laws in multiple spatial dimensions, but only the case of one-dimensional linear identity-coefficient transport equation is as yet studied.

We have shown the error estimates of the 2^{nd}-order (and the 3^{rd}-order) TVD RKDG method, however, the extension to higher order of accuracy in time is highly non-trivial, which has become available only recently. Next, we introduce the main result of error analysis in this subsection that is recently presented in [164].

Theorem 13 (Error estimate of the 4^{th}-order RKDG method)**.** *Let $\phi(\mathbf{x},t)$ be the sufficiently smooth exact solution to the hyperbolic conservation law (2.26) posed on $\bar{\Omega}\times[0,T]$ where $\bar{\Omega}=(0,1)^2$ with a constant coefficient $\mathbf{w}$. Let $\{\phi_h^n\}_{n=0,\dots,N}$ be the numerical solution to the fully discrete form of the 4^{th}-order RKDG method whose parameters satisfy a weak smoothness assumption, cf. [164, Section 2.3, 2.4, 2.5]. For a constant $C>0$ independent of mesh size h and time step Δt, the following error estimate holds true:*

$$\max_{0\le n\le N}\|\phi(\mathbf{x},t_n)-\phi_h^n\|_{\mathcal{L}^2(\bar{\Omega})}\le C(h^{k+k'}+\Delta t^4)$$

if the CFL condition $\Delta t\le c_{CFL}h$ holds for a specific Courant number c_{CFL}. The index k denotes the piecewise polynomial degree of the DG finite element space, and $k'=1$ arises from $\mathcal{Q}^k$-elements of rectangles while $k'=\frac{1}{2}$ from $\mathcal{P}^k$-elements of either rectangles or triangles.

Proof. See [164, Theorem 2.2].

□

Remark 26. *This result gives optimal order of convergence $\mathcal{O}(\Delta t^4)$ in time, while optimal $\mathcal{O}(h^{k+1})$ and quasi-optimal $\mathcal{O}(h^{k+\frac{1}{2}})$ in space. The analysis is conducted in two-dimensional linear case, but the authors claim that the result can be trivially extended to problems in arbitrary spatial dimensions, and even to nonlinear problems along the same lines as in [169, 170]. In spite of the only restriction placed on the regularity of the exact solution which has to be sufficiently smooth, we consider it an enlightening error estimate of the 4^{th}-order RKDG method for hyperbolic PDEs.*

To conclude this subsection, we introduce the most recent work by Sun and Shu in [154] that is a framework of error estimates of the RKDG method of any order for linear time-dependent PDEs. We briefly present the main result with skipping the details of the statement but refer the reader to [154, Theorem 3.2 and Corollary 3.1].

Theorem 14 (Error estimate of the RKDG method of any order for linear PDEs)**.** *Let $\phi(\mathbf{x},t)$ be the sufficiently smooth exact solution to a linear time-dependent PDE $\partial_t\phi = \mathfrak{L}\phi$ posed on $\bar{\Omega}\times[0,+\infty)$ for $\bar{\Omega}\subseteq\mathbb{R}^d$ where $\mathfrak{L}$ is an m^{th}-order differential operator, cf. Equation 5.15. Let $\{\phi_h^n\}_{n=0,\dots,N}$ be the numerical solution to the fully discrete form of the RKDG method of any order, cf. [154, Equation 1.3]. For two constants c and C independent of mesh size h and time step Δt, the following error estimate holds true:*

$$\|\phi(\mathbf{x},t_n)-\phi_h^n\|_{\mathcal{L}^2(\bar{\Omega})} \leq \exp(ct_n)\|\Pi\phi(\mathbf{x},0)-\phi_h^0\|_{\mathcal{L}^2(\bar{\Omega})} + C(\sigma+1)(h^{k+k'}+\Delta t^s)$$

under [154, Assumption 2.3, 2.4, 2.5] for stability of the fully discrete form, consistency of the RK scheme, and the linear operator Π, respectively. Here, $(1+c\Delta t)$ is used to bound the fully discrete operator under the CFL condition $\Delta t \lesssim c_{CFL}h^m$ for a specific Courant number c_{CFL}, and $\sigma(c,t_n)$ arises from the Grönwall's inequality, and C depends on the parameters of the RK scheme. The index k denotes the piecewise polynomial degree, $k'\in[0,1]$ depends on the specific problem, and s indicates the linear order of accuracy of the time integrator.

Proof. See [154, Theorem 3.2 and Corollary 3.1].

□

Remark 27. *This result may be considered an instructive extension of Theorem 13, since it is adaptable to arbitrary explicit RK schemes of any order with a variety of DG discretizations, and goes beyond the hyperbolic conservation laws. The error bound $\mathcal{O}(h^{k+k'}+\Delta t^s)$ implies that we can obtain optimal order of convergence in time while it depends on the specific problem in space. We notice that the requirement of the regularity, i.e., the exact solution has to be sufficiently smooth, still exists.*

As we have seen, all the error estimates above-mentioned are restricted either to the smoothness of the exact solution or to the linearity and dimensionality of the problem. In addition, most of the analyses do not consider specific boundary conditions. To the best of our knowledge, there is no a priori error estimate of the RKDG methods for the (possibly non-smooth) level set transport problem (5.10) available yet. However, Theorem 13 may be regarded as a useful error estimate if we assume the regularity of the solution and prescribe a periodic boundary condition to our problem.

Numerical test

Although the RKDG methods for a variety of problems have been extensively verified with respect to the convergence rates in an established literature, cf. [41], we present a

numerical example of solving the level set transport equation in two spatial dimensions by using the 4^{th}-order RKDG method with polynomial order $k=3$.

Let $\mathbf{x}=(x_1,x_2)$ be the standard Cartesian coordinate system. The PDE problem (5.10) is considered such that a real-valued level set function $\phi(\mathbf{x},t)$ is defined on a square background domain $\bar{\Omega}=(-1.2,1.2)^2$ for time $t\in[0,T]$, $T=1$, whose negative level sets represent a domain $\Omega(t)$ moving and transforming from a disk towards an airfoil shape within the unit disk $\{\mathbf{x}\in\bar{\Omega}\,|\,x_1^2+x_2^2\leq 1\}$. To this end, we define a velocity field

$$\mathbf{w}(\mathbf{x},t)=\operatorname{sgn}(0.5-t)\ z\ [-x_2,x_1]^{\mathrm{T}} \qquad \text{on } \bar{\Omega}\times[0,T] \tag{5.20}$$

that changes the direction at $t=0.5$. The parameter $z:=\max\{1-x_1^2-x_2^2,\ 0\}$ is set to avoid the background boundary. The initial geometry is described by

$$\phi_0(\mathbf{x}):=\phi(\mathbf{x},0)=(x_1-0.4)^2+(x_2-0.4)^2-0.25^2. \tag{5.21}$$

This problem has an analytic solution

$$\phi(\mathbf{x},t)=\phi_0(\mathbf{x}_0) \qquad \text{for } \mathbf{x}_0=[x_1\cos(zt)+x_2\sin(zt),x_1\sin(zt)+x_2\cos(zt)]^{\mathrm{T}} \tag{5.22}$$

that can be found through the characteristics. We measure the $\mathcal{L}^2$-error of the discrete level set domain by integrating the exact level set function (which is zero on the exact interface) along the discrete interface $\Gamma_h^n:=\{\mathbf{x}\in\bar{\Omega}\,|\,\phi_h^n=0\}$ and taking maximum for $n=0,\ldots,N$

$$\max_{0\leq n\leq N}\|\phi\|_{\mathcal{L}^2(\Gamma_h^n)}=\max_{0\leq n\leq N}\left(\int_{\Gamma_h^n}\phi^2\ ds\right)^{\frac{1}{2}}. \tag{5.23}$$

To implement the 4^{th}-order RKDG method, we generate an unstructured computational mesh consisting of triangles with an initial mesh size $h_0=0.6$ for the background domain $\bar{\Omega}$. The initial time step $\Delta t_0=\frac{T}{100}=0.01$ is set sufficiently small to satisfy the CFL condition, cf. Remark 22. The refinements in space and in time are executed in such a way that the mesh size $h=2^{-L}\ h_0$ and the time step $\Delta t=4^{-L}\Delta t_0$ for the uniform refinement level $L=0,1,2,3$.

We plot the numerical results in Figure 5.2.

The curves in Figure 5.2 show the convergence rates higher than $k+\frac{1}{2}$. We further make Table 5.1 to look into the experimental orders of convergence (EOC).

From Table 5.1, we observe that the EOC is around 3.5 when $k=3$ as the optimal choice, which is in agreement with the prediction of Theorem 13.

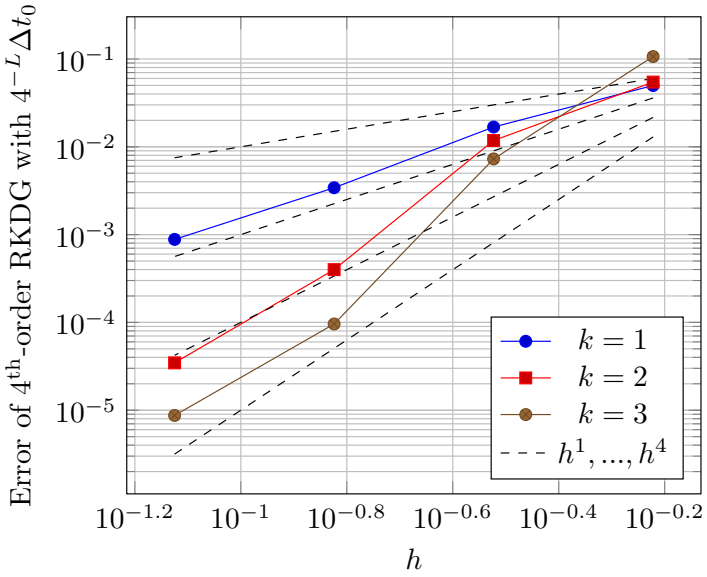

Fig. 5.2 $\mathcal{L}^2$-error convergence curves of the level set domain computed by the 4^{th}-order RKDG method for $k=1,2,3$.

Table 5.1 $\mathcal{L}^2$-error table of the level set domain computed by the 4^{th}-order RKDG method for $k=1,2,3$. The numbers are truncated to two decimal places without rounding, but the EOC in round brackets are computed based on double precision and then truncated to two decimal places without rounding.

L	$k=1$	$k=2$	$k=3$
0	$4.98\cdot10^{-2}$	$5.45\cdot10^{-2}$	$1.06\cdot10^{-1}$
1	$1.67\cdot10^{-2}$ (**1.57**)	$1.17\cdot10^{-2}$ (**2.21**)	$7.27\cdot10^{-3}$ (**3.87**)
2	$3.41\cdot10^{-3}$ (**2.29**)	$3.99\cdot10^{-4}$ (**4.88**)	$9.59\cdot10^{-5}$ (**6.24**)
3	$8.81\cdot10^{-4}$ (**1.95**)	$3.46\cdot10^{-5}$ (**3.52**)	$8.71\cdot10^{-6}$ (**3.46**)

5.3 Summary

In this chapter, we have proposed the numerical methods for solving the third sub-model of the level set evolution problem. In particular, when a physical domain is represented by a level set function, the evolution of the level set domain is governed by a hyperbolic transport equation, which can be solved numerically by the Runge–Kutta discontinuous Galerkin methods, provided that the velocity field in the equation is obtained by the surface velocity extension methods. We have introduced two different methods for extending the surface velocity other than the famous Fast Marching Method, namely, the normal diffusion and the ghost penalty extension methods that follow the same mechanisms as discussed in the last two chapters. Moreover, we have introduced the

space and time discretizations of the RKDG methods, which are sufficiently accurate and robust for hyperbolic problems, followed by several notable error estimates and a numerical test for the experimental order of convergence. This sub-model bridges the previous two sub-models together for solving the osmotic cell swelling problem as a toy model of the class of geometrically coupled solution-curvature-driven moving free boundary problems, which will be implemented in the following chapter.

Chapter 6

Computation of the Geometrically Coupled Problem

In Chapter 2 we have proposed the mathematical models of the geometrically coupled solution-curvature-driven moving *free boundary problem* (FBP). In order to solve the first sub-model numerically, in Chapter 3 we have developed the higher-order isoparametric BDF *Eulerian finite element method* (Eulerian FEM) for PDEs on a time-dependent domain enclosed by a level set hypersurface. For the second sub-model, we have developed the high-order isoparametric stabilized *trace finite element method* (TraceFEM) to compute the mean curvature vector of the bounding hypersurface in Chapter 4. To solve the third sub-model, in Chapter 5 we have introduced two extension methods for the solution-curvature-based velocity along with the high-order *Runge–Kutta discontinuous Galerkin* (RKDG) methods for the evolution of the time-dependent level set domain. In this chapter, we glue the building blocks all together towards a proof-of-concept simulation of the geometrically coupled moving FBP, of which the osmotic cell swelling problem represents as a toy model (i.e., osmosis model). As discussed in Section 2.4, each equation in the osmosis model is indeed linear but they are nonlinearly coupled into the system. A linearization is therefore necessary for solving the system of equations numerically. To this end, we will introduce two algorithms to decouple the system and to solve each linear sub-model within each time step. The first strategy which we call *weak coupling* solves each equation only once at each time step without the guarantee of uniform convergence, while the second one called *strong coupling* searches the convergence of the solution satisfying all the equations through a fixed-point iteration within each time step.

6.1 The algorithms for the coupled system

Towards the nonlinearity of the coupled system of PEDs, there are two strategies we call *weak coupling* and *strong coupling*. Roughly speaking, the weak coupling algorithm linearizes the problems and solves each sub-model just once for each time step regardless of convergence, while the strong coupling algorithm searches convergence of all the variables through a fixed-point iteration within each time step before marching to the next time step. The features of the two algorithms are summarized as follows:

- Weak coupling:

  Cheap in computational cost,

  Much more robust,

  Relatively simple in implementation,

- Strong coupling:

  Expensive in computational cost,

  Less stable and even not convergent,

  More complicated in implementation,

Next, let us introduce the two algorithms with flow chats.

6.1.1 Weak coupling algorithm

Recalling the procedure for unrolling the coupled system of equations and the corresponding notation in Section 2.4, we follow the similar lines with a time discretization. Based on a uniform partition of the time interval $(0,T] = \bigcup_{n=0,1,...,N}(t_n, t_{n+1}]$ for a variable $v^n = v(\cdot, t_n)$, the weak coupling pseudo-algorithm runs for time step $n = 0, 1, ..., N$ as follows:

(1) With a level set function ϕ^n representing the interface by its zero level set, the geometric equation (2.43a) gives the mean curvature κ^n:

$$\kappa^n \longleftarrow \mathfrak{A}(\phi^n) \tag{6.1}$$

by using the stabilized isoparametric TraceFEM developed in Chapter 4, based on a deformed mesh from the isoparametric mapping;

(2) With a scalar-valued physical quantity u^n in addition to κ^n, the geometric evolution equation (2.43b) gives the surface velocity w^n:

$$w^n \longleftarrow \mathfrak{B}(\kappa^n, u^n) \tag{6.2}$$

by simply adding the two factors;

(3) With the surface velocity w^n and the unit normal as a function of ϕ^n by (2.43e), the velocity extension equation (2.43d) and the consistency condition (2.43c) give the compatible velocity field $\mathbf{w}^n$:

$$\mathbf{w}^n \longleftarrow \mathfrak{C}(w^n, \phi^n) \tag{6.3}$$

by using the velocity extension methods presented in Section 5.1, which is then mapped from the deformed mesh back to the undeformed mesh, cf. Subsection 6.1.3 for details;

(4) With the velocity field $\mathbf{w}^n$, the level set transport equation (2.43f) based on the initial condition (2.43g) at time t_n and the boundary condition (2.43h) updates the level set function ϕ^n:

$$\phi^{n+1} \longleftarrow \mathfrak{D}(\mathbf{w}^n, \phi^n, \phi_{\bar{\Omega}}) \tag{6.4}$$

by using the RKDG methods introduced in Section 5.2, based on the undeformed background mesh;

(5) With the level set function $\phi^{n+1}, \phi^n, ..., \phi^{n+1-r}$, $r \in \mathbb{N}$, and the linearized velocity field $\mathbf{w}^n$, the diffusion equation (2.43i) based on the initial condition (2.43k) at time t_n and the boundary condition (2.43j) updates the physical quantity u^n:

$$u^{n+1} \longleftarrow \mathfrak{E}(\phi^{n+1}, \phi^n, ..., \phi^{n+1-r}, \mathbf{w}^n, u^n) \tag{6.5}$$

by using the isoparametric BDF-r Eulerian FEM developed in Chapter 3, based on a deformed mesh from the isoparametric mapping;

(6) Loop back to Step (1) with updating the time step n:

$$n \leftarrow n+1. \tag{6.6}$$

This weak coupling algorithm with linearization of the nonlinearly coupled system works well if the uniform size of time step between the time instances $\Delta t = |t_{n+1} - t_n|$ is chosen sufficiently small. Otherwise, one needs to search convergence within each time step, which gives rise to the following strong coupling strategy.

6.1.2 Strong coupling algorithm

The strong coupling algorithm indeed follows the similar lines along with its weak counterpart, but it is equipped with an additional residual function that measures the distance between the current and the updated variables within a sub-time loop. The residual function can be defined by

$$\Delta_n^m := \|\phi^m - \phi^n\| + \|u^m - u^n\| + \|\mathbf{w}^m - \mathbf{w}^n\| \leq \delta \tag{6.7}$$

where $\delta \in \mathbb{R}_+$ is a positive constant of tolerance prescribed to control the difference. We add this criterion to the end of step (5) in the weak coupling algorithm: if it holds true then we continue to (6), or else go back to (1). Recalling the steps and the corresponding notation in Subsection 6.1.1, the strong coupling pseudo-algorithm can be summarized with the in-between time step m as follows:

(A) For $n = 0, 1, ..., N$:

(1) $\kappa^m \longleftarrow \mathfrak{A}(\phi^n)$

(2) $w^m \longleftarrow \mathfrak{B}(\kappa^m, u^n)$

(3) $\mathbf{w}^m \longleftarrow \mathfrak{C}(w^m, \phi^n)$

(4) $\phi^m \longleftarrow \mathfrak{D}(\mathbf{w}^m, \phi^n, \phi_{\bar{\Omega}})$

(5) $u^m \longleftarrow \mathfrak{E}(\phi^m, \phi^n, ..., \phi^{n+1-r}, \mathbf{w}^m, u^n)$

(6) If $\Delta_n^m > \delta$ then go to (1) with $(\kappa^n, w^n, \mathbf{w}^n, \phi^n, u^n) \leftarrow (\kappa^m, w^m, \mathbf{w}^m, \phi^m, u^m)$

(B) $(\kappa^{n+1}, w^{n+1}, \mathbf{w}^{n+1}, \phi^{n+1}, u^{n+1}) \leftarrow (\kappa^m, w^m, \mathbf{w}^m, \phi^m, u^m)$ and go back to (A).

Due to the additional criterion (6), this strong coupling algorithm does not march forward to the next time step until the difference between the iterative solutions Δ_n^m is smaller than the tolerance δ. More specifically, in order to ensure the numerical solution at a time instance satisfies all the equations in the coupled system, we solve each of the sub-models multiple times and perform the fixed-point iteration to seek convergence of the solution through a sub-time loop within each time step before moving into the next time step. The strong coupling algorithm is therefore much more time-consuming – and theoretically more accurate – than the weak one.

6.1.3 Mesh transfer operator

Recall Subsection 3.1.4 and Subsection 3.2.1 where an operator is established to transfer the functions between differently mapped meshes at different time steps. Similarly, in the geometrically coupled problem we have the physical quantity u and the mean curvature κ on isoparametrically mapped meshes but the level set function ϕ on the background mesh that is undeformed, which gives rise to the requirement of using an operator to transfer the functions from the deformed mesh to the undeformed one at each time step.

More specifically, in Step (2) of the coupling algorithms we have u and κ to compute the surface velocity w on an isoparametrically mapped mesh, and in Step (3) w is extended to the velocity field $\mathbf{w}$ based on the unit normal $\mathbf{n}$ also with respect to the deformed mesh. However, in Step (4) we intend to apply the velocity field $\mathbf{w}$ (defined on the deformed mesh yet) to the undeformed background mesh in order to transport the level set function ϕ, where a mesh transfer operator is needed to send $\mathbf{w}$ to the background mesh. To this end, with the velocity fields on the background mesh and the mapped mesh denoted by $\mathbf{w}^m_{\mathcal{T}_h}$ and $\mathbf{w}^m_{\mathcal{T}_h^m}$ respectively, we add the following step between Step (3) and (4):

$$\mathbf{w}^m_{\mathcal{T}_h} \longleftarrow \Pi^0_m(\mathbf{w}^m_{\mathcal{T}_h^m})$$

where $\Pi^0_m : \mathcal{V}_h^m \to \mathcal{V}_h$ implies the mesh transfer operator analogously as in Subsection 3.1.4 and Subsection 3.2.1. Without this mesh transfer procedure, we can expect that even the strong coupling algorithm would give a low-order result only.

6.2 Numerical experiments

As we have briefly discussed in Section 1.2, generally speaking, an analytic solution to the geometrically coupled bulk-surface model is not known to exist, and even a manufactured solution is not practicable, due to the complexity of the problem. It on the one hand motivates us to develop the numerical methods aforementioned, while on the other hand it also challenges us to carry out the convergence study. In other words, we have to investigate some simplified examples in order to compare our numerical results to the exact solutions that are accessible.

Basically, we could consider three options for the convergence study. First of all, we may set super high orders for the numerical methods and then regard the result as exact solution to be compared. This approach requires sufficiently high order of accuracy in both space and time. However, the isoparametric BDF-FEM is limited to

3^{rd} order yet and the RKDG methods are known to have up to 5^{th} order in time, which are not qualified enough to be considered as exact. Secondly, a rotationally symmetric and quasi-stationary solution is possible based on the assumptions of isotropic diffusion and spherical geometry. In [132, Subsection 4.2] and in [160, Subsection 5.3.1] the authors have tested a benchmark under this configuration. Assume a circle of an initial radius R_0, and the initial physical quantity u_0 is spatially homogeneous, then the conservation of $u(t)$ ensures $u(t)\pi R(t)^2 = u_0\pi R_0^2$ for all time $t \in [0,T]$, and hence

$$\frac{dR}{dt} = -\alpha\kappa + \beta u = -\frac{\alpha}{R} + \frac{\beta u_0 R_0^2}{R^2} \tag{6.8}$$

holds true due to the mean curvature $\kappa = \frac{1}{R}$ and the geometric evolution Equation 2.2. Once this ordinary differential equation (ODE) is solved for $R(t)$, we get $u(t)$ solved and to be compared with $u_h(\cdot,t)$ which is computed by our numerical methods. This ODE does not have an explicit solution in a closed-form expression, though it can be solved numerically by some standard ODE solver at some accuracy level, namely, the solution is not truly exact. Trivially setting $u_0 = 0$ results in the third choice we take, where we have an analytic solution to the mean curvature flow, cf. Subsection 2.1.5.

In the first example, we will verify the weak and strong coupling algorithms with the simplest shrinking circle problem. As a first benchmark, we will test the coupling between the stabilized isoparametric TraceFEM for mean curvature vector and the RKDG method for level set transport, and study the error convergence based on the analytic solution to the mean curvature flow. Subsequently, we will perform a proof-of-concept numerical simulation of the full osmosis model equipped with a more flexible geometry in the second example. We will combine the three sub-models by using the coupling algorithms, and implement the proposed numerical methods to solve the geometrically coupled bulk-surface PDEs as a moving free boundary problem.

6.2.1 Mean curvature flow of shrinking circle

As a first benchmark for convergence study, we consider the shrinking circle problem, which has analytic solution in a closed-form expression, cf. Chapter 6.

Recall the ODE system (2.21) that describes a shrinking ball under the prototype mean curvature flow

$$R(t) = \left(R_0^2 - 2(d-1)t\right)^{\frac{1}{2}} \qquad \text{for } t \in [0,T),\ T = \frac{R_0^2}{2(d-1)} \tag{6.9}$$

where the initial condition $\Gamma(0) = \mathcal{B}_{R_0}(\mathbf{x}_0)$ is given. We simply take $d = 2$ and $R_0 = 1$ for an initial unit circle and get the time-dependent exact domain area

$$A(t) = \pi R(t)^2 = \pi(1 - 2t). \tag{6.10}$$

A level set function is employed to represent the initial unit circle in the standard Cartesian coordinate system $\mathbf{x} = (x_1, x_2)$ such that

$$\phi(0) = x_1^2 + x_2^2 - 1. \tag{6.11}$$

The level set domain evolves under a velocity field, which is obtained by velocity extension from the surface, defined as the *negative* mean curvature vector in (2.3). The mean curvature vector is computed by using the stabilized isoparametric TraceFEM with equivalent orders $k = q = 4$. For stabilization and extension, both the direct version and the derivative jump ghost penalty are tested. By solving the level set transport equation, the 4^{th}-order RKDG method with polynomial order $k = 4$ gives rise to a time-dependent level set solution $\phi_h(t)$ to compute the discrete domain area

$$A_h(t) = \int_{\{\phi_h(t)<0\}} 1 \, d\mathbf{x}. \tag{6.12}$$

The weak coupling algorithm and the strong one are both tested, but there is no significant difference between the numerical results, though the computational cost differs. See Figure 6.1 for a numerical simulation of the shrinking circle problem.

Analogously to (3.57) we can measure the numerical errors by defining two discrete norms

$$\|A - A_h\|^2_{\mathcal{L}^2(T)} := \sum_{n=1}^{N} \Delta t \left| \frac{A(t_n) - A_h(t_n)}{A(t_n)} \right|^2, \tag{6.13}$$

$$\|A - A_h\|_{\mathcal{L}^\infty(T)} := \max_{n=1,\dots,N} \left| \frac{A(t_n) - A_h(t_n)}{A(t_n)} \right|^2, \tag{6.14}$$

for an initial time step $\Delta t_0 = 0.02$ and a final time $T = 0.1$. The errors are scaled by $|A(t_n)|$. We generate a square background mesh on $(-1.2, 1.2)^2$ with an initial mesh size $h_0 = 0.5$. By applying successive regular refinements in space $h = 2^{-L} h_0$ and in time $\Delta t = 2^{-L} \Delta t_0$ for the refinement level $L = 0, 1, 2, 3, 4$, we plot the $\mathcal{L}^2(T)$-error and the $\mathcal{L}^\infty(T)$-error at 5 space-time levels in Figure 6.2.

From Figure 6.2 we observe that both the $\mathcal{L}^2(T)$-error and the $\mathcal{L}^\infty(T)$ of the domain area converge, with the convergence rates similar for different ghost penalty versions.

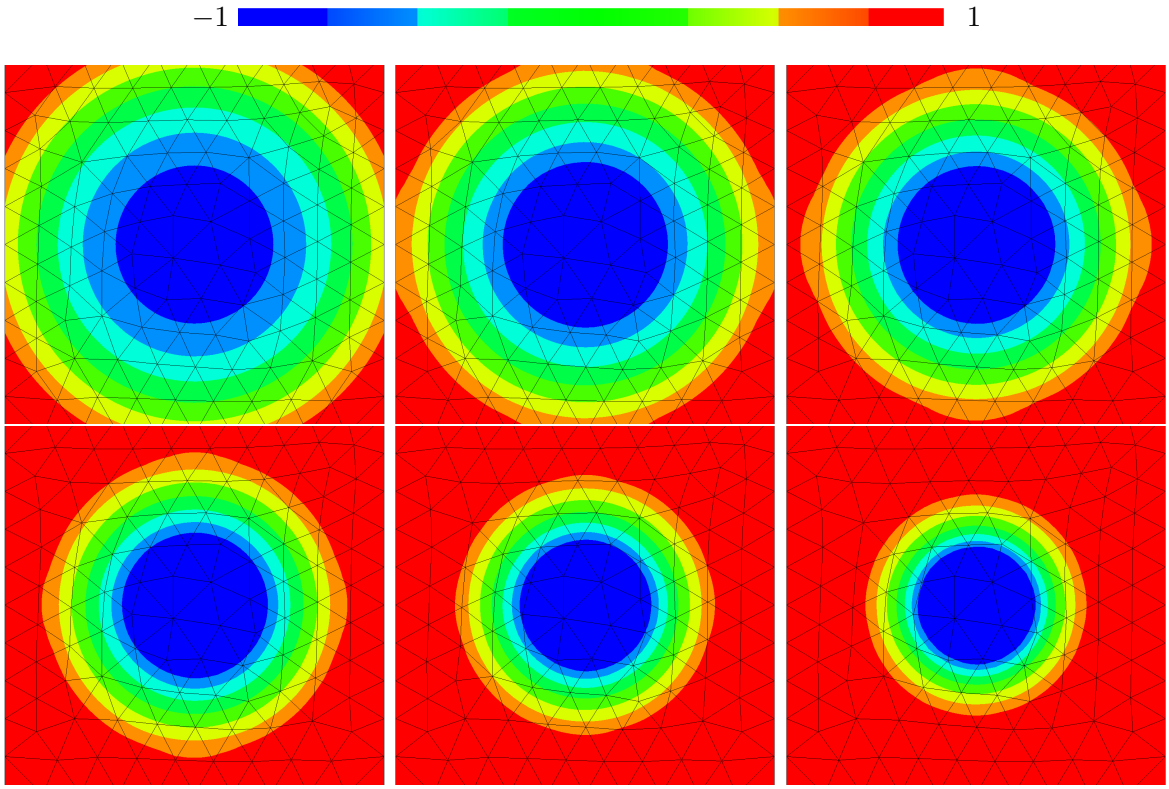

Fig. 6.1 A level set function representing a shrinking circle solved by the stabilized isoparametric TraceFEM coupled with the 4^{th}-order RKDG method. Six snapshots at six time instances.

Although the higher-order discretization methods have been applied, the experimental orders of convergence do not reach a higher rate. This is probably because of the mesh transfer operation we ignored, cf. Subsection 6.1.3.

As a bottom line, this example demonstrates that the nonlinear coupling between the two sub-models for mean curvature computation and level set transport, together as a mean curvature flow, can be achieved by using our coupling algorithms. Next, we will perform a proof-of-concept numerical simulation towards the full osmosis model.

6.2.2 Osmosis free boundary problem

As the final numerical example, we consider the fully coupled bulk-surface osmosis model, which is a two-dimensional geometrically coupled solution-curvature-driven moving free boundary problem, introduced in Section 2.4.

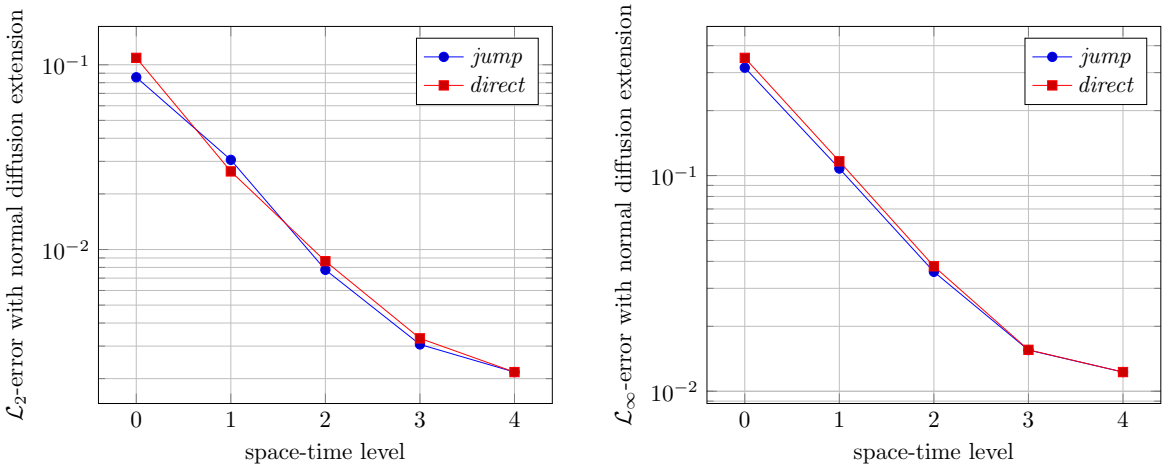

Fig. 6.2 Convergence curves of the shrinking domain area computed by the RKDG method and the stabilized isoparametric TraceFEM with normal diffusion extension. The direct version (in red) and the derivative jump (in blue) ghost peanlty are compared. Left: $\mathcal{L}^2(T)$-error. Right: $\mathcal{L}^\infty(T)$-error.

We take two initial geometries into account: a pentagram-like star polygon $\{5/2\}$ and an octagram-like $\{8/2\}$, which can be described by the level set function

$$\phi(\mathbf{x},0) = \sqrt{x_1^2+x_2^2} - (0.5 + 0.15\sin(p\ \texttt{atan2}(x_1,x_2))) = 0 \tag{6.15}$$

for $\mathbf{x} = (x_1, x_2)$ the standard Cartesian coordinate system, where $p = 5, 8$ is the number of vertices in the Schläfli symbol to denote a p-pointed star polygon, and `atan2` is the 2-argument arctangent.

On these initial domains the diffusion equation of some concentration (2.43i) is posed, with the diffusion coefficient $\nu = 1$. The initial condition (2.43k) is set to be a simple cosine function. See Figure 6.3 for the initial data and geometry.

The surface velocity in the no-flux boundary condition (2.43j) is defined by (2.43b), where the mean curvature arises from the geometric equation (2.43a). By velocity extension (2.43d) from the surface (2.43c), the velocity field is manufactured for (2.43f) to govern the evolution of the level set domain.

We plot the extended velocity vector field that drives the geometry to evolve and the contour of the varying concentration at five time instances in Figure 6.4.

From Figure 6.4 we realize that the velocity field is typically dominated by the mean curvature vector, based on the observation that the direction points inward on the convex surface and outward on the concave surface, while the concentration takes a minor effect. One may witness some kinks near the center, but we do not find

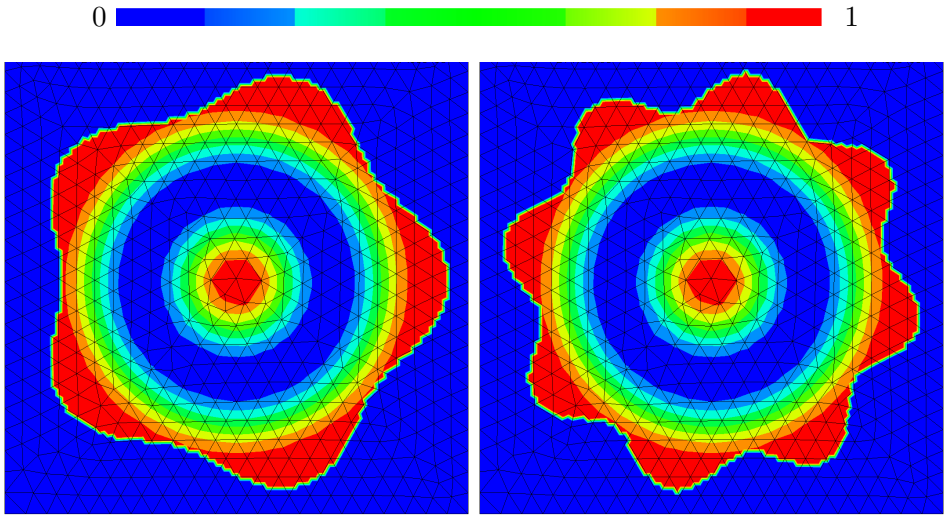

Fig. 6.3 The initial data of the diffusion equation posed on the initial geometry. Left: {5/2} pentagram; Right: {8/2} octagram; Color: The contour of the concentration.

non-smoothness when we zoom in the contours. Actually, they are just the vectors in different colors and restricted to the image quality.

We plot the contour of the concentration in a 3d view at four time instances in Figure 6.5. From Figure 6.5 we observe the diffusion phenomenon of the concentration, namely, the diffusion equation is smearing the concentration over the evolving domain. On the one hand, the concentration tends to drag the fingers out of the body, but on the other hand, the mean curvature vector drives the domain shape flowing from a star polygon towards a disk.

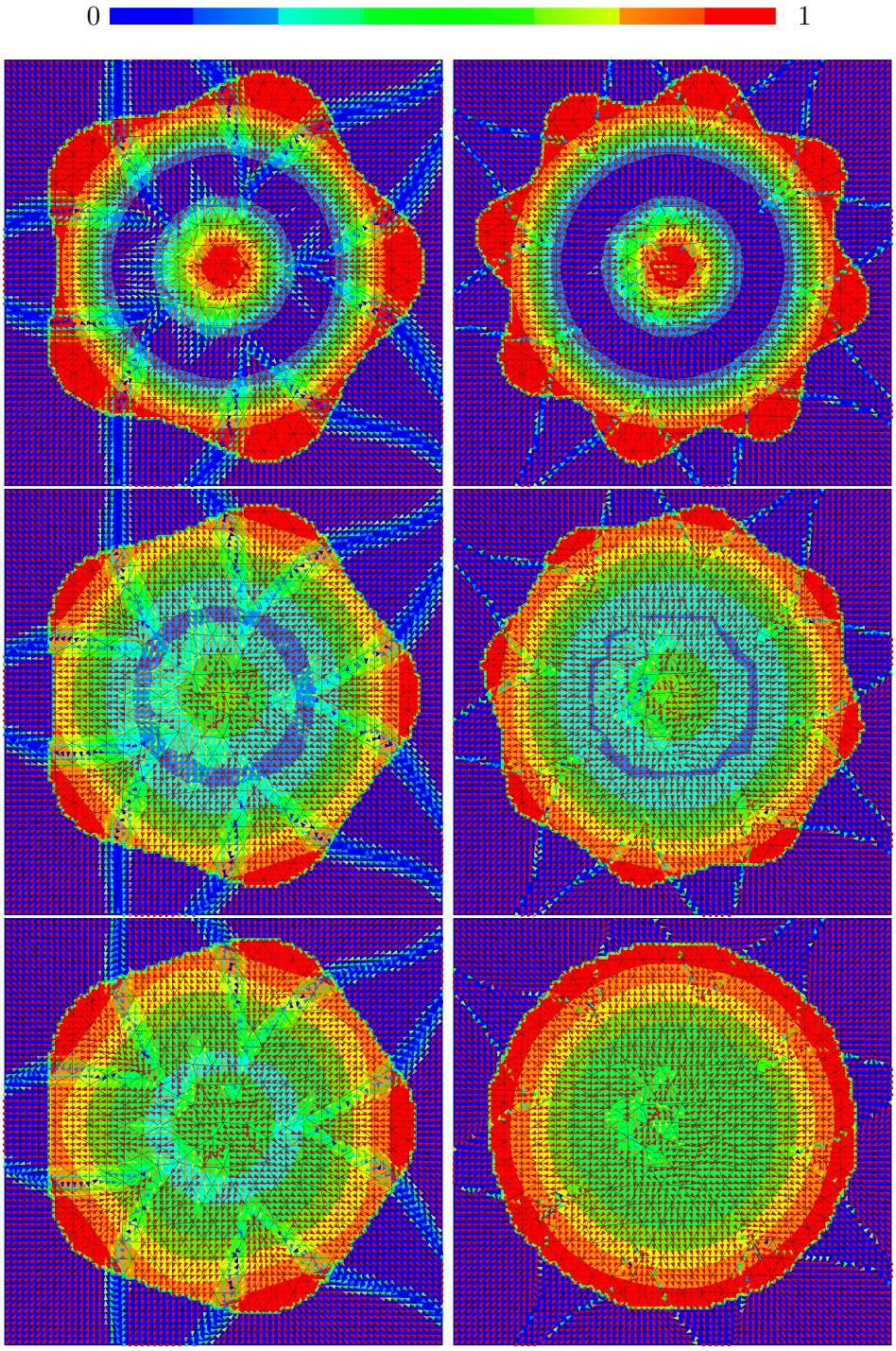

Fig. 6.4 The evolving domain with the velocity vector field and the contour of the concentration. Left: {5/2} pentagram; Right: {8/2} octagram; Color: The contour of the concentration; Vector: The velocity field.

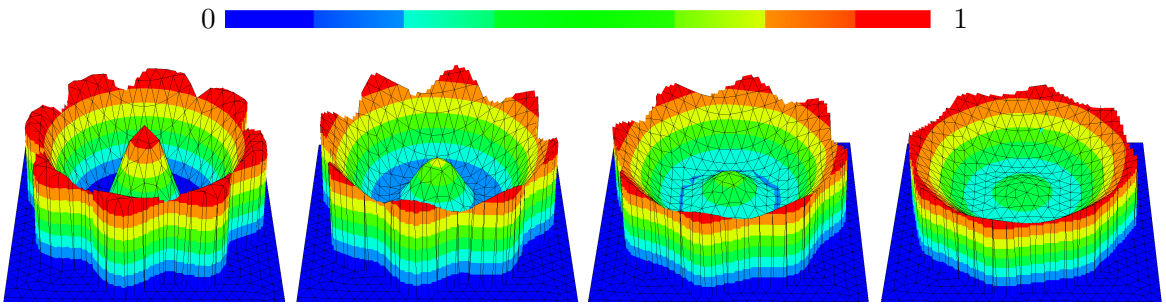

Fig. 6.5 A 3d view of the concentration on the evolving octagram-like {8/2} star polygon at four different time instances.

Chapter 7

Conclusion and Outlook

Towards the numerical simulation of the geometrically coupled solution-curvature-driven moving free boundary problem (FBP) modeled in Chapter 2, we have proposed the following discretization methods: an isoparametric BDF-Eulerian finite element method (FEM) in Chapter 3, a stabilized isoparametric trace finite element method (TraceFEM) in Chapter 4, two velocity extension methods based on ghost penalty or normal diffusion, and the Runge–Kutta discontinuous Galerkin (RKDG) FEM in Chapter 5. The numerical methods have been analyzed for provable high order of accuracy, and implemented in solving the coupled bulk-surface osmosis model in Chapter 6, where a diffusion equation is posed on a bulk evolving with a mean curvature flow of the bounding surface. In this final chapter, we summarize the most important features of these methods and the main contributions of this research. An outlook for open problems in the future work will conclude this thesis.

7.1 Summary

In this thesis, we take advantage of the geometrically unfitted discretizations for the coupled bulk-surface osmosis model where the geometry is not fitted to the underlying mesh but described implicitly by a level set function, which gives the capability of handling large deformations of the geometry. To this end, mainly two high-order unfitted discretization methods have been introduced, developed, and analyzed, namely, the isoparametric BDF-Eulerian FEM and the stabilized isoparametric TraceFEM. The former is applied for solving an advection-diffusion equation posed on a given evolving domain at provable higher order of accuracy, which is computationally efficient and robust for handling deformations or even topological changes of the geometry, and is promising to be extended for more complicated PDEs either on multi-phase

domains or on surfaces. The latter is proposed for solving the geometric equation of the discrete mean curvature vector of hypersurface, which is provably stable and arbitrarily high-order accurate. Apart from these two innovative methods, two velocity extension methods for smoothly extending the velocity from surface to bulk have also been formulated and implemented. These building blocks are constructed, together with the classical RKDG methods that solves an advection equation of the level set function in order to transport the geometry, by using strong or weak coupling strategy for the proof-of-concept simulation of the coupled bulk-surface osmosis model.

7.2 Open Problems and Future Work

As we have seen in the proof-of-concept simulation, this work towards solving the geometrically coupled solution-curvature-driven moving FBP in the sense of high-order accuracy is still very original. However, this sophisticated problem has motivated us to develop novel discretization methods that are able to solve the corresponding sub-models more accurately and efficiently. To each of these sub-models, we propose several open problems.

Firstly, to the unfitted isoparametric BDF-Eulerian FEM, it is straightforward to investigate more complicated PDE problems beyond the advection-diffusion equation. Indeed, we have tested this method with the two-phase moving interface problem in Subsection 3.3.2. A recent study on the low-order Eulerian FEM for the time-dependent Stokes problem on moving domain has been proposed in [23] and [157], where an extension to higher order of accuracy, or to the Navier–Stokes equations, is possible. Another improvement may be on the time stepping schemes other than the BDF family, where the explicit Euler scheme and the trapezoidal rule have been discussed in [89]. As an alternative the unfitted isoparametric space-time FEM in [130] can also be introduced into the coupled system instead of the Eulerian FEM. Moreover, the aforementioned methods may be further extended for PDEs from bulk to surface, cf. [103, 123, 125].

Secondly, to the stabilized isoparametric TraceFEM, one considerable open problem is the further analysis for optimal order of convergence. We have proven the arbitrarily high order of accuracy, however, the numerical experiments suggest an optimal convergence rate of $\mathcal{O}(h^{k+1} + h^q)$, which is one order better than the predicted rate of $\mathcal{O}(h^{k+1} + h^{q-1})$. The problem that if we may avoid the loss of one order of accuracy at the geometrical error is yet to be addressed. Furthermore, applying the unfitted finite element discretization to geometric objects other than the mean curvature is an

interesting topic. In particular, Deckelnick and Elliott have mentioned the Gaussian curvature and the Willmore flow in [51], and Fritz has studied the discrete Ricci curvature and the Ricci–DeTurck flow in several articles, cf. [66, 67]. Most of the works are, however, based on the fitted discretization, because in the unfitted scenario an appropriate embedding is strictly required.

Finally, to the nonlinear coupling we have found that, on the one hand, the weak coupling algorithm is computationally cheap and robust, but it may not give convergence of the solution within every time step. On the other hand, the strong coupling strategy can search the convergence point that satisfies the system of equations, but the corresponding iterations are particularly time-consuming if one chooses a small tolerance, which makes the algorithm not very applicable. Therefore, the development of an accurate and efficient linearization method based only on several consecutive solution states is a promising open problem.

To conclude, we emphasize that the potential extensions and the real-world applications of the geometrically coupled moving FBP may be far beyond the scope of this thesis, though the numerical approaches used in this thesis such as the level set method is not yet applicable to some advanced open problems. As we have stated at the beginning of Section 2.1, the idea might be extended to some geometric wave equations on a Lorentzian manifold, e.g. the Einstein field equations and the Yang-Mills equations, cf. [6, 9, 58, 147, 158, 165], which are particularly attractive to physicists and natural scientists. The study of numerical methods for geometric flows and their applications to quantum field and gauge theory seems a promising subject area, cf. [10, 12, 163]. As for the applications in state-of-the-art technology and engineering, for instance, we have seen a well-established literature regarding the numerical simulation of magnetohydrodynamics (MHD) of free surface flow for plasma physics, especially in toroidal confinement fusion reactors like a tokamak, cf. [15, 16, 69, 84, 88, 93, 117, 118, 139, 156].

Although there are still many open problems and future work to do, as Prof. David Hilbert ever said one century ago, we must know, and we will know.

Bibliography

[1] D. Adalsteinsson and J. A. Sethian, *The fast construction of extension velocities in level set methods*, Journal of Computational Physics, 148 (1999), pp. 2–22.

[2] M. Ainsworth, Mathematics of Computation, 70 (2001), pp. 1335–1337.

[3] P. Alexandroff and H. Hopf, *Topologie*, Springer, Berlin, Heidelberg, 1935.

[4] A. Alphonse, C. Elliott, and B. Stinner, *An abstract framework for parabolic PDEs on evolving spaces*, Portugaliae Mathematica, 72 (2015), p. 1–46.

[5] D. N. Arnold, F. Brezzi, B. Cockburn, and L. D. Marini, *Unified analysis of discontinuous Galerkin methods for elliptic problems*, SIAM Journal on Numerical Analysis, 39 (2002), pp. 1749–1779.

[6] M. F. Atiyah and R. Bott, *The Yang-Mills equations over Riemann surfaces*, Philosophical Transactions of the Royal Society of London. Series A, Mathematical and Physical Sciences, 308 (1983), pp. 523–615.

[7] B. Ayuso and L. D. Marini, *Discontinuous Galerkin methods for advection-diffusion-reaction problems*, SIAM Journal on Numerical Analysis, 47 (2009), pp. 1391–1420.

[8] I. Babuska, *The finite element method with penalty*, Mathematics of Computation, 27 (1973), pp. 221–228.

[9] C. Baer, N. Ginoux, and F. Pfaeffle, *Wave equations on Lorentzian manifolds and quantization*, arXiv preprint arXiv:0806.1036, (2008).

[10] I. Bakas, *Renormalization group equations and geometric flows*, arXiv preprint arXiv:hep-th/0702034, (2007).

[11] P. Bastian and C. Engwer, *An unfitted finite element method using discontinuous Galerkin*, International Journal for Numerical Methods in Engineering, 79 (2009), pp. 1557–1576.

[12] A. Bazavov and T. Chuna, *Efficient integration of gradient flow in lattice gauge theory and properties of low-storage commutator-free lie group methods*, arXiv preprint arXiv:2101.05320, (2021).

[13] R. Becker, E. Burman, and P. Hansbo, *A Nitsche extended finite element method for incompressible elasticity with discontinuous modulus of elasticity*, Comput. Methods Appl. Mech. Engrg., 198 (2009), pp. 3352–3360.

[14] T. Belytschko, N. Moes, S. Usui, and C. Parimi, *Arbitrary discontinuities in finite elements*, Int. J. Num. Meth. Eng., 50 (2001), pp. 993–1013.

[15] H. Berestycki and H. Brezis, *On a free boundary problem arising in plasma physics*, Nonlinear Analysis: Theory, Methods and Applications, 4 (1980), pp. 415–436.

[16] O. Betancourt and P. Garabedian, *Computer simulation of the toroidal equilibrium and stability of a plasma in three dimensions*, Proceedings of the National Academy of Sciences, 72 (1975), pp. 926–927.

[17] M. Botsch and O. Sorkine, *On linear variational surface deformation methods*, IEEE Transactions on Visualization and Computer Graphics, 14 (2008), p. 213–230.

[18] K. A. Brakke, *The motion of a surface by its mean curvature*, Princeton University Press, 1978.

[19] G. Bredon, J. Ewing, F. Gehring, and P. Halmos, *Topology and Geometry*, Graduate Texts in Mathematics, Springer New York, NY, 1993.

[20] S. Brendle and R. M. Schoen, *Manifolds with 1/4-pinched curvature are space forms*, arXiv preprint arXiv:0705.0766, (2007).

[21] E. Burman, *Ghost penalty*, C. R. Math. Acad. Sci. Paris, 348 (2010), pp. 1217–1220.

[22] E. Burman, S. Frei, and A. Massing, *Eulerian time-stepping schemes for the non-stationary Stokes equations on time-dependent domains*, arXiv preprint arXiv:1910.03054, (2020).

[23] E. Burman, S. Frei, and A. Massing, *Eulerian time-stepping schemes for the non-stationary Stokes equations on time-dependent domains*, Numerische Mathematik, 150 (2022), pp. 423–478.

[24] E. Burman and P. Hansbo, *Fictitious domain finite element methods using cut elements: II. a stabilized Nitsche method*, Applied Numerical Mathematics, 62 (2012), pp. 328–341.

[25] E. Burman, P. Hansbo, and M. G. Larson, *A stabilized cut finite element method for partial differential equations on surfaces: The Laplace–Beltrami operator*, Computer Methods in Applied Mechanics and Engineering, 285 (2015), pp. 188–207.

[26] E. Burman, P. Hansbo, M. G. Larson, and A. Massing, *A cut discontinuous Galerkin method for the Laplace–Beltrami operator*, IMA Journal of Numerical Analysis, 37 (2017), pp. 138–169.

[27] E. Burman, P. Hansbo, M. G. Larson, A. Massing, and S. Zahedi, *Full gradient stabilized cut finite element methods for surface partial differential equations*, Computer Methods in Applied Mechanics and Engineering, 310 (2016), pp. 278–296.

[28] J. Calvo, M. Novaga, and G. Orlandi, *Parabolic equations in time-dependent domains*, Journal of Evolution Equations, 17 (2017), p. 781–804.

[29] Y. C. Chang, T. Y. Hou, B. Merriman, and S. Osher, *A level set formulation of Eulerian interface capturing methods for incompressible fluid flows*, J. Comp. Phys., 124 (1996), pp. 449–464.

[30] G.-Q. Chen, H. Shahgholian, and J.-L. Vazquez, *Free boundary problems: the forefront of current and future developments*, Philosophical Transactions of the Royal Society A: Mathematical, Physical and Engineering Sciences, 373 (2015), p. 20140285.

[31] S. S. Chern and R. Osserman, eds., *Differential Geometry, Part 2*, vol. 27.2, Proceedings of Symposia in Pure Mathematics, American Mathematical Society, 1975.

[32] A. Y. Chernyshenko and M. A. Olshanskii, *An adaptive octree finite element method for PDEs posed on surfaces*, Computer Methods in Applied Mechanics and Engineering, 291 (2015), pp. 146–172.

[33] Q. Z. Chuwen Ma and W. Zheng, *A high-order fictitious-domain method for the advection-diffusion equation on time-varying domain*, arXiv preprint arXiv:2104.01870, (2020).

[34] B. Cockburn, J. Gopalakrishnan, and R. Lazarov, *Unified hybridization of discontinuous Galerkin, mixed, and continuous Galerkin methods for second order elliptic problems*, SIAM Journal on Numerical Analysis, 47 (2009), pp. 1319–1365.

[35] B. Cockburn and J. Guzmán, *Error estimates for the Runge–Kutta discontinuous Galerkin method for the transport equation with discontinuous initial data*, SIAM Journal on Numerical Analysis, 46 (2008), pp. 1364–1398.

[36] B. Cockburn, S. Hou, and C.-W. Shu, *The Runge–Kutta local projection discontinuous Galerkin finite element method for conservation laws. IV: The multidimensional case*, Mathematics of Computation, 54 (1990), pp. 545–581.

[37] B. Cockburn, S.-Y. Lin, and C.-W. Shu, *TVB Runge–Kutta local projection discontinuous Galerkin finite element method for conservation laws III: One-dimensional systems*, Journal of Computational Physics, 84 (1989), pp. 90–113.

[38] B. Cockburn and C.-W. Shu, *TVB Runge–Kutta local projection discontinuous Galerkin finite element method for conservation laws II: General framework*, Mathematics of Computation, 52 (1989), pp. 411–435.

[39] B. Cockburn and C.-W. Shu, *The local discontinuous Galerkin method for time-dependent convection-diffusion systems*, SIAM Journal on Numerical Analysis, 35 (1998), pp. 2440–2463.

[40] B. Cockburn and C.-W. Shu, *The Runge–Kutta discontinuous Galerkin method for conservation laws V: Multidimensional systems*, Journal of Computational Physics, 141 (1998), pp. 199–224.

[41] B. Cockburn and C.-W. Shu, *Runge–Kutta discontinuous Galerkin methods for convection-dominated problems*, Journal of Scientific Computing, 16 (2001), pp. 173–261.

[42] Cockburn, Bernardo and Shu, Chi-Wang, *The Runge–Kutta local projection P^1-discontinuous-Galerkin finite element method for scalar conservation laws*, ESAIM: M2AN, 25 (1991), pp. 337–361.

[43] R. Codina, G. Houzeaux, H. Coppola-Owen, and J. Baiges, *The fixed-mesh ALE approach for the numerical approximation of flows in moving domains*, J. Comput. Phys., 228 (2009), p. 1591–1611.

[44] W. Commons, *File:level set method.png — wikimedia commons, the free media repository*, 2020. [Online; accessed 31-December-2021].

[45] ——, *File:convex curve shortening.png — wikimedia commons, the free media repository*, 2021. [Online; accessed 31-December-2021].

[46] M. Cortez and A. Rodriguez-Bernal, *PDEs in moving time dependent domains*, (2014).

[47] J. A. Cottrell, T. J. R. Hughes, and Y. Bazilevs, *Isogeometric Analysis: Toward Integration of CAD and FEA*, Wiley Publishing, 1st ed., 2009.

[48] R. Courant, *Variational methods for the solution of problems of equilibrium and vibrations*, Bulletin of the American Mathematical Society, 49 (1943), pp. 1 – 23.

[49] C. F. Curtiss and J. O. Hirschfelder, *Integration of stiff equations*, Proceedings of the National Academy of Sciences, 38 (1952), pp. 235–243.

[50] W.-R. Dai, D.-X. Kong, and K. Liu, *Hyperbolic geometric flow (I): Short-time existence and nonlinear stability*, arXiv preprint arXiv:math/0610256, (2006).

[51] K. G. Deckelnick and C. M. Elliott, *Computation of geometric partial differential equations and mean curvature flow*, Acta Numerica, 14 (2005), pp. 139–232.

[52] L. Demkowicz, J. Kurtz, D. Pardo, M. Paszynski, W. Rachowicz, and A. Zdunek, *Computing with Hp-Adaptive Finite Elements, Vol. 1: One and two dimensional elliptic and Maxwell problems*, Chapman & Hall/CRC, 1st ed., 2007.

[53] A. Demlow, *Higher-order finite element methods and pointwise error estimates for elliptic problems on surfaces*, SIAM Journal on Numerical Analysis, 47 (2009), pp. 805–827.

[54] A. Dervieux and F. Thomasset, *A finite element method for the simulation of a Rayleigh–Taylor instability*, in Approximation Methods for Navier-Stokes Problems, R. Rautmann, ed., Berlin, Heidelberg, 1980, Springer Berlin Heidelberg, pp. 145–158.

[55] M. Desbrun, M. Meyer, P. Schröder, and A. H. Barr, *Implicit fairing of irregular meshes using diffusion and curvature flow*, in Proceedings of the 26th Annual Conference on Computer Graphics and Interactive Techniques, SIGGRAPH '99, USA, 1999, ACM Press/Addison-Wesley Publishing Co., p. 317–324.

[56] J. Donea, A. Huerta, J.-P. Ponthot, and A. Rodríguez-Ferran, *Arbitrary Lagrangian–Eulerian Methods*, John Wiley & Sons, Ltd, 2004, ch. 14.

[57] K. Ecker, *Regularity Theory for Mean Curvature Flow*, vol. 57, 01 2004.

[58] A. Einstein, *Die Feldgleichungen der Gravitation*, Sitzungsberichte der Königlich Preußischen Akademie der Wissenschaften (Berlin, (1915), pp. 844–847.

[59] C. M. Elliott and T. Ranner, *Finite element analysis for a coupled bulk-surface partial differential equation*, IMA Journal of Numerical Analysis, 33 (2013), pp. 377–402.

[60] A. Ern and J.-L. Guermond, *Theory and practice of finite elements*, Springer, New York, 2004.

[61] L. C. Evans, *Partial Differential Equations*, American Mathematical Society, 1998.

[62] A. E. Fischer and J. E. Marsden, *The Einstein equations of evolution-a geometric approach*, Journal of Mathematical Physics, 13 (1972), pp. 546–568.

[63] M. Fricke, T. Marić, A. Vucković, and D. Bothe, *A locally signed-distance preserving level set method (SDPLS) for moving interfaces*, arXiv preprint arXiv:2208.01269, (2022).

[64] T. Fries and T. Belytschko, *The generalized/extended finite element method: An overview of the method and its applications*, Int. J. Num. Meth. Eng., 84 (2010), pp. 253–304.

[65] K. Frischmuth and M. Hänler, *Numerical analysis of the closed osmometer problem*, ZAMM - Journal of Applied Mathematics and Mechanics / Zeitschrift für Angewandte Mathematik und Mechanik, 79 (1999), pp. 107–116.

[66] H. Fritz, *Finite element approximation of Ricci Curvature and simulation of Ricci–DeTurck Flow*, PhD thesis, Albert-Ludwigs-Universität Freiburg im Breisgau, March 2013.

[67] ——, *Isoparametric finite element approximation of Ricci curvature*, IMA Journal of Numerical Analysis, 33 (2013).

[68] M. Gage and R. S. Hamilton, *The heat equation shrinking convex plane curves*, Journal of Differential Geometry, 23 (1986), pp. 69 – 96.

[69] D. Giannakis, P. F. Fischer, and R. Rosner, *A spectral Galerkin method for the coupled orr–sommerfeld and induction equations for free-surface MHD*, Journal of Computational Physics, 228 (2009), pp. 1188–1233.

[70] D. Gilbarg and N. Trudinger, *Elliptic Partial Differential Equations of Second Order*, Springer, New York, 2001.

[71] R. Glowinski, T.-W. Pan, and J. Periaux, *A fictitious domain method for dirichlet problem and applications*, Computer Methods in Applied Mechanics and Engineering, 111 (1994), pp. 283–303.

[72] S. Gottlieb and C.-W. Shu, *Total variation diminishing Runge–Kutta schemes*, Math. Comput., 67 (1998), p. 73–85.

[73] J. Grande, *Eulerian finite element methods for parabolic equations on moving surfaces*, SIAM Journal on Scientific Computing, 36 (2014), pp. B248–B271.

[74] J. Grande, C. Lehrenfeld, and A. Reusken, *Analysis of a high-order trace finite element method for PDEs on level set surfaces*, SIAM Journal on Numerical Analysis, 56 (2018), pp. 228–255.

[75] J. Grande, M. A. Olshanskii, and A. Reusken, *A space-time FEM for PDEs on evolving surfaces*, in proceedings of 11th World Congress on Computational Mechanics, E. Onate, J. Oliver, and A. Huerta, eds., Eccomas. IGPM report 386 RWTH Aachen, 2014.

[76] M. A. Grayson, *The heat equation shrinks embedded plane curves to round points*, Journal of Differential Geometry, 26 (1987), pp. 285 – 314.

[77] R. E. Greene and S.-T. Yau, eds., *Differential Geometry: Partial Differential Equations on Manifolds*, vol. 54.1, Proceedings of Symposia in Pure Mathematics, American Mathematical Society, 1993.

[78] A. Grigor'yan and Y. Sun, eds., *Analysis and Partial Differential Equations on Manifolds, Fractals and Graphs*, De Gruyter, 2021.

[79] S. Gross, V. Reichelt, and A. Reusken, *A finite element based level set method for two-phase incompressible flows*, Comp. Visual. Sci., 9 (2006), pp. 239–257.

[80] R. S. Hamilton, *Three-manifolds with positive Ricci curvature*, Journal of Differential Geometry, 17 (1982), pp. 255 – 306.

[81] A. Hansbo and P. Hansbo, *An unfitted finite element method, based on Nitsche's method, for elliptic interface problems*, Comput. Methods Appl. Mech. Engrg., 191 (2002), pp. 5537–5552.

[82] P. Hansbo, M. G. Larson, and S. Zahedi, *Stabilized finite element approximation of the mean curvature vector on closed surfaces*, SIAM Journal on Numerical Analysis, 53 (2015), pp. 1806–1832.

[83] F. Heimann, *On Discontinuous- and Continuous-In-Time Unfitted Space-Time Methods for PDEs on Moving Domains*, Master's thesis, NAM, University of Göttingen, 2020.

[84] H. Huang, A. Ying, and M. Abdou, *3D MHD free surface fluid flow simulation based on magnetic-field induction equations*, Fusion Engineering and Design, 63-64 (2002), pp. 361–368.

[85] T. Hughes, J. Cottrell, and Y. Bazilevs, *Isogeometric analysis: CAD, finite elements, NURBS, exact geometry and mesh refinement*, Computer Methods in Applied Mechanics and Engineering, 194 (2005), pp. 4135–4195.

[86] G. Huisken, *Flow by mean curvature of convex surfaces into spheres*, Journal of Differential Geometry, 20 (1984), pp. 237 – 266.

[87] G. Huisken and T. Ilmanen, *The Inverse Mean Curvature Flow and the Riemannian Penrose Inequality*, Journal of Differential Geometry, 59 (2001), pp. 353 – 437.

[88] S. ichi Satake, T. Kunugi, and S. Smolentsev, *Advances in direct numerical simulation for MHD modeling of free surface flows*, Fusion Engineering and Design, 61-62 (2002), pp. 95–102.

[89] X. Jin, *Higher Order Stabilized Time Stepping in Unfitted Finite Element Method on Moving Domains*, Master's thesis, NAM, University of Göttingen, 2019.

[90] C. Johnson and J. Pitkäranta, *An analysis of the discontinuous Galerkin method for a scalar hyperbolic equation*, Mathematics of Computation, 46 (1986), pp. 1–26.

[91] G. Karniadakis, G. Sherwin, P. Karniadakis, S. Sherwin, and S. Sherwin, *Spectral/hp Element Methods for CFD*, Numerical mathematics and scientific computation, Oxford University Press, 1999.

[92] D.-X. Kong, K. Liu, and D.-L. Xu, *The hyperbolic geometric flow on Riemann surfaces*, arXiv preprint arXiv:0709.1607, (2007).

[93] T. Kunugi, S. Satake, and A. Sagara, *Direct numerical simulation of turbulent free-surface high prandtl number fluid flows in fusion reactors*, Nuclear Instruments and Methods in Physics Research Section A: Accelerators, Spectrometers, Detectors and Associated Equipment, 464 (2001), pp. 165–171. Pfoc. of the 13th Int. Symp. on Heavy Ion Intertial Fusion.

[94] W. Kutta, *Beitrag zur näherungsweisen Integration totaler Differentialgleichungen*, Zeit. Math. Phys., 46 (1901), pp. 435–53.

[95] P. LASAINT and P. RAVIART, *On a finite element method for solving the neutron transport equation*, in Mathematical Aspects of Finite Elements in Partial Differential Equations, C. de Boor, ed., Academic Press, 1974, pp. 89–123.

[96] P. D. Lax, *Functional Analysis*, Pure and Applied Mathematics: A Wiley Series of Texts, Monographs and Tracts, Wiley, 2002.

[97] C. Lehrenfeld, *The Nitsche XFEM-DG space-time method and its implementation in three space dimensions*, SIAM J. Sci. Comp., 37 (2015), pp. A245–A270.

[98] C. Lehrenfeld, *On a Space-Time Extended Finite Element Method for the Solution of a Class of Two-Phase Mass Transport Problems*, PhD thesis, RWTH Aachen, February 2015.

[99] C. Lehrenfeld, *High order unfitted finite element methods on level set domains using isoparametric mappings*, Comp. Meth. Appl. Mech. Eng., 300 (2016), pp. 716–733.

[100] ——, *A higher order isoparametric fictitious domain method for level set domains*, in Geometrically Unfitted Finite Element Methods and Applications, S. P. A. Bordas, E. Burman, M. G. Larson, and M. A. Olshanskii, eds., Springer International Publishing, 2017, pp. 65–92.

[101] C. Lehrenfeld, F. Heimann, J. Preuss, and H. von Wahl, *`ngsxfem`: Add-on to NGSolve for geometrically unfitted finite element discretizations*, Journal of Open Source Software, 6 (2021), p. 3237.

[102] C. Lehrenfeld and M. A. Olshanskii, *An Eulerian finite element method for PDEs in time-dependent domains*, ESAIM: M2AN, 53 (2019), pp. 585–614.

[103] C. Lehrenfeld, M. A. Olshanskii, and X. Xu, *A stabilized trace finite element method for partial differential equations on evolving surfaces*, SIAM Journal on Numerical Analysis, 56 (2018), pp. 1643–1672.

[104] C. Lehrenfeld and S. Rave, *Mass conservative reduced order modeling of a free boundary osmotic cell swelling problem*, Advances in Computational Mathematics, (2018), pp. 1–25.

[105] C. Lehrenfeld and A. Reusken, *Analysis of a high order unfitted finite element method for an elliptic interface problem*, IMA J. Numer. Anal., 38 (2018), pp. 1351–1387.

[106] M. Lenoir, *Optimal isoparametric finite elements and error estimates for domains involving curved boundaries*, SIAM Journal on Numerical Analysis, 23 (1986), pp. 562–580.

[107] P. Lesaint and P. A. Raviart, *On a finite element method for solving the neutron transport equation*, Publications mathématiques et informatique de Rennes, (1974).

[108] F. K. C. R. Lewy, H., *Über die partiellen differenzengleichungen der mathematischen physik*, Mathematische Annalen, 100 (1928), pp. 32–74.

[109] E. L. Lima, *The Jordan–Brouwer separation theorem for smooth hypersurfaces*, The American Mathematical Monthly, 95 (1988), pp. 39–42.

[110] F. LIPPOTH, M. A. PELETIER, and G. PROKERT, *A moving boundary problem for the Stokes equations involving osmosis: Variational modelling and short-time well-posedness*, European Journal of Applied Mathematics, 27 (2016), p. 647–666.

[111] F. Lippoth and G. Prokert, *Classical solutions for a one phase osmosis model*, Journal of Evolution Equations, 12 (2012), pp. 413–434.

[112] J. Liu, *Simple and efficient ALE methods with provable temporal accuracy up to fifth order for the Stokes equations on time varying domains*, SIAM Journal on Numerical Analysis, 51 (2013), pp. 743–772.

[113] E. Loch, *The Level Set Method for Capturing Interfaces with Applications in Two-phase Flow Problems*, PhD thesis, RWTH Aachen, September 2013.

[114] Y. Lou and C. Lehrenfeld, *Isoparametric unfitted BDF – finite element method for PDEs on evolving domains*, SIAM Journal on Numerical Analysis, 60 (2022), pp. 2069–2098.

[115] R. Massjung, *An unfitted discontinuous Galerkin method applied to elliptic interface problems*, SIAM Journal on Numerical Analysis, 50 (2012), pp. 3134–3162.

[116] R. Mittal, J. H. Seo, V. Vedula, Y. J. Choi, H. Liu, H. H. Huang, S. Jain, L. Younes, T. Abraham, and R. T. George, *Computational modeling of cardiac hemodynamics: Current status and future outlook*, Journal of Computational Physics, 305 (2016), pp. 1065–1082.

[117] S. Molokov and C. B. Reed, *Review of free-surface MHD experiments and modeling.*, U.S. Department of Energy, Office of Scientific and Technical Information, (2000).

[118] N. Morley, S. Smolentsev, R. Munipalli, M.-J. Ni, D. Gao, and M. Abdou, *Progress on the modeling of liquid metal, free surface, MHD flows for fusion liquid walls*, Fusion Engineering and Design, 72 (2004), pp. 3–34. Special Issue on Innovative High-Power Density Concepts for Fusion Plasma Chambers.

[119] N. C. Nguyen, J. Peraire, and B. Cockburn, *An implicit high-order hybridizable discontinuous Galerkin method for linear convection-diffusion equations*, J. Comput. Phys., 228 (2009), p. 3232–3254.

[120] M. A. Olshanskii and A. Reusken, *A finite element method for surface PDEs: Matrix properties*, Numer. Math., 114 (2010), pp. 491–520.

[121] M. A. Olshanskii and A. Reusken, *Error analysis of a space-time finite element method for solving PDEs on evolving surfaces*, SIAM Journal on Numerical Analysis, 52 (2014), pp. 2092–2120.

[122] M. A. Olshanskii, A. Reusken, and J. Grande, *A finite element method for elliptic equations on surfaces*, SIAM Journal on Numerical Analysis, 47 (2009), pp. 3339–3358.

[123] M. A. Olshanskii, A. Reusken, and X. Xu, *An Eulerian space-time finite element method for diffusion problems on evolving surfaces*, SIAM Journal on Numerical Analysis, 52 (2014), pp. 1354–1377.

[124] M. A. Olshanskii, A. Reusken, and X.Xu, *A stabilized finite element method for advection-diffusion equations on surfaces*, IMA J Numer. Anal., 34 (2014), pp. 732–758.

[125] M. A. Olshanskii and X. Xu, *A trace finite element method for PDEs on evolving surfaces*, SIAM Journal on Scientific Computing, 39 (2017), pp. A1301–A1319.

[126] S. Osher and R. P. Fedkiw, *Level set methods: An overview and some recent results*, J. Comp. Phys., 169 (2001), pp. 463–502.

[127] J. Parvizian, A. Düster, and E. Rank, *Finite cell method*, Computational Mechanics, 41 (2007), pp. 121–133.

[128] G. Perelman, *Finite extinction time for the solutions to the Ricci flow on certain three-manifolds*, arXiv preprint arXiv:math/0307245, (2003).

[129] C. S. Peskin and D. M. McQueen, *A three-dimensional computational method for blood flow in the heart I. immersed elastic fibers in a viscous incompressible fluid*, Journal of Computational Physics, 81 (1989), pp. 372–405.

[130] J. Preuss, *Higher Order Unfitted Isoparametric Space-Time FEM on Moving Domains*, Master's thesis, NAM, University of Göttingen, 2018.

[131] J. Pruess and G. Simonett, *Moving Interfaces and Quasilinear Parabolic Evolution Equations*, vol. 105, 01 2016.

[132] A. Rätz, *Diffuse-interface approximations of osmosis free boundary problems*, SIAM Journal on Applied Mathematics, 76 (2016), pp. 910–929.

[133] Ravindran, Sivaguru S., *Finite element approximation of dirichlet control using boundary penalty method for unsteady Navier-Stokes equations*, ESAIM: M2AN, 51 (2017), pp. 825–849.

[134] W. H. Reed and T. R. Hill, *Triangular mesh methods for the neutron transport equation*, (1973).

[135] B. Rivière, *Discontinuous Galerkin Methods for Solving Elliptic and Parabolic Equations*, Society for Industrial and Applied Mathematics, 2008.

[136] L. Rubinstein and B. Mārtuzans, *Free boundary problems related to osmotic mass transfer through semipermeable membranes*, 1995.

[137] C. Runge, *Ueber die numerische auflösung von differentialgleichungen*, Mathematische Annalen, 46 (1895), pp. 167–178.

[138] H. Samelson, *Orientability of hypersurfaces in rn*, Proceedings of the American Mathematical Society, 22 (1969), pp. 301,2.

[139] R. Samulyak, J. Du, J. Glimm, and Z. Xu, *A numerical algorithm for MHD of free surface flows at low magnetic reynolds numbers*, Journal of Computational Physics, 226 (2007), pp. 1532–1549.

[140] W. Schmaltz, *The Jordan–Brouwer separation theorem*, Lecture Notes, http://www.math.uchicago.edu/~may/VIGRE/VIGRE2009/REUPapers/Schmaltz.pdf, Dept. Math., Univ. of Chicago.

[141] J. Schöberl, *C++11 Implementation of Finite Elements in NGSolve*, Institute for Analysis and Scientific Computing, Vienna University of Technology, (2014).

[142] J. A. Sethian, *A fast marching level set method for monotonically advancing fronts*, in Proc. Natl. Acad. Sci. USA, vol. 93, 1996, pp. 1591–1595.

[143] J. A. Sethian, *A fast marching level set method for monotonically advancing fronts*, Proceedings of the National Academy of Sciences, 93 (1996), pp. 1591–1595.

[144] J. A. Sethian, *Level Set Methods: Evolving Interfaces in Geometry, Fluid Mechanics, Computer Vision and Material Science*, Cambridge University Press, 1996.

[145] ——, *Theory, algorithms, and applications of level set methods for propagating interfaces*, Acta Numerica, 5 (1996), pp. 309–395.

[146] ——, *Level set methods and fast marching methods*, Cambridge University Press, 1999.

[147] J. Shatah and M. Struwe, *Geometric wave equations*, vol. 2, Courant Lecture Notes, 2000.

[148] C.-W. Shu, *Discontinuous Galerkin method for convection-dominated time-dependent PDEs*, tech. rep., Division of Applied Mathematics, Brown University.

[149] C.-W. Shu, *Total-variation-diminishing time discretizations*, SIAM Journal on Scientific and Statistical Computing, 9 (1988), pp. 1073–1084.

[150] C.-W. Shu and S. Osher, *Efficient implementation of essentially non-oscillatory shock-capturing schemes*, Journal of Computational Physics, 77 (1988), pp. 439–471.

[151] A. Siddiqi, *Functional Analysis and Applications*, Industrial and Applied Mathematics, Springer Singapore, 2018.

[152] J. Stefan, *Über die theorie der eisbildung, insbesondere über die eisbildung im polarmeere*, Annalen der Physik, 278 (1891), pp. 269–286.

[153] B. Su, R. S. Tan, J. L. Tan, K. W. Q. Guo, J. M. Zhang, S. Leng, X. Zhao, J. C. Allen, and L. Zhong, *Cardiac MRI based numerical modeling of left ventricular fluid dynamics with mitral valve incorporated*, Journal of Biomechanics, 49 (2016), pp. 1199–1205.

[154] Z. Sun and C.-W. Shu, *Error analysis of Runge–Kutta discontinuous Galerkin methods for linear time-dependent partial differential equations*, arXiv preprint arXiv:2001.00971, (2020).

[155] B. Szabó and I. Babuska, *Finite Element Analysis*, Wiley, 1991.

[156] K. Takatani, *Mathematical modeling of incompressible MHD flows with free surface*, ISIJ International, 47 (2007), pp. 545–551.

[157] H. von Wahl, T. Richter, and C. Lehrenfeld, *An unfitted Eulerian finite element method for the time-dependent Stokes problem on moving domains*, IMA Journal of Numerical Analysis, (2021).

[158] S. Waldmann, *Geometric wave equations*, 2012.

[159] Z. Wang, *Lecture on differential manifolds: Tubular neighborhood theorem*, Lecture Notes, http://staff.ustc.edu.cn/~wangzuoq/Courses/18F-Manifolds/Notes/Lec10.pdf, School of Math. Sci., USTC.

[160] A. C. Wendler, *Monolithic Unfitted Space-Time FEM for an Osmotic Cell Swelling Problem*, Master's thesis, NAM, University of Göttingen, February 2022.

[161] Wikipedia contributors, *Level-set method — Wikipedia, the free encyclopedia*. https://en.wikipedia.org/w/index.php?title=Level-set_method&oldid=1052134992, 2021. [Online; accessed 31-December-2021].

[162] ——, *Geometric flow — Wikipedia, the free encyclopedia*. https://en.wikipedia.org/w/index.php?title=Geometric_flow&oldid=1067726842, 2022. [Online; accessed 31-December-2021].

[163] K. G. Wilson, *Confinement of quarks*, Phys. Rev. D, 10 (1974), pp. 2445–2459.

[164] Y. Xu, C.-W. Shu, and Q. Zhang, *Error estimate of the fourth-order Runge–Kutta discontinuous Galerkin methods for linear hyperbolic equations*, SIAM Journal on Numerical Analysis, 58 (2020), pp. 2885–2914.

[165] C. N. Yang and R. L. Mills, *Conservation of isotopic spin and isotopic gauge invariance*, Phys. Rev., 96 (1954), pp. 191–195.

[166] M. M. Zaal, *Well-posedness of a parabolic free boundary problem driven by diffusion and surface tension*, Mathematical Methods in the Applied Sciences, 38 (2015), pp. 380–392.

[167] S. Zahedi, *A space-time cut finite element method with quadrature in time*, in Geometrically Unfitted Finite Element Methods and Applications, Springer, 2017, pp. 281–306.

[168] Q. Zhang and C. Shu, *Error estimates to smooth solutions of Runge–Kutta discontinuous Galerkin method for symmetrizable systems of conservation laws*, SIAM Journal on Numerical Analysis, 44 (2006), pp. 1703–1720.

[169] Q. Zhang and C.-W. Shu, *Error estimates to smooth solutions of Runge–Kutta discontinuous Galerkin methods for scalar conservation laws*, SIAM Journal on Numerical Analysis, 42 (2004), pp. 641–666.

[170] ——, *Stability analysis and a priori error estimates of the third order explicit Runge–Kutta discontinuous Galerkin method for scalar conservation laws*, SIAM Journal on Numerical Analysis, 48 (2010), pp. 1038–1063.

[171] M. ZLÁMAL, *On the finite element method.*, Numerische Mathematik, 12 (1968), pp. 394–409.